



**HAL**  
open science

# Design, fabrication and characterization of a VMOS monolithic integrated optical detector

Raha Vafaei

► **To cite this version:**

Raha Vafaei. Design, fabrication and characterization of a VMOS monolithic integrated optical detector. Electric power. Université de Grenoble, 2014. English. NNT : 2014GRENT120 . tel-01317950

**HAL Id: tel-01317950**

**<https://theses.hal.science/tel-01317950>**

Submitted on 19 May 2016

**HAL** is a multi-disciplinary open access archive for the deposit and dissemination of scientific research documents, whether they are published or not. The documents may come from teaching and research institutions in France or abroad, or from public or private research centers.

L'archive ouverte pluridisciplinaire **HAL**, est destinée au dépôt et à la diffusion de documents scientifiques de niveau recherche, publiés ou non, émanant des établissements d'enseignement et de recherche français ou étrangers, des laboratoires publics ou privés.

## THÈSE

POUR OBTENIR LE GRADE DE  
DOCTEUR DE L'UNIVERSITÉ DE GRENOBLE  
**Spécialité: Génie Électrique**  
Arrêté ministériel : 7 août 2006

PRÉSENTÉE PAR

**Raha Vafaei**

THÈSE DIRIGÉE PAR **Dr. Jean-Christophe Crébier** ET  
COENCADRÉE PAR **Dr. Nicolas Rouger**

PRÉPARÉE AU SEIN DU

**Grenoble Génie Électrique Laboratoire (G2ELAB)**

DANS L'École Doctorale: **Electronique, Electrotechnique, Automatique,  
Télécommunication et Signal**

## Design, Fabrication And Characterization Of A VMOS Monolithic Integrated Optical Detector

THÈSE SOUTENUE PUBLIQUEMENT LE **1 July 2014**,

DEVANT LE JURY COMPOSÉ DE:

**M. Laurent Vivien**

Directeur de Recherche CNRS à IEF de Paris-Sud, Président

**M. Dominique Tournier**

Maître de Conférence HDR à l'INSA Lyon,

Chercheur au laboratoire AMPERE, Rapporteur

**Ms. Nathalie Batut**

Maître de Conférences HDR à Polytech' Tours,

Chercheuse au laboratoire GREMAN, Rapporteur

**Ms. Anne Kaminski-Cachopo**

Professeure à PHELMA Grenoble,

Chercheuse à l'IMEP-LAHC, Examinatrice

**M. Jean-Christophe Crébier**

Directeur de Recherche CNRS au G2ELab, Directeur de thèse

**M. Nicolas Rouger**

Chargé de Recherche CNRS au G2ELab, Co-encadrant de thèse





*Dedicated to my loving parents,  
Sara Montazemi and  
Masoud Vafaei.*



---

## Acknowledgements

The achievements during my PhD project and the experiences I have gained throughout my years here in Grenoble are the result of contributions from many people. I would like to extend my appreciation especially to the following people who have made my time here at the University of Grenoble memorable.

- First and foremost I would like to thank my supervisors Dr. Nicolas Rouger and Prof. Jean Christophe Crebier for making this research project possible and for their guidance and support throughout my thesis. Nicolas provided me with a diverse research topic that allowed me to gain experience in modelling, fabrication and characterization. Nicolas's passion and enthusiasm for scientific research had a very positive presence in my work and it inspired me to work during the good and the trying hours in the lab. Thanks to Nicolas's support I had the opportunity to attend conferences and workshops where I could interact with others in the field. I have learned a great deal from Nicolas and I will surely miss him when I leave Grenoble. I would also like to thank Jean Christophe for all his support and especially in preparation for my defense; I very much appreciated his input and advice. Having had a very limited background in power electronics when I first started here at G2ELab, I have benefited a lot from Jean Christophe's and Nicolas's in-depth knowledge in the field. I hope that I will have the opportunity to work with you again in the future.
- All my committee members, Dr. Laurent Vivien, Dr. Dominique Tournier, Dr. Nathalie Batut, Dr. Anne Kaminski-Cachopo, Dr. Jean-Christophe Crebier, and Dr. Nicolas Rouger for participating in my PhD defense and for having taken the time to read my manuscript. It is a privilege to have had the opportunity to present my work with you as my jury. I very much enjoyed our scientific discussions and I really appreciated your valuable suggestions and comments.
- Dr. Yvan Avenas for giving me the opportunity to join his research team in order to assist with the development of thermal detectors suitable for mapping temperature profiles of power components and dies.
- Dr. Benoit Thollin for his help and time in getting me up to date on the work already accomplished regarding the thermal detector project

- 
- Victor Gaude, Irene Pheng, Stephane Litaudon and Delphine Constantin for all their input and assistance during the fabrication process.
  - Loic Vincent and the Microsystem platform at Cime nanotech for their support in providing a suitable space during the characterization stage of my project.
  - Alexandre Chagoya for coming to my rescue every time I had a technical crisis with software or with my computer account at Minatec. I very much enjoyed our pleasant conversations.
  - Duc Ngoc To, Thagh-Long Le, Timothe Simonot and Julian Fernandez for their collaboration and a special thank you to Duc for his work on the first version of the experimental setups during his master internship.
  - The technical and administrative staff at G2ELab and Grenoble INP.
  - The undergraduate students who worked with me during my PhD.
  - Dr. Lukas Chrostowski, Dr. Wei shi, Dr. Behnam Faraji, Dr. Sahba Talebifard and Miguel Angel Guillen Torres with whom I have had the pleasure of working, at UBC. You have been an important part of my wonderful experience at UBC which inspired me to continue with research and science.
  - My dearest aunt Farideh, cousins Scherri and Kaveh and Gerson for driving down from Germany, Switzerland and Italy in order to attend my PhD defense. Having you there changed everything and it meant a lot to me.
  - All my amazing friends, starting with my dearest friends from around the globe, Ava Shui, Shahla Mazlooman, Hedyeh Rafii, Alison Schaap, Elin Lindon for all their support. Our friendship seems to reach beyond any distances and I am so grateful to have you as my friends.
  - Raphaelle Roy, her sweet grandmother and wonderful family for being so welcoming and making me feel at home.
  - During my time here in Grenoble, I have had the opportunity to meet so many wonderful friends. Julian Fernandez, Mathieu Leny, Jose Sanchez and Mariam Ahmed, Nathalie Sette, Andres Ovalle Villamil, Davis Montenegro and Luisa Jimena, Rachelle Hanna, Angelina Ortiz Arango, Dima Dalloul, Fanny Mesmin, Christophe Rubeck, Ni Ding, Lyubomir and Ulrike, Luiz and Cecilia, Sylvie and Morgan, Fazlollah and Nastaran, Farshid and Fatemeh, Kaustav and Ritun, and Kalle Rauma. Thank you all for the wonderful moments that have made my time in G2Elab and Grenoble unforgettable.
  - I would like to thank Julian especially for his continuous support, encouragements and kindness throughout my time here in Grenoble. Thank you for everything.
  - Last but not least, I would like to thank my parents, who have supported me throughout my life and years of education. From early on, my parents encouraged us to pursue life with passion and to not forget to question everything deeply. If I didn't

have their advice and love, I would not have become the person I am today. I would also like to thank my brother and sister for their love and for being there for me despite the gaping geographical distances.



# CONTENTS

ACKNOWLEDGEMENTS	5
LIST OF ACRONYMS	xi
NOTATIONS AND PARAMETERS	xiii
GENERAL INTRODUCTION	1
I INTRODUCTION AND MOTIVATION: INTEGRATED GALVANIC INSULATION FOR POWER DEVICES	3
I.1 POWER ELECTRONIC CONVERTERS AND POWER SEMICONDUCTOR SWITCHES	4
I.1.a Gate Driver Topologies and Insulation	7
I.1.b VDMOSFET/IGBT and their Gate Driver Requirements	9
I.1.c Towards a Fully Integrated Power Function Solution	10
I.2 GALVANIC ISOLATION FOR POWER SEMICONDUCTOR DEVICES	14
I.2.a The Need for Isolation	14
I.2.b Existing Isolation Methods	17
I.2.b-i Optical Isolation: Optocouplers	19
I.2.b-ii Inductive Isolation	21
I.2.b-iii Optical Isolation: Fiber Optics	25
I.2.b-iv Capacitive Isolation	27
I.2.c Optical Isolation: State of the Arts Under Research	27
I.3 OPTICAL DETECTION: PHYSICS AND KEY CHALLENGES	32
I.3.a Optical Absorption	33
I.3.b Photodetectors	36
I.3.b-i p-i-n and pn photodiodes	37
I.3.b-ii Schottky Junction Photodetectors: M-S, M-S-M	40
I.4 MONOLITHIC GALVANIC ISOLATION BY AN INTEGRATED PHOTO-DETECTOR (IPD)	42
I.5 THESIS OVERVIEW	50
I.5.a Methodology	50
I.5.b Organization	51
II COMPATIBLE INTEGRATED PHOTODIODES (IPDs) FOR POWER SWITCHES: MODELING, DESIGN AND TECHNOLOGY	53
II.1 INTRODUCTION	55
II.1.a IPD Structure	55

II.1.b	Design Constraints	57
II.2	FUNDAMENTALS OF DEVICE MODELLING AND SIMULATION	60
II.2.a	Built-in Potential and Depletion Region Width	60
II.2.b	Carrier Transport and Current Continuity	65
II.2.c	Photogeneration	68
II.2.d	Photocurrent	73
II.3	ANTI-REFLECTION COATING	76
II.4	STATIC ANALYSIS	81
II.4.a	DC Emitter and Collector biasing	86
II.4.b	Sensitivity to Carrier Lifetimes	91
II.5	DYNAMIC ANALYSIS	94
II.5.a	Wavelength Dependence	96
II.5.b	Emitter DC biasing	100
II.6	OPTICAL BEAM RADIUS AND POSITION ANALYSIS	102
II.7	PARASITIC ENVIRONMENT CONSTRAINTS	104
II.7.a	Electrical Activation of Parasitic BJT	104
II.7.b	Optical Activation of Parasitic BJT	108
II.8	SIMULATION AND MODELLING CONCLUSIONS AND OVERVIEW	115
<b>III</b>	<b>IPD FABRICATION AND CHARACTERIZATION</b>	<b>119</b>
III.1	INTRODUCTION	120
III.2	VD-MOSFET PLANAR FABRICATION PROCESS OVERVIEW	121
III.3	POWER BIPOLAR IPD FABRICATION PROCESS	123
III.4	IPD MASK LAYOUT DESIGNS	126
III.5	FABRICATION RESULTS	133
III.6	DC CHARACTERIZATION: SETUP AND MEASUREMENT APPROACH	138
III.6.a	First Approach: LED Light Sources	138
III.6.b	Second Approach: Xenon Light Source	142
III.6.c	MEASUREMENT RESULTS	147
III.7	AC CHARACTERIZATION: SETUP AND MEASUREMENT APPROACH	151
III.7.a	First Approach: Externally modulated LED Optical Source	151
III.7.b	Second Approach: Externally modulated Laser	152
III.7.c	Third Approach: Directly modulated Laser	154
III.8	SUMMARY	156
<b>IV</b>	<b>CONCLUSIONS AND FUTURE WORK</b>	<b>161</b>
<b>V</b>	<b>RÉSUMÉ DE LA THÈSE EN FRANÇAIS</b>	<b>165</b>
V.1	INTRODUCTION ET MOTIVATION: INTÉGRATION MONOLITHIQUE D'UNE ISOLATION OPTIQUE	166
V.1.a	L'Etat de l'Art et les Objectifs du Projet	167
V.1.b	Approches d'intégration et la Structure de IPD	171
V.2	SIMULATIONS ET CARACTÉRISATION	173
V.3	CONCLUSIONS	175

# LIST OF FIGURES

I.1	Multidisciplinary nature of power electronic design. . . . .	4
I.2	Power electronics wide application range. . . . .	5
I.3	Time line of power semiconductor devices. . . . .	6
I.4	System ratings and applications for Silicon power devices. . . . .	6
I.5	Example of a power converter and its elements. . . . .	7
I.6	Principle topology of a power electronic system. . . . .	8
I.7	Gate driver topology: energy and signal vs. signal only isolation. . . . .	8
I.8	Gate driver topology: symmetric vs. asymmetric grounded DC link. . . . .	9
I.9	Gate driver topology, transmission and insulation techniques. . . . .	9
I.10	State of the art and required future performance improvement of power electronics systems. . . . .	11
I.11	PN-insulation technology. . . . .	12
I.12	Insulation methods for monolithic integration. . . . .	13
I.13	Isolation applications. . . . .	15
I.14	Electromagnetic radiations within the system. . . . .	15
I.15	Isolated half-bridge gate driver. . . . .	16
I.16	Piezoelectric transformer and wireless transmission approach. . . . .	18
I.17	Optocoupler layout and basic mechanism. . . . .	20
I.18	Commercial optocouplers. . . . .	21
I.19	Discrete Pulse Transformer. . . . .	23
I.20	4-Channel isolation integrated. . . . .	24
I.21	Analog Devices icoupler power consumption. . . . .	24
I.22	Overview of the electromagnetic spectrum. . . . .	25
I.23	Attenuation: POF vs. GOF. . . . .	26
I.24	Fiber optic isolation. . . . .	26
I.25	Short link fiber optic approach by avago. . . . .	27
I.26	PCB integrated capacitive coupling. . . . .	27
I.27	Direct light triggered thyristor . . . . .	28
I.28	Optical triggering of 12 kV, 1 cm <sup>2</sup> 4H-SiC thyristors . . . . .	29
I.29	Hybrid-optical control by GaAs/AlGaAs based device . . . . .	29
I.30	Optical triggering by SiC bipolar transistor. . . . .	30
I.31	4H-SiC photoconductive switch . . . . .	31
I.32	Resonant gate-drive with optically isolated control signal and power supply. . . . .	32
I.33	Optoelectronic material absorption spectrum. . . . .	34
I.34	Si absorption spectrum. . . . .	34
I.35	Direct versus indirect bandgap. . . . .	35
I.36	Photodetectors with gain. . . . .	37

I.37	Depletion width tuning in Si p-i-n photodiodes....	39
I.38	Schematic structure of pn and p-i-n Photodiodes....	39
I.39	Ge pin integrated with Silicon waveguide....	39
I.40	pin-diode SFH 250 by Infineon....	40
I.41	Schematic structure of M-S and M-S-M photodiodes....	41
I.42	30 GHz MSM photodiode ...	41
I.43	40 GHz waveguide-integrated Ge MSM photodiode ...	42
I.44	Gate signal transfer approach ...	42
I.45	Hybrid integration approach ...	43
I.46	The possible solutions for an optical detector fabricated via the VDMOS process...	44
I.47	G2ELab fabricated photoreceiver, 2008 ...	44
I.48	CMOS integration approach...	46
I.49	Microscopic photos of IPDs...	46
I.50	Optical Interface Approach...	48
I.51	Optical detector and optical supply integration approach...	49
I.52	Abundance of elements in Earth crust...	50
I.53	Project perspective and approach overview...	51
II.1	IPD cross sectional view and polarization....	55
II.2	IPD simplified 1D structure cross section view showing the different regions where photogeneration may take place....	56
II.3	VD-MOSFET And Optical Detector Cross Section....	57
II.4	Integration and Control Approach...	59
II.5	IPD Input and Output Requirements...	60
II.6	Built-in junction potential and depletion region width according to the depletion region approximation....	62
II.7	Depletion Region Approximation versus Full Numerical Calculation....	63
II.8	Doping Profile Effect on the Depletion Region Approximation versus Full Numerical Calculation....	64
II.9	Carrier Mobilities in Silicon at Room Temperature....	65
II.10	Analytical modelling of the diffusion, generation and recombination dark currents for a uniformly doped pn-junction....	68
II.11	Analytical versus numerical modelling of a 1D uniformly doped pn-Junction Dark IV characteristic....	68
II.12	IPD Operation....	70
II.13	Minority Carrier modulation Due to Photogeneration....	71
II.14	Aluminium Transmittance....	72
II.15	Shadow Effect Consideration in Simulation....	72
II.16	Simple pn-Photodiode Structure....	73
II.17	Analytical modelling of the electron and hole drift and diffusion currents....	75
II.18	Analytical photocurrent model....	75
II.19	Analytical QE and Responsivity Model....	76
II.20	Optical Reflection Losses....	77
II.21	Power Reflectivity Coefficient for Si/air Interface....	78

II.22 Ideal ARC refractive Index....	78
II.23 24.7% Efficient Photocell Structure....	79
II.24 Si <sub>3</sub> N <sub>4</sub> ARC Reflectance vs. ARC Thickness....	80
II.25 Si <sub>3</sub> N <sub>4</sub> ARC Reflectivity Spectrum....	81
II.26 Si <sub>3</sub> N <sub>4</sub> ARC Reflectance Sensitivity to ARC Thickness and Wavelength....	81
II.27 Analytical Modelling: Responsivity Spectrum as a function of Biasing and Carrier Lifetime....	82
II.28 Analytical Modelling: Responsivity spectrum as a function of biasing and carrier lifetime....	83
II.29 Analytical Modelling: Responsivity spectrum as a function of optical wavelength and surface recombinations....	84
II.30 IPD Structure Cross Section View....	85
II.31 IPD dark current characteristics as a function of Emitter voltages....	86
II.32 IPD Dark Current Characteristics as a function of Collector Voltages....	87
II.33 IPD Responsivity Spectrum at 1V bias....	88
II.34 IPD responsivity spectrum dependence on Emitter DC voltages....	89
II.35 IPD responsivity spectrum dependence on Collector DC voltages....	89
II.36 Emitter Responsivity Versus Emitter and Collector DC Voltages....	90
II.37 Collector responsivity versus Emitter and Collector DC voltages....	90
II.38 Effect of Collector DC voltages....	91
II.39 Recombination rates within the IPD structure....	92
II.40 Hole Concentration Gradient versus Carrier Lifetimes....	92
II.41 Spectral Responsivity Sensitivity to Carrier Lifetimes....	93
II.42 Emitter Current Sensitivity to Carrier Lifetimes....	93
II.43 Collector Current Sensitivity to Carrier Lifetimes....	93
II.44 IPD junction capacitances versus reverse voltage....	95
II.45 The IPD simplified equivalent circuit....	96
II.46 Bode plot of the IPD frequency response....	97
II.47 Collector to Emitter photocurrent ratio....	98
II.48 IPD frequency response at 500 nm optical wavelength....	98
II.49 IPD Emitter frequency response for different optical wavelengths....	98
II.50 IPD Gain-frequency plots for different optical wavelengths....	99
II.51 IPD bandwidth as a function of the optical wavelength....	99
II.52 IPD Bandwidth as a Function of Optical Wavelength and Size....	100
II.53 IPD 3-dB Bandwidth as a function of Emitter biasing for different optical wavelengths....	100
II.54 IPD frequency response as a function of Emitter biasing for a 500 nm optical wavelength....	101
II.55 IPD 3-dB Bandwidth as a function of Emitter biasing for a 500 nm optical wavelength....	102
II.56 Photogeneration in the Base: Effect on IPD Responsivity....	103
II.57 Bandwidth sensitivity to Optical Beam. ...	103
II.58 VD-MOSFET Cross Section and Equivalent Circuit....	104
II.59 IPD Cross Section and Equivalent Circuit....	106
II.60 Substrate Transient Effect Under Dark Conditions....	107

II.61 Substrate Transient Effect Under Illumination....	107
II.62 Substrate Transient Effect as a Function of Ramp Time....	108
II.63 Photogeneration rate and Base potential gradient within the IPD structure as a function of input optical intensity at a high Collector voltage....	109
II.64 Base Potential Gradient and Emitter-Base Potential Barrier as a Function of Input Optical Intensity at a High Collector Voltage....	110
II.65 IPD Emitter and Collector behaviour versus input optical intensity at a high Collector Voltage....	111
II.66 IPD Base current behaviour versus input optical intensity at a high Collector voltage....	111
II.67 IPD Emitter and Collector Behaviour versus Input Optical Intensity at a Low Collector Voltage....	112
II.68 Potential contours and current flow lines within the IPD structure as a function of input optical intensity at a low Collector voltage....	113
II.69 Electron and Hole Concentration Profiles as a Function of Input Optical Intensity at a Low Collector Voltage....	114
II.70 Potential Profiles as a Function of Input Optical Intensity at a Low Collector Voltage....	114
III.1 VDMOS and VUMOS Structures....	121
III.2 VD-MOSFET Planar Fabrication Process Flow....	122
III.3 Bipolar IPD Process Flow....	124
III.4 Alignment Process Summary....	126
III.5 Mask Alignment Marks....	127
III.6 Mask Layout....	128
III.7 Test Modules....	129
III.8 Bipolar Transistors and Diodes....	130
III.9 Flip-Chip Integration Die Layout....	130
III.10IPD Designs with P- and P+ Base....	131
III.11IPD Cross section with DRIE Termination....	131
III.12IPD Designs with Nested Emitter Base regions....	132
III.13Example Nested IPD Design Layout Detail....	133
III.14Images of Critical Fabrication Steps....	134
III.15Fabricated IPD Designs....	136
III.16P+ Mask Leakage Test....	137
III.17IPD Emitter reverse IV....	137
III.18Previous IPD Designs....	138
III.191 <sup>st</sup> DC Setup Approach Using LED Sources....	139
III.20Newport Calibrated Detector....	139
III.212 <sup>nd</sup> DC Setup Approach Using LED Sources....	140
III.22IPD LIV with a 525 nm LED....	141
III.23IPD Responsivity for 3 Different LEDs....	141
III.24Emitter Responsivity Versus Optical Power From A 525nm LED....	142
III.25Second DC experimental setup....	143
III.26Schematic Diagram of DC experimental setup....	144

III.27	Source Optical Power Spectrum....	144
III.28	Photo of temperature Controlled chuck....	145
III.29	Temperature Control....	146
III.30	Measurement Approach....	146
III.31	Total Measurement Error....	147
III.32	IPD Current and Responsivity Measurements vs. Simulation results....	148
III.33	Substrate Breakdown Voltage....	148
III.34	Currents and Responsivity Measurements of IPD With and Without ARC....	149
III.35	The effect of contact position relative to the center of a Gaussian optical source on the IPD Responsivity....	149
III.36	The Effect of Some Different Designs on the IPD DC Responsivity....	150
III.37	The Effect of Some Different Designs on the IPD DC Responsivity....	150
III.38	High Substrate DC Voltage Effect on IPD....	151
III.39	Emitter/Base CV measurement....	152
III.40	Emitter Transient Response To A 525nm LED....	152
III.41	AC schematic and measurement setup....	153
III.42	External amplitude modulation with Green laser....	153
III.43	EOM Output versus Applied DC Voltages....	154
III.44	Step Response of The External Modulation Setup....	154
III.45	AC Setup: Direct Laser modulation....	155
III.46	IPD response to a 450 nm blue laser square signal at 10 kHz....	156
IV.1	Approach verification via a planar hybrid integration on PCB....	162
IV.2	Smart power chip integration....	164
IV.3	Smart power chip with an integrated optical chip....	164
IV.4	Optical detection and supply integration....	164
V.1	L'électronique de puissance ont une large gamme d'applications....	166
V.2	Les rayonnements électromagnétiques au sein du système....	167
V.3	Micro-transformateur....	168
V.4	Optocoupleurs....	169
V.5	Thyristor à déclenchement optique ...	169
V.6	Solutions possibles pour un photorécepteur utilisant la procédé de fabrication VDDMOS....	170
V.7	G2ELab fabricated photoreceiver, 2008 ...	171
V.8	Liaison optique appliquée à la commande des transistors de puissance....	172
V.9	Le transistor NPN vertical utilisé pour les éléments qui composent le détecteur à intégrer....	172
V.10	La représentation du circuit de l'approche d'intégration choisi et l'étude....	173
V.11	IPD réponse du spectre au polarisation à 1V....	174
V.12	Images au microscope de quelque détecteurs fabriqués....	174
V.13	Caractérisation de quelque détecteurs fabriqués. ...	175



# List of Tables

I.1	Parameters for Different Digital Isolators.....	18
I.2	Galvanic Isolation Methods .....	19
I.3	Some Selected Properties of Semiconductors Interesting for Optical and Power Electronics.....	35
I.4	Typical values of gain and response time for common photodetectors... ..	36
II.1	Summary of VD-MOSFET performance parameters dependencies on design variables.....	58
II.2	600V VDMOSFET, key layer specifications.....	58
II.3	Integrated Optical Detector Minimum Requirements .....	60
III.1	Bipolar IPD process details and specifications .....	125
III.2	Bulk and Epi Wafer Specifications .....	134
III.3	Doping Process Parameters .....	135



---

## List of Acronyms

IPD	Integrated Photo-Detector
QE	Quantum efficiency
TIA	TransImpedance Amplifier
SRP	Spreading resistance profiling
QNR	Quasi Neutral Region
ARC	Anti Reflective Coating
DUT	Device Under Test
VDMOSFET	Vertical Diffused Metal Oxide Semiconductor Field Effect Transistor
IGBT	Insulated-Gate Bipolar Transistor
BJT	Bipolar Junction Transistor
SOI	Silicon On Insulator
POF	Polymer Optical Fiber
GOF	Glass Optical Fiber
PWM	Pulse width modulation
SRH	Shockley Read Hall



---

## Notations and Parameters

Variables and Physical Constants:

Num	Symbol	Value	Unit
Acceptor Concentration	$N_A$		$cm^{-3}$
Donor Concentration	$N_D$		$cm^{-3}$
Temperature	$T$		$K$
Lifetime of electrons	$\tau_n$		$s$
Lifetime of holes	$\tau_p$		$s$
Charge of an electron	$q$	$-1,6.10^{-19}$	$C$
Permittivity of free space	$\epsilon_0$	$8,85.10^{-14}$	$F/cm$
Relative permittivity of Si	$\epsilon_R$	11,9	
Boltzmann Constant	$k$	$1,38667.10^{-23}$	$J/K$
Planck Constant	$h$	$6,6.10^{-34}$	$J.s$
Electron rest mass	$m_0$	$9,1.10^{-31}$	$kg$
Effective mass of $e^-$ in the valence band	$m_v^*$	$0,59.m_0$	$kg$
Effective mass of $e^-$ in the conduction band	$m_c^*$	$1,06.m_0$	$kg$
Thermal voltage	$V_{Th}$	$k * \frac{T}{q}$	$V$
Bandgap of Si at T=4 K	$E_{g0}$	1,12	$eV$
Bandgap of Si	$E_g$	$(E_{g0} - \frac{aT^2}{T+b})$	$eV$
Coefficient a	$a$	$4,73.10^{-4}$	$eV/K$
Coefficient b	$b$	636	$K$
Effective density of states in the conduction band.	$N_c$	$2.(\frac{2\pi m_c kT}{h^2})^{\frac{3}{2}}.10^{-6}$	$cm^{-3}$
Effective density of states in the valence band.	$N_v$	$2.(\frac{2\pi m_v kT}{h^2})^{\frac{3}{2}}.10^{-6}$	$cm^{-3}$
Intrinsic Carrier Concentration	$n_i$	$\sqrt{N_c \cdot N_v} \cdot e^{\frac{-E_g}{2kT}}$	$cm^{-3}$
Carrier thermal velocity	$v_{th}$	$\sqrt{\frac{2kT}{m^*}}.10^2$	$cm/s$
Carrier average drift velocity	$v_d$		$cm/s$
Electron mobility	$\mu_n$		$cm^2/V/s$
Hole mobility	$\mu_p$		$cm^2/V/s$
Electron diffusion coefficient	$D_n$	$\mu_n \cdot U_t$	$cm^2/s$
Hole diffusion coefficient	$D_p$	$\mu_p \cdot U_t$	$cm^2/s$
Electron diffusion path length	$L_n$	$\sqrt{D_n \cdot \tau_n}$	$cm$
Hole diffusion path length	$L_p$	$\sqrt{D_p \cdot \tau_p}$	$cm$

## Electrical Variables and Physical Constants:

Name	Symbol	Value	Unit
Built-in potential	$V_{bi}$		V
Charge density	$\rho(x)$		$C/cm^3$
Electric Potential	$\psi(x)$		V
Electric Field	$E(x)$		$V/cm$
Minority $e^-$ current density in the P region	$J_n$		$A/cm^2$
Minority $h^+$ current density in the N region	$J_p$		$A/cm^2$
Diffusion current density	$J_{diff}$		$A/cm^2$
Drift current density	$J_{dr}$		$A/cm^2$
Current density due to thermal generation	$J_{gn}$		$A/cm^2$
Current density due to thermal recombination	$J_{re}$		$A/cm^2$
Current density due to net generation and recombination	$J_{RG}$		$A/cm^2$
Resistivity	$\rho$		$\Omega \cdot cm$
Resistance of the quasi neutral N-type region	$R_N$		$\Omega$
Resistance of the quasi neutral P-type region	$R_P$		$\Omega$

## Geometric Variables:

Name	Symbol	Value	Unit
Depletion Region on the P-side of a PN junction	$X_{dp}$		cm
Depletion Region on the N-side of a PN junction	$X_{dn}$		cm
Total Depletion Region Width of a PN junction	$W_D$	$X_{dn} + X_{dp}$	cm
Position of the metallurgical junction	$X_j$		cm
Junction surface area	$A$		$cm^2$
Concentration of electrons in the N region	$n_n$		$cm^{-3}$
Concentration of electrons in the P region	$n_p$		$cm^{-3}$
Concentration of holes in the P region	$p_p$		$cm^{-3}$
Concentration of holes in the N region	$p_n$		$cm^{-3}$

## Optical Related Variables:

Name	Symbol	Value	Unit
Optical refractive index	$n$		
Optical power reflection coefficient	$R$		
Wavelength	$\lambda$		$\mu m$
Speed of light in vacuum	$c$	$3.10^8$	$m/s$
Optical absorption coefficient	$\alpha$		$cm^{-1}$
Front Surface recombination speed	$S_F$		$cm/s$
Back Surface recombination speed	$S_B$		$cm/s$
Incident optical power	$P_{opt}$		$W$
Incident optical intensity	$I_{opt}$		$W/cm^2$
Incident photon flux	$\Phi$		$Photons/cm^2/s$
Photon flux after surface reflections	$\Phi_0$	$(1 - R_{opt}) \cdot \Phi$	$Photons/cm^2/s$
Photo generation rate	$G_{op}$		$Photons/cm^3/s$
$h^+$ photocurrent density of Emitter QNR	$J_h^E$		$A/cm^2$
Photocurrent density of depletion region	$J_e^D$		$A/cm^2$
$e^-$ photocurrent density of Base QNR	$J_e^B$		$A/cm^2$
Total Photocurrent density	$J_{photo}$		$A/cm^2$
Total Photocurrent	$J_{photo} \cdot A$		$A$
Emitter Photocurrent	$I_{ph-E}$	$J_{ph-E} \cdot A$	$A$
Base Photocurrent	$I_{ph-B}$	$J_{ph-B} \cdot A$	$A$
Collector Photocurrent	$I_{ph-C}$	$J_{ph-C} \cdot A$	$A$
Emitter dark current	$I_{Dark-E}$		$A$
Base dark current	$I_{Dark-B}$		$A$
Collector dark current	$I_{Dark-C}$		$A$
Emitter total current	$I_E$	$(I_{ph-E} + I_{Dark-E})$	$A$
Base total current	$I_B$	$(I_{ph-B} + I_{Dark-B})$	$A$
Collector total current	$I_C$	$(I_{ph-C} + I_{Dark-C})$	$A$
Dark current from calibrated detector	$I_{Cal-Dark}$		$A$
Total current from calibrated detector	$I_{Cal}$		$A$
Responsivity of calibrated detector	$R_{esp-Cal}$		$A$
Dark current from device under test	$I_{DUT-Dark}$		$A$
Total current from device under test	$I_{DUT}$		$A$
Quantum efficiency	$\eta$		
Responsivity	$R$		
Emitter Responsivity	$R_E$		
Base Responsivity	$R_B$		
Collector Responsivity	$R_C$		
Rise time	$\tau_R$		$s$
Carrier transit time	$\tau_{tr}$		$s$
Carrier diffusion time	$\tau_d$		$s$
Junction capacitance	$C_j$		$F$

---

## General Introduction

In efforts of providing a high level optical solution for the galvanic isolation challenge inside power converters, more specifically between the power device and its control unit, this thesis proposes a compatible optical detector design for monolithic integration with a 600V vertical MOSFET without any modifications to the power VMOS fabrication process.

The main field of this study, is related most generally to power conversion technologies. With the widespread use of electronics in the industrial, transportation, medical and the consumer sectors, power electronic systems play a larger role in the energy equation both in terms of efficiency and cost, and thus they can have a significant impact on the environment and the economy. As a result, there is a continual interest in innovative designs which can improve the quality of energy and power conversion and management at high efficiency levels, meanwhile providing integrable generic solutions in a cost effective manner.

Power converters can be very complicated systems with many internal subsystems; nevertheless, at the heart of all power converter systems, is the power switch. The power switch places many requirements and restraints on the driving circuitry; today, it is still challenging to transfer the gating signal and sufficient energy to the power switch in a reliable and efficient manner without weight, size, design complexity, and cost penalties.

Since light provides the highest level of galvanic isolation, methods that allow its monolithic integration with the power device are of interest as the power electronic community strives for a fully integrated power function. The optical galvanic solutions proposed in the literature mainly target pulse applications based on wide bandgap semiconductors which are favoured due to their high thermal conductivity and high breakdown voltage capabilities. Compared to the recent state of the art where large laser sources are required to transfer the command signal with sufficient energy, the proposed monolithically integrated photodetector (IPD) isolates the command signal only and the required switching energy is supplied via an amplification stage. The proposed IPD fabrication is 100% compatible with the vertical power switch fabrication process and hence there are no additional cost or processing complexity penalties. This IPD can be triggered by an optical beam with a few  $\mu\text{W}$ s of power, thus it allows for a range of low power, low cost, and small optical sources such as semiconductor lasers and LEDs. The output of the optical detector will be

a current signal in the range of a few 100s of nAs. This output current signal contains only the control information; in order to provide the sufficient energy required to switch the VD-MOSFET, the output of the optical detector will be amplified at a TIA stage before feeding the gate of the VDMOSFET.

Chapter 1 of this thesis aims to motivate the reader via illustrating the dynamic context surrounding the challenges involved in creating a novel integrated galvanic isolations for drivers, as well as the current state of the art before finally introducing our proposed integrable, low power, optical isolation approach. In chapter 2, the relevant modelling approach and finite element simulation results for the possible IPD structures reveal the operation mechanisms of the IPD and its static and dynamic performances as a function of input optical wavelength, optical power, small signal frequency and IPD biasing conditions. Moreover, the limitations imposed by the vertical power device structure and the power device floating substrate potential, on the IPD performance and operation mode are analysed through modelling and simulations. The results of these analysis are used to develop best design practices for the IPDs and to identify the optimum range for values of available design variables and the optimum operation settings. The fabrication procedure and results as well as the characterization approach, the experimental setup and measurement results are provided in chapter 3. A number of different IPDs were designed with a variety of Emitter and Base doping region and contact geometrical features including nested, pixelated, and comb structures. The IPDs were coated with a  $\text{Si}_3\text{N}_4$  anti reflective coating optimized for maximum optical transmission at a wavelength of 500 nm. The spectral responsivity of the detectors from 400nm up to near infra-red wavelengths has been measured and a peak Emitter responsivity of 0.2 A/W at 500nm was achieved with the IPD Emitter reversed biased at 1V. Measurement results show a low Emitter capacitance in the range of 10pF-35pF for detectors of diameter  $50\mu\text{m}$  to  $200\mu\text{m}$ . Initial AC measurements indicate a high bandwidth above 20MHz.

## Chapter I

---

# Introduction And Motivation: Integrated Galvanic Insulation for Power Devices

---

### SOMMAIRE

---

I.1	POWER ELECTRONIC CONVERTERS AND POWER SEMICONDUCTOR SWITCHES	4
I.1.a	Gate Driver Topologies and Insulation	7
I.1.b	VDMOSFET/IGBT and their Gate Driver Requirements	9
I.1.c	Towards a Fully Integrated Power Function Solution	10
I.2	GALVANIC ISOLATION FOR POWER SEMICONDUCTOR DEVICES	14
I.2.a	The Need for Isolation	14
I.2.b	Existing Isolation Methods	17
I.2.c	Optical Isolation: State of the Arts Under Research	27
I.3	OPTICAL DETECTION: PHYSICS AND KEY CHALLENGES	32
I.3.a	Optical Absorption	33
I.3.b	Photodetectors	36
I.4	MONOLITHIC GALVANIC ISOLATION BY AN INTEGRATED PHOTO-DETECTOR (IPD)	42
I.5	THESIS OVERVIEW	50
I.5.a	Methodology	50
I.5.b	Organization	51

---

### Abstract

*In order to justify and show the function and placement of this project within the field of power electronics, we begin by giving a brief overview of where the different power transistor technologies can be applied as well as some basic information on power electronic converter topologies; the power switch structure, its basic operation and requirements with a focus on the gate driver and its galvanic isolation requirement is also introduced. Since this thesis is also tackling an integration challenge, the different integration methods used for the power switch environment are also presented in order to explain the technology choice for the optical detector in terms of compatibility and cost. A summary, comparing and contrasting the state of the art for different galvanic isolation solutions is provided in order to describe where and why the monolithic optical solution is appropriate. Also, the state of the art on optical detectors is included in order to provide the reader with a complete list of solutions in terms of design, material and technology and to justify our chosen optical detector design and system approach. The overall system topology, design and mode of operation for the proposed optical solution are presented in subsection I.4.*

## I.1 Power Electronic Converters and Power Semiconductor Switches

Power Electronic is a multidisciplinary field that requires an in-depth knowledge of several related fields as shown by the diagram of figure I.1 [1].

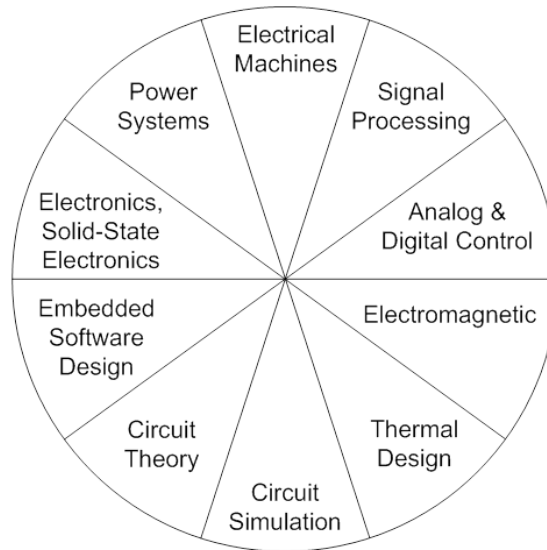


Figure I.1: Multidisciplinary nature of power electronic design. All these fields are governed under power electronic standards.

The field of power electronics is a branch of electronics that is concerned with maintaining and regulating electrical power conversions and exchanges between sources and loads [2]. In order to efficiently convert electrical energy from one form to another or to change the voltage or frequency levels or any combination of these, electrical systems called power converters are designed specific to the application at hand. One approach in classifying the different families of power converters is via considering the type of input and output signals which are either alternating current (AC) or direct current (DC) signals:

- DC-DC (Choppers): DC-DC converters convert input DC voltages to other DC voltages at the output and they can work with sources such as batteries and photovoltaic cells. Some examples of DC-DC power converters include bulk, boost, bulk-boost, half bridge and full bridge [3].
- AC-DC (Rectifier): AC-DC converters convert input AC voltages to DC voltages at the output. These converters can be found on most house appliances where electrical devices/systems require DC inputs meanwhile only AC sources are available. These converters can cover applications with a wide range of power, voltage, and frequency levels such as washers, dryers, computers, cellular phones and televisions [3].
- DC-AC (Inverters): DC-AC converters convert input DC voltages to AC voltages at the output; the voltage and frequency levels may be fixed or variable. In variable speed drives (ASDs) an input AC signal is first rectified to a DC signal and then

converted to another AC output with a different frequency and voltage level by employing a DC-AC inverter. Other examples include DC-AC inverters for photovoltaic systems, for motors control and emergency lighting. [3]

- AC-AC (Cyclo-converter): AC-AC converters such as Cyclo-converters, convert input AC waveforms to other AC waveforms with a different voltage and frequency. Some applications include compressor and wind-tunnel drives, or for variable-speed applications such as cement kilns [3].

As depicted in figure I.2, power converters are used for a wide range of applications. The voltage (volts to giga-volts) and current (milliamperes to hundreds of Amps) levels as well as the power (watts to megawatts) conversions performed by power converters are far larger than those encountered in linear electronics, making the manipulation of such large flows of power challenging both in terms of safety and efficiency as well as system volume and cost. These challenges are addressed by employing power semiconductor transistors and passive elements to create switched mode based units or otherwise known as commutation cells, that can regulate and manage flows of power between different power supplies and loads. Thus, the power switch is at the heart of all power converter systems. The emergence of power switches in the 1950s was initiated by the invention of solid state transistors at bell-labs in 1947 [4] which has revolutionized the world of electronics. In case of interest, a time line of the evolution of electronic devices with a focus on power devices is shown in figure I.3. It should be noted that diamond devices are also of high interest in the power electronic field, however, to this day there are no commercial diamond power devices available in the market where as GaAs, SiC and GaN devices are commercially available.

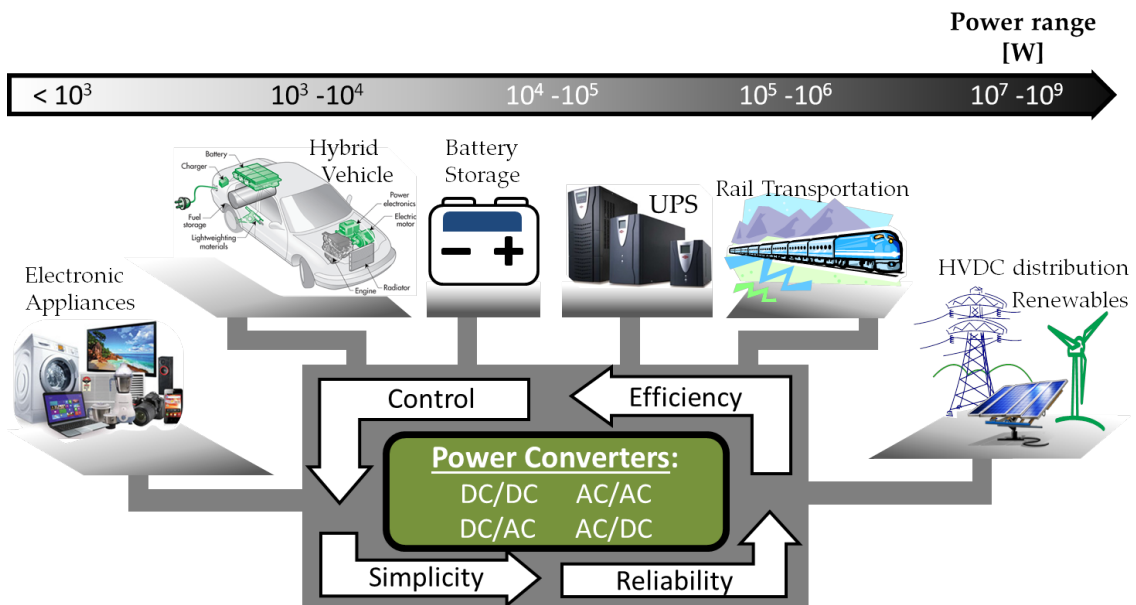


Figure I.2: Power electronic solutions are used for a wide range of applications.

There are different types of power semiconductor devices available for a specified application depending on the required control mode, voltage, current, power and frequency ratings. As summarized in figure I.4, there is a compromise between the system power

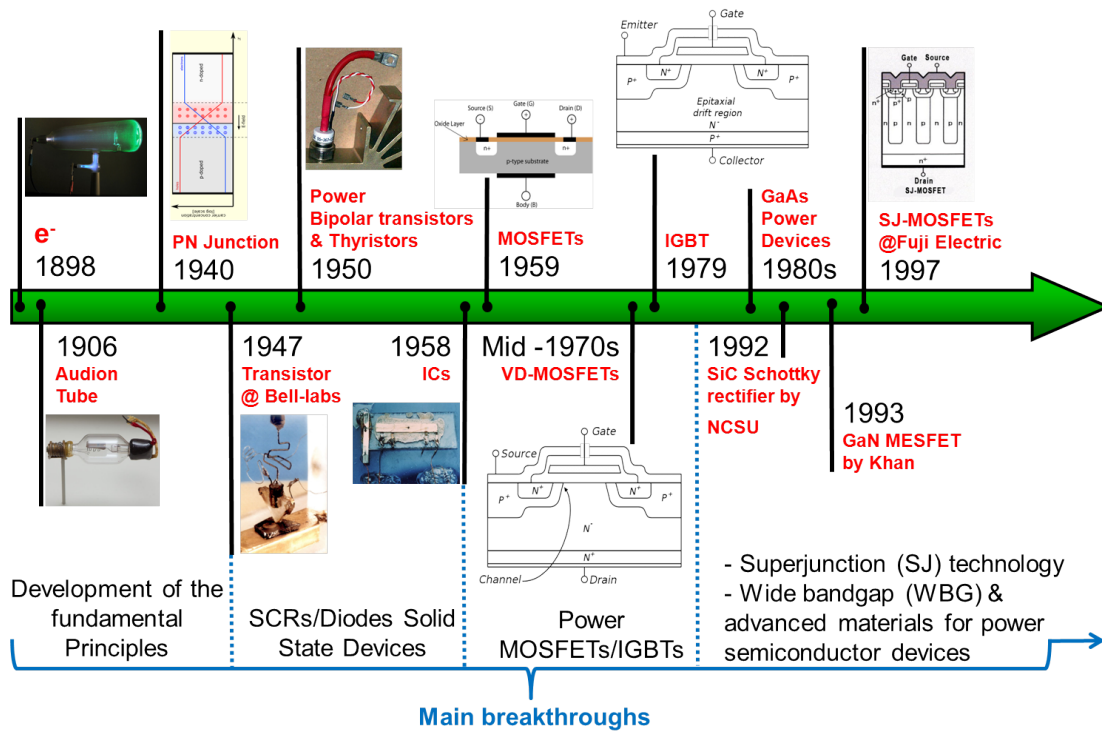


Figure I.3: Evolution of power electronic semiconductor devices.

rating and its operating frequency. Thyristors have low bandwidths but they can handle large voltages and currents, making them the optimum solution for such applications as high power HVDC transmission lines. IGBTs are suitable for a wide range of medium power and medium frequency applications that still demand a significant current handling capability: from several hundred watts in small drives to megawatts in wind power installations. Applications with higher operating frequency requirements, lower power ratings (under a few hundred watts) and lower current ratings (a few amperes), employ power MOSFET devices [5].

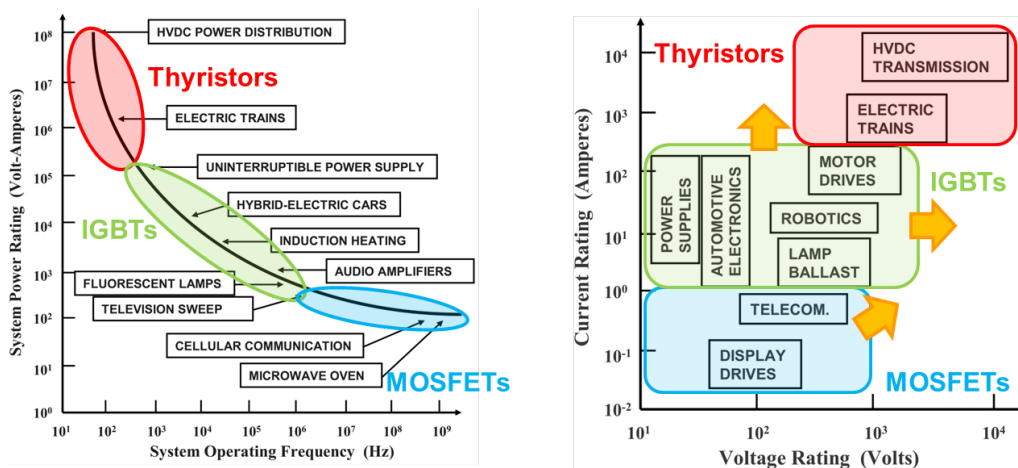


Figure I.4: System ratings and applications for Silicon power devices. The orange arrows indicate the possible extension of future devices into the not yet covered areas [5].

### I.1.a Gate Driver Topologies and Insulation

As shown in the DC-DC power converter example of figure I.5, a power converter may include many different elements including many commutation cells, passive devices used for filtering, printed circuit boards and cooling systems.

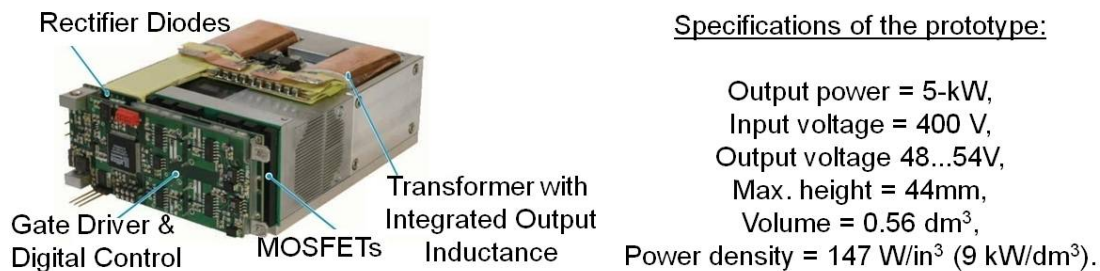


Figure I.5: Phase-shift dc/dc converter with current doubler output optimized with respect to power density [6].

In a power converter, an external micro-controller (MC) generates the gating signal patterns via pulse-width modulation (PWM) which are transmitted to the gate driver who in turn controls the switches accordingly; the controlled switches connect the load either to the supply voltage (i.e. PWM high) or to ground (i.e. PWM low). The gate driver and its extended monitoring and sensing functions provide an interface between the external MC and the power switches. Figure I.6 shows the different functional blocks involved in creating the switching action; here, the driver is divided into a primary and a secondary side and any gating information and power supply to the secondary side is transferred over inductive isolators (i.e. pulse transformer) from the primary side. This isolation is required to protect the circuits connected to the MC level potentials from the circuits connected to the potential levels of the power device and it can be implemented by two approaches as depicted in figure I.7:(a) the isolation transfers both the gating signal and the required energy to directly drive the switch as it was shown in the example of figure I.6 or (b) the isolation transfers only the gating signal to a pre-amplifying stage which will provide sufficient energy to drive the gate.

On one hand, depending on the power system topology and the voltage and power requirements of a specific application, a suitable isolation device could be chosen from the pool of isolation techniques available. On the other hand, the choice of isolation impacts the reliability and noise levels in the system as well as the driver circuitry and costs [2]. For configurations with a symmetric DC link as shown in figure I.8(a), galvanic isolation and signal insulation can be provided by isolators such as optocouplers, optic fiber, transformers, wireless RF transmission, or capacitors; these different solutions will be reviewed in the next section. For asymmetric DC link configurations, it is theoretically possible to insulate the potential of the high side driver as shown in figure I.8(b); the most common method to implement this type of potential separation is by integrating a level shifter. The main advantages of a level shifter are its low cost and ease of wafer level integration; however, this method does not provide a galvanic isolation and is only suitable for lower

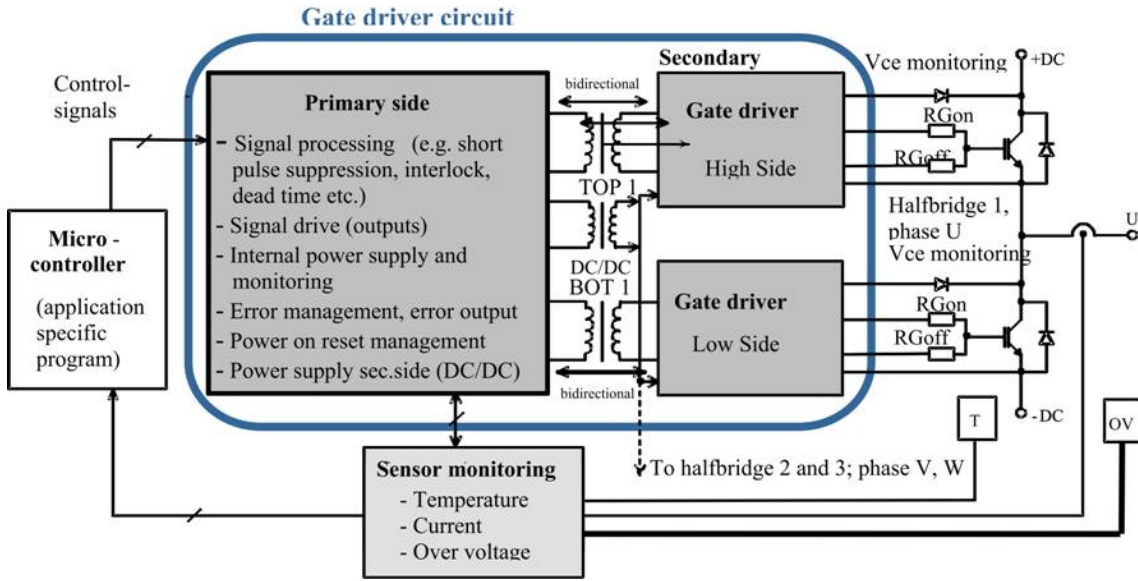


Figure I.6: Principle topology of a power electronic system showing the elements in the power switch environment. This topology is often adapted for each half bridge [2].

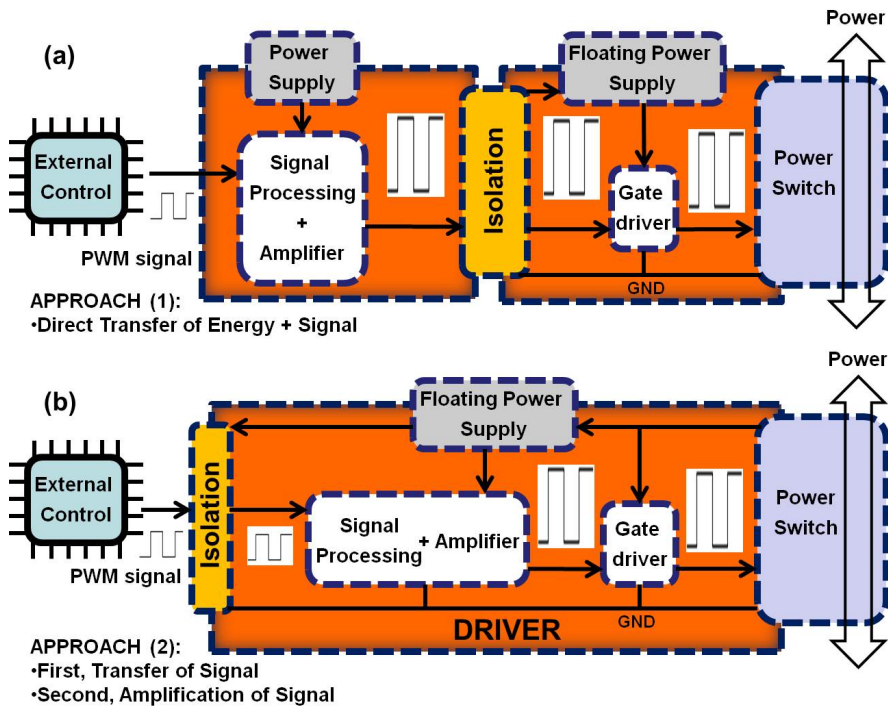


Figure I.7: Principle gate driver topology: (a)energy and signal versus (b) signal only isolation). The dashed lines represent functions that maybe be implemented discretely but also have potential for integration. For example, the power supply, and the isolation can be all integrated within the driver.

operation power levels [2]. Figure I.9 by Semikron Elektronik in 2010 shows a summary of the different isolation methods available for different driver topologies and depending on the requirement range of applications.

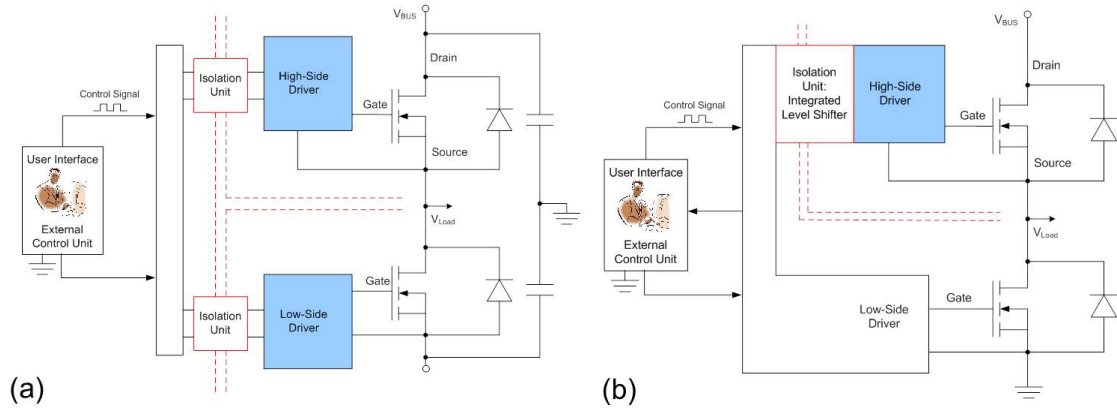


Figure I.8: (a) Example of symmetric grounded DC link with external isolation device and (b) asymmetric grounded DC link with integrated level shifter [2].

Driver type	Insulation	Signal transmission	Energy transmission	Application
Driver IC (Single, Halfbridge, Sixpack etc.)	no galvanic insulation	Level shifter (mainly for high side)	Bootstrap- circuit (for high side)	low power < 5kW
Hybrid drive (Single, Halfbridge, Sixpack etc.)	galvanic insulation	Opto-coupler Pulse transformer Fibre optic	DC/DC converter	medium power (5 ... 100 kW) high power (> 100kW)

Figure I.9: Gate driver topologies, insulation and transmission principles depending on the application range [2].

### I.1.b VDMOSFET/IGBT and their Gate Driver Requirements

As previously stated, power transistors are at the heart of the power converter. The power transistors in commutation cells switch between two states, either with a terminal voltage approximately equal to the nominal voltage level and a minimum possible current level or visa versa. The most important characteristics for power switch elements are their:

- Blocking voltages

- Passing current levels (DC current levels are limited due to rising temperatures meanwhile current pulses are limited by the layout.)
- Minimum on-state voltages which determine the conduction losses
- Minimum voltage drops during switching times which give the commutation losses
- Control mode (i.e. voltage vs. current control, turn-on and/or turn-off control).

The blocking voltage and current level are set by the specific requirements of different applications and are implemented during the design process by mainly tuning the thickness of the drift region, and the cross sectional area of the device. Although it is always desired to minimize the power losses in any application, commutation losses can be more problematic in higher frequency applications. In general, there are two main concerns regarding the switch mode operation that must be considered in any converter, (1) switching power losses (2) and the electromagnetic interferences from the large electrical entities being switched [7].

The insulating gate oxide of power MOSFET and IGBT means that no gate drive current is required during steady state operation; however, when switching, a gate drive current is required to charge and discharge the input capacitance. A large input capacitance has 2 major effects: (1) longer switching time intervals and higher losses at higher operating frequencies, and (2) a larger gate drive current requirement which in turn increases the gate drive circuit cost and size. The input capacitance can be reduced by reducing the device area, however, a smaller area translates to a higher on-state resistance and higher current densities which result in higher power transistor on-state losses per  $\text{cm}^2$ . The main compromise in the gate driver design is between a fast drive for reduced switching losses and a slow drive for reduced parasitic noises (EMC) from the voltage transients. Thus, it is desired to minimize the parasitic inductance of the drive loop in order to reduce the required switching time (i.e. smaller input capacitance) and the parasitic noises (i.e. smaller gate-drain capacitance to gate-source capacitance ratio to avoid a shoot through current). Next, the gate resistance  $R_G$  must be chosen appropriately to control the switching time of the device;  $R_G$  must be low enough to avoid a Miller drawback but large enough to control the device speed [7]. Thus one approach is to employ two  $R_G$ s in parallel; initially a large  $R_G$  is connected at the turn-on to minimize overshoots from parasitics in the power converter loop, then a second  $R_G$  is connected in parallel to reduce the overall  $R_G$  and avoid a Miller drawback. Equation 1.1 evaluates the Miller drawback limit.

$$\left[\frac{dV_D}{dt}\right]_{max} = \frac{V_{TH}}{R_G C_{GD}} [7] \quad (\text{I.1})$$

Where  $V_D$  = drain voltage,  $V_{TH}$  = threshold voltage, and  $C_{GD}$  = gate-drain capacitance.

### **I.1.c Towards a Fully Integrated Power Function Solution**

In order to identify the future of power electronics and to develop new technologies to surpass the currently faced technological barriers, a set of workshops and meetings (i.e. AIST

Power Electronics New Wave Workshops, CPES Technology Roadmap Workshops, ECPE Workshops on Power Electronics Research and Technology Roadmaps) are organized by some of the large power electronic research centres (European Center for Power Electronics (ECPE)[8], Center for Power Electronics Systems (CPES) of USA [9], Japan National Institute of Advanced Science and Technology - Power Electronics Research Center (AIST-PERC) [10]). The trends for improvements of power electronic systems was represented by J.W. Kolar and colleagues at the 6th CIPS international conference as shown in figure I.10. Furthermore, the importance of integration alongside other challenges such as packaging, reliability and cost reduction [11], has been identified as one of the technological barriers for the future vision of society in 2020.

The growing efforts of industry and research institutes towards a power integrated function has lead to the development of more complex techniques in order to integrate the low power elements with the high power elements. On the positive side, this integration reduces the number of discrete components which reduces the overall system volume and weight, lowers the costs and gains higher reliability; however, potential complications from higher voltages and currents,  $dV/dt$  and  $di/dt$  and thermal effects must be carefully considered [12][13]. In the literature, it is found that the integration of the power elements with drive, amplification and protection functions has already been achieved monolithically for lower power range ( $I < 10A$ ,  $V < 600V$ ) and in hybrid mode for the power range  $30A < I < 100A$ ,  $600V < V < 1200V$  [14].

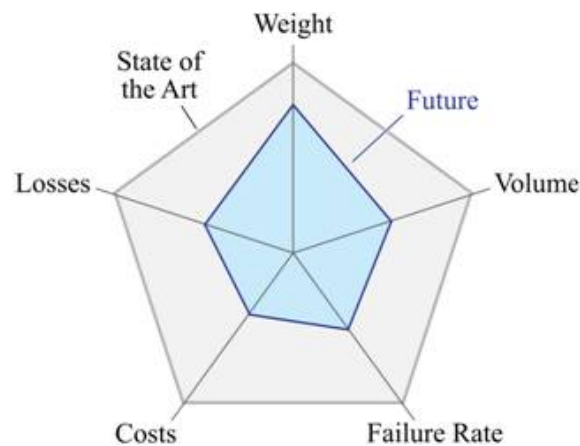


Figure I.10: State of the art and required future performance improvement of power electronics systems [14].

Since in this thesis we investigate a galvanic isolation for the monolithic mode of integration with power transistors, here, a review of the trends and methods of monolithic integration in power electronics is provided.

The key enabling technologies for the development of monolithic integration in power electronics are: (1) PN-junction insulation [15][16], (2) dielectric insulation by SOI [17]. Today by mixing these techniques, new solutions have become available.

In the literature, it has been reported that by controlling the thickness of the epitaxial layer, the level of doping concentration and the size of the edge termination structures, the PN-insulation method can be scaled for voltages from 600 V to 1200 V [2]. This technique allows the integration of sensitive analog systems that maybe required on the high side driver. The cross section of 600 V/1200 V device structures with PN-insulation that were presented by Dr. Takahashi at the 2000 CIPS meetings is demonstrated in figure I.11 (a). Photos of chips with different driver topologies and PN-termination structures fabricated by ST Microelectronics (STM) in 2003 and International Rectifier (IR) in 2008 are shown in figures I.11 (b), (c) and (d). The PN-insulation technology has its drawbacks. The leakage currents from the PN structures lead to self-heating (limiting the maximum operating temperature to roughly 150 ° C) and increased losses. Also and even more importantly, the internal parasitic thyristor structures can be activated in case of negative voltage transients at the driver output. Some solutions have been proposed [18], however they do not completely eliminate this issue [2].

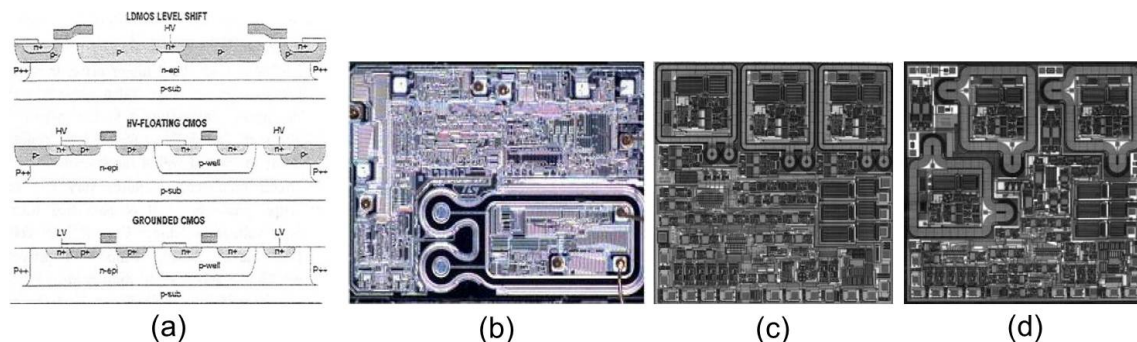


Figure I.11: (a) Fundamental device structures of a 600 V/1200 V PN-insulation technology [19]. ICs in PN-junction insulation by different manufacturers: (b) 600 V, 650/400 mA Halfbridge-driver with differential level-shifters embedded within the termination structure by STM [16] (c) 600V, 500/250mA Sixpack-driver with level-shifters located separately by IR [20] (d) 1200V, 500/250mA Sixpack-driver with differential level-shifters embedded within the termination structure by IR [20].

The use of SOI technology provides insulation by means of a dielectric layer; as a result, the issue of the parasitic turn-on of the internal thyristor that existed in the PN-insulation structures is eliminated. This has allowed the full integration of bipolar devices (i.e. IGBTs and diodes) and their driver and monitoring functions on a single chip. Figure I.12 (a) shows the cross sectional view of some of the fundamental device structures of a 500 V SOI-CMOS platform by Mitsubishi [21]. Figure I.12 (b) shows an integrated gate driver and 500 V, 1 A inverter in SOI [22]. In 2010, the university of Tennessee reported a SOI based integrated gate driver for high voltage and high temperature SiC FETs [23]. The drawbacks of SOI insulation in comparison to PN-junction termination is mainly the implementation cost. Although SOI technology allows the integration of high voltage devices, current levels are still limited due to the lateral structure of the integrated devices.

Insulation of low voltage components by formations of P+ walls is a mixed technology



Integration of piezo-resistive galvanic solutions fabricated on silicon membrane devices are also anticipated to emerge in the future [12].

## I.2 Galvanic Isolation for Power Semiconductor Devices

Isolation circuits provide protection against unwanted and/or hazardous voltages and currents. The maximum permissible signal noise level and EMI requirements are important considerations in any power converter design and even more so when integrating sensitive control functions closer to the power unit. It is crucial for the integrity of the system to carefully consider the thermal and electromagnetic interactions between the different functions in the system.

An EMI filter should provide immunity against high frequency current and voltage transients, parasitics, stray inductances and coupling capacitances. There are internal perturbation sources such as the magnetic fields around high power devices (e.g. power transistors and power diodes), and external sources of EMI such as high power cables, motors, RF radiations or other sources in the environment that must be considered in the design process.

After giving a basic review on the needs for isolation, the existing isolation methods are discussed, compared and contrasted.

### I.2.a The Need for Isolation

Figure I.13 gives an overview of the basic applications for circuit isolation; their needs are: (a) user safety, (b) equipment/circuit protection from high  $dv/dt$  or  $di/dt$ , (c) noise perturbations, (d) and ground loops. In an electrical system there are different number of signals flowing through different paths at all times; any unwanted interactions between these signals may degrade high-fidelity signals, damage components, jeopardize the overall system and/or cause harm to the user. A signal flowing through an electrical system may experience interferences from errors induced due to ground loops, floating supplies and floating references [7]. Depending on the signal levels, distances between conducting paths, and the surrounding material permittivity and permeability, electromagnetic interferences could be induced through capacitive or inductive coupling. Electromagnetic and heat (thermal management challenges are not studied in this thesis) radiations between the different power switch functions on the driver side are two main challenges that need to be carefully considered during the design stage [27]; these interactions are depicted in figure I.14. These problems are solved by implementing isolation components where necessary such that the flow of information is uninterrupted meanwhile unwanted currents are blocked [28].

Applications with a size limitation (i.e. cell phones), require high frequency gate drivers in order to allow for the size reduction of the output passive filters. As already discussed, MOSFETS are superior to IGBTs and power BJTs for higher frequency and medium to low power applications where the switching losses dominate the overall power losses [7].

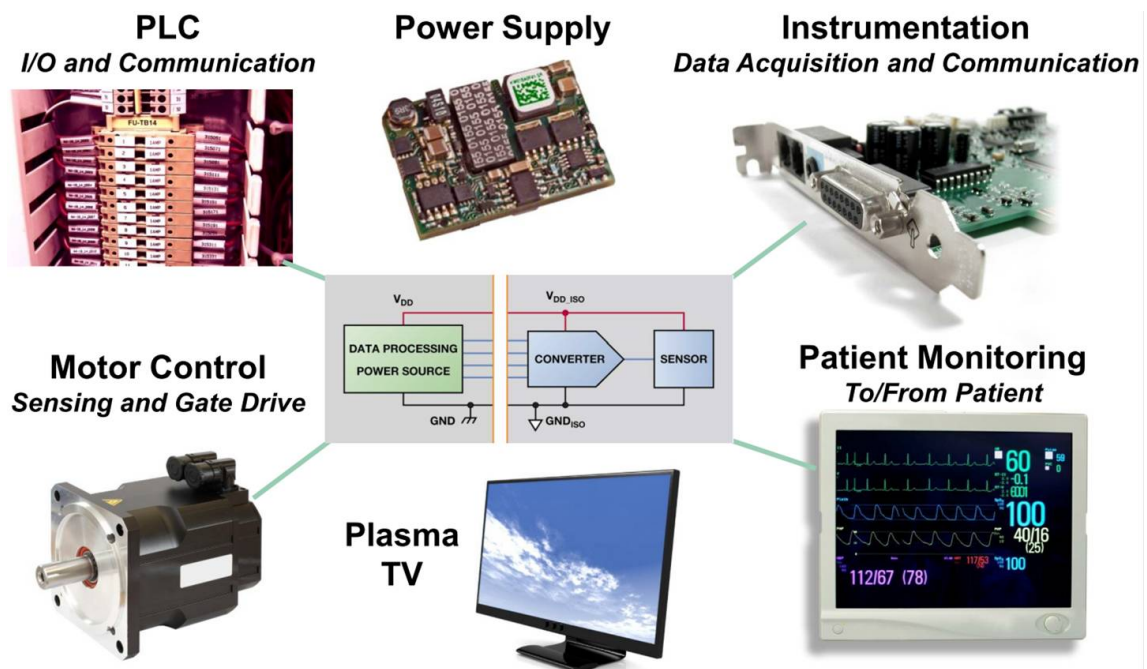


Figure I.13: Applications in need of Isolation. [29].

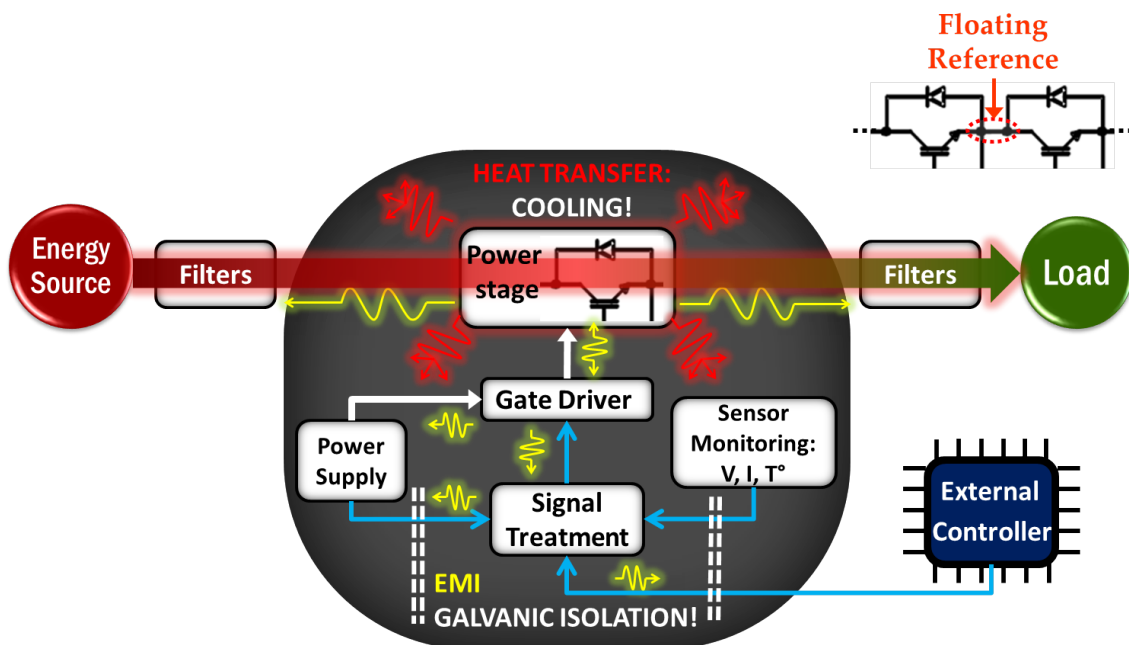


Figure I.14: Electromagnetic and thermal radiations between the power switch functions within the system.

Fully integrated driver solutions are highly desirable, since bringing the driver as close as possible to the power MOSFET will reduce interconnections and the parasitic elements (inductances and capacitance) that could contribute to the switching losses. This trend of miniaturizing and integrating all the power functions closer to the power switch requires the design and implementation of integrated galvanic isolations in order to insure the safety of the low power circuitries from the high power units.

In power converters, the high voltage transients of the middle point of the commutation cell are a major source of conducted and radiated EMI. In the basic half-bridge example shown in figure I.15 the source of the high-side power transistor is floating; depending on the state of the transistor, the voltage of the source can be anywhere between zero volt and that of the bus voltage. In the series connected configurations, the high side driver may need to apply very large voltages to the gate, in order to achieve the gate-source threshold (e.g. 15V to 20V or 2V to 3V). In example, for a switch with a 15 V gate-source threshold, if the bus voltage is at 600 V and the high-side transistor is ON, then  $V_s = 600$  V; now, if the transistor must remain ON, at least 615 V must be applied to the gate to achieve the minimum required  $V_{gs}$  potential difference of 15 V.

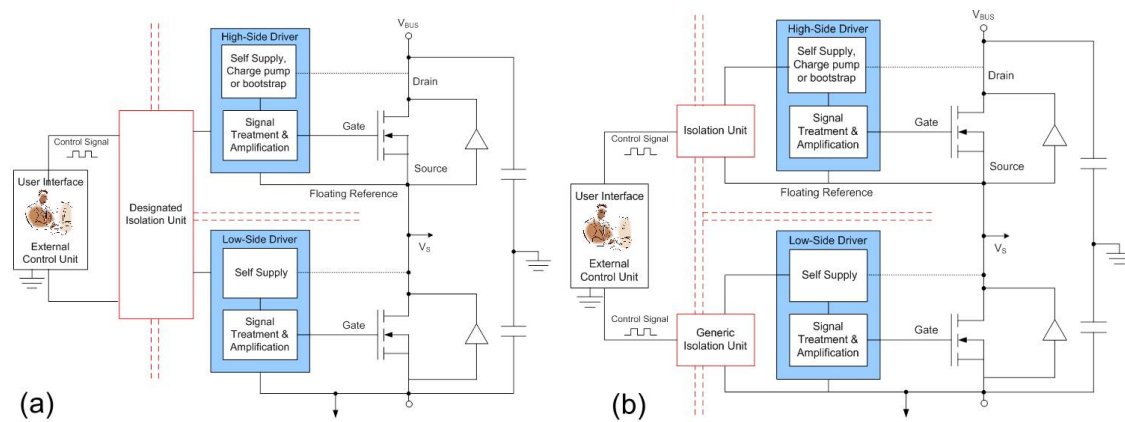


Figure I.15: (a) Dedicated and (b) generic dual isolation system for a high voltage half-bridge gate driver.

There are different configurations available for the high-side driver supply with one of the most common being the 'bootstrap'. In the bootstrap configuration the energy required for the gate is stored in an external capacitor, moreover, a separate bus voltage from the power transistor bus is required. Self supply approaches for driving the high-side [30] have also been developed, where the energy for the gate is drawn from the same bus line that supplies the power functions. In all the different types of drivers, the gate signal is isolated by one of these classical methods: electromagnetic or piezoelectric transformers (pulsed or digital) [31] [32] [33] [34] [35], optocouplers [36] [37] [38] [39], optical-fibers, capacitive couplers [40], HF wireless transmitter and receiver [41] or level shifters [42].

An ideal galvanic isolation unit should transmit the gating information under the following conditions:

- No signal degradation in terms of amplitude, frequency or phase
- No difference in propagation delay time between multiple channels also known as channel to channel skew
- No propagation time delay for an isolator input event to appear at the isolator output
- Infinite immunity against electric and magnetic field radiations
- No power consumption penalty
- No cost penalty
- Infinite common-mode transient immunity (the ability to reject fast common-mode transients such as high or noisy currents in ground conductors)
- No output impedance
- No footprint penalty
- Scalable and easy to integrate in the driver.

This ideal list considers only the galvanic isolation of the information signal; if the galvanic isolation unit is also to provide the gating signal energy, then it must be able to transfer the necessary gating signal voltage levels as well. These two different solutions (i.e. signal only or signal + energy isolation unit) were presented earlier in figure I.7. Although the ideal isolation solution does not exist, the functional list above serves as a benchmark for evaluating the different types of isolation methods available in the industry and the latest proposals made by research institutes.

### I.2.b Existing Isolation Methods

The datasheets of different manufacturers and suppliers reveal that in general, the required isolation for driving power semiconductors (e.g. IGBTs and MOSFETs) with reverse voltage ratings as high as 1200 V - 1700 V is provided by transformers [43]; however, for higher blocking voltages, optical solutions are more suitable. Meanwhile, for blocking voltages below 600 V - 800 V all the different isolation techniques can be employed such as: transformers (integrated-planar or discrete pulse transformers), optocouplers, fiber optics (not worth the costs here), capacitive isolators, magneto-resistors, piezoelectric isolators. RF transmitter/receivers and piezoelectric drivers are under research [31] [44]; figure I.16 (a) and (b) show examples of a piezoelectric transformer and wireless transmission approach for MOSFET and IGBT drivers respectively.

From all the available solutions, the most common isolation techniques are achieved through the following mechanisms: optical coupling, inductive coupling or capacitive coupling. A comparison of the different digital isolation methods is shown in table I.1.

On one hand, optical couplers and digital transformers are much more efficient in terms of size and cost in comparison to optical fibers and pulse transformers. On the other hand,

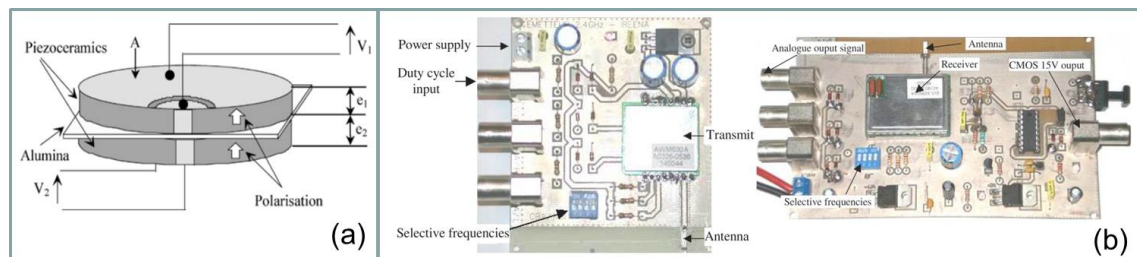


Figure I.16: (a) Typical structure of the piezoelectric transformer matched to the gate driver [31] (b) The experimental transmitter and receiver used for the wireless IGBT drive control [44].

Coupling Method	Bandwidth	Transient Immunity $dV/dt$	UL1577 (VRMS)	Magnetic Field Immunity
Inductive	50-100 Mbps	$\sim 25-75 \text{ kV}/\mu\text{s}$	$\sim 2.5-5 \text{ KV}$	
Optical (Discrete)	25-50 Mbps	$\sim 10-50 \text{ kV}/\mu\text{s}$	$\sim 3.75-7.5 \text{ KV}$	+
Capacitive	150 Mbps	$\sim 25 \text{ kV}/\mu\text{s}$	$\sim 2500 \text{ V}$	++

Table I.1: Parameters for Different Digital Isolators. This information was collected from the datasheets of different suppliers such as Texas Instruments[45], Avago Technology[46], Fairchild, and Analog Devices[43]. Note that the transient immunity limit of optocouplers is due to the close proximity of the LED and the detector as imposed by the packaging; this is explained in section I.2.b-i.

optical couplers and digital transformers can't transmit sufficient energy for the driver electronics and thus they require an amplification step; moreover, they are suitable for applications with small to medium voltages. Of course, pulse transformers can be used to deliver both the signal and the energy for small to medium application, but at higher voltages ( $>1200 \text{ V}$ ) the transformer starts to consume too much space on the PCB; this is where optical fibers are most practical. A summary of the main advantages and disadvantages of each of the isolation methods is given in table I.2.

Method	Advantages	Disadvantages
Pulse Transformer	<ul style="list-style-type: none"> <li>• Energy + Data transfer</li> <li>• High frequency</li> <li>• High insulation</li> </ul>	<ul style="list-style-type: none"> <li>• AC signal transfer only</li> <li>• Large footprint on PCB</li> <li>• Hybrid construction methods only</li> <li>• Suceptibility to transients</li> </ul>
Coreless Transformer	<ul style="list-style-type: none"> <li>• Cost</li> <li>• Ease of integration</li> <li>• High frequency</li> </ul>	<ul style="list-style-type: none"> <li>• No energy transfer</li> <li>• Suceptibility to transients</li> </ul>
Piezoelectric Transformer	<ul style="list-style-type: none"> <li>• High frequency</li> </ul>	<ul style="list-style-type: none"> <li>• No energy transfer</li> <li>• Limited insulation voltage</li> </ul>
Optocoupler	<ul style="list-style-type: none"> <li>• AC + DC data transfer</li> <li>• Cost</li> <li>• Inherently immune to EMI</li> </ul>	<ul style="list-style-type: none"> <li>• No energy transfer</li> <li>• Poor timing (propagation delays + slow rise and fall times)</li> <li>• Power consumption</li> </ul>
Fiber Optic	<ul style="list-style-type: none"> <li>• AC + DC data transfer</li> <li>• No coupling capacity</li> <li>• Inherently immune to EMI</li> </ul>	<ul style="list-style-type: none"> <li>• No energy transfer</li> <li>• Cost</li> </ul>
Capacitive	<ul style="list-style-type: none"> <li>• Cost</li> <li>• Immune to magnetic fields</li> </ul>	<ul style="list-style-type: none"> <li>• High coupling capacitance</li> <li>• No energy transfer</li> <li>• AC signal transfer only</li> </ul>

Table I.2: Galvanic Isolation Methods

### I.2.b-i Optical Isolation: Optocouplers

The value of optical isolation through the use of a semiconductor emitter and a detector was first recognized in 1963 by Akmenkalns, et al. (US patent 3,417,249) [47]. Today, optocouplers are the predominant form of isolation and are very reliable for isolating feedback paths from the high power units to the control unit, for transmitting gating signals to a circuit floating at high voltages, or for isolation of high precision and low-level circuitries that are sensitive to noise [48].

In an optocoupler, an optical detector absorbs light emitted by an LED and converts it back into a current that can be sensed at the output. The LED emission should match the absorption spectrum of the detector for improved efficiency. Additional circuitry is needed on the input side to drive the LED, and on the output side to treat (demodulate, amplify, generate voltage) the induced current signal. The LED and the photodetector are packaged together in close proximity. The space between the emitter and the detector is filled by a transparent dielectric such as glass or plastic. The wire bonding configuration, the distance between the LED and the detector and the dielectric constant of the transparent filling determine the breakdown voltage and the transient limitations of the optocoupler. Figure I.17 shows the cross section view of the two main physical layouts found inside the standard dual in-line optocoupler packaging. In comparison to the planar layout, the silicon dome layout offers a higher precision in alignment between components and allows for larger gaps which in turn offer a higher voltage breakdown and transient performance.

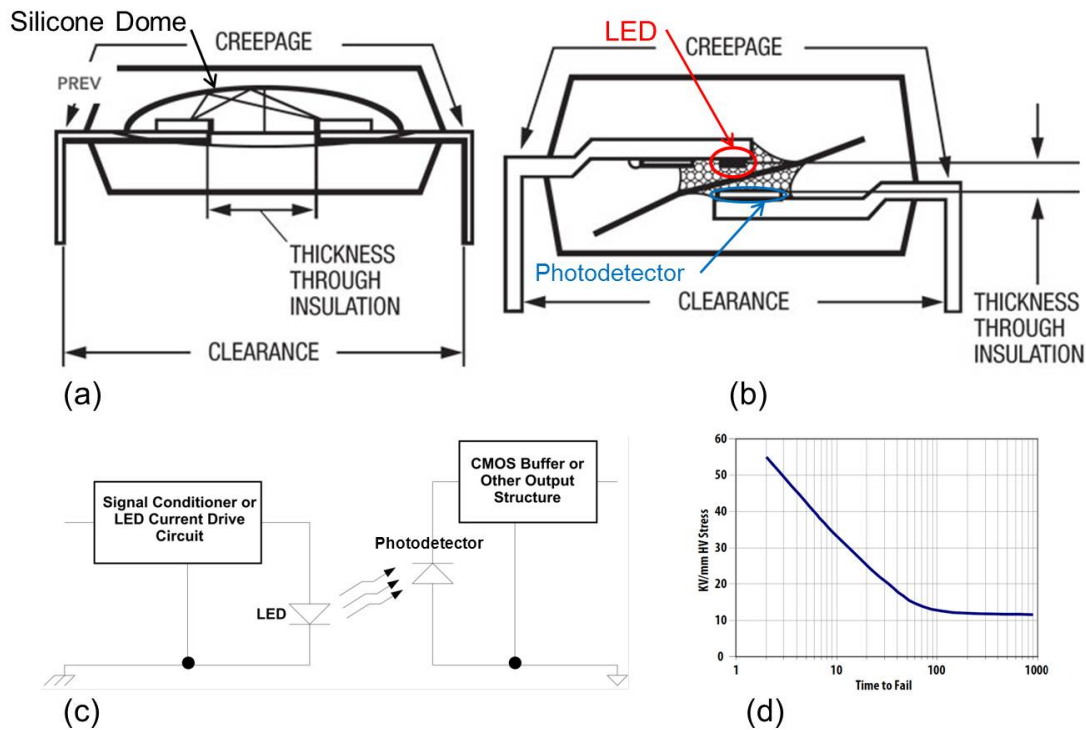


Figure I.17: Optocoupler layout in standard dual in-line packaging and basic mechanism.(a) Silicone dome layout [49](b) Planar layout [49](c) Basic optocoupler mechanism [45] (d) Insulation aging effect. Typical Polymer space charge degradation characteristic [28].

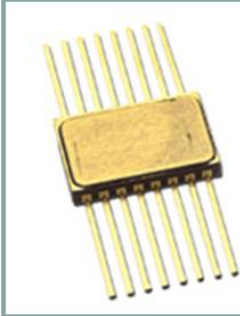
Moreover, the transparent silicone dome surrounding the LED and the detector minimizes losses by reflecting all stray light rays back onto the detector surface.

Optocouplers benefit from their inherent immunity to external electromagnetic radiation, their compatibility with both AC and DC transmission, and their well developed and low-cost fabrication technology; however, they suffer from reliability and performance issues that render them impractical for certain range of applications. The shortcomings of optocouplers stem from the inherent problems of LEDs and photo-detectors; moreover, as mentioned earlier, packaging sets the upper limit on the operating transient ( $10 \text{ kV}/\mu\text{s}$ ) and breakdown voltage ( $<10 \text{ kV}$  for specific solutions). Figure I.18 shows some examples of commercial optocouplers offered by Avago.

Optocouplers have a low current transfer ratio CTR (ratio of LED driving current to photodetector output current) due to the inefficiency of the photodetector in converting the light produced by the LED source into current. Typically, an LED current of 5 to 25 mA is required to turn on the photo-detector. In addition, LED's emission drops over its lifetime, requiring higher driving currents for the same output optical power. This is a reliability issue that is accelerated at higher temperatures and higher operating frequencies [32] [45].

10-Pin**	Wide Body**	8-Pin**		S016		(a)
						Package
13.0 13.0	10.0 9.6	8.0 7.4	7.4 7.1	8.3 8.3	4.5 4.9	Creepage (mm)
2.0	1.0	0.5	0.08	0.5	0.08	Clearance (mm)
2262	1414	891	630	1230	560	Internal Clearance (mm)
7500	5000	3750/5000	3750	5000	2500	IEC/EN/DIN EN 60747-5-2/5 $V_{norm}$ ( $V_{peak}$ )
						UL 1577 $V_{iso}$ ( $V_{rms}$ )



(b)

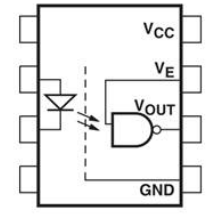


Figure I.18: Commercial optocouplers.(a) Some plastic optocouplers by Avago [50]. (b) HCPL-665K, hermetically Sealed, High Speed: 10 Mbd, High CMR: > 10,000 V/ $\mu$ s, 2500 Vdc withstand test, Logic Gate Optocouplers [51].

Other problems with optocouplers originate from the fundamental characteristics of phototransistors; these include speed, delays and timing errors. The time required to charge/discharge the phototransistor capacitances cause propagation delays and limit the operating speed; meanwhile the asymmetrical charge/discharge characteristics induce timing errors on the input pulse widths. Using a PIN photodiode in place of a phototransistor can improve the operating frequency (or in other words the data transfer rate) of the optocoupler at a cost of reduced CTR (since there is no transistor gain in a diode) [32] [52].

Another issue with optocouplers is channel to channel timing mismatches. A channel to channel mismatch refers to the dead time that may occur if two transistors (two channels) are not switched at exactly the same time. For example, when the high-side switch is turned off, ideally the low-side switch should turn on with zero timing mismatch; such channel to channel mismatches manifest itself in a reduction in efficiency. This problem emanates from the discrete fabrication of optocouplers [53].

### I.2.b-ii Inductive Isolation

Inductive based coupling techniques use a changing magnetic field to transfer information and energy across an isolation barrier. The most common form of magnetic coupling is the transformer. A basic transformer consists of a ferro-magnetic material at its core, and two (or more) wire windings. As stated in Faraday's Law of Induction, an alternating cur-

rent running through the primary coil generates a changing magnetic field which creates a varying magnetic flux in the core of the transformer. This varying magnetic flux is shared through the core with the secondary winding, which in turn induces a voltage across the secondary winding. Now if a load is connected to the secondary winding, a current can flow. The transformer core material has a high permeability relative to air; its purpose is to minimize magnetizing currents, and to confine the magnetic flux close to the windings. The strength of the transformer's magnetic field depends on the current magnitude, the permeability of the ferro-magnetic core, and the structure of the primary and secondary coils [54]. The different types of transformers used for isolation are discussed next, including: discrete pulse transformer, integrated planar coreless transformer, integrated planar transformer with a ferro-magnetic core.

Generally it is desired for the transformer to have a high transient response such that the rectangular electrical pulses have highly steep edges; the slower the rising and falling edges, the higher will be the commutation losses. The transient and breakdown voltage performance of the transformer is limited by the coupling capacitance between its secondary and primary coils; high quality isolation and careful design is required. A useful parameter that defines the transformer characteristic, is its voltage-time integral. The voltage-time integral is the product of the pulse duration and its peak voltage. In general, the larger the voltage-time integral of a pulse transformer, the more expensive and the larger the size of the transformer [45] [53] [7]. There are many research groups working on transformer solutions for the power switch driver control [55] [56].

There are two main approaches when using inductive coupling: (1) Integrated signal and power approach (2) or discrete signal and power approach. The latter is implemented most effectively with integrated digital micro-transformers and the former by discrete medium-high power pulse-transformers.

High power pulse-transformers are classically used for fast high voltage drive applications. They are also used for pulsed power applications such as power generation for radar and particle accelerators [57].

On the positive side, isolation transformers have a relatively high energy transfer efficiency, accurate timing and small delays; thus, they have a low power consumption and a speed (up to 1 MHz) advantage over optocouplers. Another strong advantage of transformers, is their ability to deliver both the drive order and the required energy; thus, there is no need for any additional amplification circuitry although other circuits may still be required (ex. safety circuitry) [45] [53].

On the negative side, transformer performance may suffer in applications requiring duty cycles above 50%. Transformers are ideal for AC signal transfer only and any energy stored in their core must be dumped every half a cycle. Consequently, their output voltage swings between positive and negative values in order to maintain a zero voltage-time as depicted in I.19(b). The negative voltage drive guarantees the turn-off state of the power switch despite noises from parasitics and unwanted  $dv/dt$  induced voltages; however, this

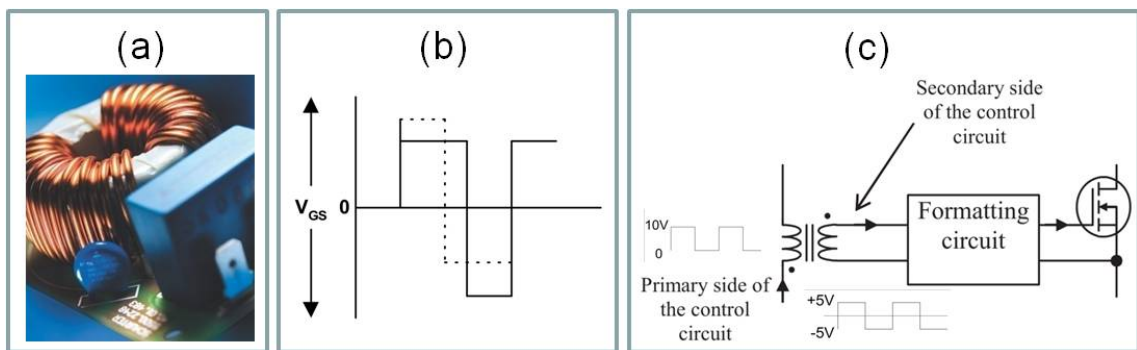


Figure I.19: (a) Power pulse transformer used for driving power switches [58]. (b) Volt-seconds across winding must balance [59]. (c) Basic Transformer-Isolated Gate Drive [7].

negative voltage comes at a cost to efficiency. Since some of the applied voltage is in the negative output voltage and some in the positive voltage, not all the applied voltage is available for turning on the power switch; this can result in efficiency losses that increase with an increasing duty cycle [45] [53] [60] [61]. Figure I.19(c) shows a basic isolated gate drive approach via a discrete pulse transformer. Since the discrete pulse transformer transfers the required energy to directly drive the gate of the power switch, a larger operating voltage means a larger pulse voltage-time integral; this results in a significant increase of the transformer size as can be seen in the example of figure I.19(a). Yet another problem is ringing which emanates from the large transient gate drive currents flowing in the inductive coils of the transformer; ringing can cause unwanted switching of the gate [53].

Unlike the pulse transformer discrete approach, digital isolator gate drivers adapt the transformer approach to isolation to digital signals at semiconductor chip-scale level. These digital micro-transformers use the metal process in standard CMOS integrated-circuits for their coil formation; a polyimide insulation layer (around  $20\mu\text{m}$  for 5 kV isolation) isolates the primary and secondary coils. A cross sectional view of such a transformer by ADI is depicted in figure I.20(b) and its use in a fully integrated converter on a single PCB board is shown in figure I.20(c). These micro-transformers can provide isolation between 3kV-5kV with a CMTI of  $50\text{-kV}/\mu\text{s}$  while switching at up to 1 MHz and operating temperatures from  $-40^\circ\text{C}$  to  $+125^\circ\text{C}$ . Compared to optocouplers and pulse transformers, the monolithic CMOS transformer technology provides superior timing accuracy, smaller footprint, lower power consumption, and higher reliability [53].

Despite their many benefits, the core-less digital micro-transformers are still susceptible to external magnetic fields and their isolation level is limited by the insulating Polyimide layer and its packaging.

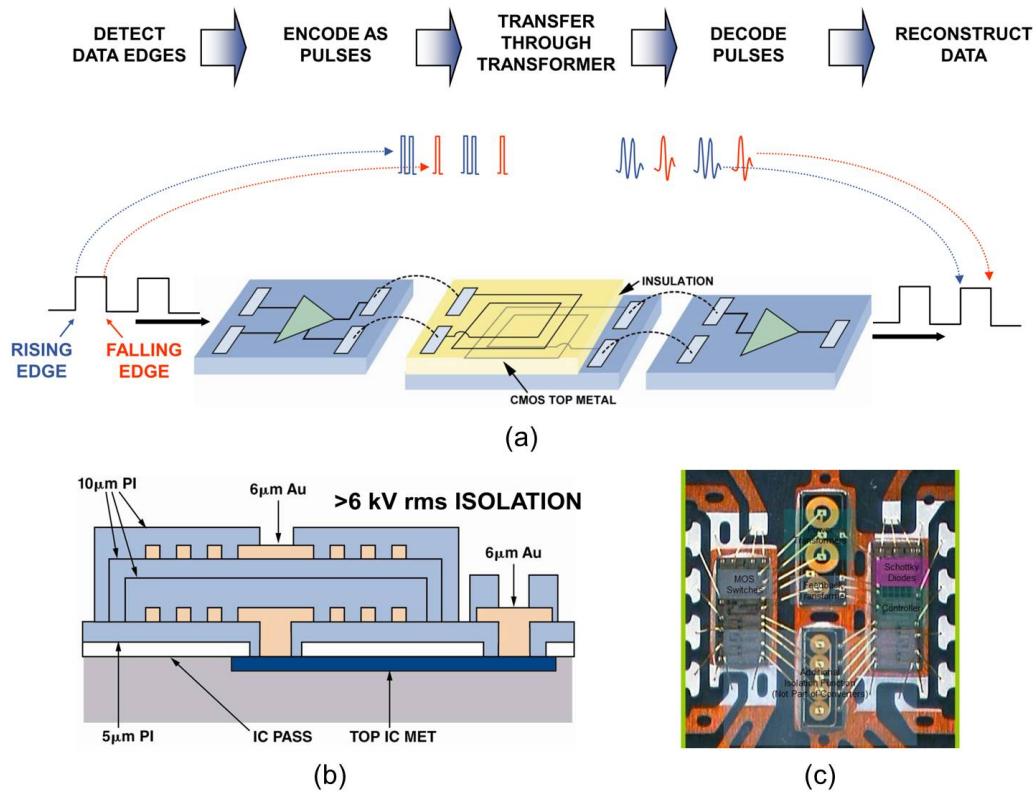


Figure I.20: Analog Devices micro-transformer integrated isolation [29].(a) Signal transmission operational diagram via a micro-transformer.(b) Transformer Structures. Primary: Two Coils Connected in Center-Tapped.  $L = 8 \text{ nH}$ ,  $R = 0.8 \text{ } \Omega$ ,  $C_s = 0.38 \text{ pF}$ ,  $Q = 19$  at 300 MHz. Radius =  $460 \text{ } \mu\text{m}$ , Turns = 3, Width =  $60 \text{ } \mu\text{m}$ , Space =  $7 \text{ } \mu\text{m}$ . Secondary (1:1 for 5 V output): Two Coils Connected in Center-Tapped.  $L = 8 \text{ nH}$ ,  $R = 0.8 \text{ } \Omega$ ,  $C_s = 1.2 \text{ pF}$ ,  $Q = 13$  at 300 MHz. Radius =  $460 \text{ } \mu\text{m}$ , Turns = 3, Width =  $60 \text{ } \mu\text{m}$ , Space =  $7 \text{ } \mu\text{m}$  (c) A 4-Channel iCoupler isolator integrated with a 500 mW DC-to-DC converter and Half-Bridge gate driver in a 16-Lead SOIC package; the controller and the rectifier diodes are on the right and the power switches are on the left. The transformers are in the middle; the larger power transformers are on top. The smaller transformers on the bottom transfer the isolated PWM signals.

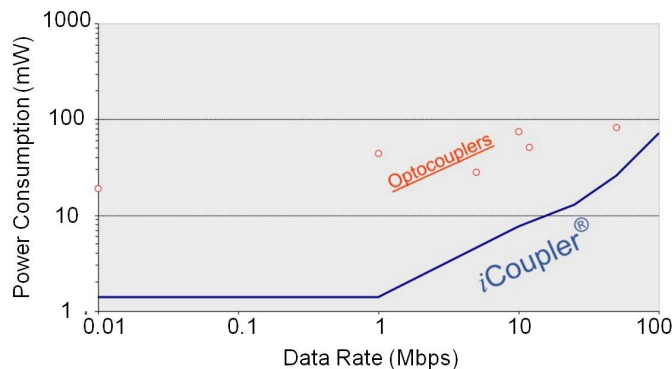


Figure I.21: Analog Devices icoupler showing power consumption benefits up to 90% compared to optocouplers.This data is from 2010 [29].

### I.2.b-iii Optical Isolation: Fiber Optics

In contrast to optocouplers where an LED and an optical receiver are packaged together in close proximity, the approach taken by fiber optic solutions separates the transmitter from the receiver through an optical fiber link, and in doing so, the minimum creepage distance that limits the performance of optocouplers is eliminated.

Figure I.22 summarizes the electromagnetic spectrum from different perspectives and provides a detailed overview of the optical range. The interesting regions in the optical range of the electromagnetic spectrum are the IR range for silica glass optical fiber (GOF) and the visible range for the polymer optical fibers (POF). The multi-mode (MM) and single-mode (SM) GOFs provide optical windows in wavelengths such as 850 nm, 1310 nm and most commonly 1550 nm. The low attenuation at these optical windows makes the GOF fibers ideal for long distance communications; however, the GOF fiber lacks mechanical strength and bending flexibility. Thus, in some applications, particularly for short length transmissions (from a few feet to longer distances below a few meters), polymer optical fibers (POF) have been developed. POF has two major draw backs relative to GOF fibers, namely: significantly lower bandwidth and much higher attenuation. Figure I.23 shows the optical attenuation spectrum of glass and some polymer fibers. Figure I.24(c) shows the standard structure of GOF and POF fibers. Despite their performance limitations, POF is of interest to researchers for two main reasons: (1) their handling and preparation ease (2) their ease of alignment and packaging due to their large core diameters [62] [63].

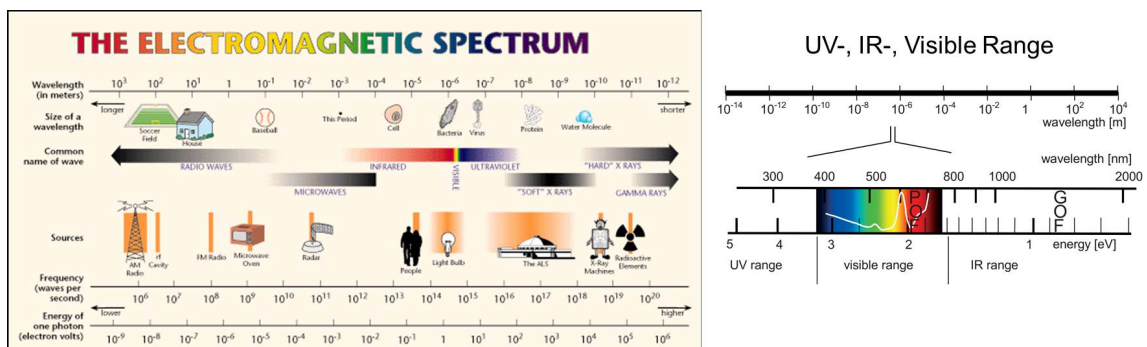


Figure I.22: Electromagnetic spectrum and an overview of the optical range [64] [63].

Optical fiber isolation solutions provide the highest isolation level in comparison to the other existing isolation systems due to the inherent immunity of light to electromagnetic radiation and their theoretically infinite isolation (no coupling capacity) level. Thus, for medium-high voltage applications and in common industrial environments with electromagnetic radiating components, optical fiber solutions are chosen despite their size penalty. As shown in figure I.25 (a), for high voltages ( $>1000$  V) a few to several centimetres of minimum creepage distance is recommended according to the IEC 664-1:1992 standard. Figure I.24 (a) shows a basic optical fiber link: it includes a transmitter, transmission medium and a receiver. Figure I.24 (b) shows the fiber optic approach taken by Avago

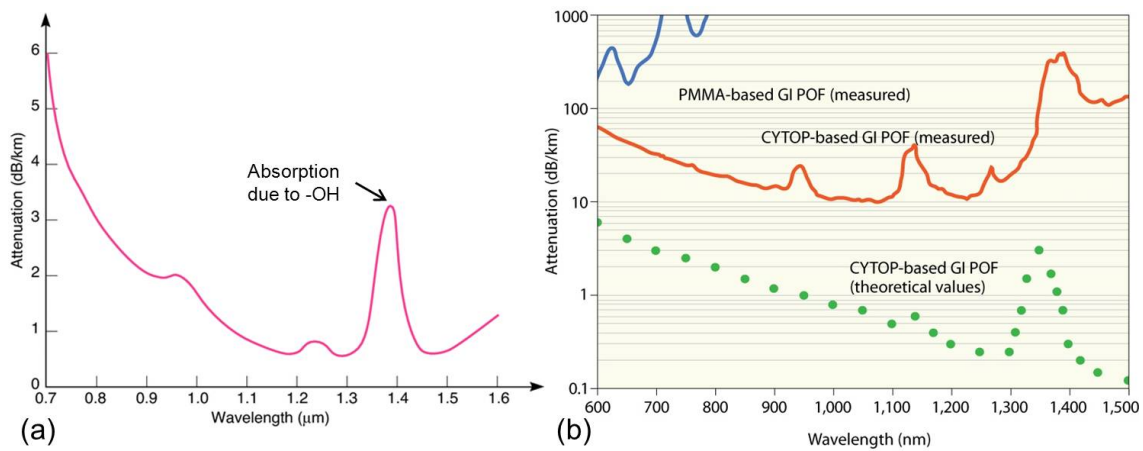


Figure I.23: A plot of typical attenuation profile vs. wavelength for GOF and POF. (a) Attenuation profile of typical a GOF by Newport [65]. (b) Attenuation profile of POFs as reported by Nature in 2009 [62].

technologies; here, the input of the optical short link board, shown in figure I.25 (b), provides an interface to the controller, meanwhile its output is directly connected to the high voltage IGBT driver [66]. Moreover, optical receiver and emitter modules equipped with their required drivers, as shown in the example of figure I.25 (c), are available for easy integration of optical links which can be operated in temperatures ranging from -40°C to 85°C.

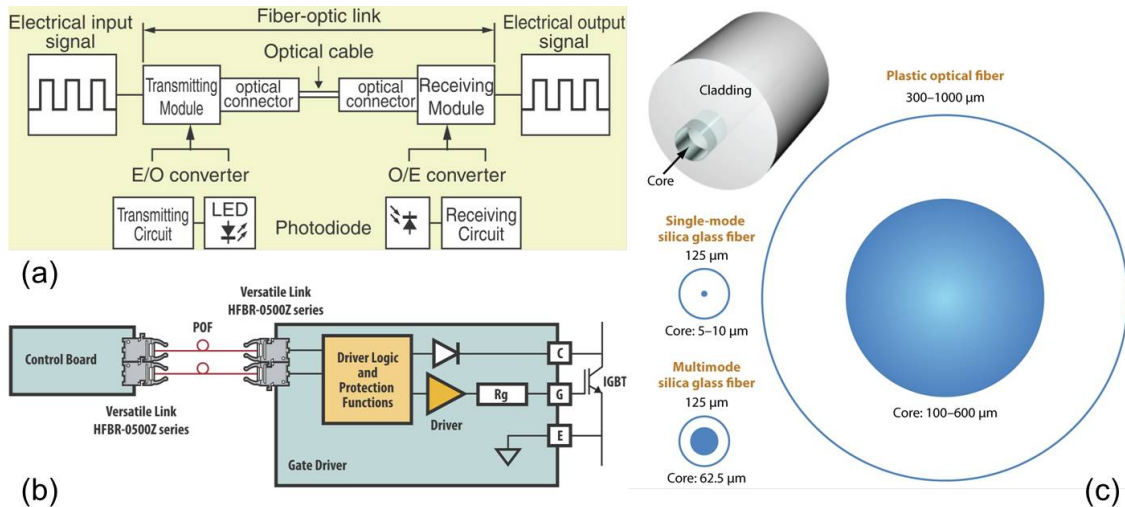


Figure I.24: (a) Fiber optic link connecting the transmitter, receiver and the transmission line. The transmitter includes an optical source such as LED or laser. The receiver includes an optical detector and TIA. The transmission line here is an optical fiber (another possibility is SOI waveguide). (b) IGBT gate driver via fiber optic isolation. The HFBR-0500Z is an Avago product [66]. (c) General construction of an optical fiber [62].

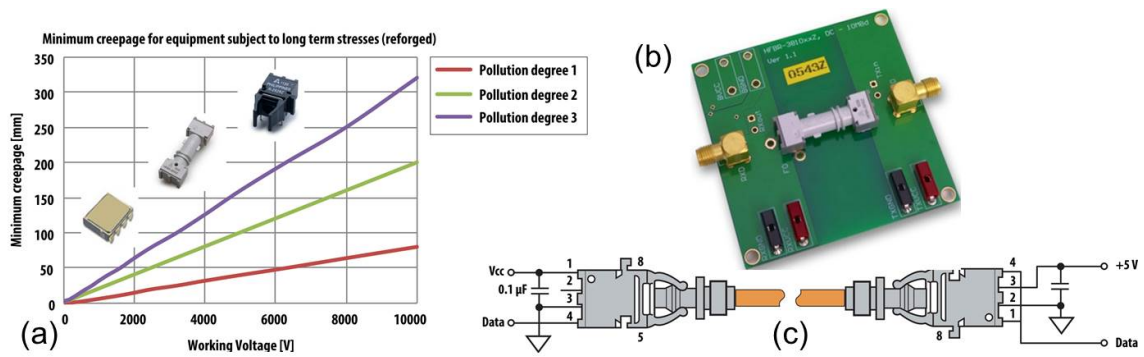


Figure I.25: (a) Minimum creepage distance by IEC 60664-1:2002 (b) HFBR-3810Z Optical Short-Link. (c) HFBR-1629/2529Z Circuit Diagram for 50 MBd Data Rate [66].

### I.2.b-iv Capacitive Isolation

Digital isolators using capacitive coupling employ a changing electric field to transmit data across a dielectric barrier. Capacitive isolators are small in size and efficient in energy transfer which allows their integration at low costs. They are immune to magnetic fields which enables their usage in environments with harsh magnetic radiation. Compared to optocouplers, capacitive isolators can be two or three times faster but they are typically larger than optocouplers. They can drive semiconductor switches with reverse voltages as high as approximately 700 V. Their  $dV/dt$  is limited by their capacitance value and are typically around  $20kV/\mu s$  up to  $50kV/\mu s$ . An isolating IGBT driver with PCB integrated capacitive coupling elements was reported in 2010 that operated at a DC link of 400 V with  $dV/dt$  stability as high as  $240kV/\mu s$  [40]; this work is demonstrated in figure I.26.

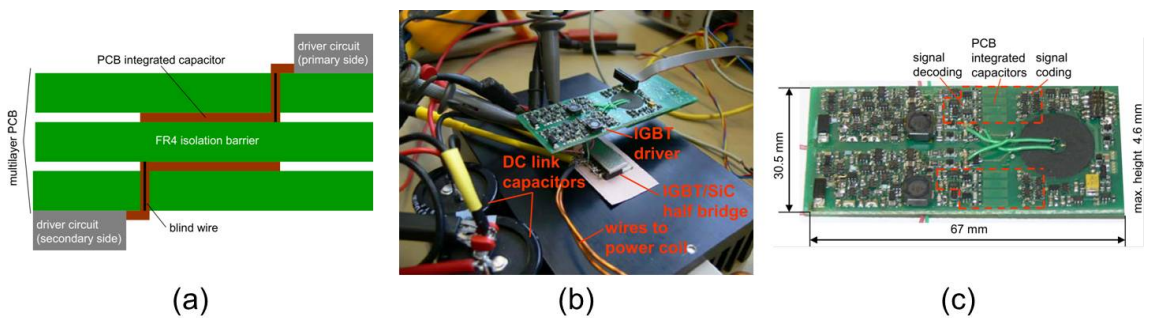


Figure I.26: Insulating IGBT driver with PCB integrated capacitive coupling as reported in CIPS 2010 conference [40]. (a) Proposed layout for PCB integrated capacitors to reach large clearance and creepage distances. (b) Photo of the buck-boost measurement setup (c) Prototype of an IGBT half bridge driver with PCB integrated capacitive coupling elements.

### I.2.c Optical Isolation: State of the Arts Under Research

In high voltage direct current (HVDC) applications, where several thyristors are stacked in series to support several hundred kV, fiber optics are used to carry the isolated gate

triggering signals between the external command units and the high voltages of the thyristor based AC/DC converters. The Light Triggered Thyristors (LTT) eliminate the high voltage gating electronics that were a cause of lifetime issues in the past. Commercially available LTT solutions require several tens of mWs of optical power and can handle hundreds of kVs and tens of kAs; figure I.27 shows an example thyristor from Siemens and demonstrates the difference between LTT and the traditional electrical triggered thyristor (ETT) approach. LTTs have been demonstrated in the literature [67] [68]; in 2013, optical triggering of a 12 kV,  $I_{max}=270A$ ,  $1cm^2$  4H-SiC thyristor was reported [69]. Figure I.28 shows the device cross section and top view as well as the device current and voltage time dependencies. As explained earlier, the main advantage of using fiber optics over optocouplers is their infinite immunity to EMI whereas optocouplers are limited by capacitive couplings in their small packaging environment.

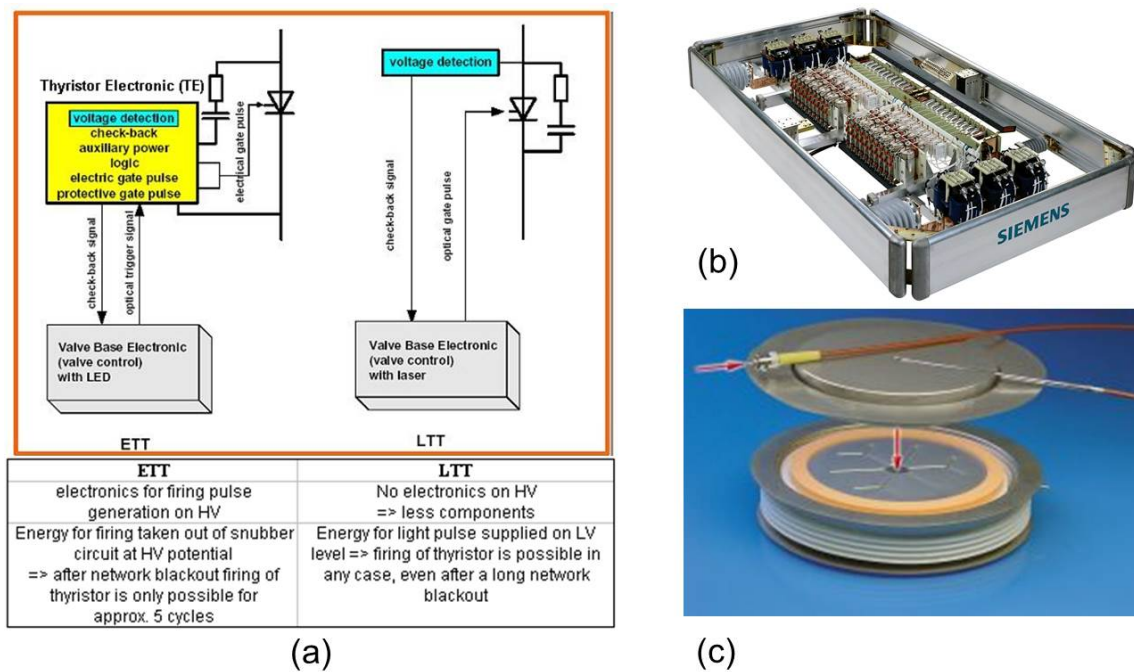


Figure I.27: (a) Comparison of direct light triggered thyristor (LTT) and electrical triggered thyristor (ETT). (b) Typical LTT thyristor module. (c) Direct-light triggered thyristor [70].

There are some signal + energy optical solutions reported in the literature for power MOSFETs and IGBTs. A group in Chicago, Illinois working with Dr. Mazumder have several publications during the years 2006-2009, on optically-activated gate control of power semiconductor devices based on externally optical triggered GaAs power transistors [71] [36]. They have fabricated GaAs/AlGaAs lateral switches that are connected to the gate of power switches. Photogeneration in the GaAs/AlGaAs devices modulates the gate resistance of the power switch and in turn allows control of the switch by light. Figure I.29 demonstrates this approach as well as the device structure and hybrid packaging scheme. These hybrid devices have much better optical properties compared to the SiC solutions

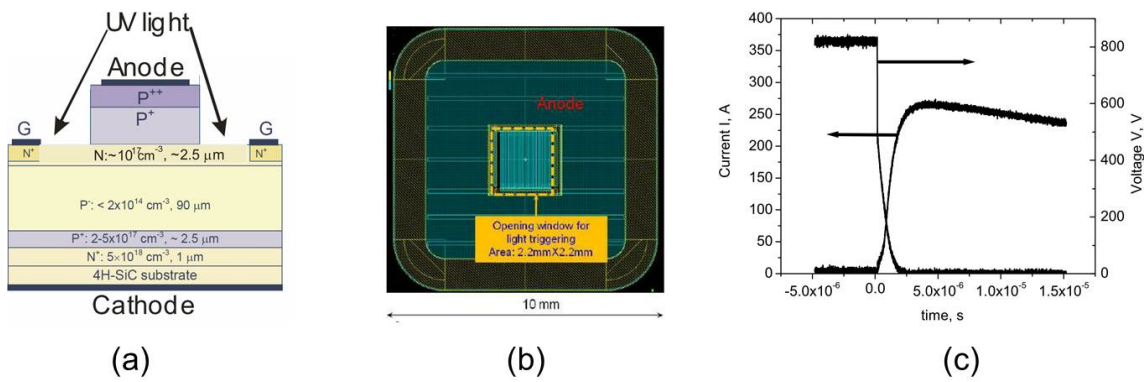


Figure I.28: Optical triggering of 12 kV, 1 cm<sup>2</sup> 4H-SiC thyristors [69]. (a) Cross sectional, and (b) top views of 12 kV, 1 cm<sup>2</sup> optically triggered 4H-SiC thyristor. (c) Time dependencies of voltage and current during switch-on process of 12 kV, 1 cm<sup>2</sup> 4H-SiC thyristor.

thanks to the optical properties of GaAs. Their switching control was demonstrated for Si-based power MOSFET and IGBT, SiC based VJFET and SiC based DMOSFET when triggered by a 800 nm wavelength light source [36]. The optical powers used are between 0.5 W to a couple of Watts; however we were not able to estimate their optical to electrical efficiency due to lack of information provided. This hybrid solution, is much more expensive than the optocouplers available in the market, however the major advantages here are the compact hybrid integration, high temperature and high voltage tolerances that maybe required for high demanding applications that are willing to pay the cost. Moreover, only a part of the gate current is supplied by light since the transistor still needs a floating supply to be operational.

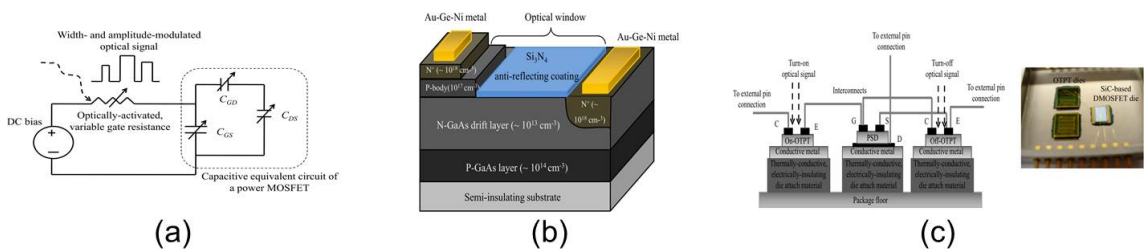


Figure I.29: Hybrid-optical control by GaAs/AlGaAs based device. [36] (a) Variable-gate-resistance based optically-activated gate control. (b) Device structure. (c) Hybrid packaging scheme and a prototype with SiC power MOSFET.

A group at the University of South Carolina under direction of Dr. Islam have reported optical solutions in SiC for pulsed power applications. Dr. Islam and team, reported in 2009, a 1 mm<sup>2</sup> 4H-SiC p-i-n diode solution that when triggered by a 337.1 laser pulse with 1.2 mJ in 600 ps, would generate a 0.5 A current pulse with FWHM of 180 ns [72]. In 2010, the same group at the university of South Carolina improved their overall optical to electrical conversion efficiency by using a different approach. This time instead of a p-i-n diode, they use the internal current gain (approximately 11) inside a SiC bipolar

transistor structure to amplify the photogenerated current [73]. The test circuit and the reported SiC photo transistor design are shown in figure I.30; having biased the  $0.5 \text{ mm}^2$  SiC photo transistor at 1200 V, a  $200 \text{ A/cm}^2$  current pulse with a FWHM of 180 ns was reported when triggering by a 337.1 nm laser pulse with 0.5 mJ in 600 ps [73]. Although this solution is more efficient than the 2009 p-i-n diode and provides high temperature and high power capabilities, it requires a lot of optical power (800 kW peak power compared to 2 MW for the p-i-n diode solution) and the transistor responsivity is roughly  $2 \mu\text{A/W}$ . In 2012, a group at Kyoto University of Japan published results showing the temperature-independent photo-response of a 4H-SiC photodiode for temperatures as high as 300 degrees [74] when illuminated by a 300 W Xenon optical source for wavelengths in the range of 280 nm to 365 nm.

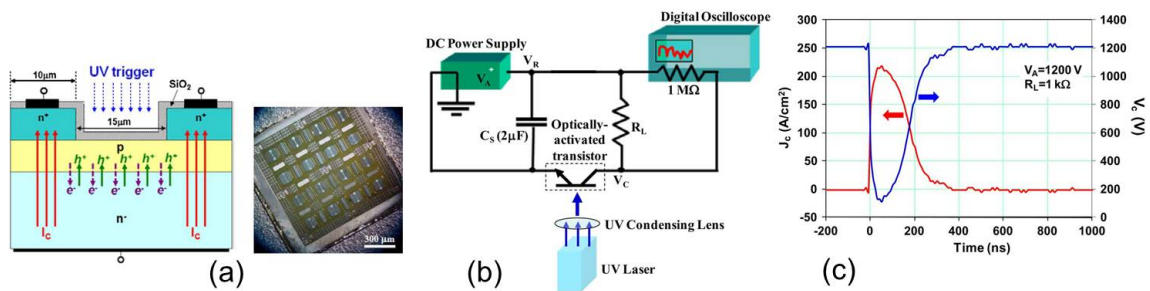


Figure I.30: Optical triggering by SiC Bipolar Transistor [73]. (a) Schematic (b) Test circuit for optical switching evaluation. (c) Collector voltage and current waveforms of the optically activated transistor when activated by a single laser pulse. The applied reverse voltage was 1200 V.

Another group at the Texas Tech. University reported a 4H-SiC photoconductive switch that achieved a peak photocurrent of 14 A into a  $25\text{-}\Omega$  load when operated at 15 kV/cm and triggered by a pulsed Nd:YAG laser. An optical parametric oscillator was used in conjunction with the pulsed laser, in order to scan the wavelength from 345 to 510 nm while monitoring the photocurrent and laser energy. The 14 A maximum reported photocurrent corresponds to a 336 nm wavelength, a lasing energy of roughly  $500 \mu\text{J}$ . The maximum efficiency point of the device is around  $0.1 \text{ mA}/\mu\text{J-V}$  which is very low as maybe expected due to the optical absorption properties of SiC. They implemented a gridded semi-transparent contact for higher current uniformity and lower optical reflection losses [75]. Figure I.31 shows their device and characterization results.

In the examples above, all the solutions share the same approach in terms of both delivering the required gate-drive circuit power as well as optically isolating the gating signal. In the signal and power approach, the optical isolation has to transfer the signal voltage levels needed to switch the gate; thus, a large amount of optical power maybe required depending on the gate-drive circuit power consumption and specially if the combination of the optical coupling interface (i.e. reflection losses due to refractive index mismatches and/or misalignment) and the photodetector (i.e. low optical power to current conversion efficiency due to poor material optical absorption coefficient and/or short

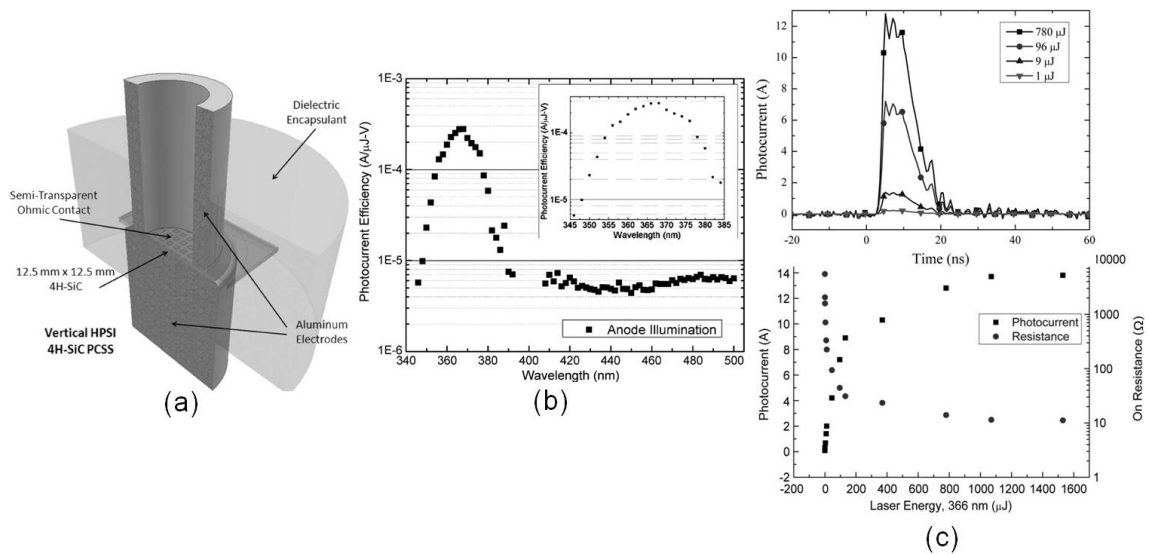


Figure I.31: (a) Cross section of the vertical photoconductive showing the gridded thin-film contact and the hollow electrode. (b) Dependence of photocurrent efficiency on wavelength. (Inset) Detailed view of the photocurrent efficiency peak at 366 nm. (c) (top) Change in photocurrent with various trigger energies. (bottom) Saturation of photocurrent and ON-state resistance with increasing laser energy. Both tests with anode triggering [75].

carrier lifetimes, and/or the structural design) have a poor optical to electrical conversion efficiency. Moreover, the works of the research teams above, all favour wide bandgap materials (i.e. SiC) due to their high thermal and voltage capabilities that are compatible with power electronic applications. However, such wide bandgap devices are only sensitive in the ultraviolet wavelength range of the electromagnetic spectrum where compact, efficient and cost effective optical sources such as semiconductor laser diodes are either very limited or not available.

In 2013, Dr.Fujita presented in IEEE power electronics transactions, an energy + signal optical isolation unit, where the DC power supply consisted of two 400 mW continuous wave (CW) laser diodes (SDL-2320-L2: JDSU) connected via two 1.5m optical fibers, to two 12V photovoltaic power converters (PPC-12E: JDSU) suitable in the 810nm wavelength range. The gating control signal isolation was provided by an optical fiber connection between an optical signal transmitter (GP1FAV55TK0F: SHARP) and receiver (GP1FAV55RK0F: SHARP). The key to successfully lowering the optical power level requirement was in lowering the driver power consumption. Dr.Fujita proposed a resonant gate-drive circuit (figure I.32 (a)) that allowed a reduction in the power consumption of the gate driver by up to 10 times (power consumptions as low as 25 mW at 100 kHz operating frequency were reported). The concept was demonstrated on 500 V, 20 A MOSFET buck converter with 600 V, 12 A flyback diodes, and also on 1400 V, 300 A, IGBTs as shown in figures I.32(b) and (c) respectively.

Relative to the previous signal+power optical isolation approaches, the work demonstrated by Dr.Fujita's team shows the potential for a practical solution in terms of power

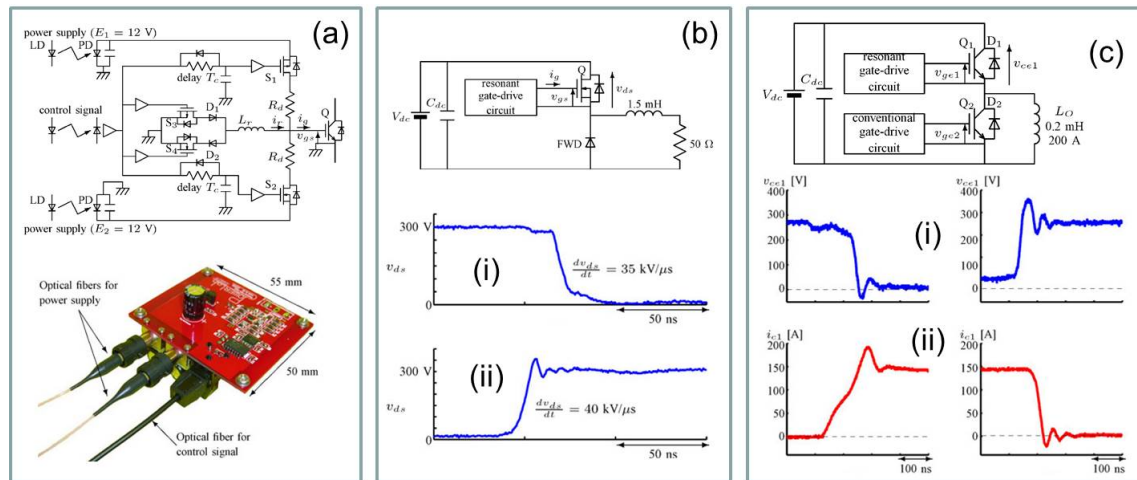


Figure I.32: Resonant gate-drive with optically isolated control signal and power supply. [76] (a) Top: Proposed resonant gate-drive circuit equipped with optical isolation of both control signal and power supply. Bottom: Photograph of the proposed resonant gate-drive circuit. (b) Experimental setup and experimental waveforms of drain-to-source voltage, when the main MOSFET Q is turned (i) ON and (ii) OFF. (c) Experimental setup and experimental waveforms of double-pulse test, when the upper IGBT Q1 is turned (i) ON and (ii) OFF.

consumption. Nevertheless, this demonstrated optical isolation unit is based on discrete components which lacks the scalability and footprint advantages that come with a monolithic integration approach. To the best of our knowledge, although many hybrid solutions have been proposed, there has not been any low power optical isolation solutions proposed in the literature suitable for monolithic integration with VDMOSFET and IGBT power switches. As it was discussed in subsection I.4, in this thesis we will investigate such a monolithic optical solution. Moreover, to recap, our approach is to isolate only the control signal which can later be amplified by additional CMOS or integrated VMOS circuitries. Once the proposed monolithic optical control signal approach is verified, energy + signal solutions can be pursued by monolithic integration of a light triggered DC supply cell (as it will be presented in subsection I.4). Moreover, this approach can be extended to materials such as GaN for higher temperature and voltage applications. In the next section, the different types of optical detectors as well as the main principles of photogeneration are discussed with the aim to identify the most suitable IPD designs.

### I.3 Optical Detection: Physics and Key Challenges

Semiconductor photodetectors are primarily used in the field of optical fiber communications for demodulation of optical signals back into electrical signals. These applications operate in the wavelength range of 800 nm - 1600 nm and they require high sensitivity, high bandwidth and low noise optical detectors. In this project we search for an optimum photodetector design for monolithic integration with a VDMOSFET on Silicon. Due to the material restriction and fabrication process of Silicon based power MOSFETs, the de-

sign, fabrication, operating conditions and performance of the IPD will be different from the highly optimized discrete optical detectors available in the market.

### I.3.a Optical Absorption

Photodetector operation consists of three basic processes: (1) carrier generation by optical absorption of an incident light (2) carrier transport and/or current gain mechanisms if present, and (3) carrier extraction at terminals to generate the output signal.

Incident light (electromagnetic radiation) entering a material has a probability of transferring a fraction of its energy to the internal energy of the host matter. This process is referred to as absorption and it results in an attenuation of the light intensity as it propagates further into the material. This absorption process occurs through the energy interactions between the photons from the radiating field and the particles present in the observer material; for example, the interaction of photons with phonons and electrons of the matter can result in changes in the vibrational or the electronic quantum mechanical state of the molecules of the host material. Optical absorption is dependent on the internal molecular and atomic structure of the material as well as the frequency of the light; it is also dependent on environmental conditions such as temperature, intensity of the electromagnetic radiation and pressure [77].

Figure I.33 shows the optical absorption spectrum of some different materials that are the key players competing in the optoelectronic industry. As it can be seen Ge is highly competitive for all wavelengths below 1500 nm. InGaAs is the most popular material in the long wavelength regime and has been used heavily for 1300 nm - 1600 nm detectors. In the short wavelength regime more specifically below 800 nm, GaAs has been the top candidate. Figure I.34 shows the optical absorption coefficient,  $\alpha$ , of Silicon as a function of wavelength,  $\lambda$ , at 300 K. Although Silicon detectors exist in the market; they are mostly used in the visible range due to their current conversion efficiency limitation in the UV (surface recombination losses due to short absorption depth) and near infra-red (approaching bandgap limitation). There are two main reasons why there are less Silicon photodetectors available compared to materials such as GaAs and InGaAs: (1) fiber optic communication is at 1550 nm wavelength and as seen in figure I.34 absorption in Si suffers strongly at long wavelengths (limited to 1100 nm), (2) In the short wavelength regime, InP (though not commonly used due to cost and complexity), GaAs and Ge offer a much higher carrier saturation velocity (as indicated by the mobility values listed in table I.3) which results in much higher bandwidths (in optical communications detectors above 500 GHz are commonly available and the race is to reach THz ) in comparison to Silicon. Table I.3, lists some important properties of different materials that are interesting for optical applications in power electronics [77] [78].

Semiconductor materials with direct bandgaps where the bottom of the conduction band ( $E_c$ ) and the top of the valance band ( $E_v$ ) line up in the momentum space are very efficient in photon absorption and are ideal for making optical devices such as lasers; material compositions consisting of elements from group III and V of the periodic table have

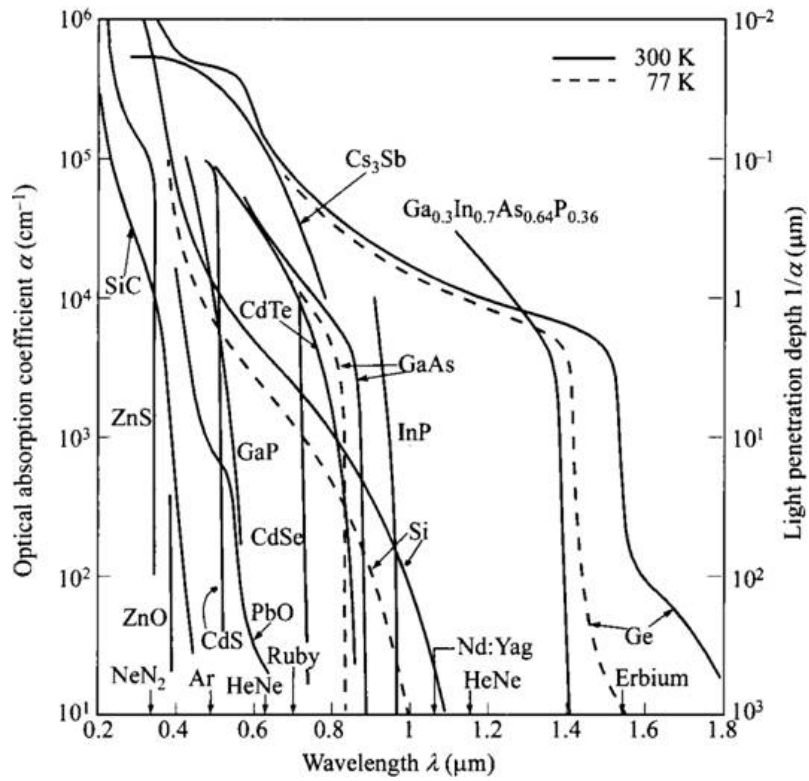


Figure I.33: Optical absorption coefficients for different photodetector materials. [78]

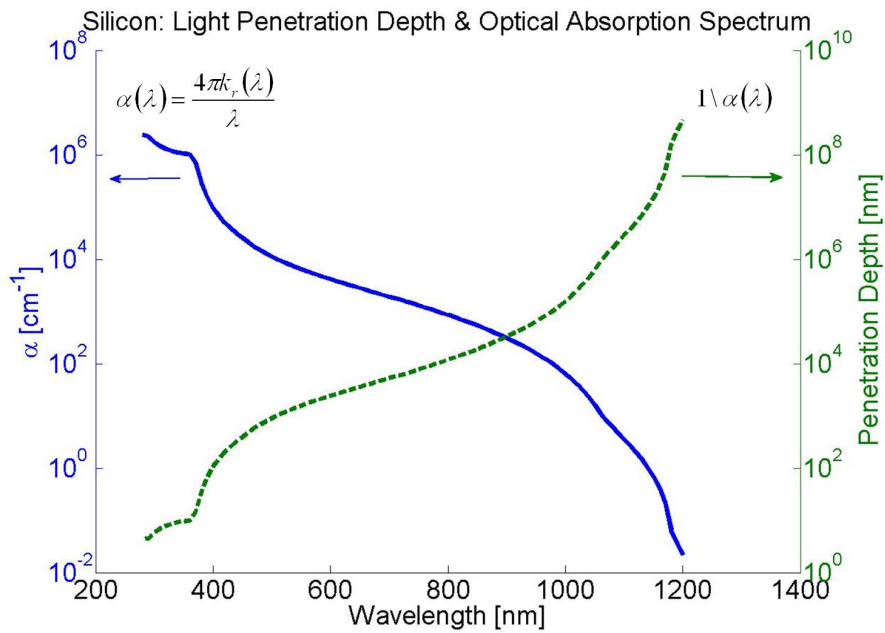


Figure I.34: Silicon absorption spectrum

Properties	Si	GaAs	4H-SiC	GaN	Ge	Diamond
Bandgap [eV]	1.1	1.43	3.26	3.45	0.67	5.45
Thermal Expansion $\times 10^{-6}$ [K $^{-1}$ ]	2.6	5.7		5.6	5.9	1
Thermal Conductivity [W/(cm K)]	1.5	0.46	4.9	1.3	0.58	20
Dielectric Constant	11.8	12.5		11	16	9.7
Breakdown Field $\times 10^5$ [V/cm]	6	6	30	>50	1	100
Electron Mobility [cm $^2$ /(V.s)]	1500	8500	1000	1250	3900	2200
Hole Mobility [cm $^2$ /(V.s)]	600	400	50	250	1900	1600

Table I.3: Some Selected Properties of Semiconductors Interesting for Optical and Power Electronics. The values of parameters listed here are function of other parameters such as doping and impurity level concentration, Temperature, etc. This table is provided for a comparative purposes only [79].

direct bandgaps, i.e. GaAs, InP. In materials with an indirect bandgap, a transition from the valence band to the conduction band requires a change in both the momentum and energy; thus, transitions from valence band to the conduction band are improbable and inefficient. Figure I.35 demonstrates the difference in the energy versus crystal momentum space of direct bandgap and indirect bandgap and its implications on electron transitions. An optical frequency ( $\nu$  in Hz) with photon energy ( $h\nu$ , where  $h$  is Planck's constant) higher than the bandgap energy ( $E_g = E_c - E_v$ ) of the material can interact with the electrons in the valence band and liberate them to the conduction band as long as both energy and momentum are conserved. Exciton generation (i.e. due to fabrication defects) and free carrier absorption are some internal loss mechanisms that reduce the optical absorption efficiency of the material. Silicon at 300 K, has a direct bandgap of 4.10 eV and an indirect bandgap of 1.11 eV.

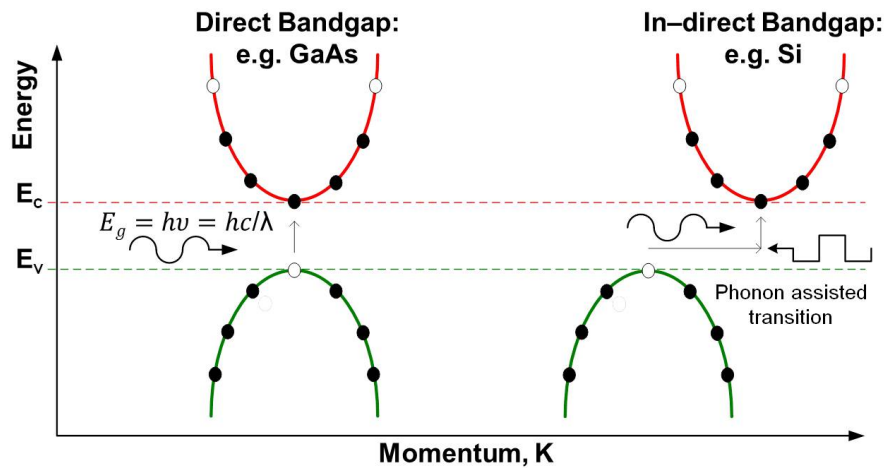


Figure I.35: Direct energy excitation of electron from valance to conduction band in direct bandgap versus phonon assisted transition in indirect bandgap materials.

### I.3.b Photodetectors

The different kinds of photodetectors can be divided into two groups: (1) without gain, and (2) with gain. The first group includes different types of photodiodes. The second group includes: phototransistors, avalanche photodiodes and photoconductors. Table I.4 provides an overview of performance parameters for some common types of photodetectors.

Photodetector	Gain	Response Time [s]	Transit-Time Limited 3-dB Bandwidth
Photoconductor	$1-10^6$	$10^{-8}-10^{-3}$	35 MHz-350 Hz
Photodiodes p-n junction	1	$10^{-11}$	35 GHz
p-i-n junction	1	$10^{-10}-10^{-8}$	3.5 GHz-35 MHz
M-S diode	1	$10^{-11}$	35 GHz
Avalanche Photodiode	$10^2-10^4$	$10^{-10}$	3.5 GHz
Phototransistor	$10^2-10^3$	$10^{-6}$	350 kHz

Table I.4: Typical values of gain and response time for common photodetectors [78]. These values are not exact as they depend on many parameters such as doping concentration levels, design (size and structure), applied voltages, temperature, etc; these values are given for comparative purposes. Moreover, the 3-dB bandwidths listed here are ideal as they are based on transit-time limitations. It is most likely that the device bandwidth is RC-limited which takes into account the packaging and contact parasitics.

As shown in table I.4, generally, photodetectors with gain are relatively slower than the ones without gain (using materials other than Si, such as GaAs based structures, bandwidths of several 100 MHz have been reported [80]). An exception to this rule is the avalanche photodiode (APD), where electrons are produced in a highly doped layer and are multiplied and accelerated by means of a local field [78]. Figure I.36 (a) shows a typical structure of APDs. APDs can have a gain-bandwidth product in the hundreds of giga hertz, however, this high gain (typically 10 dB more sensitive than p-i-n photodiodes [63]) comes at a price of increased noise and a high reverse bias voltage (the voltage is adjusted for the optimum gain condition) requirement. In our proposed application and approach, the high voltage (i.e. 15V) supply of the gate driver is available on the receiver side and thus, it could be used to bias the APD. Figure I.36 (b) shows the basic structure of a phototransistor. In phototransistors, photogenerated carriers in the base can benefit from the internal gain of a bipolar transistor; moreover, the extra noise complications and high voltage requirements of the APD are eliminated. Thanks to the bipolar gain, the phototransistor can offer an improved light to current transfer ratio compared to photodiode structures which is one reason why it is widely used in optocouplers. On the negative side, phototransistor switching speeds are limited (<several hundred kHz) by the charging and discharging times of the emitter and collector capacitances [78]. Another photodetector with gain abilities is the photoconductor structure shown in figure I.36 (c). Photoconductors consist of a bulk absorbing layer with ohmic contacts to collect the photo current generated in the bulk. Through careful design considerations such as short contact spacings, and material choice and fabrication process allowing for high carrier mobilities, the

carrier transit times between contacts can be minimized while the carrier lifetimes maximized in order to maximize the gain of the photoconductor. The long lifetimes required for the gain, result in the reduction of the photoconductor modulation bandwidth (below several MHz in Silicon) down to several decades below the bandwidth of photodiodes [78].

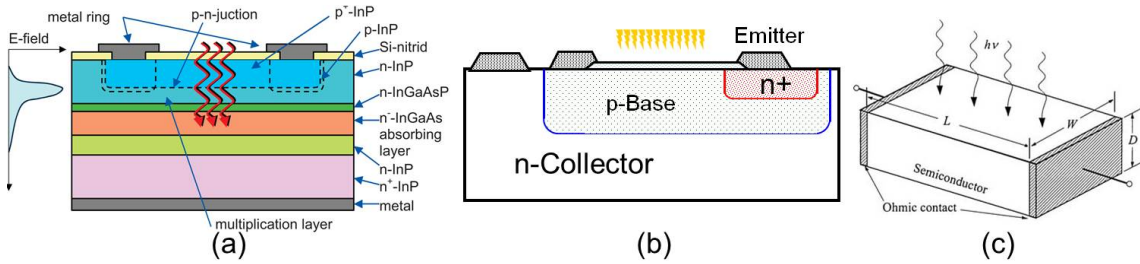


Figure I.36: Photodetectors with gain. (a) Avalanche photodiode [63] (b) Phototransistor structure. (c) Photoconductor structure showing the basic operating principle. Typical structures would have integrated contact fingers on the surface which would cause shadow effect but increase the gain [78].

Since we are aiming for an IPD solution with a fast time response ( $>50$  MHz) as well as a reasonable efficiency, in the following subsections, we will introduce the more suitable options available in the photodiode family: p-n junction, p-i-n junction, Metal-semiconductor (M-S), and Metal-semiconductor-Metal (MSM) devices. Although we've chosen not to focus on the APD structure here, future investigation of the pros (i.e. gain, speed) and cons (i.e. noise and data susceptibility, power consumption) of this structure could be of interest for our approach. Moreover, in this thesis only a conventional signal only transfer approach is explored. Never the less, it should be pointed out that for the future integration approach proposed in figure I.51, where the DC supply could be integrated by an isolated optical interface, the photodetector structure can be optimized for maximized current conversion efficiency without any bandwidth restrictions. Thus, for the DC supply, the photodetectors with gain such as the photoconductor can be a good candidate. Also, due to time limitations, M-S-M devices were not investigated; however, the following introduction serves to propose the need for future investigations of this device as a possible candidate for our application. Moreover, it should be added that quantum-well photodetectors and heterojunction photodetectors will not be considered since they require very specialized fabrication and design process that is not compatible for integration with the Silicon power switches or CMOS.

### I.3.b-i p-i-n and pn photodiodes

Photodiodes separate the photo-generated carriers (electrons and holes) by means of an electric field, e.g. a PN junction. The optical to electrical transfer efficiency of a device is often referred to as its quantum efficiency (QE). The QE parameter represents the ratio of the number of output electrons to the number of input photons and it is given by [78],

$$\eta = \frac{I_{ph}}{q\Phi} = \frac{AJ_{tot}/q}{P_{opt}/h\nu} = (1 - R)\left[1 - \frac{\exp(-\alpha W_D)}{1 + \alpha L_p}\right] \quad (I.2)$$

where  $I_{ph}$  is the photocurrent,  $\Phi$  is the photon flux,  $J_{tot}$  is the total current density including drift and diffusion currents,  $P_{opt}$  is the average optical signal power,  $R$  is the reflection coefficient,  $A$  is the device area,  $W_D$  is the depletion region width, and  $L_p$  is the minority carrier (holes) diffusion length. Another metric used for evaluating the sensitivity of a detector in reference to the optical power is the responsivity [78],

$$\mathfrak{R} = \frac{I_{ph}}{P_{opt}} = \frac{\eta q}{h\nu} = \frac{\eta\lambda(\mu m)}{1.24} [A/W] \quad (I.3)$$

As it can be seen from equation I.2, minimizing reflections and wider  $W_D$  increases the QE of the device. Reflections are minimized through the application of an anti-reflective coating layer. The  $W_D$  of a p-n photodiode is controlled by the impurity doping levels and diffusion times.

The p-i-n photodiode is a special case of p-n photodiodes where the insertion of a thick intrinsic region insures that a depletion region larger than the absorption depth ( $>1/\alpha$ ) of the light can be created by applying only a small voltage. For a large QE, a wide absorption layer is necessary (absorption depth is a function of wavelength as it was shown in figure I.34); however, this leads to longer transit times (time required for carriers to drift across the depletion region) which in turn reduces the bandwidth performance of the detector. Thus, the compromise between QE and frequency response is tuned by the design of the depletion region width,  $W_D$  as shown in the plot of figure I.37. Figure I.38 (a) shows the p-n and p-i-n photodiode schematic structures. In general, p-i-n photodiode benefits from a much larger responsivity relative to a simple p-n photodiode; however, for very wide intrinsic layers, long transit times through the intrinsic region can limit the p-i-n bandwidth. Moreover, the neutral region in a p-n photodiode contributes to series resistance which is a source of noise. The different characteristics of p-n photodiodes are presented in detail in the following chapters as we discuss the modelling, fabrication and characterization of the proposed p-n IPD.

In the research community, there has been a growing effort in optical detectors that are compatible for integration with CMOS technology [81] [82] [83] [84] as well as its necessary optical interconnection network. Since the main demand for such integrated photodetectors is in the telecommunication field, a lot of attention have been focused on fabricating Ge devices on Silicon and SOI wafers [85] [86] [87]. Recently, Dr.Laurent Vivien and his team, reported a 120 GHz, 10  $\mu m$  long lateral p-i-n Ge photodetector integrated with silicon waveguides at its end with a responsivity of 0.8 A/W at 1550 nm.

To the best of our knowledge there aren't a lot of research in the integration of visible range (specially below 600 nm wavelength) photodetectors in Si. The visible range is specially of interest for short range POF communication systems. The p-i-n photodiode and its parameters presented in figure I.40 , is a POF suitable, commercially available product by Infineon [63].

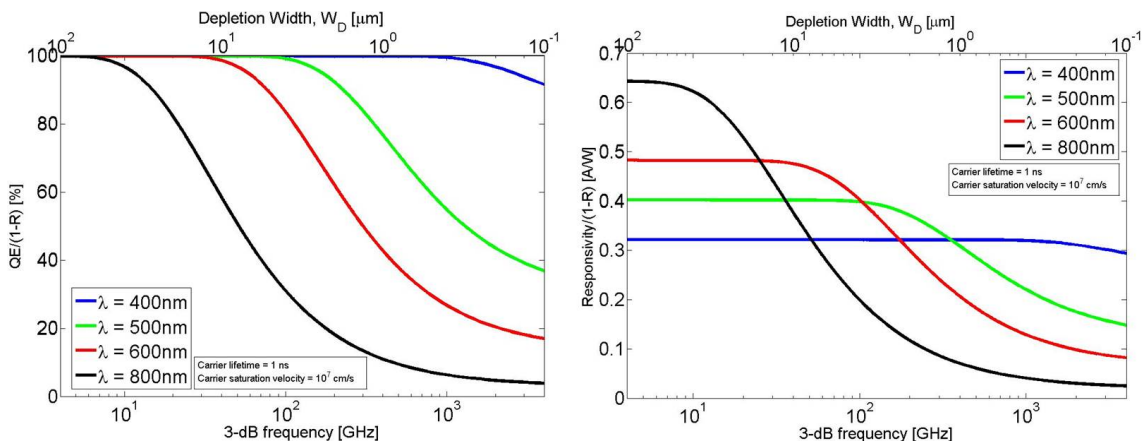


Figure I.37: Depletion width tuning in Si p-i-n Photodiodes and its effect on transit-time limited 3-dB bandwidth, QE and Responsivity. It is assumed that carriers are drifting at saturation velocity of  $10^7$  cm/s and there are no diffusion currents. Thus, these curves over estimated the ideal bandwidth limits as well as QE and Responsivity values, specially for p-n diodes with small  $W_D$ . Optical power reflection coefficient as a function of wavelength is considered for a Silicon/air interface. Moreover, these trends are sensitive to carrier life time values. A life time of 1 ns was assumed.

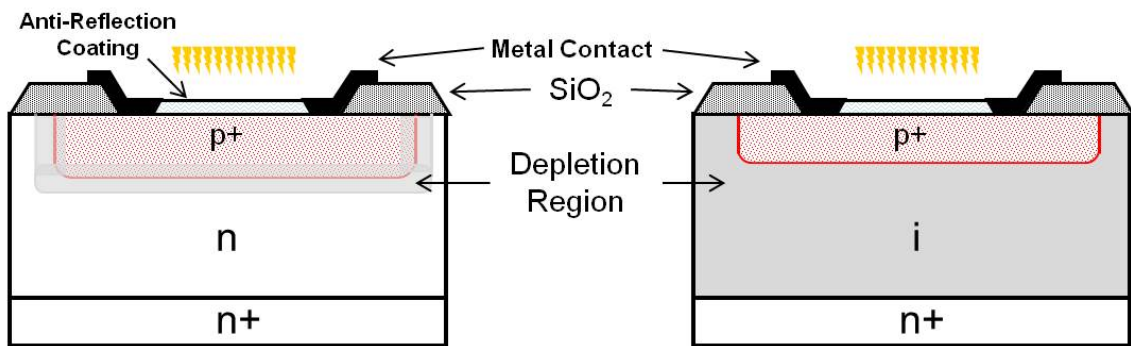


Figure I.38: Schematic structure of pn or p-i-n Photodiodes.

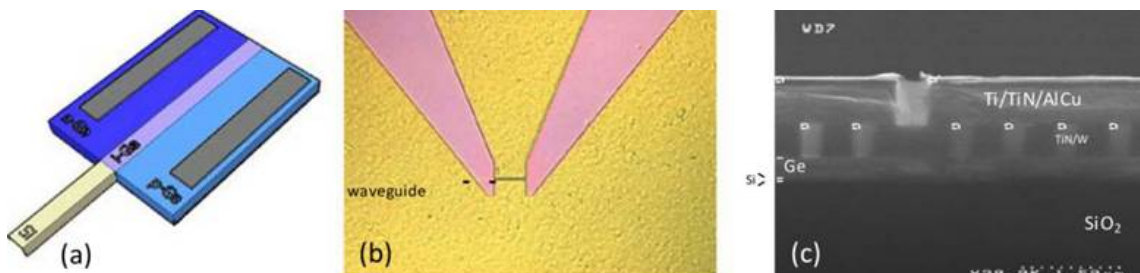


Figure I.39: (a) Schematic view of a lateral pin Ge photodetector integrated at the end of a Si waveguide. The length was  $10 \mu\text{m}$ . (b) Top-view optical microscopy and cross-sectional SEM images of the Ge PD. (c) SEM cross-section (perpendicular to the waveguide direction) [86].

Parameter	Symbol	Unit	Value
operation temperature	$T_{op}$	$^{\circ}C$	-40 .. +85
max. reverse voltage	$U_R$	V	30
wavelength of the best sensitivity	$\lambda_{S\ max}$	nm	850
sensitive range ( $S \geq 0.1 \cdot S_{max}$ )	$\lambda$	nm	400 .. 1100
dark current ( $U_R = 20\ V$ )	$I_R$	nA	1 ( $\leq 10$ )
junction capacity ( $f = 1\ MHz, U_R = 0\ V$ )	$C_0$	pF	11
junction capacity ( $f = 1\ MHz, U_R = 20\ V$ )	$C_{20}$	pF	2.3
rise and fall time (10% - 90%, $R_L = 50\ \Omega, U_R = 30\ V, \lambda = 880\ nm$ )	$t_r, t_f$	ns	10
photo current (10 mW in the POF, $U_R = 5\ V$ ) for 660 nm and 950 nm	$I_P$	$\mu A$	3 (660 nm) 4 (950 nm)

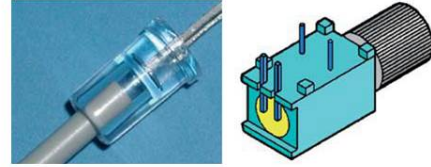


Figure I.40: pin-diode SFH 250 by Infineon for 1.0 mm/2.2 mm POF (right with a housing for clamping the POF with a screw) [63]

### I.3.b-ii Schottky Junction Photodetectors: M-S, M-S-M

Metal-semiconductor (M-S) photodetectors are based on Schottky junctions which are formed at the metal contact and semiconductor bulk interface. M-S photodetectors can be operated in two modes [78]:

1. For  $h\nu > E_g$ : As shown in figure I.41 (a), the layer under the contact could also be lightly doped to create a Metal-i-n photodiode whose QE is defined by the same expression I.2 used to define the QE of a p-i-n photodiode. In this case, light is absorbed in the semiconductor and the metal layers should be very thin (roughly a few 10s of nm in thickness) in order to minimize reflection and absorption losses due to the metal contact layer.
2. For  $q\phi_B < h\nu < E_g$ : As long as the incident light has energy higher than the Schottky barrier ( $q\phi_B$ ), photons can be absorbed in the metal layer and collected by the semiconductor. In this case light can enter the device through the semiconductor interface rather than the metal interface, allowing for a thicker (lower resistance) metal layer. The structure of such a device is shown in figure I.41 (b).

Some of the main advantages of M-S photodetectors are: their high speeds (the p-n junction minority charge storage is eliminated here since dark currents in Schottky diodes are not based on minority diffusion currents) and their long wavelength detection abilities without the need of thick devices or narrow bandgap semiconductors. In addition to long wavelength detection, it is possible to have short wavelength detection (in the UV and visible range) by choosing the right material and careful design. Moreover, a Schottky barrier does not require high temperature annealing [78].

Another type of photodetector is the M-S-M photodetector which uses two Schottky barriers back to back as shown in figure I.41(c). Unlike the M-S photodetector, light is absorbed in the semiconductor and not in the metal layer. The main benefit of the M-S-M structures are their high speed (they can have capacitance values roughly half the capacitance value of a p-i-n photodiode with a similar QE) and compatibility with CMOS technology [78]. Very fast M-S-M photodetectors suitable for the visible range have been

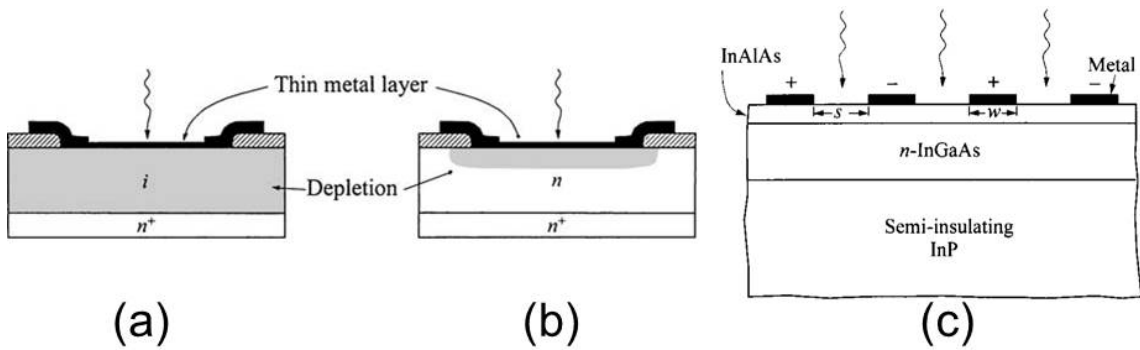


Figure I.41: (a) Schematic structure of metal-i-n photodiode. (b) Metal-semiconductor photodiode structure. (c) The MSM photodiode is consisted of planar interlinked metal semiconductor contacts. The top layer (InAlAs) serves to reduce the dark current by providing a higher barrier height [78].

demonstrated such as the 30 GHz device shown in figure I.42. However, for such high speeds, finger spacings of  $1 \mu\text{m}$  are needed which lead to voltage dependency challenges [63]. In the IR range, IBM has reported CMOS compatible waveguide-integrated M-S-M photodetectors with up to 40 GHz bandwidth, and responsivities of  $0.41 \text{ A/W}$  at 1 V for  $1.3 \mu\text{m}$  wavelength and  $0.14 \text{ A/W}$  at 1 V for  $1.4 \mu\text{m}$  wavelength. Their approach and an SEM image of their device is depicted in figure I.43 [83].

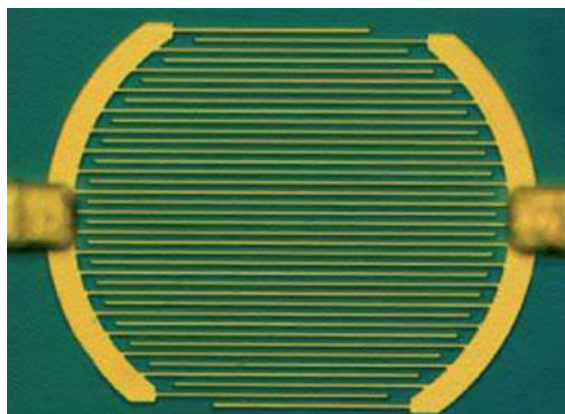


Figure I.42: 30 GHz MSM photodiode (diode made by Astri HongKong) [78]

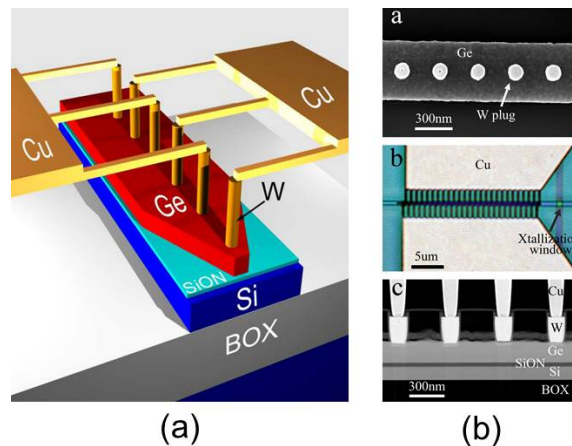


Figure I.43: 40 GHz waveguide-integrated Ge MSM photodiode by IBM [83]

## I.4 Monolithic Galvanic Isolation by an Integrated Photo-Detector (IPD)

As discussed previously, galvanic isolation methods that allow monolithic integration with the power device are of interest as the power electronic community strives for a fully integrated power function. From the many different galvanic isolation methods, optical solutions provide the highest level of isolation (these different methods will be discussed in detail in the next section). In his 2008 thesis, Dr. Nicolas Rouger proposed an optical detector that could be realized using the same fabrication process used for constructing the VDMOSFET power device; this optical detector could then be used as a monolithic galvanic isolation device [88]. In this approach, as demonstrated by figure I.44, the gating signal is generated by an external optical source, the optical signal is then guided to the power chip where a monolithic optical detector will transform the received optical signal to an electrical current signal. An amplification and signal treatment stage is required between the optical detector and the gate of the power switch in order to demodulate the gating signal, change the current into voltage and provide sufficient energy; this stage could be either monolithically integrated within the power device environment or fabricated on a CMOS chip and connected using flip chip technology as shown in figure I.45.

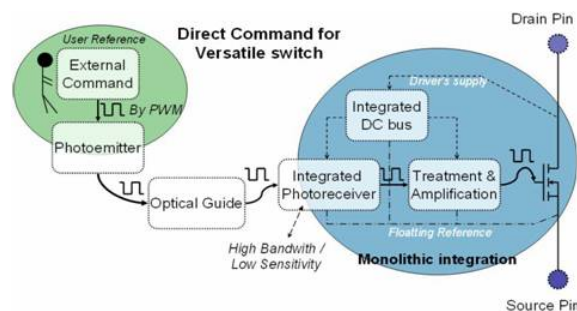


Figure I.44: Gate signal transfer approach using a photo detector as a monolithic galvanic isolator. [37].

Since maintaining a low cost is a major consideration, only integrated photo detector

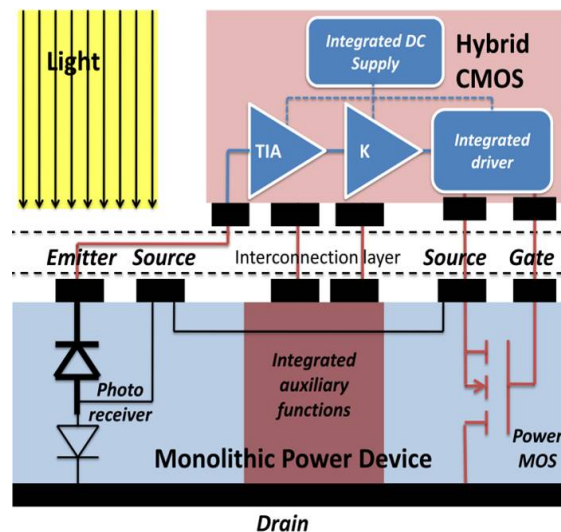


Figure I.45: Integration approach: a monolithically integrated photodiode, connected to a flip-chipped readout circuit (TransImpedance Amplifier (TIA) + K voltage gain), a gate driver and an efficient self driver supply. The integrated auxiliary unit includes the necessary sensor monitoring and power supply functions [89].

(IPD) structures are considered practical which would not require significant additional fabrication costs compared to the cost of the standard VDDMOSFET fabrication process. Since the IPD and the power device are integrated in the same substrate, it is important that the IPD does not compromise the performance of the power switch and visa versa. Four structures were considered as shown in figure I.46 [88], from which, only the first was found acceptable for further investigation. It was found that only the top emitter/base junction could be used since the second base/collector junction would be strongly effected by the floating voltagess of the backside drain contact of the power device; thus, the third solution is not suitable. The fourth solution which is a planar bipolar transistor could theoretically offer a transistor gain for the photo generated current, however, since the base has to be always connected to the lowest potential in order to avoid the parasitic turn-on of the internal BJT, it is not possible to control this transistor. The second structure was also rejected since the P+ region would result in a lower junction breakdown voltage. Thus, as shown in the first structure of figure I.46, the Emitter-Base N+/P- junction is chosen for the optical-detector. In this particular connection, The drain of the power switch is on the back side and the anode/P- of the IPD is connected to the Source of the power switch. As long as the base is connected to the lowest potential such that the N+/P- junction and the P-/Nv junction are both reversed biased at all times, the emitter photo generated leakage current will serve as the input electrical signal for the VMOS gate control. The advantage of this design is its monolithic integration compatibility with the already existing VD-MOSFET fabrication process and thus without the need of new fabrication steps [88] [89].

Figure I.47(a) shows a photo of a  $100\mu\text{m}$  diameter IPD that was fabricated in 2008 and its current-voltage (IV) characteristic as a function of an arbitrary incident light is shown in figure I.47(b). Using this light-current-voltage (LIV) measurement, its respon-

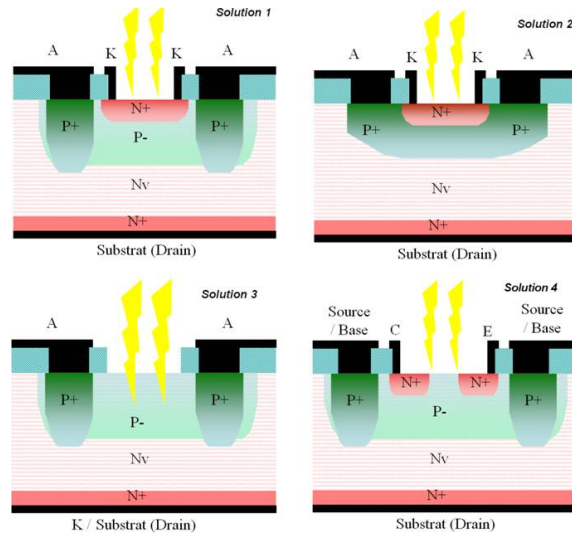


Figure I.46: The possible solutions for an optical detector fabricated via the VDMOS process. [88].

sensitivity was estimated to be 0.03 A/W [88] with a non-calibrated 600 nm wavelength laser as the optical source.

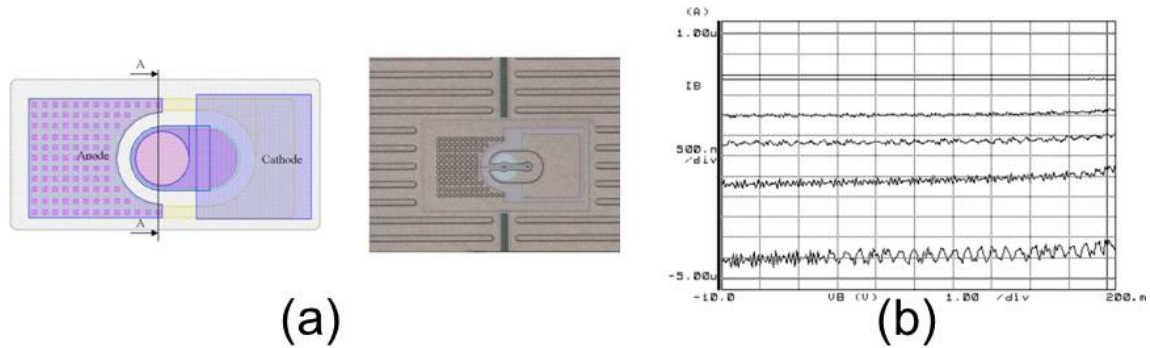


Figure I.47: (a) Left: Design of the photoreceiver in Cadence Virtuoso, using the power transistors 9 mask levels. Right: Snapshot of a fabricated receiver. [37] [88]. (b) Reverse I(V) static characteristic of one integrated photoreceiver, under different irradiation (Emitter grounded,  $V_{base}$  and  $I_{base}$  are shown) [37] [88].

Although the initial results are promising, further in depth experimental, modelling alongside more accurate and advanced DC and AC measurement systems are required for a complete characterization of the IPD; only then, it can be conclude if the proposed IPD is truly a suitable candidate and compatible for monolithic integration with the 600 V vertical power switches. Moreover, a full characterization will allow defining the optimum design and operating conditions of the IPD. This thesis, aims to accomplish these mentioned objectives above. The required characterization objectives are specified below:

- Effects of the pn-junction design (doping levels, junction depth, thickness of absorp-

tion layer, etc) on the QE, Responsivity, bandwidth, and noise of the IPD

- Effects of  $\lambda$ , Emitter and Collector voltages, temperature, and optical power level on the QE, Responsivity, Bandwidth, and noise of the IPD
- Effects of the high DC voltages from the backside collector on the Responsivity, bandwidth, and noise
- Effects of the high transients voltages from the backside collector on the Responsivity, bandwidth, and noise.

Through analytical modelling in Matlab and Finite Element simulations in Silvaco, qualitative effects of the design parameters and operating conditions on the IPD performance parameters are studied. These modelling results provide educated quantitative design estimates for the IPD prototypes. After the design and fabrication of the IPD prototypes, they need to be experimentally characterized. To achieve reliable and accurate measurements, DC and AC electro optical setups were carefully developed.

Ideally, a fully integrated solution would incorporate the optical source, optical detector, optical interconnects and the required electronic circuitries as well as the power elements all together on one integrated chip. Some of the main challenges on the path to realizing such an ideal integrated electro optic solution for high temperature(i.e. 100°C) Silicon power chips are: (1) efficient Si optical sources have yet to be invented, (2) even in Silicon material, optical detectors, optical interconnects, CMOS electronics, and vertical power devices all have different fabrication technologies, (3) leakage currents which contribute to noise as well as optical indices which effect optical wavelengths and optical absorption coefficients are a function of temperature. Leaving the optical source aside, there are three main blocks that require attention in order to implement and demonstrate the IPD: (1) the integrated optical detector, (2) a compatible TIA (flip-chipped or monolithically integrated), and (3)the optical interface required to route and transfer the input optical light to the optical detector. Some possible integration approaches for these three main blocks are discussed below.

1. The integrated optical detector: This IPD can be integrated on the CMOS driver chip or the power chip as shown in figure I.48 and I.50 respectively, and provides a low power, high bandwidth optical galvanic isolation. A variety of designs based on the pn-junction photodiode are investigated and will be presented in detail in the second chapter; some photos of the fabricated samples are shown in figure I.49. Also, the possibility of integrating photodetector designs other than the pn-junction based photodiode were assessed in the previous section. In all cases the IPD must not be affected by the environment (i.e. the parasitic internal BJT structure in the VDMOSFET) and operating conditions of the power device which include temperature and high voltage (DC and transient) perturbations. Moreover, the IPD should not compromise the performance of the power device or add a cost penalty, thus the

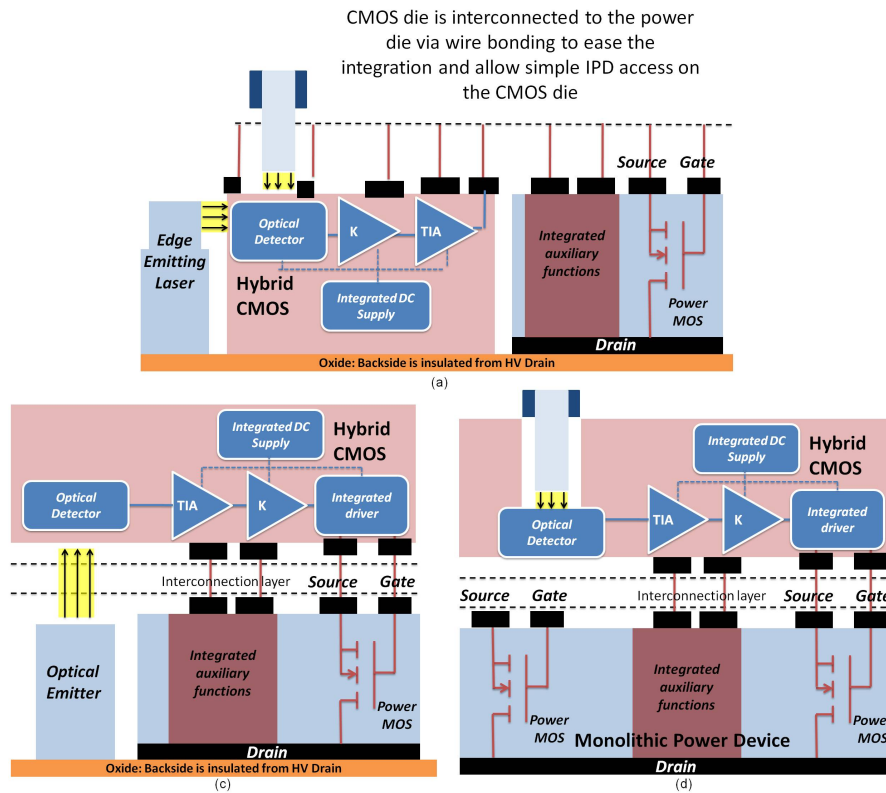


Figure I.48: Hybrid CMOS integration approach : a CMOS chip with integrated photodiode, readout circuit (TransImpedance Amplifier (TIA) + K voltage gain), a gate driver and an efficient self driver supply (a) is connected to the power die by wire bonding. A Direct bonded copper (DBC) would be used for better insulation between chips and effective heat dissipation. Light is supplied to the detector by means of an optical fiber or an edge emitting laser. (b) The CMOS is flip-chipped on the power die. light is supplied by a surface emitting laser or LED placed on the same plane as the power die (in this case isolation level is limited by the dielectric layer between the light source and the detector). (c) light is supplied to the detector by means of optical fiber and a deep trench.

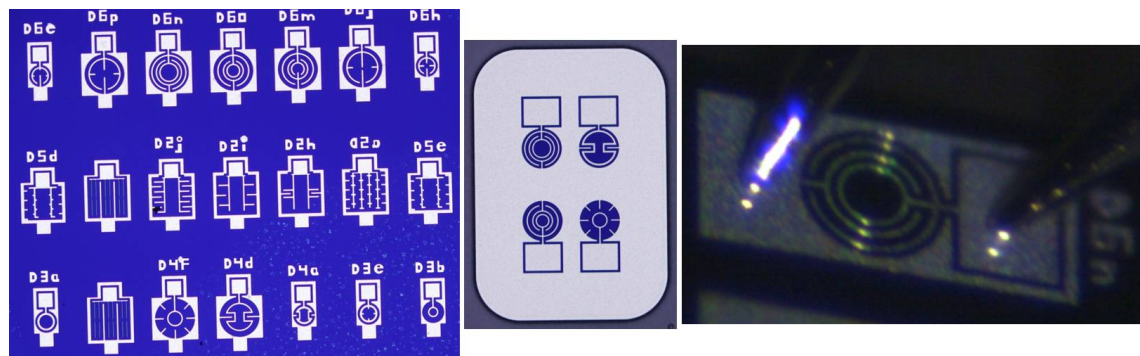


Figure I.49: To the left, a microscopic photo of the fabricated IPD. In the middle, a microscopic photo of the fabricated IPD with DRIE trench to allow high voltage testing. To the right, a photo of one of the fabricated optical detectors under test. These optical detectors also include an anti-reflective coating layer.

fabrication technology is highly constrained by the power device.

2. TIA: The design of the TIA is under progress by Thanh Long Le [90] who is a PHD student at G2ELab currently working with Dr.Rouger and Dr.Crebier. The TIA can be fabricated in the CMOS chip or it can be monolithically integrated in the power chip as presented in figure I.45. The main challenge of the TIA is its ability to provide a sufficient gain (an output voltage of a few 100s of mV for an input current of less than  $1\mu\text{A}$ ) without increasing noise or limiting the bandwidth (minimizing the input capacitance of the TIA is desired).
3. Optical interface: Fiber optics and waveguides are two different possible approaches; optical fibers can be more practical than a waveguide network when the optical source needs to be further from the IPD, however. For an IPD integrated in a CMOS chip, figure I.48 demonstrates two possible approaches for the optical interface, (1) optical fiber and deep trench, or (2) an optical source (i.e. LED or vertical-cavity surface emitting laser (VCSEL)) aligned beneath the flip-chipped CMOS. For the power chip integration mode, 4 possible optical interfacing approaches are presented in figure I.50. Depending on the design of the IPD, the IPD could either be horizontally or vertically triggered by light. Figure I.50 (a) shows the two triggering orientations of an optical fiber. In figure I.50 (b) the IPD is edge triggered by an aligned optical chip where light is coupled through free space from the optical source (an LED or an edge emitting laser) to the IPD (note that edge triggered IPD designs are different from vertically triggered designs). The optical interface can also be achieved through waveguide based optical interconnections either via a hybrid mode as shown in figure I.50 (c) or a monolithic mode as shown in figure I.50 (d). In all the cases presented here, the waveguides and optical fibers must be chosen and designed to work with the optical wavelengths used by the Silicon IPD. Using waveguides reduces optical alignment challenges meanwhile allowing easy optical routing throughout the chip; however, waveguide designs must have sufficiently low losses and compatible temperature tolerances.

The different integration modes presented above all only deliver the control signal through the optical interface and they all require a floating supply in order to supply the required energy to switch the gate. Another novel integration approach is presented in figure I.51 which includes a second IPD that would be biased under the conditions of a solar cell; the generated voltage at terminals of this second IPD can then be converted by a DC-DC converter to charge a storage capacitor for power supply purposes. This approach can simplify the CMOS circuitry since the floating power supply is eliminated. In this case, a more powerful optical source with a DC and AC component would be required in order to deliver both the energy and the gating signal.

Even though Silicon is not the ideal material for making optical detectors, it has been the dominant material of choice in electronics due to its excellent compromise between

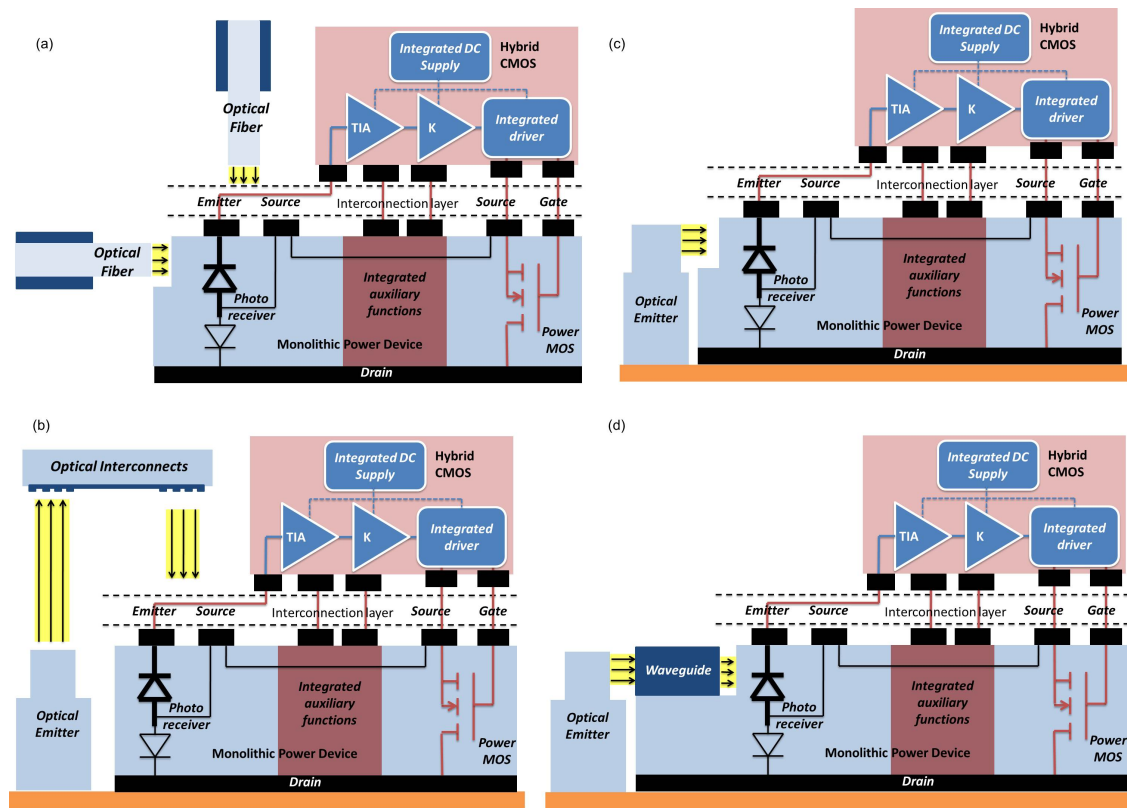


Figure I.50: Hybrid Integration approach : a CMOS chip with readout circuit (TransImpedance Amplifier (TIA) + K voltage gain), a gate driver and an efficient self driver supply flip-chipped on the power chip with IPD. (a) Light can be edge or vertically coupled to the IPD by means of an optical fiber. (b) A flip-chip optical interconnect chip can provide light coupling by means of grating couplers and routing by waveguides. (c) An optical source such as an LED or an edge emitting laser can be aligned to edge trigger the IPD in free space. (d) Waveguides can be integrated directly onto the power chip to rout the optical signals.

cost and performance. Although there are growing interests in developing power devices in wide bandgap materials (advantages include higher thermal conductivity and breakdown voltages) such as GaAs, SiC, GaN, and diamond, it is worth noting that Silicon continues to hold one major advantage, namely that Silicon technology is cheaper. Looking at costs, it could be argued that Silicon has benefited from large amounts of investments for many years that has led to its cost efficient and mature technology; this implies, that with enough investments new technologies will be developed for wide bandgap materials that can eventually surpass the cost barrier set by Silicon. In spite of the fast developments of new materials, it could be also debated that Silicon technology will continue to grow, develop and remain a key player in the future of electronics mainly thanks to its natural abundance. Referring to figure I.52, Silicon and Oxygen (which is Silicon's native oxide) are the most two abundant elements on earth. Thus in this thesis, we will focus on silicon compatible technologies with potential for monolithic integration; moreover, this work is potentially transferable to other material platforms. Materials from group III-V such as GaAs and GaN (GaN has a higher thermal and voltage capability over GaAs and SiC)

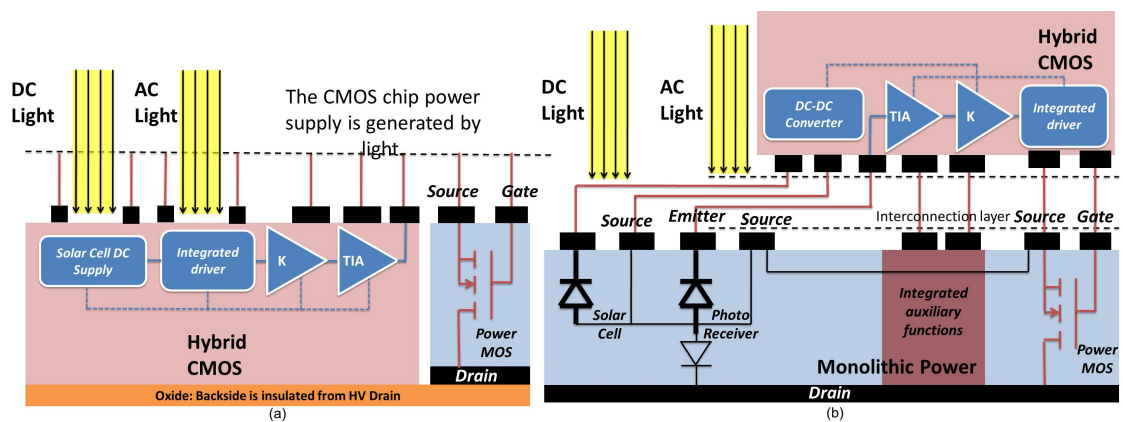


Figure I.51: Optical detector and optical supply integration approach. One IPD receives an optical PWM signal and outputs the gating PWM current signal, meanwhile, a second IPD receives a DC optical power and outputs a voltage signal for supplying the required power. In this approach the auxiliary unit no longer includes supply functions; current and temperature sensing functions are still required. (a) The CMOS chip and the power die are connected on a DBC via wire bonding. The two optical detectors are integrated in the CMOS chip (b) The two optical detectors are integrated in the power die. Since the second IPD is used as a solar cell to output a voltage, it needs to be forward biased; in this case the parasitic bipolar is an issue and needs to be suppressed from turning on.

offer much higher optical conversion efficiencies relative to other groups of materials (i.e. SiC), and thus they are ideal for making optical sources and detectors. Moreover, it can be predicted that with assumed material growth maturity (currently SiC and GaAs have more mature material growth over GaN) in the future, GaN could provide one of the most promising platforms for integrated electro optic solutions in power electronics.

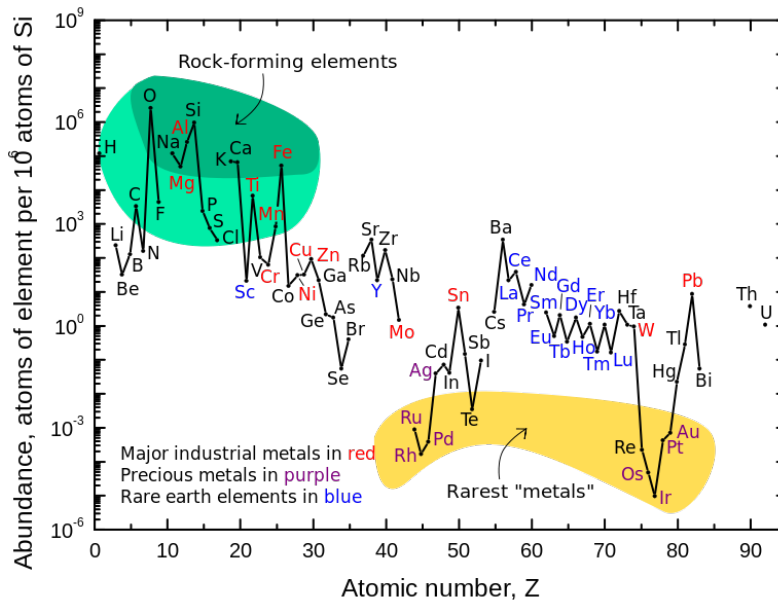


Figure I.52: Abundance (atom fraction) of the chemical elements in Earth's upper continental crust as a function of atomic number. The rarest elements in the crust (shown in yellow) are the most dense. They were further rarefied in the crust by being siderophile (iron-loving) elements, in the Goldschmidt classification of elements. Siderophiles were depleted by being relocated into the Earth's core. Their abundance in meteoroid materials is relatively higher. Additionally, tellurium and selenium have been depleted from the crust due to formation of volatile hydrides. [91].

## I.5 Thesis Overview

In efforts of providing a novel high level optical solution for the galvanic isolation challenge inside power converters, more specifically between the power device and its control unit, this thesis proposes a compatible optical detector design for monolithic integration with a 600 V vertical MOSFET without any modifications to the power VMOS fabrication process. The proposed optical detector can be triggered by an optical beam of minimum  $1 \mu\text{W}$ , thus it allows for a range of low power, low cost, and small optical sources such as semiconductor lasers and LEDs. The output of the optical detector will be a current signal in the range of a few of  $\mu\text{As}$ . This output current signal contains only the control information; in order to provide the sufficient energy required to switch the VD-MOSFET, the output of the optical detector will be amplified at a TIA stage before feeding the gate of the VDMOSFET. The project perspective and approach are illustrated in figure I.53.

### I.5.a Methodology

The optical detectors and VDMOSFET devices presented in this thesis were fabricated using the standard VMOS process at the CIME Nanotech/Minatec cleanroom facilities in Grenoble. Each research cycle starts with an idea emerging from literature review and brain storming sessions. The models are chosen based on Silicon material, semiconductor and optical theories and VMOS fabrication standards. The devices are simulated and

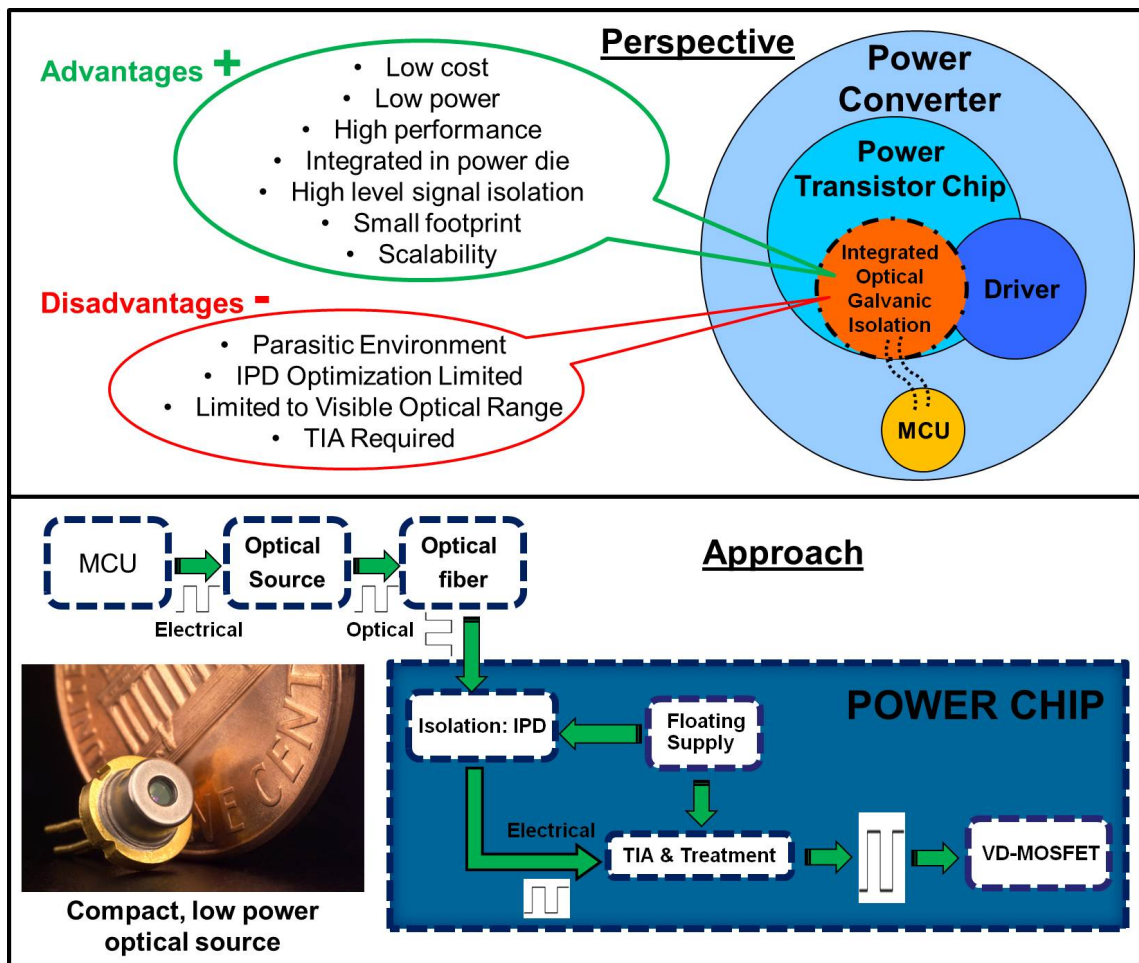


Figure I.53: Project perspective and approach overview.

optimized using analytical methods and numerical tools such as Silvaco and Athena. Next, mask layouts were designed using Cadence tools. Once the designs were fabricated and measured, the collected data were processed and analysed using Matlab tools. The designs were then improved by feedbacks from comparing the experimental and the simulation results (during the course of this thesis, only one fabrication run was done). Moreover, in each research cycle, the limitations of the experimental setup were identified and improved, the flexibility of the measurement procedure was enhanced, and further functionalities were added. Furthermore, the fabrication tolerances, errors and effects were identified and can be taken into consideration at the start of future research cycles.

### I.5.b Organization

Chapter 2 introduces the optical detector structure and explains its compatibility with the VD-MOSFET fabrication standards. The design and modelling approach for the detector are provided in detail. In chapter 3, the characterization results of the optical detectors as well as the DC and AC electro optical measurement set-ups used to characterize the fabricated devices are presented.



## Chapter II

---

# Compatible Integrated Photodiodes (IPDs) for Power Switches: Modeling, Design and Technology

*Essentially, all models are wrong, but some are useful.*

George Edward Pelham Box

### SOMMAIRE

---

II.1 INTRODUCTION . . . . .	55
II.1.a IPD Structure . . . . .	55
II.1.b Design Constraints . . . . .	57
II.2 FUNDAMENTALS OF DEVICE MODELLING AND SIMULATION . . . . .	60
II.2.a Built-in Potential and Depletion Region Width . . . . .	60
II.2.b Carrier Transport and Current Continuity . . . . .	65
II.2.c Photogeneration . . . . .	68
II.2.d Photocurrent . . . . .	73
II.3 ANTI-REFLECTION COATING . . . . .	76
II.4 STATIC ANALYSIS . . . . .	81
II.4.a DC Emitter and Collector biasing . . . . .	86
II.4.b Sensitivity to Carrier Lifetimes . . . . .	91
II.5 DYNAMIC ANALYSIS . . . . .	94
II.5.a Wavelength Dependence . . . . .	96
II.5.b Emitter DC biasing . . . . .	100
II.6 OPTICAL BEAM RADIUS AND POSITION ANALYSIS . . . . .	102
II.7 PARASITIC ENVIRONMENT CONSTRAINTS . . . . .	104
II.7.a Electrical Activation of Parasitic BJT . . . . .	104
II.7.b Optical Activation of Parasitic BJT . . . . .	108
II.8 SIMULATION AND MODELLING CONCLUSIONS AND OVERVIEW . . . . .	115

---

### Abstract

*In order to obtain an in-depth understanding of the proposed integrated photodetector behaviour and its achievable performance range, suitable operation region and limitations in consideration of the imposed vertical structure, parasitic environment and operating conditions of the power switch, this chapter conducts a number of studies via analytical modelling and finite element simulation. We start by reviewing the fundamental basis of physics of semiconductor devices specially relevant for modelling pn-junction devices. Next, the static and dynamic performance of the IPD is modelled*

*and simulated as function of design, material and operation input parameters such as doping profile (limited by VDMOSFET), optical wavelength, optical intensity, applied voltages, device area, optical beam size, shading, carrier lifetimes, and substrate DC and transient high voltages.*

## II.1 Introduction

This chapter demonstrates the modelling and simulation approach used to study the monolithic integration of the photodetector (IPD) with the power transistor as well as the design. The IPD structure is introduced and the design approach, device operation and performance limitations are described using analytical models, 2D and 3D finite element simulations in Silvaco. The IPD responsivity and bandwidth are studied as a function of the following variables: doping profiles, carrier lifetimes, applied voltages, optical wavelength, optical intensity, IPD sensitive area, shading factor and illuminated region.

### II.1.a IPD Structure

The IPD is a three terminal device with two top contacts and one back contact corresponding to the Emitter, Base and the Substrate/Collector respectively. Figure II.1 (a) shows the cross sectional view of the IPD as well as a simple lumped circuit model.

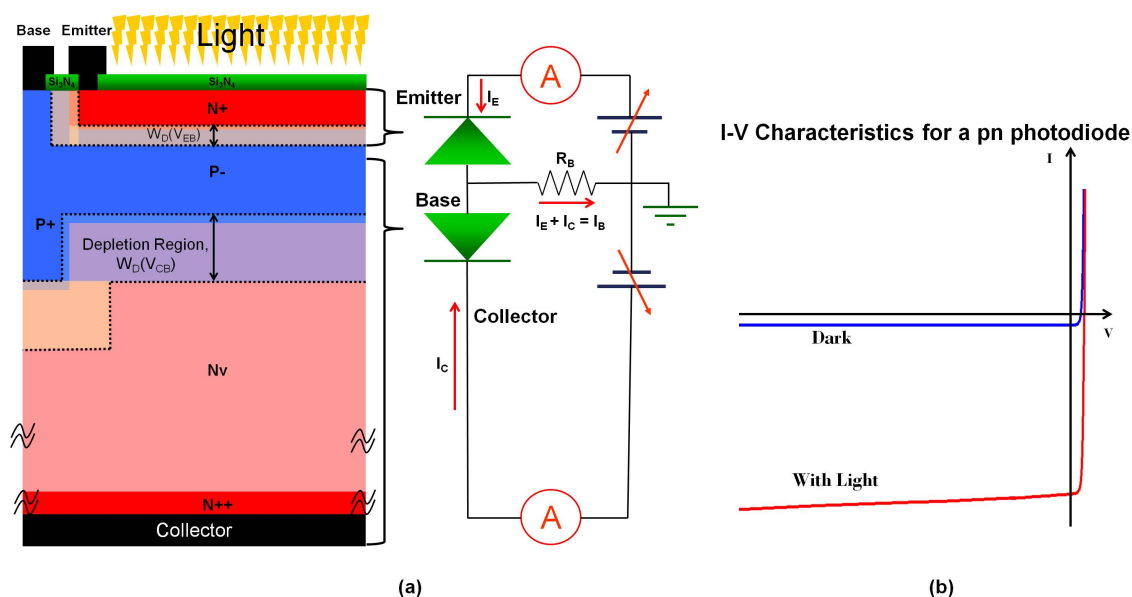


Figure II.1: (a) IPD structure cross sectional view and polarization. In this case there are no external load resistances considered. The Base resistance and the contact resistances contributes to the series resistance of the Base. (b) I-V characteristic for a pn photodiode with and without light.

In this circuit, the IPD is modelled as two back to back diodes instead of a bipolar model; this simplification (two diode model instead of a bipolar model) is possible since the IPD can only be operated with the two junctions under reverse bias conditions (bipolar off state). With both junctions reversed biased, only the leakage currents from the junctions are flowing through the device when there is no light. If for some reason one of the junctions becomes forward biased (i.e. due to substrate transients), the bipolar model needs to be considered. Moreover, the circuit of figure II.1 includes a Base resistance which represents all the series resistances associated with the Base semiconductor resistance, the Base contact resistance and the Base metal resistance. There are other series resistances

in the Emitter and the Collector, however, the Base resistance is more significant to the IPD performance. The Emitter resistance is generally very low since the Emitter is highly doped and thus it has a much lower resistivity compared to the Base region. The lightly doped Collector region has a much higher resistance relative to the Base region, however, this resistance becomes insignificant to the IPD performance as long as there isn't a significant amount of photocurrent generated in the Collector region. When the device is illuminated by incident photons of energy  $h\nu$ , it experiences a notable increase in its reverse current as shown in the IV plot of figure II.1 (b). The magnitude of the generated current is proportional to the intensity of the light as long as there are no non-linear effects.

The intensity of the light decays exponentially with penetration depth and its magnitude is also wavelength dependent as depicted in figure II.2. A portion of the optical intensity will generate electron-hole pairs that will modify the free carrier distribution within the device and can generate a detectable current if collected by the electric field across the junction. The ratio of photons to detectable electrons is called quantum efficiency, QE. As it can be seen from figure II.2, photogeneration can take place in a number of different areas within the IPD, including the Emitter neutral region, Emitter-Base drift depletion region, Base neutral region, Collector-Base drift depletion region and the Substrate/Collector neutral region. In order to improve the QE of the device, long carrier lifetimes and a thicker emitter region and depletion region are desired to allow for more optical absorption.

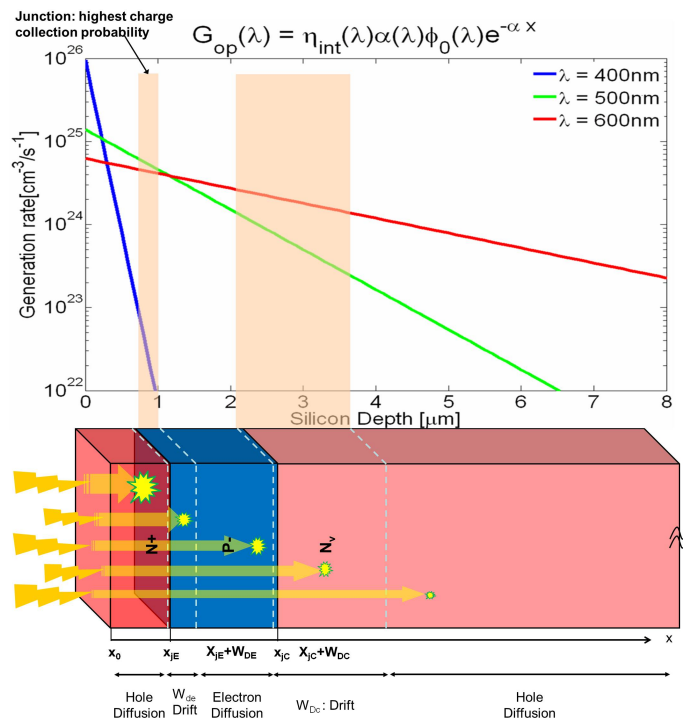


Figure II.2: IPD simplified 1D structure cross section view showing the different regions where photogeneration may take place. Carrier generation rate is dependent on the optical wavelength and decays exponentially with penetration depth into the device.

### II.1.b Design Constraints

The cross section schematic of the VD-MOSFET power transistor and its optical isolation device in the monolithic integration mode is shown in figure II.3. In this monolithic integration approach, the VD-MOSFET and the IPD share the same doping profiles which in turn determine the internal resistivity [ $\Omega.cm$ ], built-in junction potentials, capacitances [ $pF/cm^2$ ], voltage and transient limitations of both the IPD and the VDMOSFET structures. The fabrication technology fixes the vertical structures and doping profiles which must satisfy the VD-MOSFET performance requirements as well as maximize the performance of the IPD. The technology and parasitic environment constraints are identified in the following subsections.

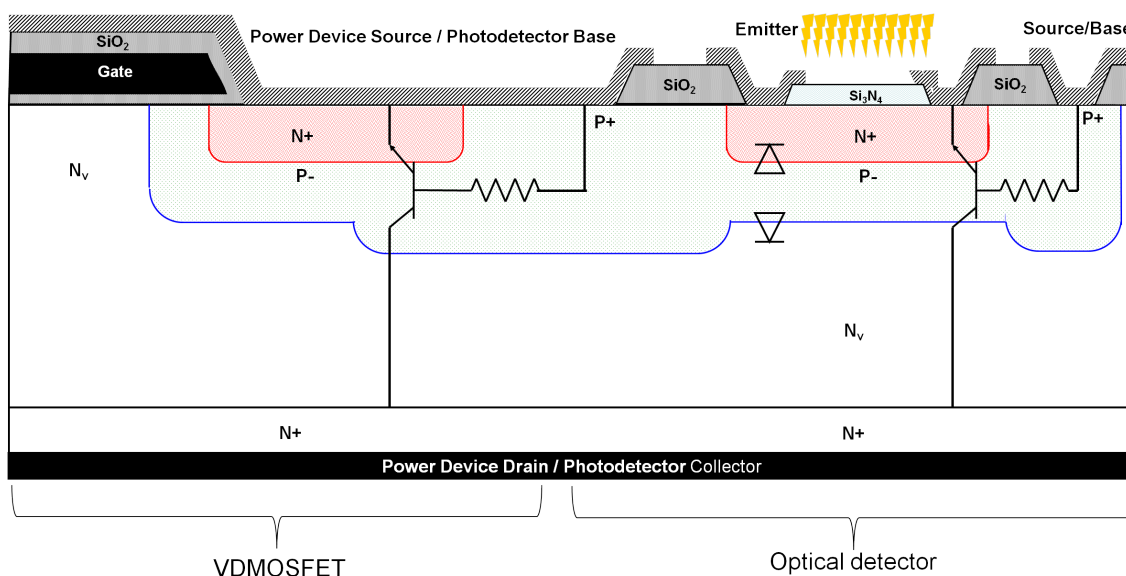


Figure II.3: A cross section view showing the VD-MOSFET and its optical isolation in the same substrate.

In the VD-MOSFET structure, the N+ doped source region is separated from the lightly doped  $N_v$  region by a P- base region, resulting in the formation of two junctions:  $J_{EB}$  and  $J_{CB}$ . A voltage applied to the gate, forms a channel in the p- region underneath the gate oxide; this process is the same as in the MOSFETs used in microelectronics although the channel location and length is different from that of microelectronics. After a channel is formed, a voltage applied between the source and the drain can result in a current flow. Once the current passes through the channel, it then enters a parasitic JFET region which is formed by the  $N_v$  region sandwiched between the two adjacent P- regions, before finally flowing through the substrate and into the drain [7] [5]. Table II.1 provides an overview of which design parameters are linked to the different performance parameters of the power VD-MOSFET. The design parameters of interest for the IPD optimization are highlighted in yellow in table II.1.

Table II.2 lists the main layers in a VD-MOSFET structure and some typical values for doping levels and layer thicknesses [7]. The minimum surface doping concentrations

	$L_G$	$e_{Oxide}$	Emitter $N_D^+$	Base $N_A^-$	Substrate $N_v$	Thickness Emitter	Thickness Base	Thickness $N_v$
$V_{BD}$				X	X		X	X
$R_{Channel}$	X	X				X	X	
$R_{Drift}$					X			X
$V_T$	X	X		X				
Bandwidth	X	X	X	X				

Table II.1: Summary of VD-MOSFET performance parameters dependencies on design variables, where  $V_{BD}$  is the breakdown voltage,  $R_{Channel}$  is the MOSFET channel resistance,  $R_{Drift}$  is the resistance of the substrate  $N_v$  region, and  $V_T$  is the MOSFET threshold voltage.

(roughly  $5 \times 10^{19}$  [atoms.cm<sup>-3</sup>] for N-type Si, and  $1 \times 10^{18}$  [atoms.cm<sup>-3</sup>] for P-type Si [92]) are fixed in order to create ohmic contacts.

Layer/Region	Doping [cm <sup>-3</sup> ]	Thickness
$SiO_2$ - Gate		50-100 nm
Si -Source	N+ $10^{19}$	0.5-0.7 $\mu m$
Si - Base, Channel	P- $10^{16}$	2 $\mu m$
Si - Base, Contact Well	P+ $10^{19}$	3 $\mu m$
Si - Epi-Drift Layer	Nv $10^{14} - 10^{16}$	50 $\mu m$
Si - Substrate, Drain	N++ $10^{19}$	300-600 $\mu m$

Table II.2: 600V VDMOSFET, key layer specifications. The  $N_v$  doping concentration range of  $10^{14}cm^{-3}$  to  $10^{16}cm^{-3}$  corresponds to a 600V to 100V VMOS respectively. [7]

Figure II.4 (a) shows the anatomy and the application of an optical interconnect link for the optical control of a power transistor. First, light is generated by a continuous wave laser and modulated by an electro optical modulator which requires its own electrical driver. Then, the optical signal travels through a waveguide or an optical fiber or free space to the receiving end where it is converted back into an electrical signal by a photodetector. The photodetector output current is then converted into a voltage signal and amplified via a TIA before being treated to drive the power transistor gate. Figure II.4 (b), depicts the electrical circuit diagram of the integrated IPD and its associated VDMOSFET as adapted in our approach. In this approach which was introduced and discussed in chapter 1, the photodetector is integrated in the power die alongside the VD-MOSFET.

The IPD needs to be optimized for successful interaction with three main subsystems:

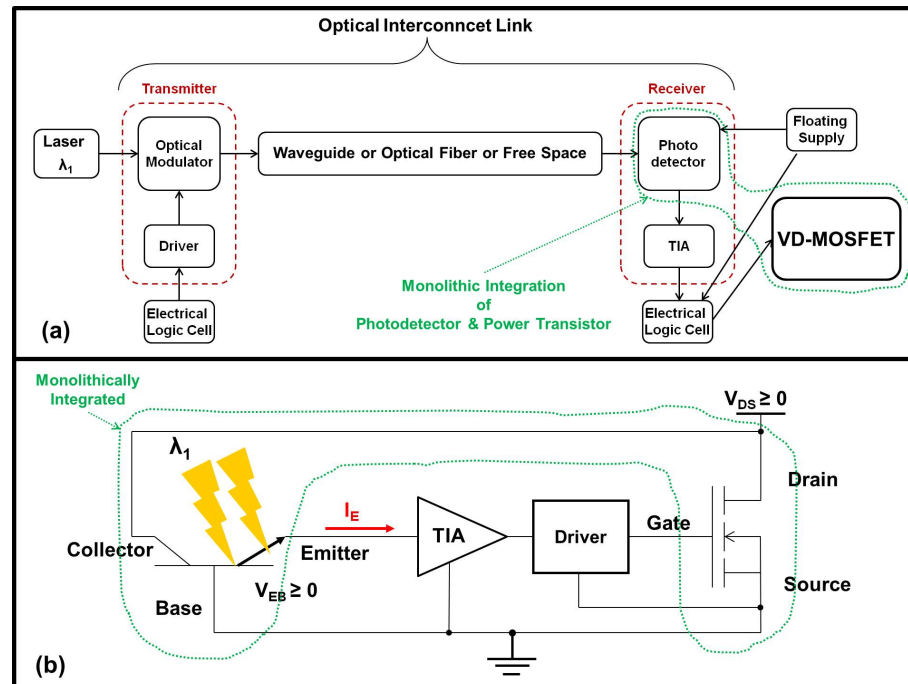


Figure II.4: (a) Optical Link applied to power transistor gate control. (b) The chosen integration approach and study.

1. The Power Transistor: The IPD's performance should stay unaffected by the power switch operating conditions and parasitic environment. The IPD's structure must be compatible with the planar VMOS fabrication process of a 600 V VDMOSFET; thus the doping profile is fixed by that of the VDMOSFET.
2. The Optical Interface: In order to use low power, compact optical sources, the optical coupling factor into the IPD needs to be maximized; thus an ARC layer and an optimized shading factor (contact design) are needed.
3. The TIA Interface: In order to reduce the design tolerances of the TIA, the output current of the IPD needs to be maximized, meanwhile its output impedance and dark current level must be minimized. There is a compromise between maximizing the output current and the bandwidth.

The optical and electrical operation settings, the design variables and output performance parameters of the IPD are shown in the diagram of figure II.5. Table II.3 gives an overview of the main initial design requirements for the IPD. Reducing the optical power requirements down to a few micro-watts would allow the use of small and cost effective sources such as LEDs. In order to reduce the amount of required amplification at the TIA stage, the minimum output current of the detector should be in the range of  $1 \mu\text{A}$  which in turn corresponds to a minimum responsivity of  $0.1 \text{ A/W}$ . Maximizing the device bandwidth performance would result in reduced delays and enable the use of a higher frequency carrier modulation technique.

Now that the device structure and requirements have been introduced, we will proceed by giving a more in-depth explanation of the device operation via analytical modelling and

numerical simulations.

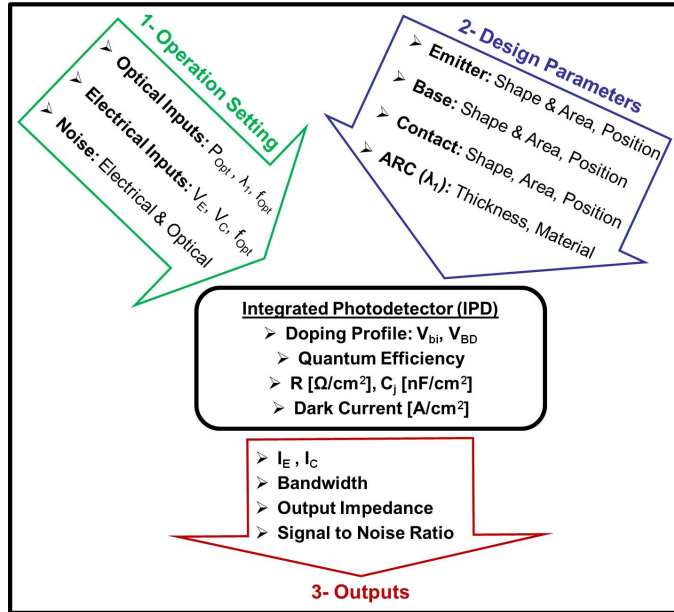


Figure II.5: Input/Output black box view of the IPD.

Responsivity [A/W]	Optical Power [ $\mu W$ ]	Output Current [ $\mu A$ ]	Bandwidth [MHz]	Fabrication	VDMOSFET parasitics	VDMOSFET Performance
Min. 0.1	Min 10	Min. 1	Min. 10	VDMOSFET Compatible	Independent	Non- interfering

Table II.3: Integrated Optical Detector Minimum Requirements

## II.2 Fundamentals of Device Modelling and Simulation

The pn-junction theory as established first by Shockley and then extended by Sah, Mol, and Noyce, serves as the fundamental basis for the physics of semiconductor devices [93] [94] [95]. These basic theories are used here in modelling the proposed IPD. The following subsections give an overview of the set of fundamental equations that are linked together in order to study the electrical and optical behaviour of the IPD and to acquire some insights into the internal physical mechanisms of the device.

### II.2.a Built-in Potential and Depletion Region Width

The charge density  $\rho$  profile within the depletion region of a pn-junction device plays a critical role in the operation of the device since it defines the electric field  $E$  and the electric potential  $\psi$  distributions. Applying Maxwell's equation to a one dimensional problem, the

relationship between net charge concentration, electric field and the electric potential as a function of distance  $x$  can be stated as in equation II.1.

$$\frac{d^2\psi(x)}{dx^2} = -\frac{dE(x)}{dx} = -\frac{\rho(x)}{\epsilon} = \frac{q}{\epsilon}[n(x) - p(x) + N_A^-(x) - N_D^+(x)] \quad (\text{II.1})$$

Equation II.1 is known as the Poisson's equation and it states to important relations: (1) the gradient of the electric field  $E(x)$  with respect to distance  $x$  is proportional to the net charge concentration at  $x$  by the dielectric constant  $\epsilon$  of the semiconductor material, in our case that of Silicon. (2) The negative gradient of the electric potential  $\psi(x)$  with respect to distance  $x$  is equal to the electric field  $E(x)$ . Applying Maxwell Boltzmann statistics, the charge density  $\rho(x)$  can be expressed as:

$$q[N_D(x) - n_i e^{\psi(x)/V_{th}}] \quad 0 \leq x \leq x_{dn}(V) \quad (\text{II.2})$$

$$q[n_i e^{-\psi(x)/V_{th}} - N_A(x)] \quad -x_{dp}(V) \leq x \leq 0 \quad (\text{II.3})$$

where the metallurgical junction is assumed to be at  $x = \text{zero}$ , with the depletion region width on the n-side marked by  $x_{dn}$  and the depletion region width on the p-side marked by  $-x_{dp}$ . In Atlas, equations II.2 and II.3 are substituted into equation II.1, and the resulting non linear equation is numerically solved for the electric field and the potential distributions. In order to avoid complex numerical calculations, the depletion region approximation method is used for the analytical modelling of the IPD which assumes that there are no free carriers within the depletion region,  $n(x) \approx p(x) \approx 0$ ,

$$n(x), p(x) \ll N_D(x) \quad 0 \leq x \leq x_{dn}(V) \quad (\text{II.4})$$

$$n(x), p(x) \ll N_A(x) \quad -x_{dp}(V) \leq x \leq 0 \quad (\text{II.5})$$

The depletion region approximation simplifies the smooth transition of carrier densities across the junction into a box profile, resulting in an abrupt change at  $x_{dn}$  and  $-x_{dp}$ . Thus equation II.1 can be reduced to,

$$\frac{d^2\psi(x)}{dx^2} \approx \frac{qN_D(x)}{\epsilon} \quad 0 \leq x \leq x_{dn}(V) \quad (\text{II.6})$$

$$\frac{d^2\psi(x)}{dx^2} \approx \frac{-qN_A(x)}{\epsilon} \quad -x_{dp}(V) \leq x \leq 0 \quad (\text{II.7})$$

Integrating equations II.6 and II.7, gives the electric field distributions as a function of distance space ( $x$ ) and voltage ( $V$ ),

$$E(x, V) = \frac{-qN_D}{\epsilon}(x_{dn}(V) - x) \quad 0 \leq x \leq x_{dn}(V) \quad (\text{II.8})$$

$$E(x, V) = -\frac{qN_A}{\epsilon}(x_{dp}(V) + x) \quad -x_{dp}(V) \leq x \leq 0 \quad (\text{II.9})$$

Integrating equations II.8 and II.9 gives the potential distribution:

$$\psi_n(x) = \psi(0) + \frac{qN_D}{\epsilon} \left(x - \frac{x_{dn}(V)}{2}\right)x \quad 0 \leq x \leq x_{dn}(V) \quad (\text{II.10})$$

$$\psi_p(x) = -\frac{qN_A}{2\epsilon} (x_{dp}(V) + x)^2 \quad -x_{dp}(V) \leq x \leq 0 \quad (\text{II.11})$$

Where  $\psi_n(x)$  and  $\psi_p(x)$  are the electric potentials in the n-type and p-type regions. Using equations II.10 and II.11, when no external voltages are applied, the built in potential across the junction is:

$$\psi_{bi} = |\psi_n| + \psi_p = \frac{q}{2\epsilon} (N_D x_{dn}(V)^2 + N_A x_{dp}(V)^2) \quad (\text{II.12})$$

At thermal equilibrium the electric field is zero in the QNRs and by charge neutrality the total negative charges equal the total positive charges:

$$N_A x_{dp}(V) = N_D x_{dn}(V) \quad (\text{II.13})$$

Combining equations II.12 and II.13, the depletion region width can be defined as:

$$x_{dn}(V) + x_{dp}(V) = W_D(V) = \sqrt{\frac{2\epsilon}{q} [\psi_{bi} + V_a] \left(\frac{1}{N_D} + \frac{1}{N_A}\right)} \quad (\text{II.14})$$

where  $V_a$  has been added to account for any external applied voltages; if no voltage is applied,  $V_a$  is zero. The total voltage  $V$  equals  $\psi_{bi} + V_a$ . In equation II.14 it is assumed that all the potential difference due to an applied voltage appears across the junction. Figure II.6 shows the relations between the built-in potential, depletion region width on the n and p sides of the junction, and the total depletion region width.

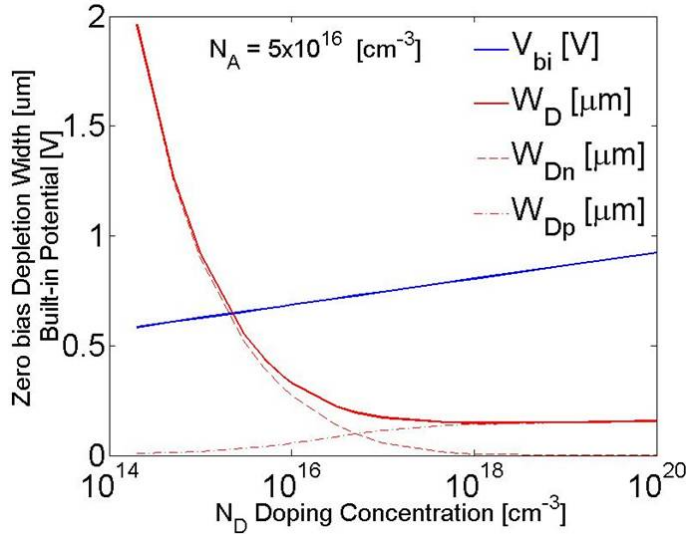


Figure II.6: Built-in junction potential and depletion region width as a function of doping concentration according to the depletion region approximation for a uniformly doped p-n junction. Zero applied voltage.

The free carrier concentrations for electrons and holes as well as the net uniform doping profile for the Silicon IPD n-p-n structure with Emitter  $N_D = 1 \times 10^{20}$ , Base  $N_A = 5 \times 10^{16}$

and Collector  $N_D = 2 \times 10^{14}$  is depicted in figure II.7 (a) as evaluated by a full numerical simulation in Atlas. Figures II.7 (b) and II.7 (c) demonstrate the difference between the Atlas simulation results and the depletion region approximation for the corresponding Emitter junction electric field and the potential distributions. The small difference in these results arises from the different charge density profiles considered; in Atlas, the profile of charge density is given by  $\rho(x) = [n(x) - p(x) + N_A^-(x) - N_D^+(x)]/q$  (the sum of the three plots in figure II.7 (a)) where as in the depletion region approximation it is given by  $\rho(x) = [N_A^-(x) - N_D^+(x)]/q$  (represented by the net doping in figure II.7 (a)).

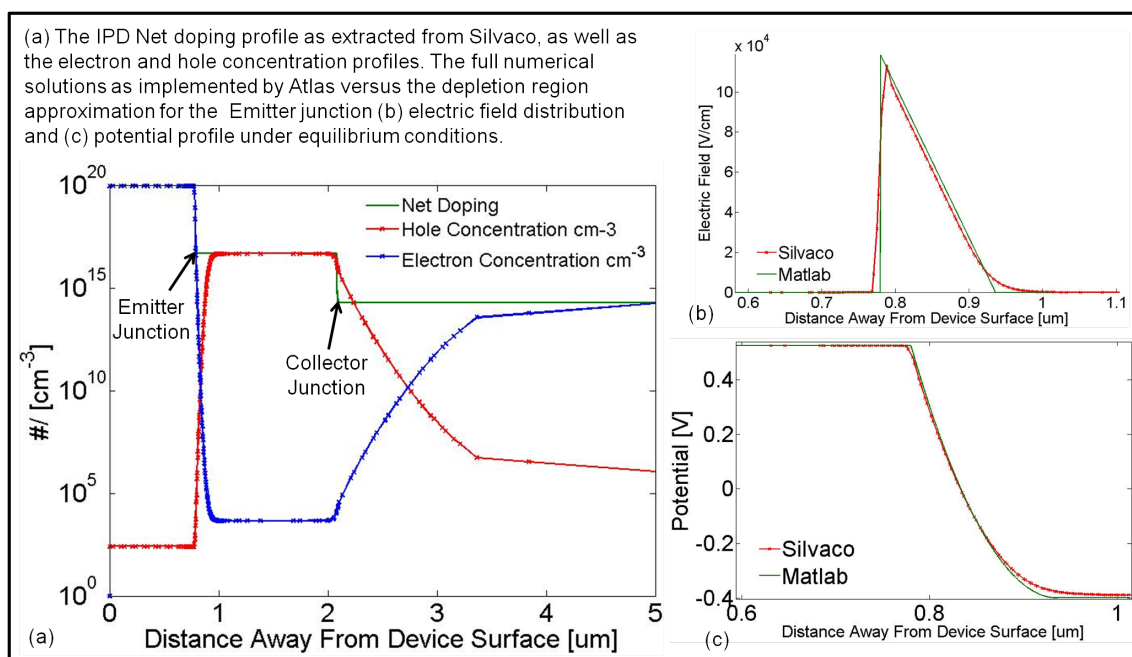


Figure II.7: The depletion region approximation versus the full numerical computation (via Atlas) for the n-p-n structure of the IPD with uniform doping profiles. The depicted distributions here correspond to a 0V applied bias.

The values of  $W_D$  and  $\psi$  are strongly dependent on the doping profiles and applied voltages. Although figure II.7 shows a promising consistency between the numerical and the analytical evaluations of  $W_D$  and  $\psi$ , a uniform doping profile based on the surface doping concentration is not realistic. The doping profiles for the case of a double diffused junction through ion implantation results in Gaussian distributions of the dopants. Solving the Poisson equations for a Gaussian distribution is a challenging task since there are no analytical solutions for the integration of a Gaussian function within finite limits. Atlas handles this challenge through numerical evaluations of the error function. The blue curve in Figure II.8 (a), is an SRP measurement from a sample that has been processed via the VMOS fabrication procedure at the CIME nanotech fabrication facilities. Assuming that the SRP measurement depicted in figure II.8 (a) roughly represents the true doping profile, the doping profile plotted in green as implemented by the Gaussian functions in Atlas, underestimates the amount of dopants specially in the Base region. In order to have a more accurate doping profile, the fabrication procedure can be simulated in Athena; however,

simulations in Athena can be rather heavy and time consuming specially for larger structures. To correct for this error and avoid heavy simulations in Athena, the SRP doping profile in Atlas can be fitted by the summation of two or more overlapping Gaussian profiles as shown in red in figure II.8 (a). Figure II.8 (b) shows the resulting electric field and potential distributions corresponding to the Gaussian fitted doping profile as evaluated in Atlas. In order to improve the depletion region approximation used for the analytical modelling, the area underneath the fitted-Gaussian profile can be integrated to evaluate an average doping concentration that would be representative of the total number of dopants in each region as depicted in figure II.8 (a) in black. Figure II.8 (c) and (d) show the differences in the electric field and the potential distributions for the gaussian fitted doping profile (GFDP) in comparison to the simple uniform doping profile (SUDP) based on the surface doping concentration, and the integrated uniform doping profile (IUDP) based on the total number of dopants in the region.

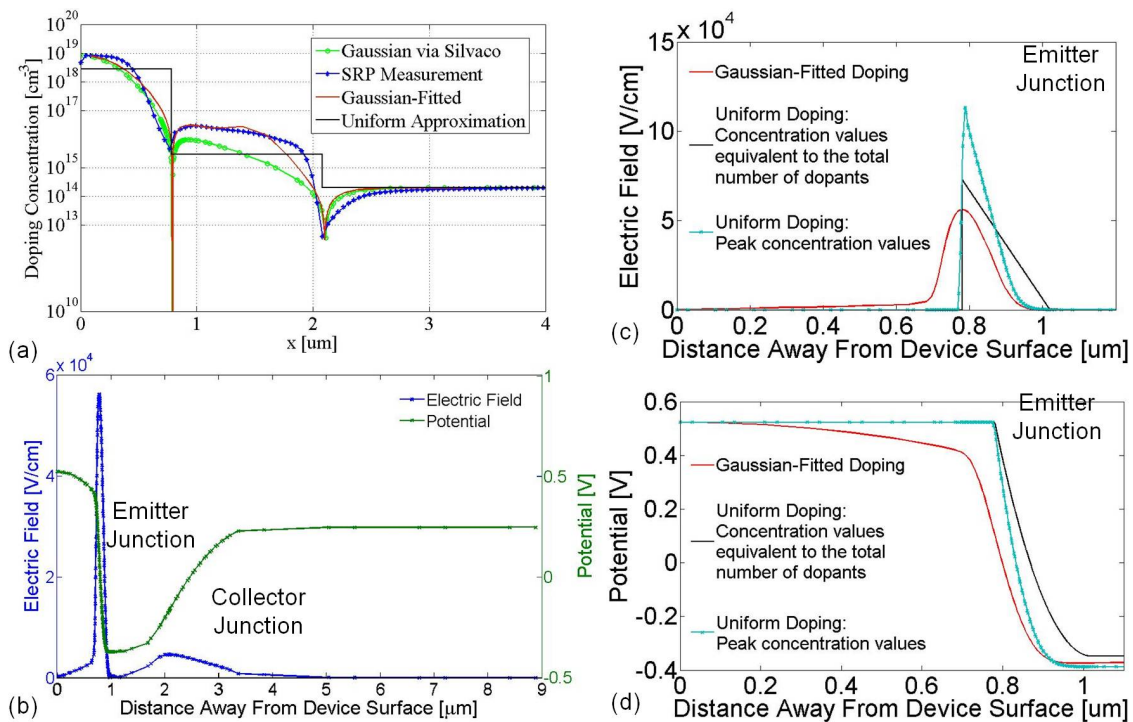


Figure II.8: (a) Three different approximations to the SRP measured doping profile of the IPD. The blue line shows the SRP measurement. The green line shows the approximated doping profile via the Gaussian functions available in Atlas. The red line shows the approximated doping profile via adding multiple Gaussian functions to better fit the SRP measurement. The black line shows the equivalent uniform doping profile to the Gaussian fitted profile. (b) The electric field and potential distributions in the Emitter and Collector junctions of the IPD as evaluated by Atlas corresponding to a fitted Gaussian profile at a 0V bias. The effect of three doping profiles: (1) uniform doping based on the peak dopant concentrations at the surface, (2) SRP-fitted profile based on Gaussian functions (3) uniform doping based on the total number of dopants in each region (c) on the Emitter electric field and (d) potential distributions. The plots correspond to a 0 V applied bias.

## II.2.b Carrier Transport and Current Continuity

When a small electric field is applied across a piece of Silicon, carriers are transported in the direction of the electric field with an average drift velocity:

$$\nu_d = \mu E \quad (\text{II.15})$$

Where mobility  $\mu$  [ $\text{cm}^2/\text{V}\cdot\text{s}$ ] is a material dependent parameter that expresses how easily carriers can be transported across the material under an applied electric field. Mobility is controlled by scattering events and thus it is a strong function of temperature, impurity and defect concentrations. Figure II.9 shows the analytical model for the electron  $\mu_n$  and hole  $\mu_p$  mobilities as a function of impurity concentrations at room temperature. The difference between the  $\mu_n$  and  $\mu_p$  mobilities arises from the difference in their effective masses [78].

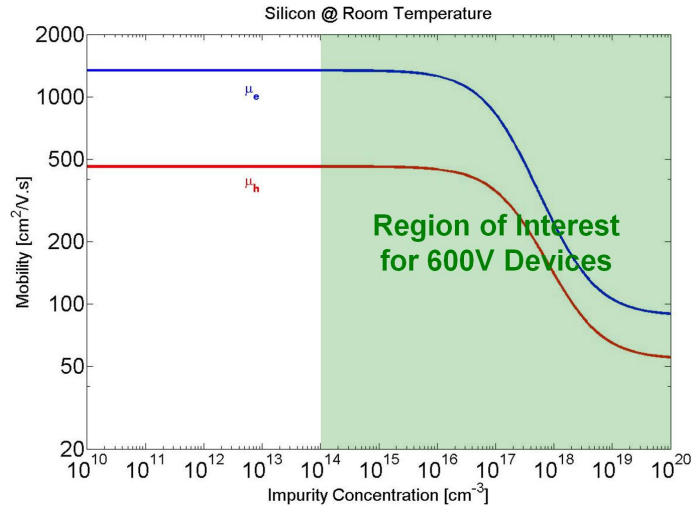


Figure II.9: Electron and hole mobility dependence on the total impurity concentration at Room Temperature. Reproduced from Sze [78].

The linear dependence of carrier drift velocity on the mobility is valid for low electric fields where carrier drift velocities are much lower than their average thermal velocities

$$\nu_{th} = \sqrt{\frac{3kT}{m^*}} \quad (\text{II.16})$$

In equation II.16,  $k$  represents the Boltzmann's constant,  $T$  the temperature in degrees Kelvin, and  $m^*$  the carrier (electron or hole) effective mass. For a high electric field that results in a carrier drift velocity close to the carrier thermal velocity, non linearities effects in the mobility cause the saturation of the carrier velocity. The saturation velocities of carriers in Silicon are ( $10^7$ )  $\text{cm/s}$  at room temperature and ( $8 \times 10^6$ )  $\text{cm/s}$  at  $100^\circ\text{C}$ . The critical electric field that results in the saturation of electrons and holes are ( $6 \times 10^4$ )  $\text{V/cm}$  and ( $24 \times 10^4$ )  $\text{V/cm}$  respectively at room temperature. For very high electric fields ( $>$  the critical electric field), impact ionization starts to take place (e.g. avalanche breakdown of a np-junction) [78].

Our analytical Matlab model uses equation II.15, and thus, this model is valid for the case of a low electric field. Moreover, as long as device dimensions are not comparable to the carrier mean free path, ballistic transport mechanisms can be ignored. Under the influence of an electric field, carriers begin to contribute to a current flow in the direction of the applied electric field referred to as the drift current,

$$J_{dr} = -q[n\mu_n + p\mu_p]E = \sigma E = \frac{1}{\rho}E \quad (\text{II.17})$$

where  $\sigma$  is the conductivity and  $\rho$  is the resistivity. From equation II.17, it is evident that conductivity of Silicon has a direct and strong dependence on the doping densities through the carrier concentrations, meanwhile, it has a weaker and inverse dependence on the doping densities through the carrier mobilities. Overall, Silicon conductivity increases (non-linearly) with increased doping densities. The models used in this thesis assume complete ionization of the dopants.

Current may also flow in absence of an electric field as long as there is a carrier concentration gradient present within the device, also known as diffusion current [78].

$$J_{diff} = q[D_n \frac{dn}{dx}n - D_p \frac{dp}{dx}p] \quad (\text{II.18})$$

$D_n$  and  $D_p$  are the carrier diffusivities and can be related to carrier mobilities through Einstein's relation [78],

$$D = [kT/q]\mu \quad (\text{II.19})$$

where  $D$  and  $\mu$  may represents electron and hole parameters. Combining equations II.17 and II.18, the total steady state current densities for a one dimensional case yields to the drift-diffusion equations [78],

$$J_n = -qn\mu_n E + qD_n \frac{dn}{dx}n \quad (\text{II.20})$$

$$J_p = -qp\mu_p E - qD_p \frac{dp}{dx}p \quad (\text{II.21})$$

These equations do not consider the effects of external magnetic fields that can reduce the current via magneto resistive mechanisms [78].

The steady-state continuity equations for electrons in the p-type Base region and the holes in the n-type Emitter region are established according to [78] [96]:

$$\frac{\partial n}{\partial t} = \frac{1}{q} \frac{dJ_n}{dx} - R_n + G_n \quad (\text{II.22})$$

$$\frac{\partial p}{\partial t} = -\frac{1}{q} \frac{dJ_p}{dx} - R_p + G_p \quad (\text{II.23})$$

Where  $R_n$  and  $R_p$  are the electron and hole recombination rates, and  $G_n$  and  $G_p$  are the electron and hole generation rates respectively. Under the low injection assumption

( $p \ll (n \approx n_0)$  in the n-type region), equations II.21 and II.20 can be combined with the Einstein relation II.19 to solve for the electron and hole density functions:

$$p_n(x, V) - p_{n0} = p_{n0} \left[ e^{\left(\frac{qV}{kT}\right)} - 1 \right] e^{-\frac{x-x_{dp}(V)}{L_p}} \quad (\text{II.24})$$

$$n_p(x, V) - n_{p0} = n_{p0} \left[ e^{\left(\frac{qV}{kT}\right)} - 1 \right] e^{-\frac{x-x_{dp}(V)}{L_n}} \quad (\text{II.25})$$

Where  $n_p$  and  $p_n$  are the electron and hole minority densities on the p-type and the n-type region respectively.  $n_{p0}$  and  $p_{n0}$  are the equilibrium electron and hole densities on the p-type and the n-type region respectively. The electron diffusion current on the p-side and the hole diffusion current on the n-side follow according to:

$$J_n(x, V) = -qD_n \frac{dn_p}{dx} \Big|_{x_{dp}} = \frac{qD_n n_{p0}}{L_n} \left[ e^{\left(\frac{qV}{kT}\right)} - 1 \right] \quad (\text{II.26})$$

$$J_p(x, V) = -qD_p \frac{dp_n}{dx} \Big|_{x_{dn}} = \frac{qD_p p_{n0}}{L_p} \left[ e^{\left(\frac{qV}{kT}\right)} - 1 \right] \quad (\text{II.27})$$

Where the total diffusion current is given by the sum of equations II.26 and II.27; this result is the famous Shockley equation for an ideal diode. A homogeneously doped semiconductor device at equilibrium will be in a steady state where  $pn = n_i^2$ , where  $n_i$  is the intrinsic carrier concentration. If an external force such as an applied voltage disturbs the steady state balance ( $pn \ll n_i^2$  under reverse bias and  $pn \gg n_i^2$  under forward bias), generation and recombination mechanisms attempt to return the semiconductor to its equilibrium state. There are a number of different generation and recombination processes that may include phonon transitions, photon transitions, surface recombinations, tunnelling, Auger transitions, and Shockley-Read-Hall (SRH) capture and emission processes. Since this work is not concerned with sub-micron design, tunnelling is assumed to be negligible. Also since Silicon has an indirect bandgap, direct radiative transitions through photon emission are also assumed to be negligible [78] [96]. For the analytical model, approximations of SRH generation, recombination processes through localized traps within the energy bandgap are considered:

$$J_{gn}(V) = \frac{qn_i W_D(V)}{t_n + t_p} \quad (\text{II.28})$$

$$J_{re}(V) = \frac{qn_i W_D(V)}{t_n + t_p} e^{\left(\frac{qV}{2kT}\right)} \quad (\text{II.29})$$

In the above approximation it is assumed that all traps are halfway between the bandgap and thus a maximum recombination rate is considered through most part of the depletion region. Figure II.10 shows the diffusion, generation and recombination currents for a uniformly doped pn-junction under forward and reverse bias conditions.

The simulations in Atlas link together the electrostatic potential expressed in equation II.1 with charge transport models in order to solve the electrical behaviour of a device. The default transport model used within Atlas to express the continuity equations is the drift-diffusion model. Figure II.11 shows the Emitter current as a function of Emitter

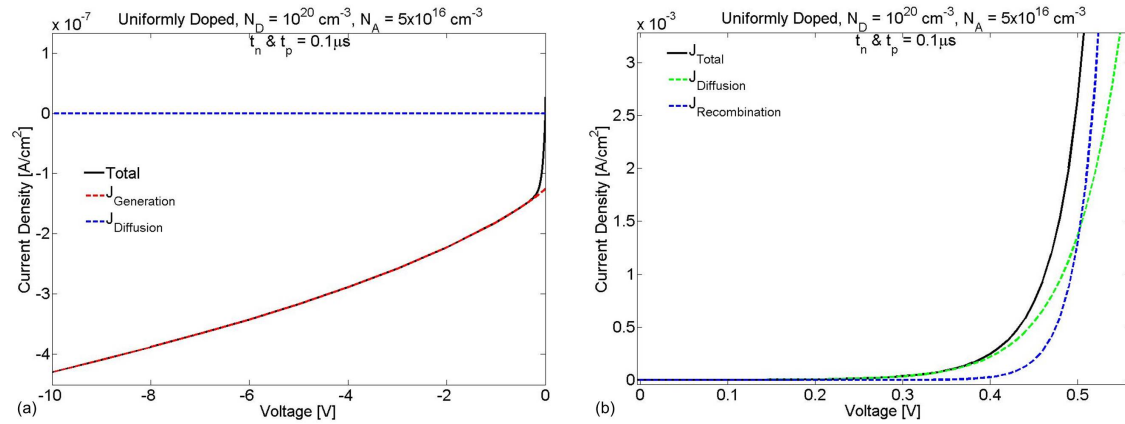


Figure II.10: Analytical modelling of the diffusion, generation and recombination dark currents for a uniformly doped pn-junction under (a) under reverse bias and (b) under forward bias. Impact ionization is not considered here and thus the breakdown is not modelled.

voltage as evaluated by Atlas compared to the analytical result for a 1D, uniformly doped pn-Junction diode. The Atlas simulation of figure II.11 is performed under very simple conditions with the following models activated only: the concentration dependent mobility model and the Shockley-Read-Hall recombination model.

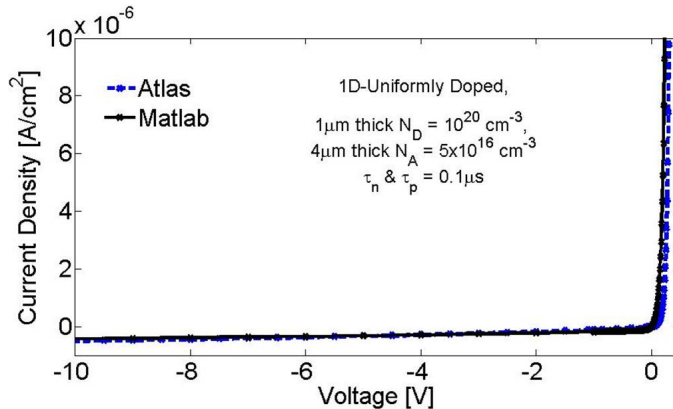


Figure II.11: Analytical versus numerical modelling of a 1D uniformly doped pn-Junction Dark IV characteristic. Impact ionization is not considered here and thus the breakdown is not modelled.

### II.2.c Photogeneration

As depicted in the schematic representation of figure II.12 (a), the VD-MOSFET cross-sectional structure provides a number of different regions for the optical generation of carriers: N+ Emitter quasi-neutral region (QNR), Emitter/Base depletion region, p-Base QNR, Collector/Base depletion region, and Nv Collector QNR. All generated carriers that are not lost due to recombination processes, will either contribute to an Emitter current or a Collector current. Figure II.12 (b), shows a schematic of the energy band diagram

for the IPD with both the Emitter and the Collector junctions under reverse bias; this configuration is the biasing requirement of the IPD under operation. Light absorption generates electron-hole pairs that can be extracted by the metal contacts of the semiconductor device. Figure II.13 shows the minority carrier modulation from a dark state to an illuminated state within the IPD structure as evaluated by numerical simulations in Atlas. From this plot, it is observed that the minority carrier concentrations increase tremendously relative to the dark state when the structure is illuminated by a 1  $\mu\text{W}$ , 500 nm optical beam. This minority carrier concentration can then diffuse and be collected at the junctions.

The electron-hole photogeneration rate can be defined as a function of incident photon flux density per unit bandwidth  $\phi_0$ , device area  $A$ , optical absorption coefficient  $\alpha(\lambda)$ , and a power reflection coefficient  $R$ . This relation is explained by the Beer-Lambert law and is expressed in equation II.30.

$$G_{op}(x, \lambda) = \phi_0(\lambda)\alpha(\lambda)e^{-\alpha(\lambda)x} \quad (\text{II.30})$$

$$\phi_0 = \frac{P_{opt}(1 - R(\lambda))}{Ah\nu} \quad (\text{II.31})$$

where wavelength and photon energy are related to each other through:

$$\lambda = \frac{c}{\nu} = \frac{1.24}{h\nu(\text{eV})} [\mu\text{m}] \quad (\text{II.32})$$

As light travels deeper into the device its intensity drops exponentially due to absorption; thus, the electron and hole generation rates also decay exponentially with optical propagation length as depicted in figure II.12 (c) (was also shown earlier in figure II.2). This implies that there is a carrier concentration gradient, with the higher concentration of carriers near the surface and a decrease in the carrier concentration deeper into the device. Due to this gradient, electron-hole pairs generated in QNRs, move away from the surface by diffusion and contribute to diffusion currents as long as they are generated within a minority carrier diffusion length away from a depletion region. Near the IPD surface, the Emitter responsivity suffers mostly by surface recombinations due to dangling bonds of the last mono-layer of atoms caused by the disruption of the crystal lattice periodicity at the surface of the device. The diffusing carriers inside the emitter region suffer from low losses since the emitter region is not very thick (i.e. carrier diffusion path lengths  $>$  distance to the junction). When the carriers reach the emitter/base region, the electrons are reflected by the junction potential barrier where as the holes are swept away across the junction by the electric field and will be collected by the base contact. The carriers that are generated in the base will also move deeper into the device by diffusion until they reach the base/collector junction. At this junction, it is the electrons that are swept away across the junction meanwhile the holes are reflected by the build in junction potential. Any carriers generated in the collector region will contribute to the Collector current instead of the desired Emitter current. The carriers generated within the Emitter/Base and Collector/Base depletion regions are separated by the electric field

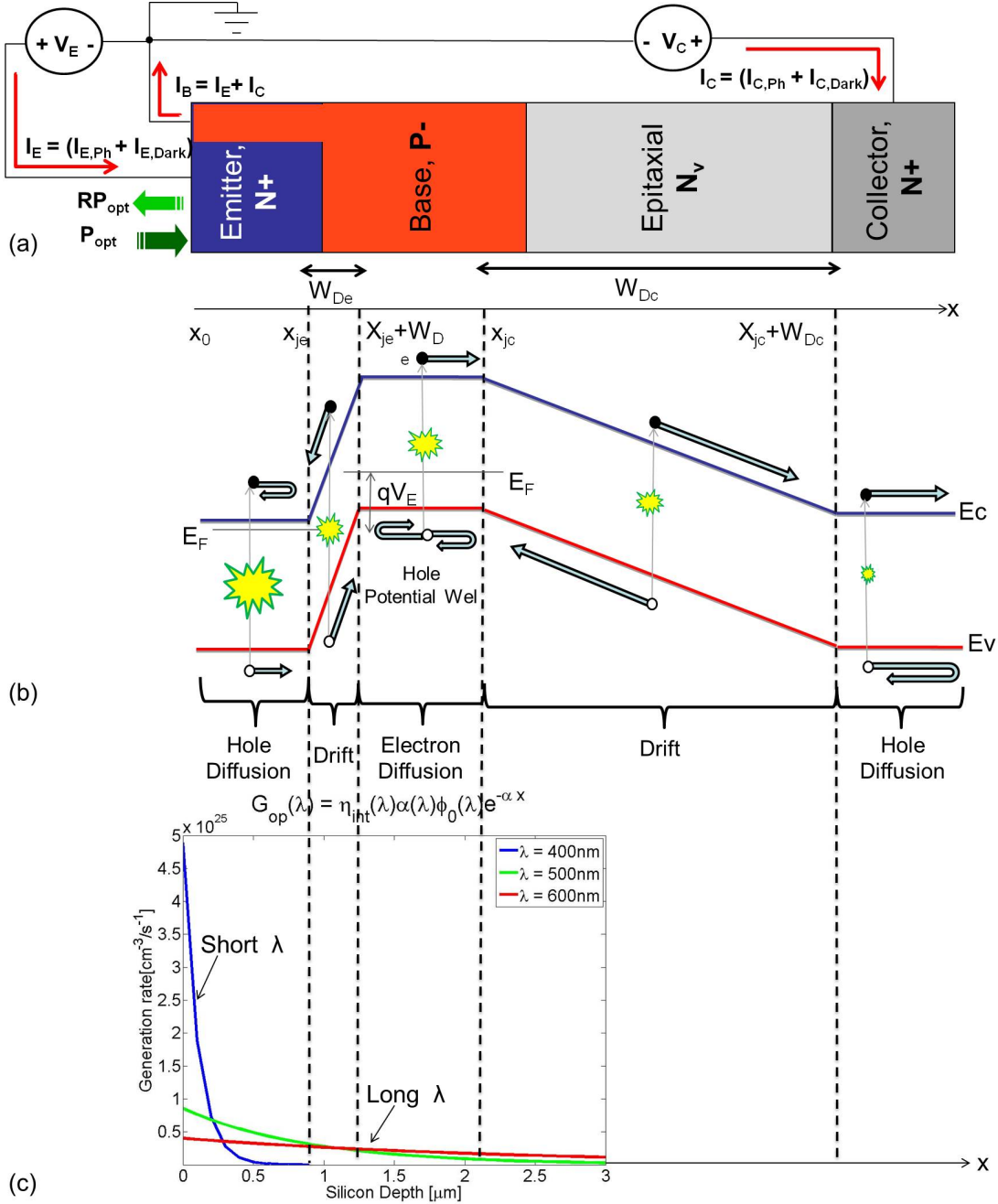


Figure II.12: (a) Cross-sectional view of the IPD. An optical interface with a power reflectivity coefficient of  $R$ , will transmit  $(1-RP_{opt})$  of an incident optical power  $P_{opt}$  to the device. (b) The energy band diagram with both the Emitter and the Collector junctions under reverse bias. The widths of the drift regions are voltage dependent. (c) The optical carrier generation for a 400 nm, 500 nm, and 600 nm light. Reflection coefficients corresponding to an air-Silicon interface are considered.

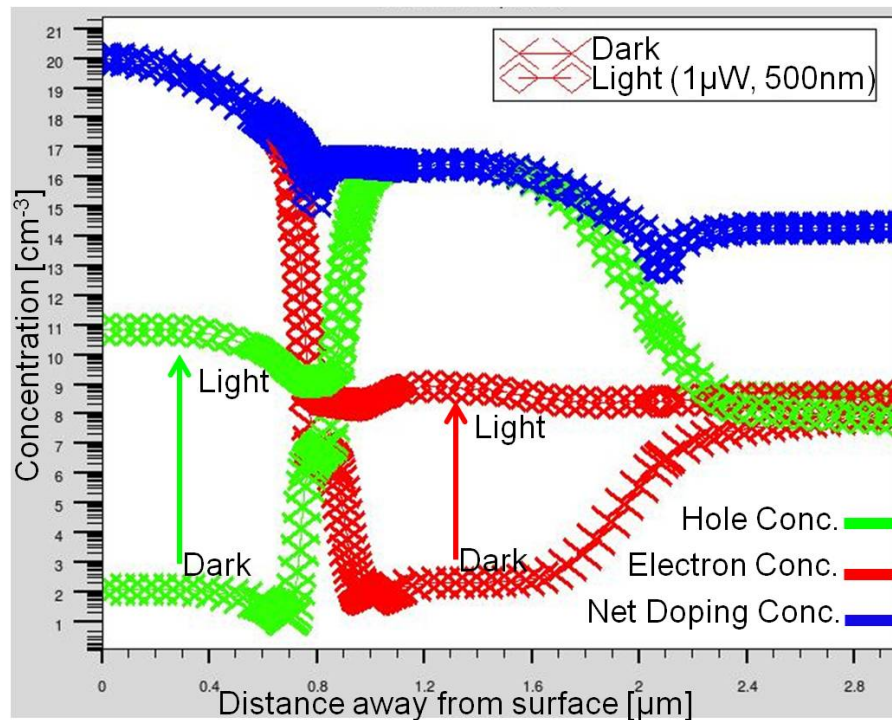


Figure II.13: Minority Carrier modulation Due to Photogeneration.

across the junctions and contribute to the Emitter and Collector drift currents respectively.

Moreover, longer wavelengths contribute to higher carrier generations deeper in the device, and suffer from lower reflection coefficients at the device surface. Given a fixed doping profile, an optimum operating wavelength of light can be defined in order to maximize the IPD Emitter current.

Silvaco provides a device simulator named Luminous, which enables optoelectronic simulations once it is combined with one of the electrical simulator tools such as Atlas. In Luminous, optical sources are defined via geometric optical ray tracing. The real component of the complex refractive index of the material is used for the evaluation of reflections, refractions, polarizations, and dispersions; meanwhile, the imaginary component of the complex refractive index of the material is used in the optical absorption and photogeneration models in order to evaluate the carrier concentrations [97]. The following considerations and assumptions have been implemented in the optical Finite Element (FEM) simulations of this thesis:

- The refractive index of the Aluminium contact layer has been modified to account for the Shadow effects. Figure II.14 shows the optical transmittance of Aluminium as a function of its thickness. Figure II.15 shows the shadow effect of the contacts on the photogeneration within a simulated structure.
- All optical sources are defined with a normal incident angle
- The refractive indices are wavelength dependent

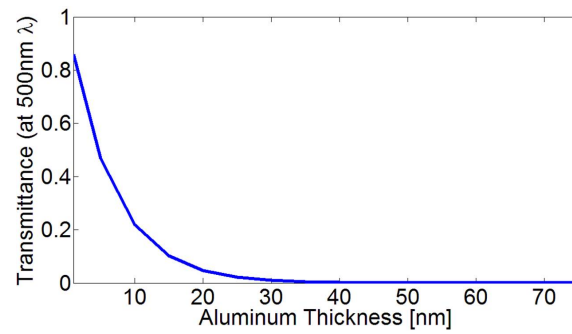


Figure II.14: Transmission through a thin film of Aluminium as a function of the film thickness.

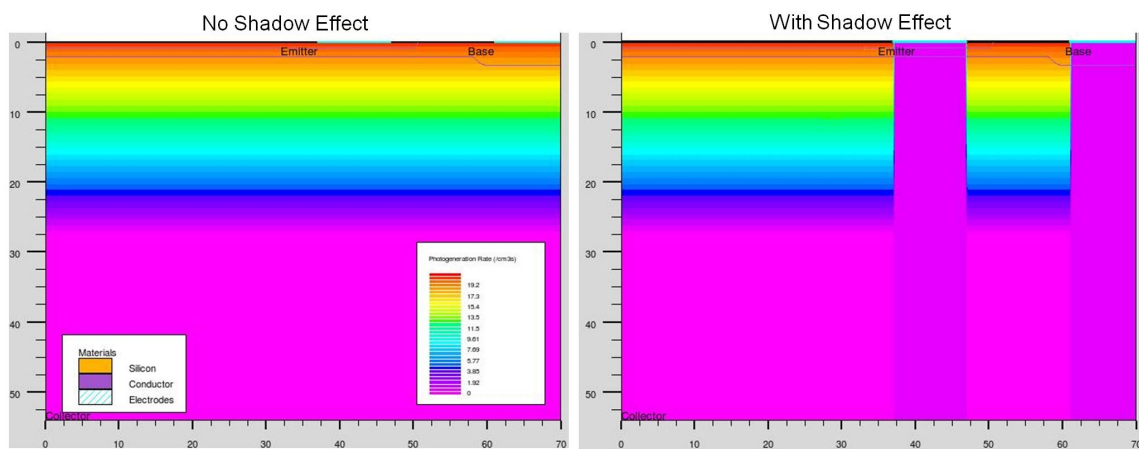


Figure II.15: The structure file on the left doesn't consider the contact shadow Effect. In the structure on the right, the imaginary component of the conductor material's refractive index has been set to 1000 to consider a 0% optical transmittance through the metal contact regions.

### II.2.d Photocurrent

Figure II.12 (b) shows the three main regions that may contribute to the Emitter photocurrent: the top QNR, the depletion region of the Emitter-Base junction, and the QNR in the Base. The total Emitter photocurrent can be written as:

$$J_{photo} = J_h^E(\lambda, I_{opt}, X, V) + J_e^D(\lambda, I_{opt}, X, V) + J_e^B(\lambda, I_{opt}, X, V)A \quad (II.33)$$

Where,  $J_h^E$  is the hole photocurrent contribution from the Emitter QNR,  $J_e^D$  is the photocurrent contribution from the depletion region,  $J_e^B$  is the electron photocurrent contribution from the Base QNR,  $\lambda$  is the wavelength of the incident light,  $I_{opt}$  is the incident optical intensity,  $V$  is voltage,  $X$  is the distance, and  $A$  is constant used to represent the ratio of the base width that contributes to the Emitter current rather than the Collector current.

In this section, the Emitter-Base junction of the IPD is modelled and used to estimate the Emitter spectral response of the IPD. Thus, the effects of the Substrate and the Collector-Base junction are not included. The simplified structure used for the analytical modelling is the N+ Emitter P-Base structure shown in figure II.16. The analytical model here is developed under the following assumptions:

- A one dimensional abrupt junction,
- Low level carrier injection condition,
- Uniform doping, uniform lifetime and uniform mobility,
- A 100% quantum efficiency inside the depletion region (in reality, defects may cause some recombinations or inter-band and exciton generations may lower the internal QE in this region),
- Material refractive indices are wavelength dependent.

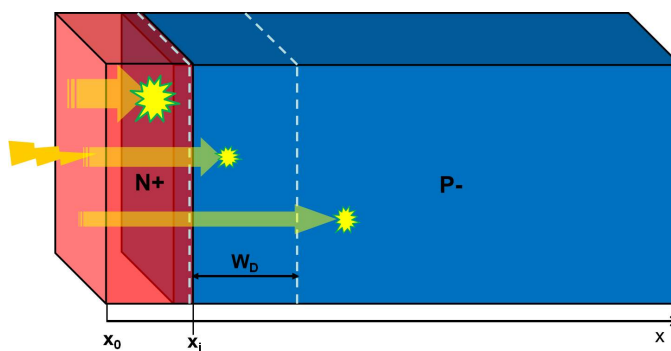


Figure II.16: Simple pn-Photodiode Structure.

In order to arrive at an analytical equation for the photocurrent, we start by substituting equations II.30 and II.21 into the continuity equation II.23 to obtain a general solution for the hole distribution in the uniformly doped Emitter region [78] [96]:

$$p_n - p_{n0} = C_2 \cdot \cosh\left(\frac{x}{L_p}\right) + C_3 \cdot \sinh\left(\frac{x}{L_p}\right) - \frac{\alpha\phi(1-R)\tau_p}{\alpha^2 L_p^2 - 1} e^{(-\alpha x)} \quad (\text{II.34})$$

where  $L_p = \sqrt{D_p\tau_p}$  is the minority carrier diffusion length, and  $C_2$  and  $C_3$  are constants.

Considering that the excess carrier density near the edge of the depletion region at  $X = X_j$  is almost entirely swept away by the electric field [78] [96]:

$$p_n - p_{n0} \approx 0 \quad (\text{II.35})$$

and that at the surface of the device, the carriers are removed via surface recombinations at a velocity of  $S_F$  [78] [96]:

$$D_p \frac{dp}{dx} \Big|_{x=0} = S_F(p(0) - p_0) \quad (\text{II.36})$$

Solving for  $C_2$  and  $C_3$  using the boundary conditions of equations II.36 and II.35, the hole photocurrent density at the edge of the depletion region on the Emitter side is [78] [96]

$$J_h^E = \left[ \frac{q\phi(1-R)\alpha L_p}{\alpha^2 L_p^2 - 1} \right] \left[ \frac{\left(\frac{S_F L_p}{D_p} + \alpha L_p\right) - e^{(-\alpha x_j)} \left[ \frac{S_F L_p}{D_p} \cosh\left(\frac{x_j}{L_p}\right) + \sinh\left(\frac{x_j}{L_p}\right) \right]}{(S_F L_p / D_p) \sin(x_j / L_p) + \cosh(x_j / L_p)} \right] - \alpha L_p e^{(-\alpha x_j)} \quad (\text{II.37})$$

The electron photocurrent from the Base region given by equation II.40, is evaluated in a similar fashion to that described for the electron photocurrent in the Emitter using the boundary conditions II.38 and II.39 [78] [96]:

$$n_p - n_{p0} \Big|_{x_j + W_D} \approx 0 \quad (\text{II.38})$$

$$\left( D_p \frac{dn}{dx} \right) \Big|_{x=H} = S_B(n(0) - n_0) \quad (\text{II.39})$$

$$J_e^B = \left[ \frac{q\phi(1-R)\alpha L_n}{\alpha^2 L_n^2 - 1} \right] e^{(-\alpha(x_j + W_D))} \left[ \alpha L_n - \frac{\left(\frac{S_B L_n}{D_n}\right) [\cosh\left(\frac{H}{L_n}\right) - e^{(-\alpha H)}] + \sinh\left(\frac{H}{L_n}\right) + \alpha L_n e^{(-\alpha H)}}{(S_B L_n / D_n) \sinh(H / L_n) + \cosh(H / L_n)} \right] \quad (\text{II.40})$$

Where  $H$  is the width of the Base region contributing to the Emitter current.

Due to the large built in electric field present in the depletion region, it is reasonable to assume that the generated carriers are separated and swept away before having the chance to recombine within the Emitter-Base depletion region. Thus, all the absorbed photons contribute to the space charge drift photocurrent and the electron continuity equation can be reduced to [96]:

$$\frac{1}{q} \frac{J_e^D}{dx} + G_{op} = 0 \quad (\text{II.41})$$

Using the depletion region approximation to solve for the depletion region width  $W_D$ , and integrating over  $X_j < X < (X_j + W_D)$  the drift photocurrent is [96]:

$$J_e^D = q\phi(\lambda)[1 - R(\lambda)]e^{-\alpha(\lambda)x_j}[1 - e^{-\alpha(\lambda)W_D}] \quad (\text{II.42})$$

Although equation II.42 is written for the electron photocurrent, it should be noted that the photocurrent could be evaluated for the electrons or holes as per the explanation given above.

We will apply this model to the Emitter-Base junction of figure II.16 with  $N_D = 1 \times 10^{20}$ , a  $4 \mu\text{m}$  thick Base layer  $N_A = 5 \times 10^{16}$  and the junction position at  $X_j = 1 \mu\text{m}$ . Figure II.17 depicts the current-voltage characteristics of the different photocurrent components from the different regions of the photodiode. The accuracy of the model is verified through comparison with numerical results from Atlas as shown in figure II.18.

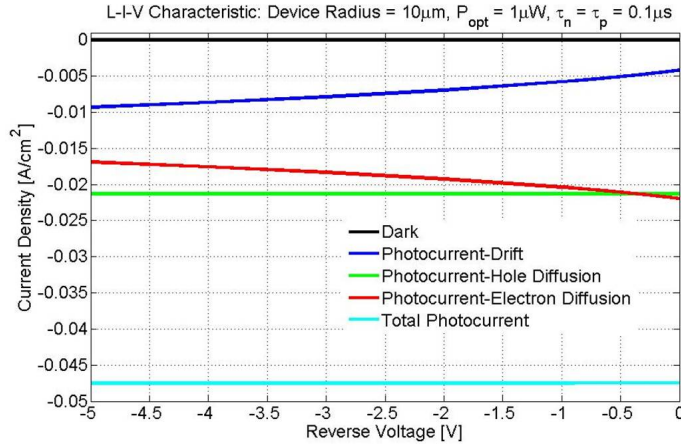


Figure II.17: Analytical modelling of the different current components in a 1D-uniformly doped pn-junction photodiode. An Air-Silicon interface is considered.

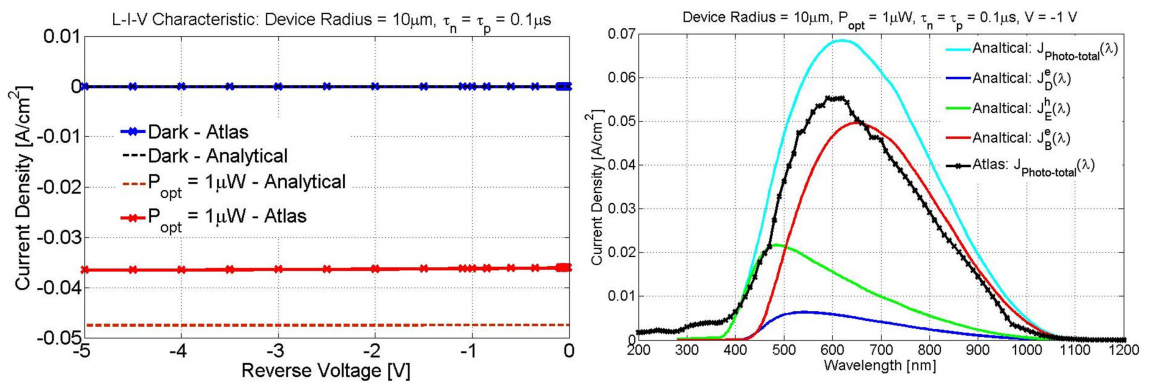


Figure II.18: Analytical modelling of photocurrent ( $I_{opt}, V, \lambda$ ) in a 1D-uniformly doped pn-junction photodiode. An Air-Silicon interface is considered.

As it was introduced in Chapter 1, the quantum efficiency QE metric is used to express the number of carriers per photon [78],

$$\eta(\lambda) = \frac{I_{ph}(\lambda)}{q\Phi(\lambda)} = \frac{AJ_{tot}(\lambda)/q}{P_{opt}(\lambda)/h\nu} \quad (\text{II.43})$$

where  $I_{ph}$  is the photocurrent,  $\Phi$  is the photon flux,  $J_{tot}$  is the total photocurrent density including drift and diffusion currents, and  $P_{opt}$  is the average optical signal power. Equation II.44 gives the externally observed QE; dividing  $I_{ph}$  by  $q\Phi(\lambda)[1 - R(\lambda)]$ , where  $R(\lambda)$  represents the reflection coefficient, gives the internal QE. The ideal internal QE is a step function that is equal to one for  $h\nu \geq E_g$  and zero for  $h\nu \leq E_g$ . Another metric used for evaluating the sensitivity of a detector in reference to the optical power is the responsivity [78],

$$\mathfrak{R}(\lambda) = \frac{I_{ph}(\lambda)}{P_{opt}(\lambda)} = \frac{\eta(\lambda)q}{h\nu} = \frac{\eta(\lambda)\lambda(\mu m)}{1.24} [A/W] \quad (II.44)$$

The QE and Responsivity corresponding to the photocurrent spectral response of figure II.18 are shown in figure II.19.

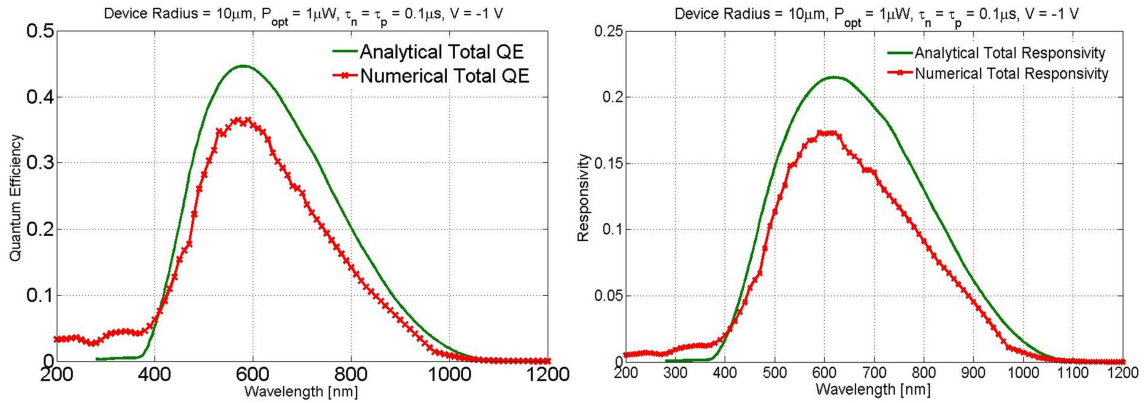


Figure II.19: QE and Responsivity spectrum of a 1D-uniformly doped pn-junction photodiode when illuminated by a 1  $\mu$ W uniform optical source.

### II.3 Anti-reflection Coating

When a photodetector is illuminated by a light source, not all of the incident light intensity have the chance to be absorbed by the photodetector. There are two main sources of optical losses in photodetectors:

1. Material: The photodetector optical absorption efficiency is dependent on the material absorption coefficient which is mathematically expressed as the imaginary part of the refractive index of a material. Furthermore, the absorption coefficient is a function of wavelength and the maximum wavelength of light absorb-able by a material is given by the material's bandgap. Any optical energy that is not absorbed by the material contributes to the optical losses.
2. Reflections: Optical losses due to reflections may be divided into two categories. (1) Losses from reflections at the air to Silicon interface, (2) and losses from any unwanted absorptions in the contacts and/or reflections at the air to metal contact interface also known as shading losses. Shading losses are considered when discussing the contact design.

Figure II.20 shows the possible optical loss opportunities as well as the exponential decay of optical power with distance travelled into the Si substrate as predicted by the Beer-Lambert law.

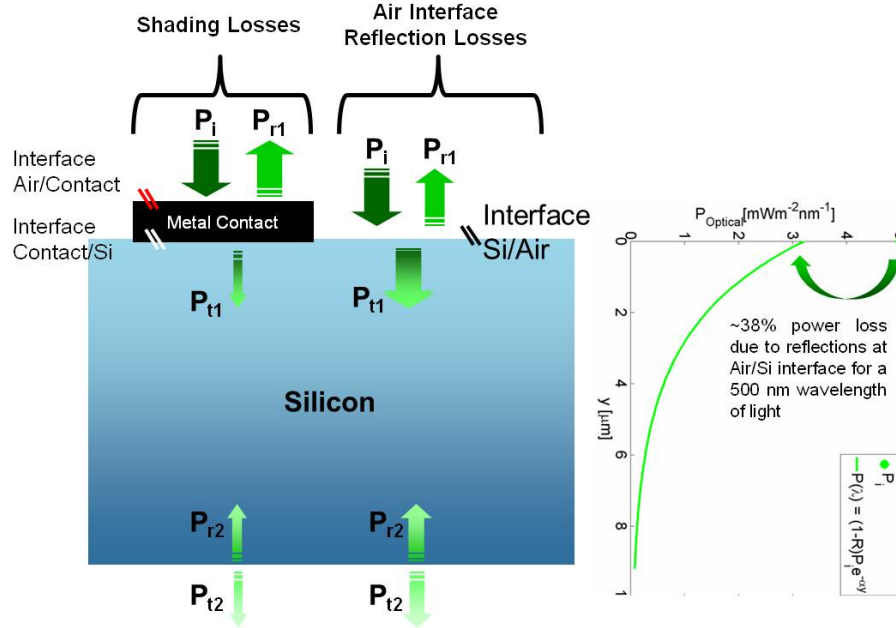


Figure II.20: Optical reflection losses. Losses due to metal contact shading effect. Losses due to reflections at the air/Silicon interface. Note that any optical power that makes it to the end of the device, will experience a second reflection at the backside air/Si interface.

Reflections at the air/Si interface occur due to mismatches in the refractive indices of air and Si. Air has a reference refractive index ( $n_{Air}$ ) of 1 and Si has a relatively large refractive ( $n_{Si}$ ) index of roughly 3.5 at wavelengths near 800 nm and above (for a wavelength of 500 nm,  $n_{Si}$  is roughly 4). The power reflectivity coefficient between air and Silicon at normal incident is depicted in figure II.21 and it can be calculated by equation II.45 [98].

$$R = \frac{(n_{si}(\lambda) - n_{Air})^2 + k_{si}(\lambda)^2}{(n_{si}(\lambda) + n_{Air})^2 + k_{si}(\lambda)^2} \quad (\text{II.45})$$

Where  $\kappa_{si}$  is the imaginary part of the complex refractive index of Silicon. Since the IPD doping profile is optimized for a 500 nm wavelength operation, there will be an immediate optical intensity loss at the detector surface of around 38% as shown in figure II.21. These reflections occur due to the sharp change in the medium refractive index as light propagates from a lower index region (i.e. air) into a high index Silicon. Reflections can be minimized by the addition of a thin film on the surface of the IPD in order to ease the transition between air to Silicon. The thin film material should have a refractive index  $n_{Air} < n_{coating} < n_{Si}$ , and a thickness that would enforce destructive interference of the reflected waves and constructive interference of the transmitted waves [99] as shown in

figure II.22(a).

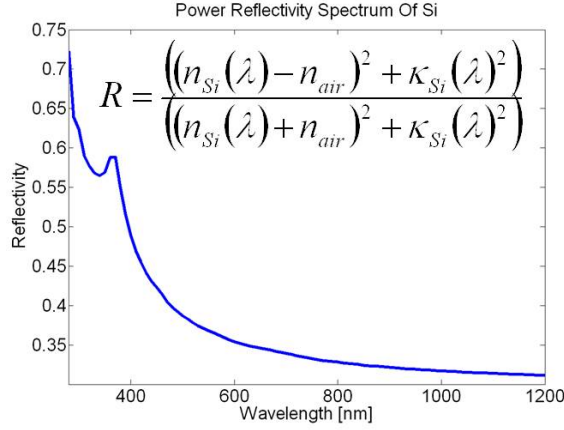


Figure II.21: Power Reflectivity Coefficient for Si/air Interface.

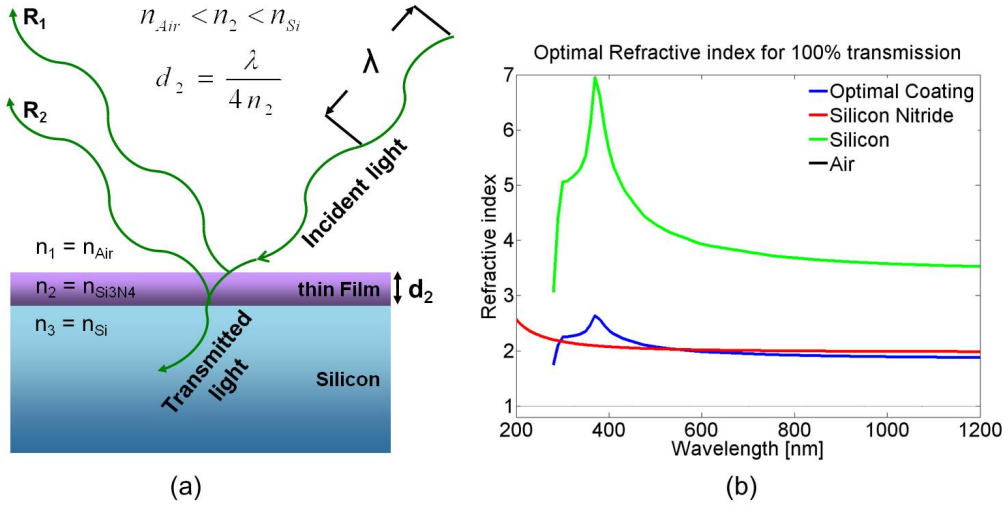


Figure II.22: (a) The thin film refractive index and thickness conditions required for ARC. (b) the matching case of the refractive index of  $\text{Si}_3\text{N}_4$  with that of an ideal ARC for Silicon.

For a thin dielectric film with thickness of no more than a few hundreds of nanometres, it can be assumed that absorption is negligible (lossless media). At normal incidence, the interface amplitude reflection coefficient of a thin film with a refractive index  $n_2$  and thickness  $d_2$  sandwiched between air  $n_1$  and Silicon  $n_3$ , is given by the Fresnel reflection coefficient [99]

$$r = \frac{\left[ \frac{n_1 - n_2}{n_1 + n_2} \right] + \left[ \frac{n_2 - n_3}{n_2 + n_3} \right] e^{-i2\phi}}{1 + \left[ \frac{n_1 - n_2}{n_1 + n_2} \right] + \left[ \frac{n_2 - n_3}{n_2 + n_3} \right] e^{-i2\phi}} \quad (\text{II.46})$$

where the phase is  $\phi = 2 \cdot \pi \cdot n_2 \cdot d_2 / \lambda$ . The reflection coefficient goes to zero when [99]

$$r = \left[ \frac{n_1 - n_2}{n_1 + n_2} \right] + \left[ \frac{n_2 - n_3}{n_2 + n_3} \right] e^{-i2\phi} = 0 \quad (\text{II.47})$$

This zero condition is satisfied for [99]

$$n_2 = \sqrt{n_1 n_3} \quad \text{and} \quad \phi = \pi/2, 3\pi/2, 5\pi/2, 7\pi/2 \dots \quad (\text{II.48})$$

A material with refractive index spectrum of  $n_2$  as shown in figure II.22(b), represents an ideal ARC layer that would suppress reflections at any wavelength when designed with an appropriate thickness. The refractive index of  $\text{Si}_3\text{N}_4$  plotted in red in figure II.22(b), reveals a close proximity to the ideal  $n_2$  specially for wavelengths above 450 nm (at 548 nm there is an exact match). At 500 nm, the refractive index of  $\text{Si}_3\text{N}_4$  is roughly 1.8% lower than that of  $n_2$ ; however, the refractive index of  $\text{Si}_3\text{N}_4$  may vary due to the quality of fabrication and so the values shown in figure II.22(b) maybe slightly different from case to case. By adding a single  $\text{Si}_3\text{N}_4$  ARC layer with an optimized thickness for the 500 nm wavelength application, reflections of a single wavelength (500 nm in this case) can be nearly eliminated. In a more complex approach, a multi-cavity etalon can be created by stacking different ARC materials to eliminate reflections at different wavelengths. In solar cell designs, the amount of light coupled-in can be enhanced further by texturing the front surface of the solar cell as shown in the schematic of figure II.23. In this project, the IPDs will have a single layer of  $\text{Si}_3\text{N}_4$  ARC with a uniform thickness.

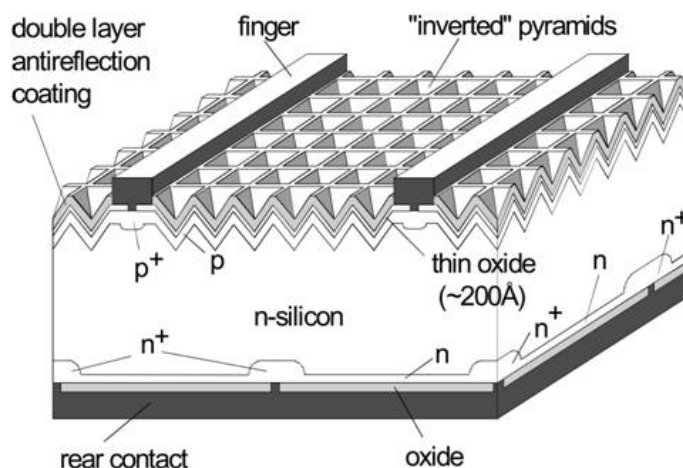


Figure II.23: Schematic of the solar cell structure for a Si cell with a 24.7% world-record efficiency, via J.Zhao et al [100].

The phase condition in equation II.48 indicates that a thin film with a refractive index of  $n_2$  and a thickness of a quarter-wave will result in zero reflections of the wave. Plugging  $n_2$  in to  $\phi$  for  $\lambda=500$  nm results in a minimum ARC thickness requirement of around 61 nm. Periodic solutions for the ARC thickness exists for every half-wave increments in the phase. Figure II.24 shows how the reflectance coefficient moves between a minimum when the waves destructively interfere, and a maximum when the waves constructively interfere.

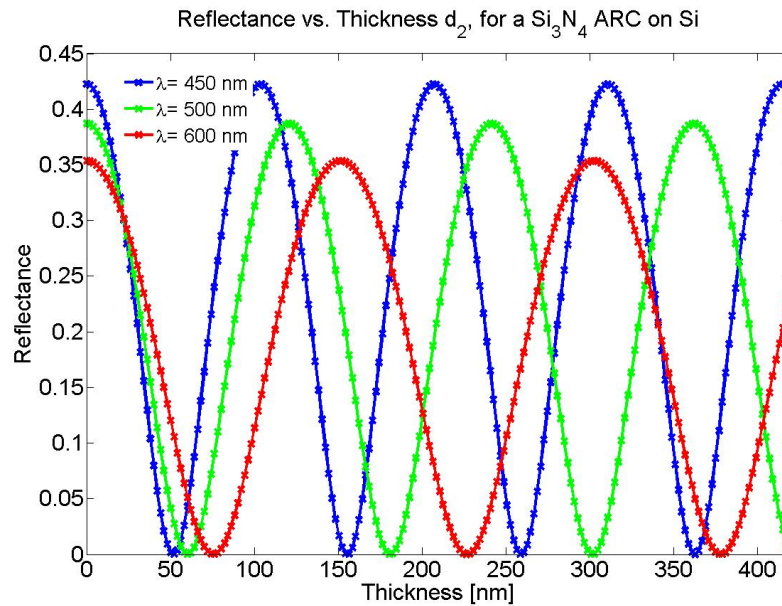


Figure II.24:  $\text{Si}_3\text{N}_4$  ARC Reflectance Sensitivity to ARC Thickness for different wavelengths. Shorter wavelengths have shorter optimized thickness period relative to longer wavelengths. This increase in thickness periodicity is linear with increasing wavelength. Also shorter wavelengths have sharper filter characteristics due to their shorter thickness periodicity and higher maximum reflectivity. Absorption within ARC is not modelled.

The matlab analytical and finite element simulation results of the ARC design show an agreement and are depicted in figure II.25. Figure II.26 (a) demonstrates the reflectance sensitivity to ARC thickness changes of the first period thickness  $\pm 10$  nm. Changes in the ARC thickness may arise from limitations in thin film growth control during fabrication of the  $\text{Si}_3\text{N}_4$  layer. A deviation of  $\pm 10$  nm from the first period thickness (roughly 61 nm) results in a maximum reflection loss of 4%. Applying thicker optimized ARC layers results in a sharper filter characteristic around the operating wavelength as it can be observed in figure II.25. The increase sensitivity to the operating wavelength as a function of thicker optimized ARC layers is evident in the envelope of the plot in figure II.26 (b). Figure II.26 (b) also shows that in the case of the first order thickness, the  $\text{Si}_3\text{N}_4$  ARC coating will reduce the power reflection losses down to approximately 1% for operating wavelengths between 470 nm and 545 nm.

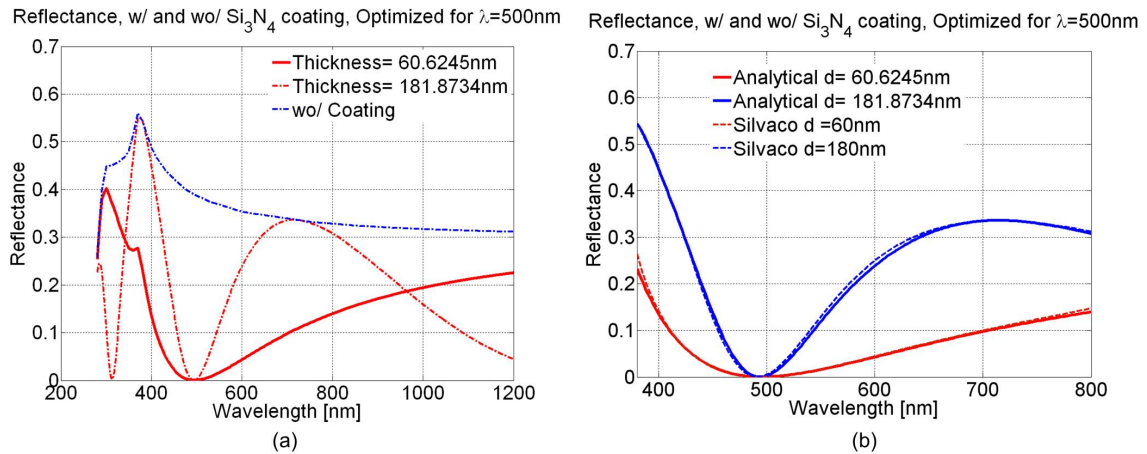


Figure II.25: Si<sub>3</sub>N<sub>4</sub> ARC Reflectivity Spectrum. (a) The effect of adding a Si<sub>3</sub>N<sub>4</sub> ARC (red) with two different thicknesses optimized for a 500 nm wavelength is demonstrated compared to the case without an ARC (blue). The results were obtained using the Fresnel equations above. (b) The ARC is implemented into the Silvaco simulations and the concurrence between Silvaco (dotted lines) and the analytical (solid lines) equations is validated.

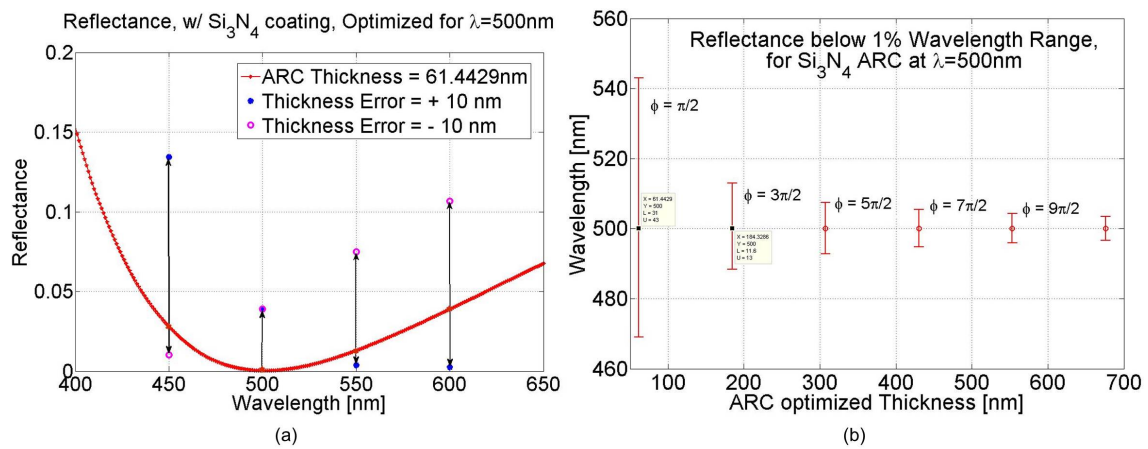


Figure II.26: (a) A zoomed in view around 500 nm region of the reflectivity spectrum from figure II.25. The reflectance sensitivity to ARC thickness changes of the first period thickness +/- 10 nm are shown by the blue and pink markers respectively. (b) The wavelength range where the power reflectivity coefficient remains below 1%, for the first 6 periodic thicknesses optimized for a 500 nm wavelength are shown.

## II.4 Static Analysis

The analytical model developed in section II.2.d consists of many assumptions and simplifications; however, it is still useful for qualitative analysis of the photodiode structure. Figure II.27 shows the spectral Responsivity components from the different regions of the photodiode with an ARC optimized for 500 nm wavelength, when the photodiode is reversed biased at 1V and 10V. When the carriers have long lifetimes such that all generated carriers contribute to the photocurrent, increasing the reverse bias doesn't effect the total

current as shown in figure II.27 (a). Although for the case of the IPD structure (N+ Emitter, P-Base, N $\nu$  Collector), where most of the current in the Base doesn't contribute to the Emitter current, a higher reverse bias can still increase the Emitter current by stealing away the carriers in the Base that would have otherwise contributed to the Collector current. Moreover, impact ionization is not modelled here; these effects will be investigated via Atlas simulations. Figure II.27 (b) in comparison to figure II.27 (a) demonstrates the effect of reduction in carrier lifetimes. When the carrier lifetimes become low enough to be comparable to carrier diffusion times, the photocurrents suffer due to recombinations; In this case, extending the depletion region width by increasing the reverse bias can improve the photocurrent level. Figure II.28 shows the voltage dependencies of the components of the photodiode Responsivity for the case of short carrier lifetimes, compared to long carrier lifetimes. As it is expected, the depletion region and the P- region currents are strongly dependent on the biasing condition since the changes in the depletion region appear almost completely across the P- region and not the N+ region.

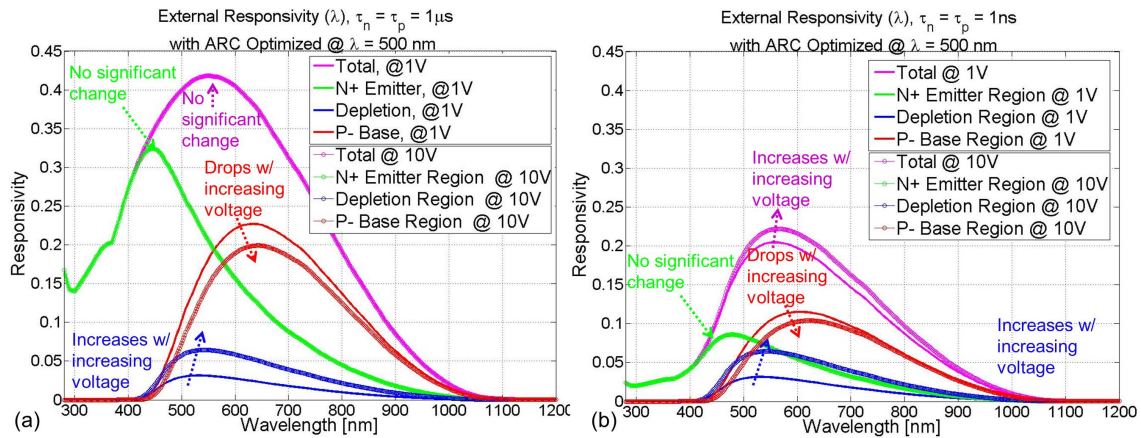


Figure II.27: Analytical modelling of a photodiode Responsivity as a function of optical wavelength. The contributions and wavelength dependencies from the different regions of the photodiode including the Emitter, depletion region, the Base and the total are shown. The structure considered has a top Emitter layer  $N_D = 1 \times 10^{20}$ , a  $5 \mu\text{m}$  thick Base layer  $N_A = 5 \times 10^{16}$  and the junction position at  $X_j = 1 \mu\text{m}$ . (a) The effect of biasing when carriers have long lifetimes relative to their transit times. (b) The effect of biasing when carriers lifetimes are comparable with transit times.

Another parameter effecting the photodiode current level, is the surface recombination rate. The presence of defects or impurities at the surface of the device where the Silicon lattice is disrupted provides a high probability of carrier recombinations depending on the velocity with which the minority carriers move toward the surface. Figure II.29 depicts the effect of surface recombinations ( $S_F = 1 \times 10^7 \text{ cm/s}$ , this is the saturation velocity) at the top N+ region meanwhile there are no surface recombinations ( $S_B = 1$ ) at the P-surface. As expected, shorter wavelengths that have relatively shorter absorption depths suffer strongly due to surface recombinations, where as longer wavelengths with longer penetration depths are less and less affected.

The analytical modelling here is of value in terms of qualitative analysis, however we

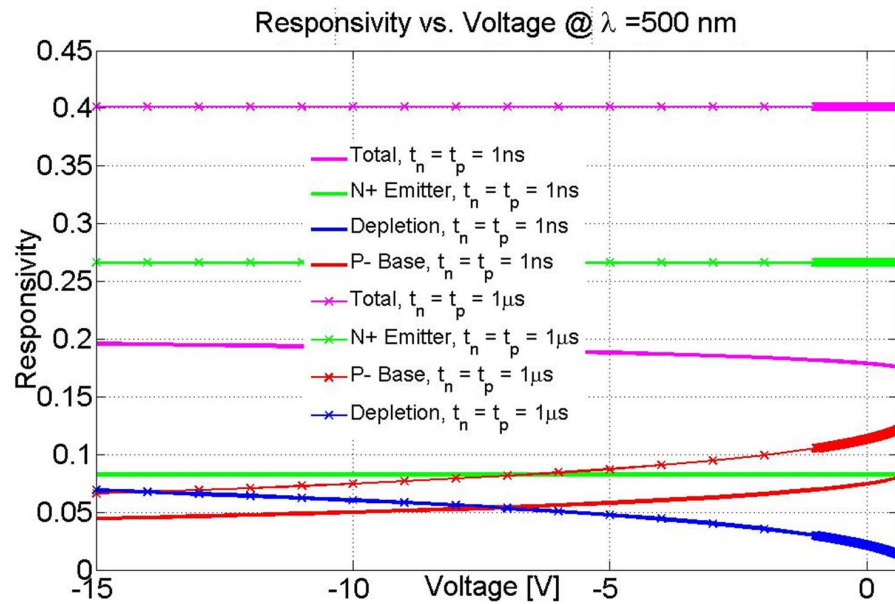


Figure II.28: Analytical modelling of the responsivity contributions from the different regions of the photodiode including the Emitter, depletion region, and the Base as a function of dependencies on biasing and carrier lifetimes. The structure considered has a top Emitter layer  $N_A = 5 \times 10^{16}$ , a  $5 \mu\text{m}$  thick Base layer  $N_D = 1 \times 10^{20}$  and the junction position at  $X_j = 1 \mu\text{m}$ . The effect of biasing when carriers have long or short lifetimes is illustrated.

will continue by means of numerical simulations in order to better capture the complexity of the design and to shed more light on the following problems:

- A more complex model to include the effects of Shockley-Read-hall transitions, Auger recombination, band-gap narrowing, impact ionization, carrier mobilities dependence on doping concentration and electric field levels
- 2D and 3D effects
- Gaussian doping Profiles
- The effects of the substrate DC and Transient voltages
- The effect of resistances in the neutral regions
- The effects of applied voltages on the Responsivity and Bandwidth
- The effects of light intensity on the Responsivity and Bandwidth
- The effect of carrier lifetimes on the Responsivity and Bandwidth
- The inherent parasitic bipolar effects

The schematic view of the IPD structure in figure II.30 depicts the two different photocurrents that can be measured when the IPD structure is exposed to light with energy

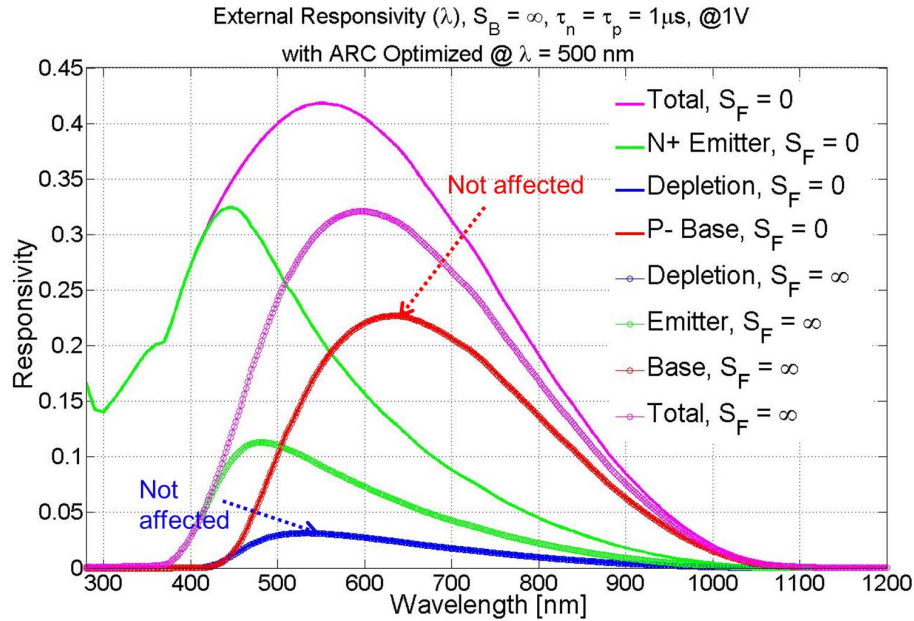


Figure II.29: Analytical modelling of the responsivity contributions from the different regions of the photodiode including the Emitter, depletion region, and the Base as a function of dependencies on optical wavelength and surface recombinations. The structure considered has a top Emitter layer  $N_A = 5 \times 10^{16}$ , a  $5 \mu\text{m}$  thick Base layer  $N_D = 1 \times 10^{20}$  and the junction position at  $X_j = 1\mu\text{m}$ . The effect of surface recombinations at the top Emitter surface meanwhile assuming there are no surface recombinations at the Base surface is illustrated.

$h\nu$  higher than the energy bandgap of Silicon. The Emitter and Collector current density trends as a function of the Emitter voltage shown in figure II.30, are numerical results from a  $50 \mu\text{m}$  radius IPD when the collector is reversed biased at 1 V, both carrier lifetimes are  $1 \mu\text{s}$ , and the light source is a  $500 \text{ nm}$  wavelength with a  $50 \mu\text{m}$  beam radius and a uniform distribution. As it can be seen, for optical powers up to  $100 \mu\text{W}$ , the IPD has a linear response. The IPD static behaviour and performance is a function of a combination of many parameters including:

- Emitter and Collector voltages
- Optical Intensity level and distribution
- Anti-reflective coating ARC design
- Carrier lifetimes
- Substrate Transients
- Contact and doping well geometry
- Temperature

The simulations in this section will study the effect of some of these parameters on the DC behaviour of the device in order to identify the critical parameters that can be

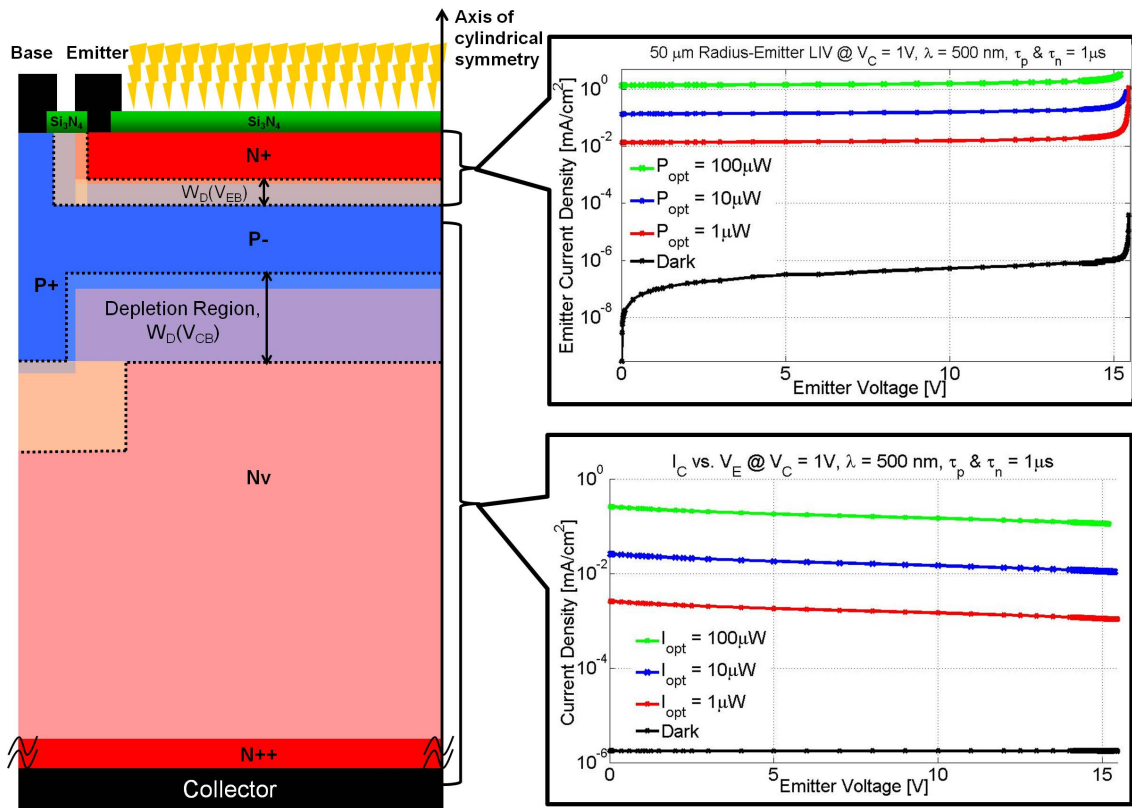


Figure II.30: IPD Structure Cross Section View and its two possible photocurrents corresponding to the two junctions present within the structure.

optimized. The large number of parameters demands for launching many simulations and thus it is desired to avoid long simulations whenever possible. The simulation time is a strong function of the mesh and the number and complexity of the models activated. Thus, there is a trade off between accuracy and time. In these simulations we have decided to use 2D structures that can be simulated in 3D via a cylindrical axis of symmetry. The use of an axis of symmetry allows the reduction of simulation time at the cost of limiting our study to 3D symmetrical structures (i.e. all contacts are round and symmetrical, therefore, all the quantities are solved in cylindrical coordinates). To further reduce the amount of simulation time, the thickness of the N++ Silicon substrate was set to  $5 \mu\text{m}$  only; this  $5 \mu\text{m}$  substrate layer in addition to the  $50 \mu\text{m}$  thick intrinsic region of the IPD structure is more than  $2\times$  the optical penetration depth of a  $800 \text{ nm}$  wavelength and hence it is a negligible source of error. For very simple structures, a simple mesh was manually created whose resolution was a function of junction and contact location as well as distance away from the surface. However, achieving an appropriate (zero obtuse angles) and optimized (location and number of mesh points) mesh around 2D Gaussian doping profiles is a challenging task when done manually; in order to solve these meshing challenges automatically, the mesh used in the structure files of the electrical and optical simulations presented here were created in DevEdit. Moreover, only the minimum number of models relevant to the study are activated. The assumptions and conditions considered in all the Silvaco Finite Element simulations during this work are listed below:

- Gaussian fitted doping profiles as depicted in the GFDP curve of figure II.8 (a).
- Models activated: Shockley-Read-hall, Auger recombination, band-gap narrowing, impact ionization (Grant), concentration and field dependent mobilities
- The refractive index of Aluminium contact layers have been modified to account for the Shadow effects
- All optical sources are defined with a normal incident angle
- The refractive indices are wavelength dependent
- Constant carrier lifetimes
- Temperature = 300 K

#### II.4.a DC Emitter and Collector biasing

Figure II.31 and II.32 show the Emitter  $J_E$  and the Collector  $J_C$  dark current densities as a function of the Emitter and the Collector reverse voltages respectively with carrier lifetimes of 1  $\mu$ s.

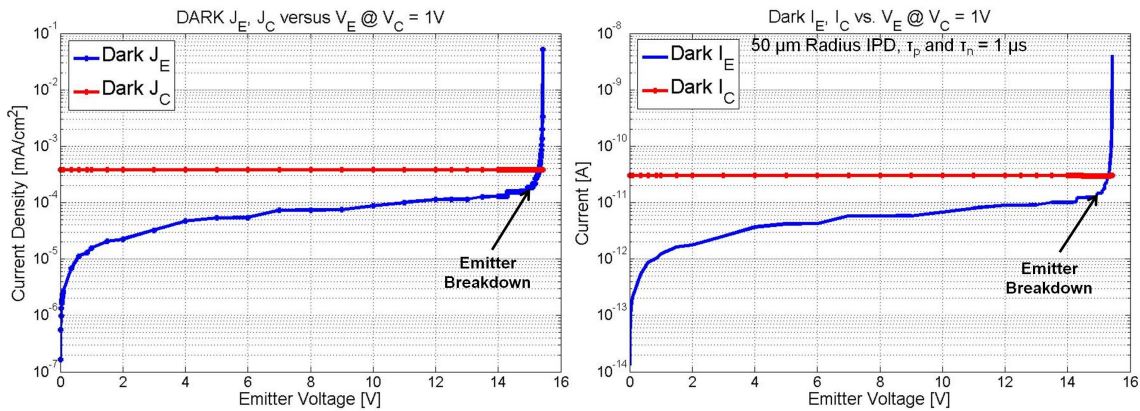


Figure II.31: Dark current voltage characteristics for a 50  $\mu$ m IPD as modelled in Silvaco with the carrier lifetimes set to 1  $\mu$ s and having activated the Grant model in order to represent the effect of avalanche ionization. The Emitter and Collector dark current densities as a function of  $V_E$  for a Gaussian-fitted doping profile are shown on the left, and the current values are shown on the right.

As observed, when the two junctions are reversed biased, one junction's dark current is not a function of the other junction. The Emitter junction breakdown is around 15 V and its dark current density is in the range of 15  $nA/cm^2$  to 150  $nA/cm^2$  for an Emitter voltage range of 1 V to 14 V. The Collector junction breakdown is around 650 V and its dark current density is in the range of 350  $nA/cm^2$  at 1 V reverse bias, to 10  $\mu A/cm^2$  at 600 V reverse bias at room temperature. These dark currents set the minimum detectable photocurrent level which in turn determine the minimum optical intensity required for an IPD responsivity. The junction dark current densities are a function of the diffusion currents given in equations II.26 and II.27, and the generation current of equation II.28 all

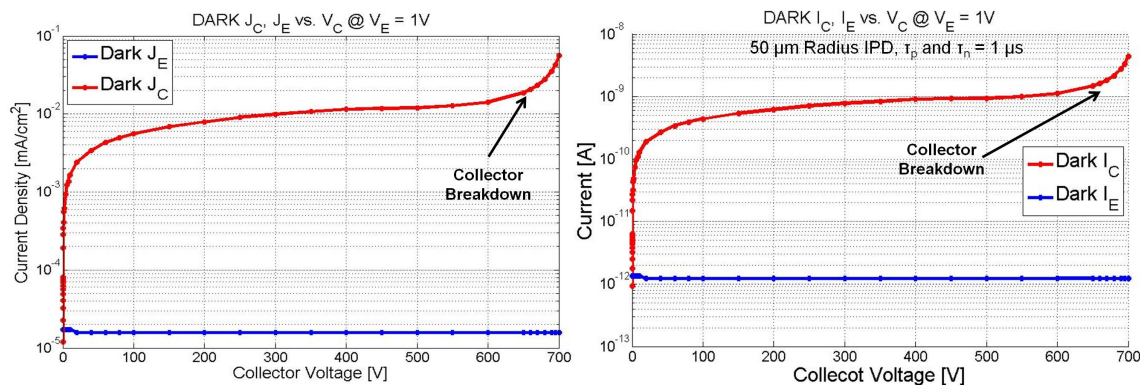


Figure II.32: Dark Current Voltage Characteristics for a 50  $\mu\text{m}$  IPD as modelled in Silvaco with the carrier lifetimes set to 1  $\mu\text{s}$  and having activated the Grant model in order to represent the effect of avalanche ionization. The Emitter and Collector dark current densities as a function of  $V_C$  for a Gaussian-fitted doping profile are shown on the left, and the current values are shown on the right.

which are functions of temperature. The diffusion current has an exponential dependence on temperature but since  $n_i$  is not too large for the case of Si, the generation current may dominate at room temperatures. The diffusion current may however dominate with increasing temperatures. Thus, the noise floor will increase approximately as  $e^{(-E_g/(kT))}$  with temperature, where  $E_g$  is the energy bandgap of Si [78]. In order to minimize the dark current levels, IPDs with smaller Emitter junction cross sectional areas and enhanced responsivities are preferred.

Another issue concerning the Emitter and Collector dark current levels is the resistive IR drops in the Base region. Current flowing through the Base modifies local voltage levels due to the resistances along its path. Since the current flowing through the Base is the sum of the Emitter and Collector dark and photogenerated currents, lower dark current levels allow higher photocurrent levels for a giving Base resistance.

Figure II.33 (a) shows the optical spectral response of the different currents flowing through the structure. This result is in agreement with the discussion in section II.2.c. The Emitter photocurrent is maximized for optical wavelengths around 500 nm, meanwhile the Collector photocurrent is maximized for optical wavelengths around 850 nm. Figure II.33 (b), shows the QEs of the IPD corresponding to the currents of figure II.33 (a). In these simulations, an optical beam width equal to the exposed photo-sensitive area of the Emitter region is used in order to show the maximum efficiency achievable without contact shadow losses.

Figure II.33 (c) shows the responsivities for the case of 100% QE in red and after reflection losses in green as well as the internal and external responsivities of the IPD (Emitter) in blue and black respectively. As it can be seen, the IPD responsivity departs substantially from the ideal case. The external responsivities from the different regions of the structure are shown in figure II.33 (d).

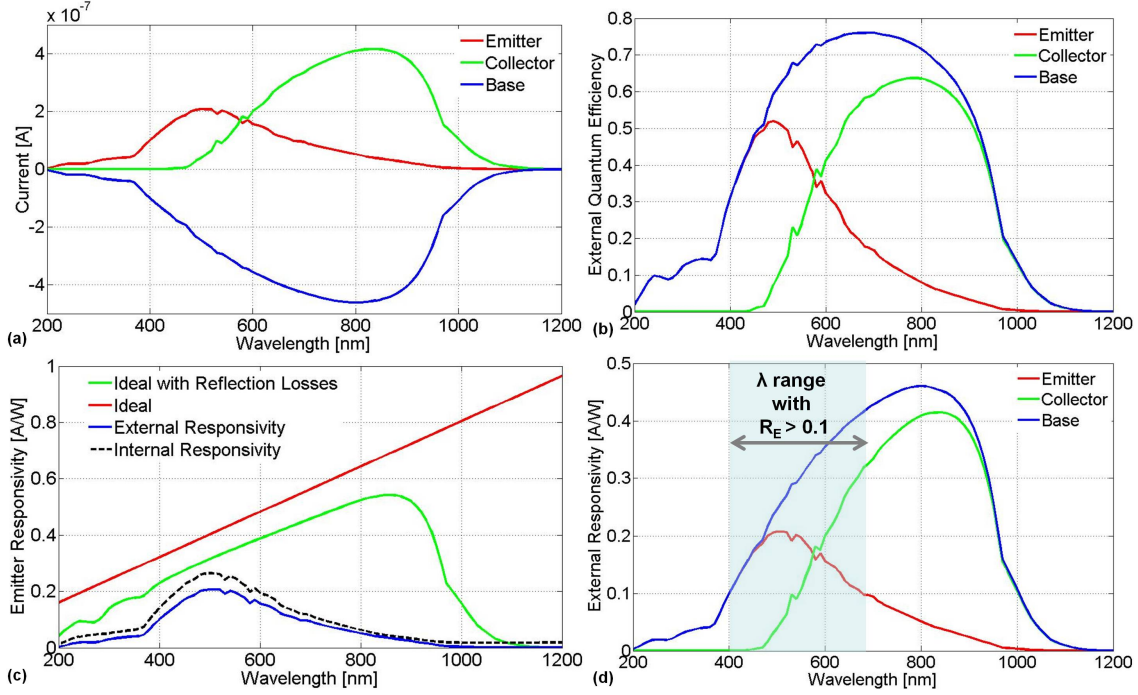


Figure II.33: Spectral responsivity results at  $V_E = V_C = 1$  V,  $\tau_n = \tau_p = 1$   $\mu$ s,  $P_{opt} = 1$   $\mu$ W for an IPD with a 50  $\mu$ m radius Emitter region. (a) Spectral currents and their corresponding (b) QEs from the Emitter, Collector and Base regions of the IPD. (c) for the case of 100% QE in red and after reflection losses in green. The internal and external responsivities of the IPD (Emitter) are in blue and black respectively. (d) Components of spectral responsivity with a uniformly distributed optical beam corresponding to the Emitter, Collector and Base regions of the IPD. The beam radius is 37  $\mu$ m which is equal to the exposed area of the Emitter region. Thus, there are no shading losses.

The currents flowing through the structure are dependent on the biasing conditions as illustrated in figures II.34 and II.35.

In these simulations, an optical beam width equal to the area of the Emitter region is used in order to include the avalanche effect which occurs earlier at the junction corners compared to the flat junction areas (the electric field increases with smaller bent radii of the junction). A consequence of the larger beam radius is a lower efficiency due to the contact shadow losses. Increases in  $V_E$  results in the widening of the Emitter junction depletion region, which mostly extends into the P-Base region. Since the depletion region has the highest probability of carrier collection, increasing  $W_D$  of the Emitter junction results in an increased carrier collection efficiency at this junction. Increases in the Emitter current are coupled with decreases in the Collector current since most of the additional carriers being collected from the extension of  $W_D$  used to be collected by the Collector junction. Moreover, an exponential increase in the Emitter responsivity can be achieved by operating the device in the avalanche mode. Figures II.36 and II.37 show the evolution of the Emitter and Collector responsivities with Emitter and Collector DC voltages at several optical wavelengths. For an optical wavelengths close to 500 nm, roughly a 15% increase in the responsivity can be expected when increasing the Emitter voltage to 10 V

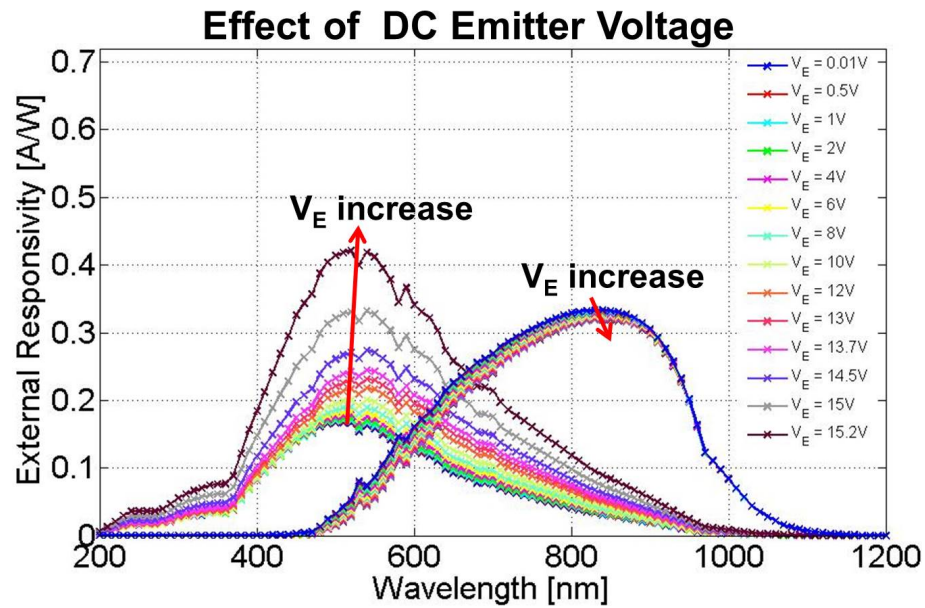


Figure II.34: Emitter and Collector responsivities as a function of  $V_E$  with the Collector reversed biased at 1 V, and 1  $\mu$ s carrier lifetimes. The optical source has a 51  $\mu$ m beam radius and the Emitter radius is 50  $\mu$ m.

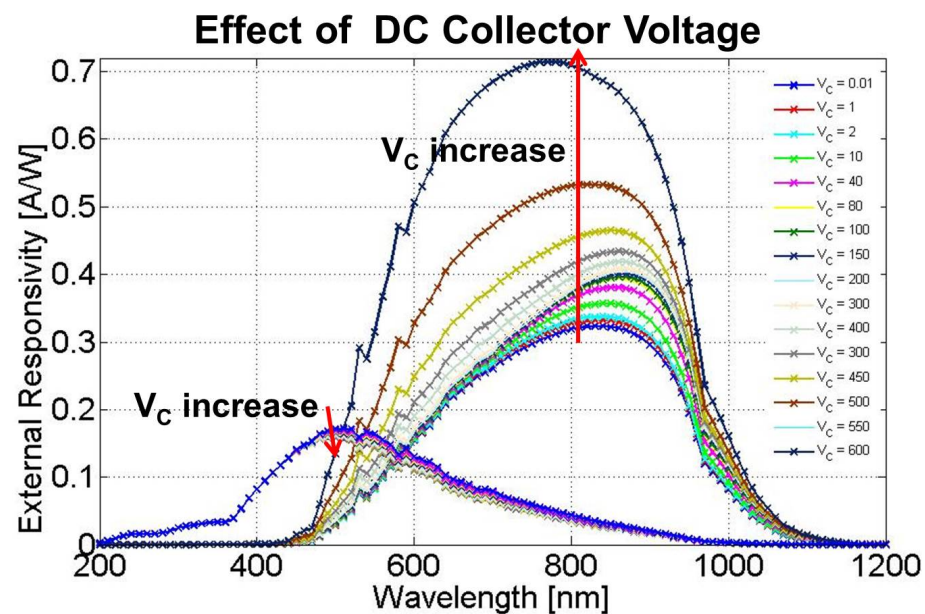


Figure II.35: Emitter and Collector responsivities as a function of Collector voltage with the Emitter reversed biased at 1 V, and 1  $\mu$ s carrier lifetimes. The optical source has a 51  $\mu$ m beam radius and the Emitter radius is 50  $\mu$ m.

(before avalanche gain) with the substrate reversed biased at 1 V.

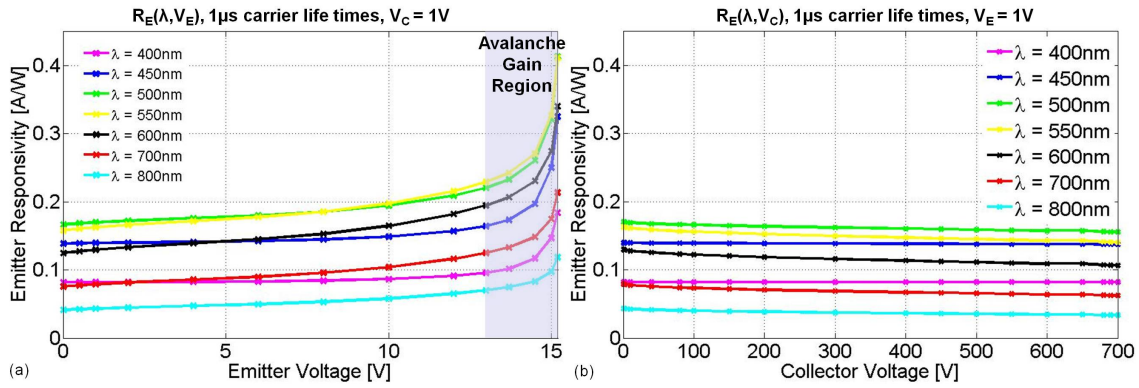


Figure II.36: (a)  $R_E$  versus  $V_E$  with the Collector reversed biased at 1 V. (b)  $R_E$  versus  $V_C$  with the Emitter reversed biased at 1 V. A value of  $1\mu\text{s}$  was used for the carrier lifetimes. The optical source has a  $51\mu\text{m}$  beam radius and the Emitter radius is  $50\mu\text{m}$ .

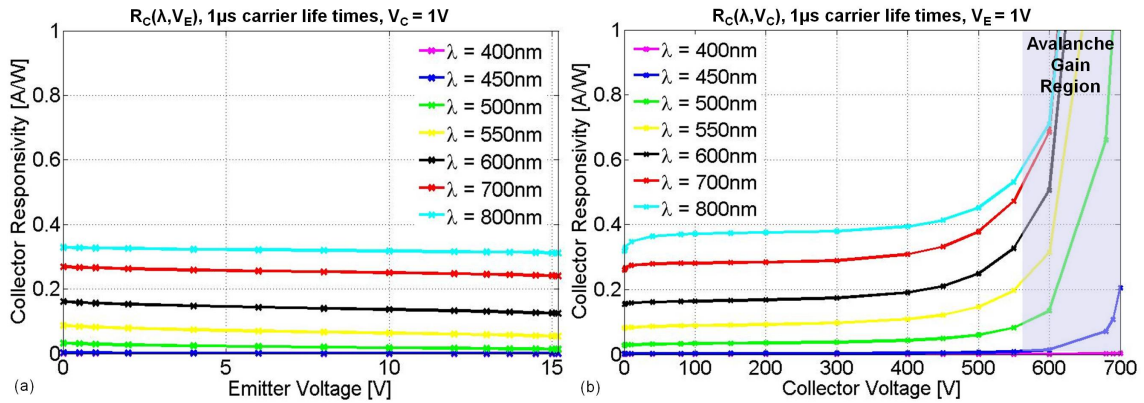


Figure II.37: (a) Collector responsivity versus Emitter voltage with the Collector reversed biased at 1 V. (b) Collector responsivity versus Collector voltage with the Emitter reversed biased at 1 V. A value of  $\mu\text{s}$  was used for the carrier lifetimes.

The choice of operating wavelength is a compromise between minimizing the effect of high DC substrate voltages on the IPD output current and maximizing the IPD output current. The effect of the substrate voltage on the optical wavelength corresponding to the maximum IPD output current is about  $+10\text{nm}$  for a substrate voltage increase from 1 V to 700 V. Figure II.38 illustrates the operating wavelength compromise. As an example, the stage succeeding an IPD that is illuminated by a 500 nm optical wavelength, should be able to tolerate reductions of around 8% in its input current level.

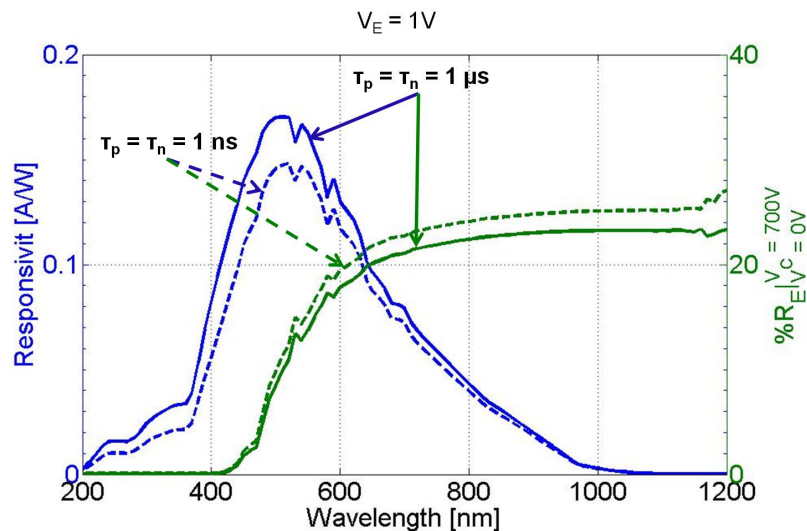


Figure II.38: The effect of Collector voltages on the Emitter as a function of optical wavelength. The range of wavelengths affected by the high DC substrate voltages depends on the carrier lifetimes. Wavelengths with higher photogeneration rates within the Base region have a stronger dependence on the substrate voltages. The green line defined as,  $\%R$ , represents the percent decrease in the Emitter spectral responsivity when the substrate DC reverse voltage level is at 700V relative to when it is at 0V.

#### II.4.b Sensitivity to Carrier Lifetimes

The method used to fabricate a Silicon wafer and the photodetector processing have a critical impact on the defect concentration levels within the material. The rate of SRH recombination is contingent upon the number of defects present within the Silicon wafer and moreover, it increases with higher doping levels [101]. Auger recombination is also more likely in heavily doped material. The overall effect of the different recombination processes within the device are reflected in the minority carrier diffusion length and the minority carrier lifetime parameters. Thus, the minority carrier lifetime plays a key role in the efficiency of the photodetector.

A number of simulations invoking the SRH and Auger recombination processes were performed when the device is illuminated in steady state conditions using a number of different fixed carrier lifetimes. In order to decouple the effect of electron and hole lifetimes on the device efficiency, when varying one carrier lifetime the other was kept constant at  $1\mu s$ . The IPD structure shown in figure II.39 (a) shows the different regions of the device where recombination occurs. The result of recombination rate gradient for minority (hole) carrier lifetimes of 0.1 ns, 0.5 ns, 1ns, 5ns, 10ns, 50ns, 100ns, 500ns, and  $1\mu s$ , corresponding to a vertical cut-line from the surface of the device to a depth of  $1\mu m$  is shown in figure II.39 (b).

The effect of carrier lifetimes on the minority (holes) carrier concentration gradient and hence the minority carrier the diffusion length is depicted in figure II.40. This decrease in the minority diffusion length with shorter lifetime results in a lower number of carrier

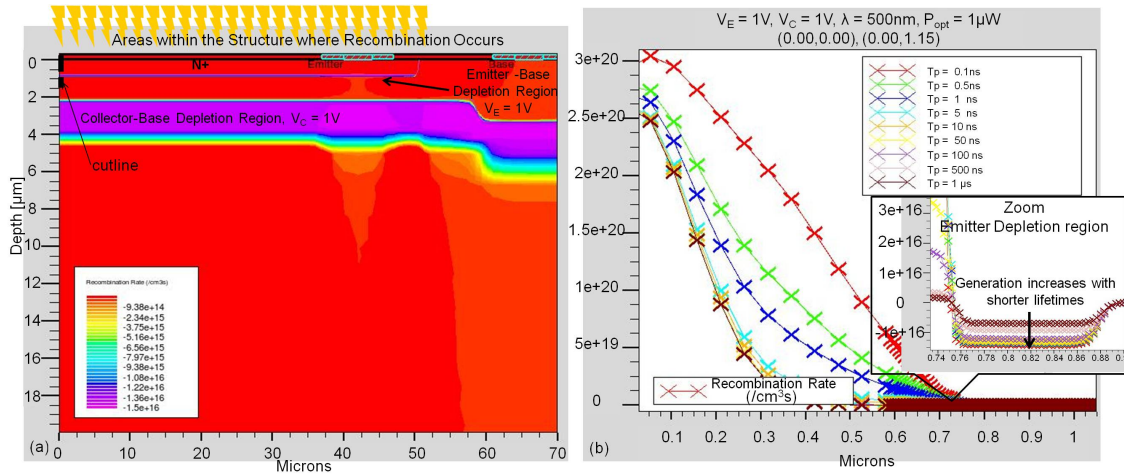


Figure II.39: (a) Recombination areas within the IPD structure where recombination occurs are shown in red. Generation processes dominate within the depletion regions as shown in purple. Note: A wide range of recombination rates have been saturated to the zero recombination rate represented by the color red. (b) The effect of minority carrier lifetime on the recombination rate corresponding to a vertical cut-line from the surface of the device to a depth of 1 μm. The optical source has a uniform distribution and 1 μW of power.

density reaching the junction and thus a reduced current density as shown in figure II.41. This effect is more severe if the minority carriers have to travel longer distances before being collected by the junction (i.e. a deep junction versus a shallow junction).

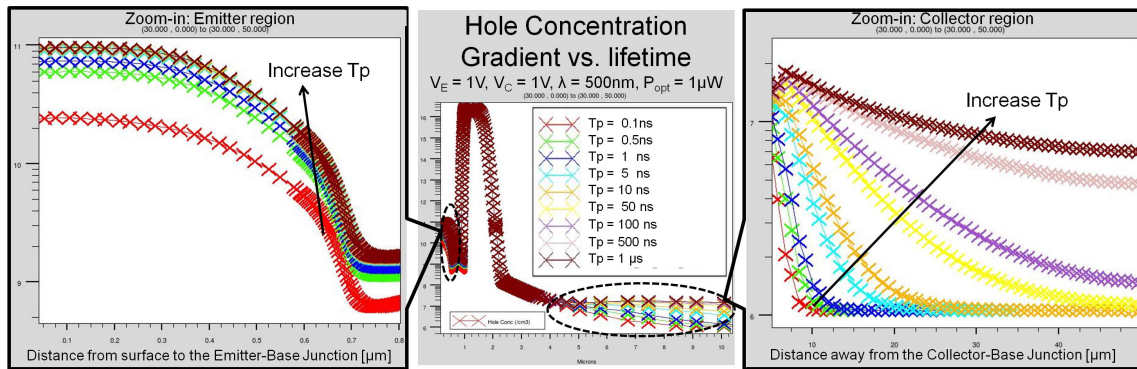


Figure II.40: Hole concentration gradient versus Carrier Lifetimes. Left: Emitter Region. Right: Collector Region.

The Emitter and Collector responsivities of the IPD structure as a function of minority carrier lifetimes are plotted in figure II.42 and II.43 respectively.

Minority carriers generated in shallower depths due to the absorption of shorter optical wavelengths, have to travel longer distances relative to carriers generated by longer wavelengths. Thus, the IPD Emitter efficiency is more sensitive to shorter lifetimes when a short wavelength optical source is used. Since the diffusion currents in both the Emitter

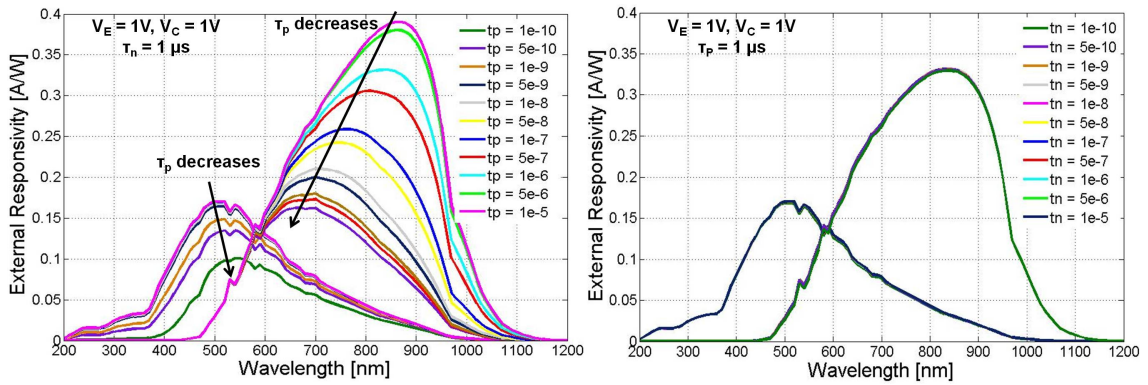


Figure II.41: Spectral Responsivity Sensitivity to Carrier Lifetimes. Left: Sensitivity to the lifetime of holes. Right: Sensitivity to the lifetime of electrons.

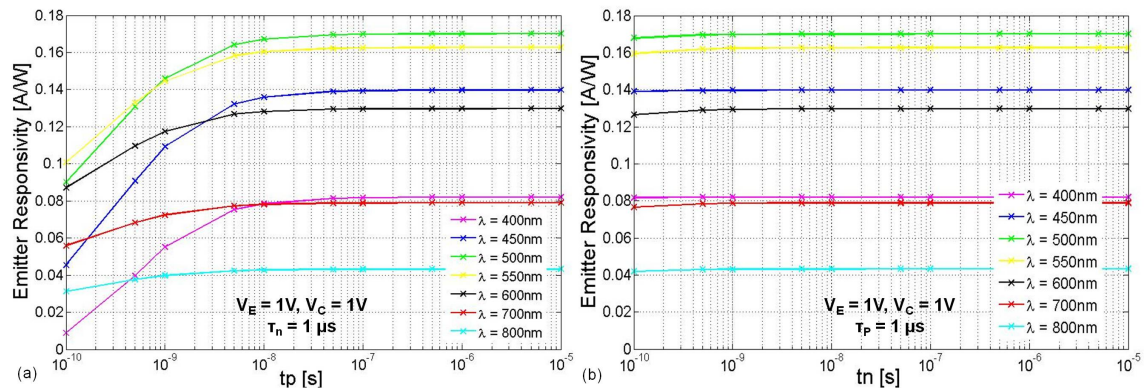


Figure II.42: Emitter Current Sensitivity to Carrier Lifetimes. (a) Sensitivity to the lifetime of holes. (b) Sensitivity to the lifetime of electrons.

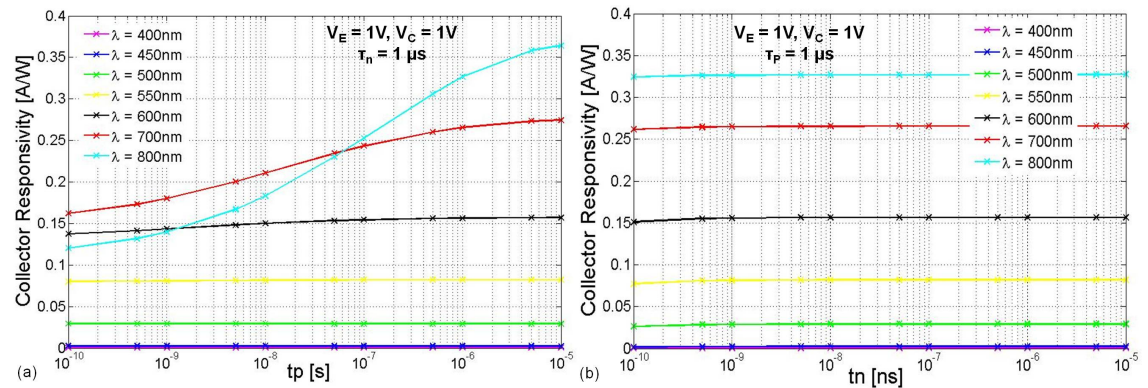


Figure II.43: Collector Current Sensitivity to Carrier Lifetimes. (a) Sensitivity to the lifetime of holes. (b) Sensitivity to the lifetime of electrons.

and the Collector junction are almost entirely due to the diffusion of holes, the efficiency of these two junctions are more coupled with the hole lifetime rather than the electron lifetime. This result predicts that for structures with a lifetime shorter than 10 ns, the IPD efficiency begins to suffer; the efficiency could be improved via using a shallower junction, a wider depletion region, or having p-doped Emitter; however, as discussed earlier the doping profile optimization is limited by the VD-MOSFET. The effect of the design constraints on the IPD efficiency can be compensated by using high quality wafers with intrinsically higher carrier lifetimes. In addition, long lifetimes can limit the frequency response of a diffusion limited device; hence there is a compromise. In addition to the compromise between efficiency and bandwidth of the IPD, the impact of lifetime on the body diode and MOSFET should also be considered. Since MOSFETs are unipolar devices, in other words there are no minority carriers, their performance is not much effected by the carrier lifetimes. However the body diode is a bipolar device, in other words there are minority and majority carriers flowing through the device; when switching this diode, the time required for the excess carrier density to diminish via recombination depends on the minority carrier lifetimes which in turn determine the turn-off time of the device. Thus, the carrier lifetime optimization needs to consider both the IPD and the body diode requirements.

## II.5 Dynamic Analysis

The speed of a photodiode can be limited due to one of the following factors:

- Long carrier transit times  $t_{tr}$ : Carrier transit across the depletion region is a fast process since carriers will be drifting at saturation velocities  $v_{sat}$  [78] if the field is high enough. Transit time across a depletion region with width  $W_D$  is given by:

$$t_{tr} = \frac{W_D}{v_{sat}} \quad (\text{II.49})$$

If the incident photons are all absorbed at the edge of the depletion region on the N-type Emitter side, the response time will be limited by the saturation velocity of the holes. In our IPD design, the depletion region width is rather thin specially at low Emitter voltages. To approximate  $t_{tr}$ , we can consider the maximum electric field in the Emitter-Base depletion region at 1 V reverse bias from figure II.8 (b) to be  $5 \times 10^4 \text{V/cm}$ , and the hole mobility of  $50 \text{cm}^2/\text{V.s}$  from figure II.9 to calculate the hole velocity of approximately  $2.5 \times 10^6 \text{cm/s}$ . A depletion region of approximately  $0.5 \mu\text{m}$  as estimated from figure II.8 (b), in combination with the calculated carrier velocity results in a  $t_{tr}$  of 0.2 ps which corresponds to a cut-off frequency above hundreds of GHz. Hence, the IPD is most likely not transit limited.

- Long carrier diffusion times,  $t_d$ : If the incident photons are absorbed outside the depletion region they will diffuse a distance  $x$  in a time given by [78]:

$$t_d = \frac{4x^2}{\pi^2 D_p} \quad (\text{II.50})$$

Carrier diffusion is a much slower process compared to drift and can be as long as the carrier lifetimes. The carrier lifetime limit can be observed in the long-tails of a photodiode impulse response.

- The RC time constant,  $t_{RC}$ :  $t_{RC}$  includes series resistances (i.e. from the QNRs and contacts) as well as junction capacitances of the photodiode equivalent circuit model. The series resistance from the QNR is determined by the resistivity and the width (with Emitter and Base top contacts, carriers move laterally between contacts) of the region, and the distance between contacts. The junction capacitance is directly proportional to the area of the diffused region (i.e. the Base), inversely proportional to the width of the depletion region and also dependent on the reverse bias:

$$C_j = \frac{\epsilon_{Si}\epsilon_0 A}{W_D(V)} \quad (\text{II.51})$$

where  $\epsilon_{Si}$  and  $\epsilon_0$  are the relative permittivity of Silicon and the permittivity of free space respectively, and  $V$  is the junction reverse bias. Figure II.44 shows the capacitance of the IPD versus reverse bias voltage as approximated by a uniformly doped abrupt junction.

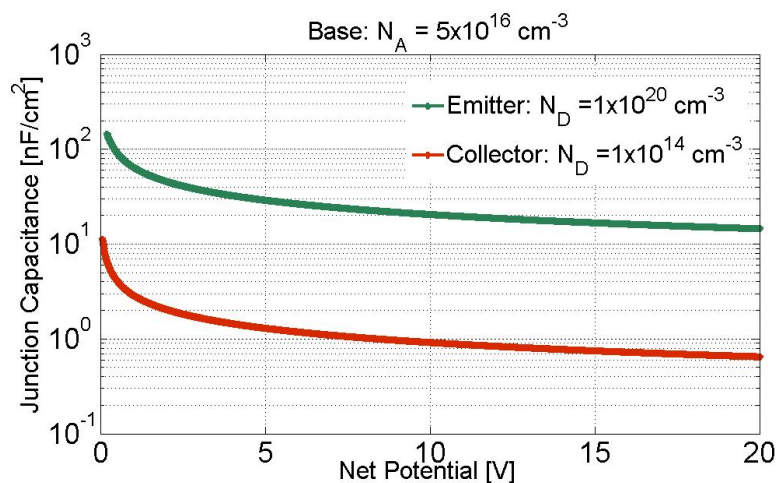


Figure II.44: IPD junction capacitances versus reverse voltage. The capacitance values here are calculated based on the effective width of the depletion region and doesn't consider the sidewall contribution.

- The bandwidth limit imposed by the input impedance of the TIA stage,
- The RC limitations from packaging: This can be minimized by careful layout and the use of short leads.

In the case of pin photodetector, the frequency response is transit limited. However, in the case of our IPD since most of the active region of the device is not depleted, the device

response time is limited by a combination of all the factors listed above. Considering the IPD without the limitations of packaging and TIA input impedance, its total response time can be determined by:

$$t_R = \sqrt{t_d^2 + t_{tr}^2 + t_{RC}^2} \quad (\text{II.52})$$

where  $t_R$  is the time it takes for the current signal to rise from 10% to 90% of its final value.  $t_R$  is used to quantify the frequency at which the IPD response is reduced by 3 dB, also referred to as the frequency response of the device:

$$t_R \approx \frac{0.35}{f_{3dB}} \quad (\text{II.53})$$

### II.5.a Wavelength Dependence

Figure II.45 (a) and (b) show a simplified equivalent circuit and its corresponding Thevenin model that can be used to study the frequency response of the IPD structure.

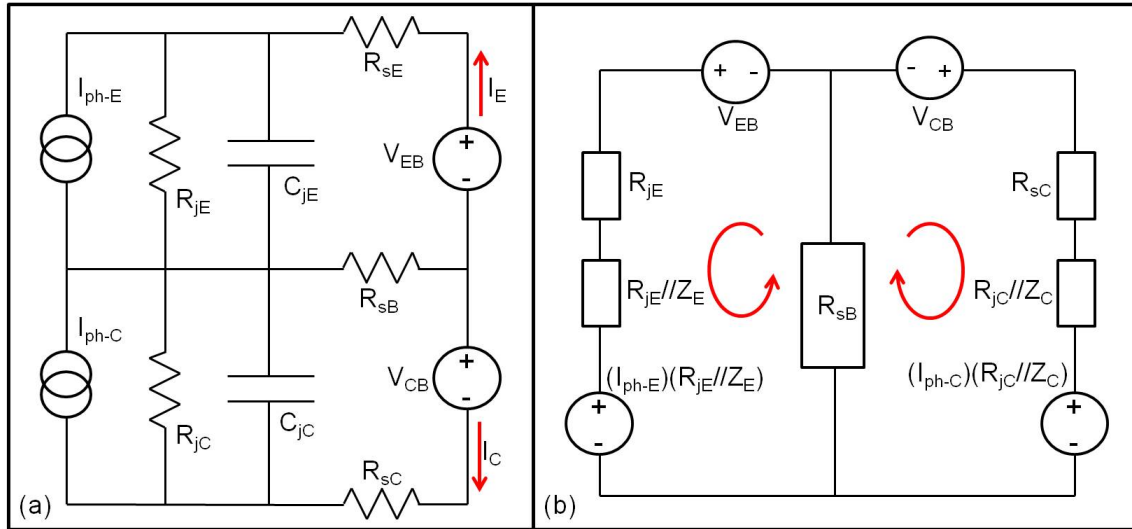


Figure II.45: (a) A simplified equivalent circuit and (b) its corresponding Thevenin circuit that can be used to study the frequency response of the IPD structure.

From figure II.45 (b), equations II.54 and II.55 can be written to represent the current loops.

$$(I_{Ph-E})(R_{jE} // Z_E) - I_E(R_{jE} // Z_E) - I_E R_{sE} + V_{EB} - R_{sB}(I_E + I_C) = 0 \quad (\text{II.54})$$

$$(I_{Ph-C})(R_{jC} // Z_C) - I_C(R_{jC} // Z_C) - I_C R_{sC} + V_{CB} - R_{sB}(I_E + I_C) = 0 \quad (\text{II.55})$$

where  $Z_E$  and  $Z_C$  are the equivalent impedances for the Emitter and Collector junction capacitances,  $R_{jE}$  and  $R_{jC}$  are the Emitter and Collector junction resistances (ideally infinite),  $R_{sE}$ ,  $R_{sB}$  and  $R_{sC}$  are the Emitter, Base and Collector series resistances respectively,  $I_{Ph-E}$  and  $I_{Ph-C}$  are the Emitter and Collector photocurrents,  $I_E$  and  $I_C$  are the

output current responses from the IPD. Noise is not considered here. Considering DC bias conditions,  $V_{CB}$  and  $V_{CB}$  can be omitted from equation II.54 and II.55.  $I_E$  and  $I_C$  can then be written as:

$$I_E = \frac{(I_{Ph-E})(R_{jE}/Z_E) - R_{sB}I_C}{(R_{jE}/Z_E) + R_{sE} + R_{sB}} \quad (\text{II.56})$$

$$I_C = \frac{(I_{Ph-C})(R_{jC}/Z_C) - R_{sB}I_E}{(R_{jC}/Z_C) + R_{sC} + R_{sB}} \quad (\text{II.57})$$

Substituting equation II.57 into equation II.56 gives:

$$I_E = \frac{\frac{(I_{Ph-E})(R_{jE}/Z_E)}{(R_{jE}/Z_E) + R_{sE} + R_{sB}} - \frac{(I_{Ph-C})(R_{jC}/Z_C)R_{sB}}{[(R_{jC}/Z_C) + R_{sC} + R_{sB}][(R_{jE}/Z_E) + R_{sE} + R_{sB}]}}{1 - \frac{R_{sB}^2}{[(R_{jC}/Z_C) + R_{sC} + R_{sB}][(R_{jE}/Z_E) + R_{sE} + R_{sB}]}} \quad (\text{II.58})$$

The result of equation II.58 shows that the dynamic response of  $I_E$  is a function of the Collector parameters. Using the result of equation II.58, the high frequency behaviour of the IPD structure is modelled in matlab bode plots as shown in figure II.46.

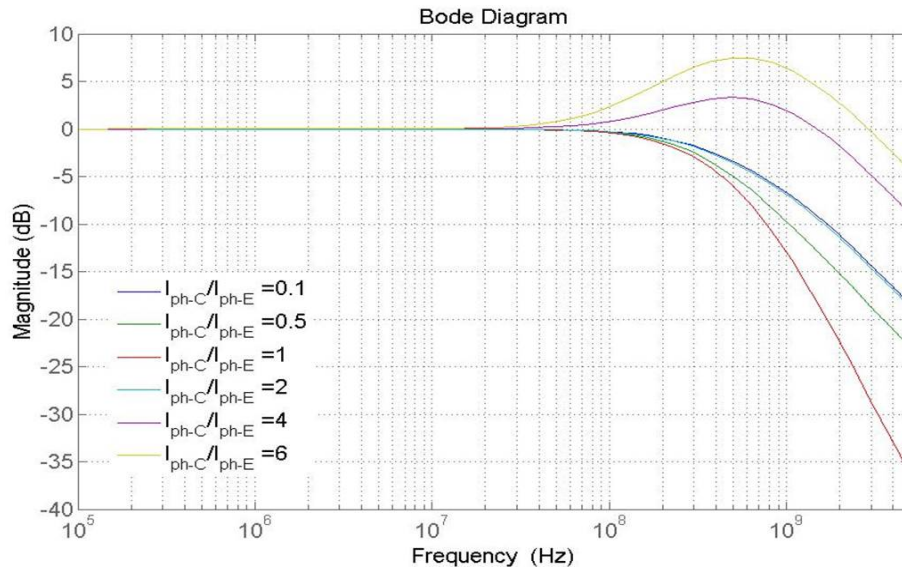


Figure II.46: Bode plot of the IPD frequency response according to equation II.58 where,  $R_{jE} = R_{jC} = 100 \text{ M}\Omega$ ,  $R_{sE} = 0.5 \text{ }\Omega$ ,  $R_{sB} = 10 \text{ }\Omega$ ,  $R_{sC} = 30 \text{ }\Omega$ ,  $C_{jE} = 30 \text{ pF}$ ,  $C_{jC} = 8 \text{ pF}$ .

In these plots,  $I_{Ph-C}$  is taken to be 0.1, 0.5, 1, 2, 4, and 6 times the value of  $I_{Ph-E}$ . The ratio of  $I_{Ph-C}$  to  $I_{Ph-E}$  represents the operating wavelength; this ratio is lower for shorter wavelengths where the Emitter has a high efficiency relative to the Collector, and the ratio grows for longer wavelengths where the Collector efficiency dominates over that of the Emitter as depicted in figure II.47. The frequency response is investigated further via numerical simulations in Atlas for our specific IPD structure and the results for an optical wavelength of 500 nm are shown in figure II.48. The Emitter and Collector current responses and gain-frequency plots for optical wavelengths of 400 nm, 450 nm, 500 nm,

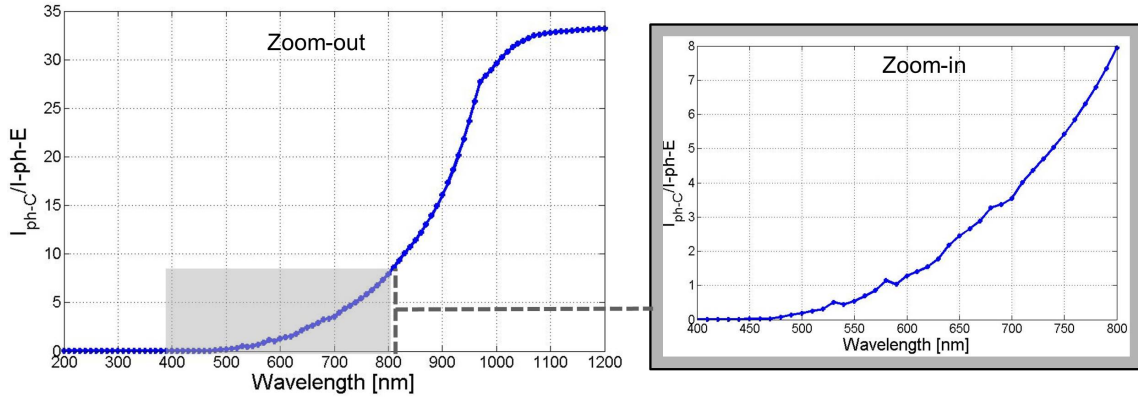


Figure II.47: Collector to Emitter photocurrent ratio.

550 nm, 600 nm, 650 nm, 700 nm, 750 nm, and 800 nm are depicted in figures II.49 and II.50.

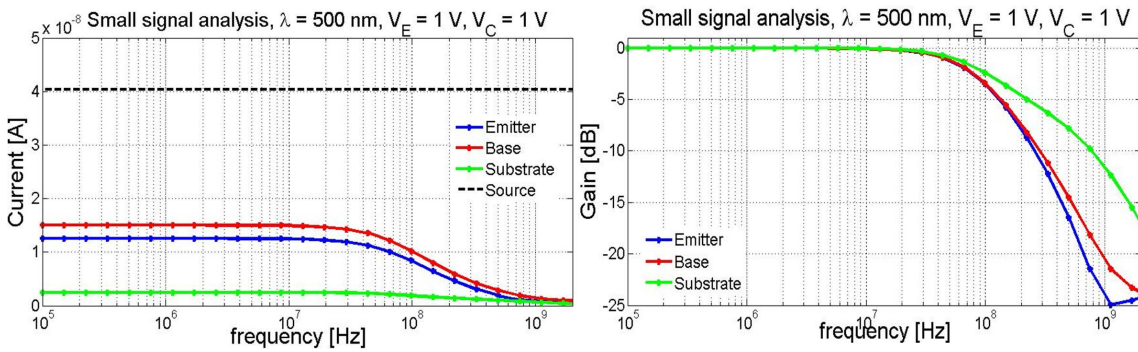


Figure II.48: IPD frequency response at 500 nm optical wavelength as evaluated by numerical analysis in Atlas. Left: Current levels including the small signal response plus the DC levels. Right: Normalized gain as defined by  $20 \cdot \log_{10}(I_i) / \log_{10}(I_L F_i)$ , where  $I_i$  is the DC plus small signal current magnitude of each region  $i$  being the Emitter, the Collector or the Base, and  $I_L F_i$  is the corresponding region's DC current magnitude at low frequencies.

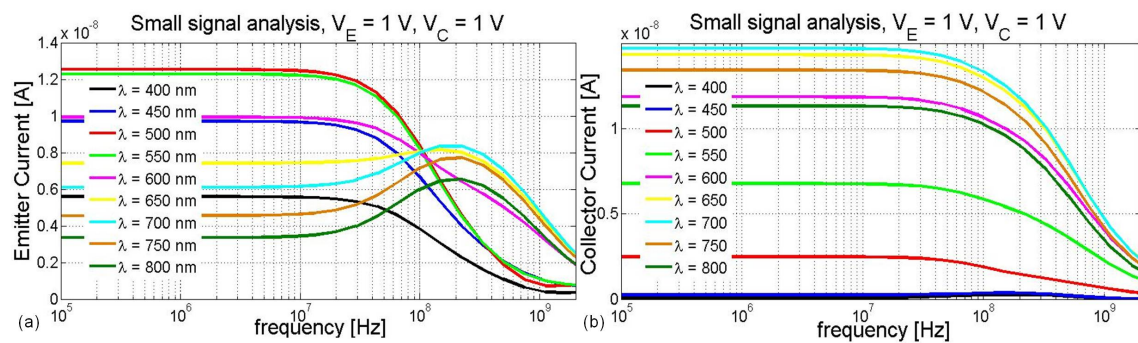


Figure II.49: IPD Emitter frequency response for different optical wavelengths as evaluated by numerical analysis in Atlas.

The results from Atlas show a wavelength dependence in the IPD frequency response

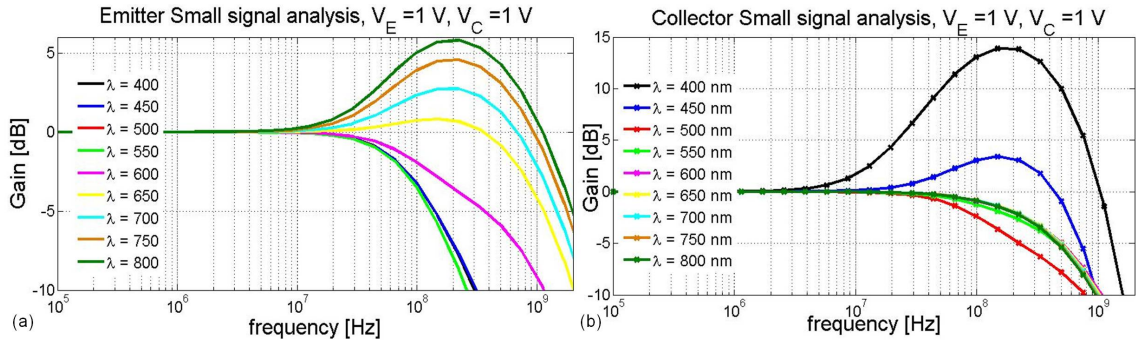


Figure II.50: IPD Gain-frequency plots for different optical wavelengths as evaluated by numerical analysis in Atlas.

similar to that predicted by the transfer function of equation II.58; this dependency is summarized in figure II.51. Thus there is a wavelength region ( $\sim$  for  $\lambda \leq 600 \text{ nm}$ ) where the effect of the Collector on the Emitter bandwidth is insignificant. For longer wavelengths where a larger Collector current is flowing through the Base region causes an increase in the Emitter bandwidth.

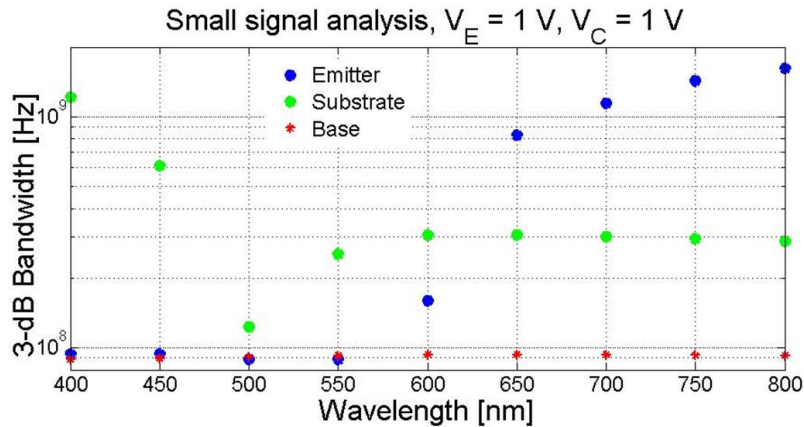


Figure II.51: IPD bandwidth as a function of the optical wavelength as evaluated by numerical analysis in Atlas.

The same simulation is then repeated for different device areas with the Emitter radius of  $50 \mu\text{m}$ ,  $40 \mu\text{m}$  and  $25 \mu\text{m}$ , meanwhile maintaining a constant 33% shading factor. As shown in the results of figure II.52, for wavelengths where the Collector doesn't effect the Emitter bandwidth, the Emitter bandwidth is inversely proportional with the device area.

Moreover, simulations using different small signal amplitudes showed no effect on the frequency response.

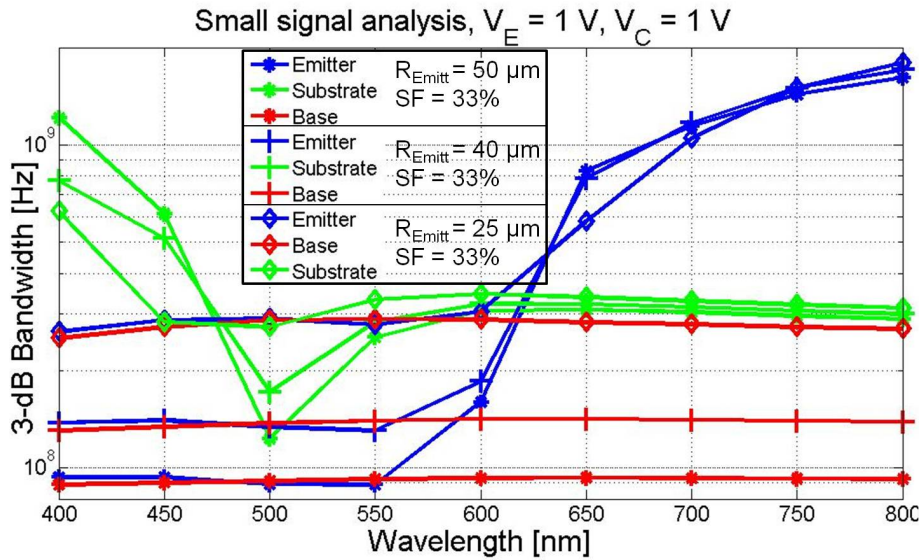


Figure II.52: IPD bandwidth as a function of optical wavelength for different device sizes as evaluated by numerical analysis in Atlas.

### II.5.b Emitter DC biasing

The Emitter junction capacitance and the Collector junction capacitance are strong functions of the Emitter and the Collector voltages respectively. IPD 3-dB bandwidth as a function of Emitter biasing for different optical wavelengths as evaluated by numerical analysis in Atlas is summarized in figure II.53.

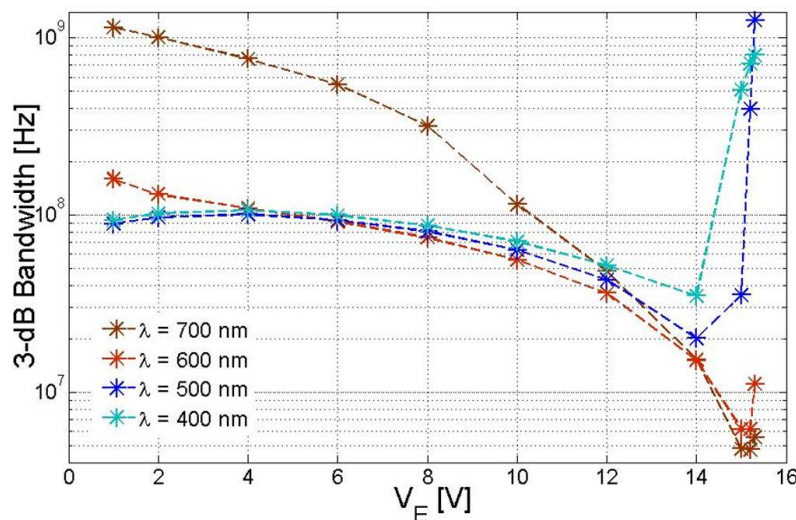


Figure II.53: IPD 3-dB bandwidth as a function of Emitter biasing for different optical wavelengths as evaluated by numerical analysis in Atlas.

The effect of Emitter DC bias on the Emitter, Collector, and Base currents and frequency responses are investigated via Atlas simulations. Figure II.54 and II.55 show the results in detail for the case of a 500 nm wavelength when the Collector/Base junction is fixed at a reverse bias of 1V. These results need to be investigated further.

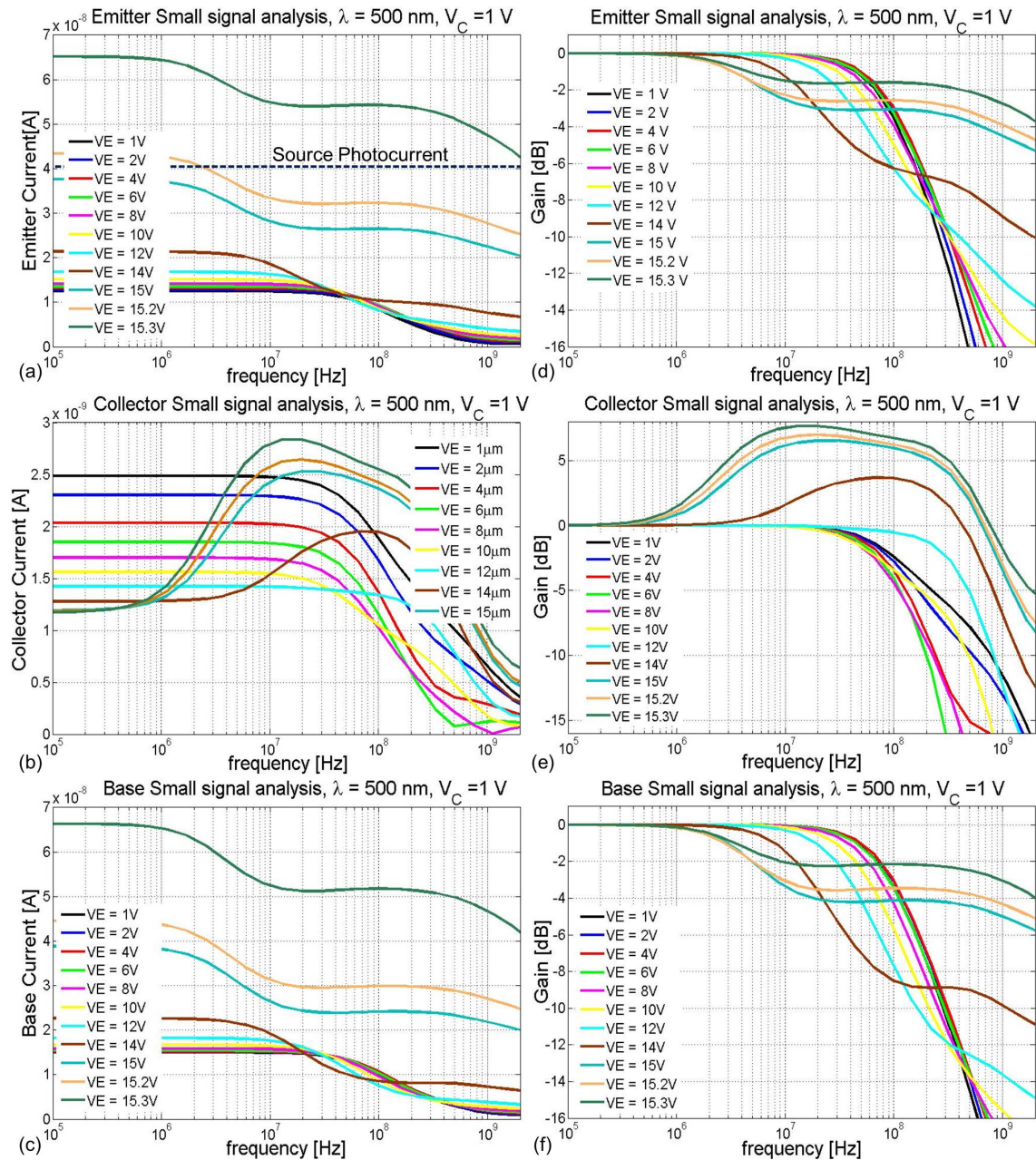


Figure II.54: IPD frequency response as a function of Emitter biasing for a 500 nm optical wavelength as evaluated by numerical analysis in Atlas.

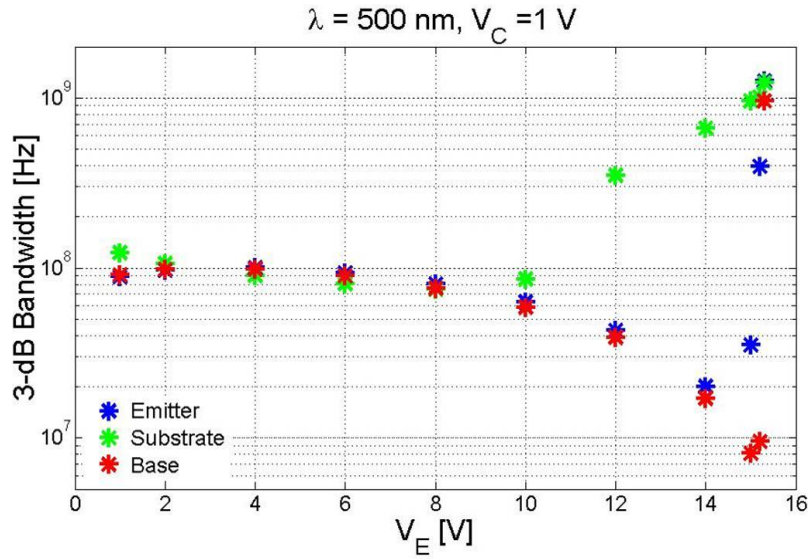


Figure II.55: IPD 3-dB bandwidth as a function of Emitter biasing for a 500 nm optical wavelength as evaluated by numerical analysis in Atlas.

## II.6 Optical Beam Radius and Position Analysis

Simulations in Atlas show the effect of carrier generation in the Emitter and the Base as well as the shadow effect of the metal contacts on the IPD efficiency as displayed in the results of figure II.56. In these simulations, a  $1 \mu\text{W}$  uniform optical beam of light was aligned to the center of the IPD. The width of the optical beam was varied while keeping the same total optical power. A decrease in the Emitter responsivity and an increase in the Collector responsivity is observed as the optical beam width extends into the base region. This result agrees with the explanation of carrier dynamics provided in figure II.12 (b). Thus, the Emitter responsivity is maximized by adjusting the optical beam width to be well within the Emitter region. The rise in the responsivity for very small beam widths is a consequence of the non-linear dependence on optical intensity. Moreover, the contact shadow effect on the responsivity will be much less severe for a Gaussian optical source as long as the contacts are close to the outer boundary of the device.

The effect of beam width is also investigated on the bandwidth of the IPD. Figure II.57 shows that for a 500 nm wavelength source, the Emitter bandwidth decreases with an increasing optical beam radius.

The change in beam width effects the total series resistances as well as the junction capacitance. A smaller beam radius activates a smaller area of the junction and hence a smaller junction capacitance. Meanwhile, a smaller beam radius implies that the effective series resistance is larger compared to a larger beam radius where the same amount of photogenerated carriers would on average have a shorter distance to travel before being collected by the contacts. In the case of the intrinsic (not including contact or packaging series resistances) IPD bandwidth, if the sheet resistance of the QNRs are small enough, this change in the resistance may not be significant except for very large devices. Moreover, since carrier diffusion times are mostly a function of the width (distance the minority

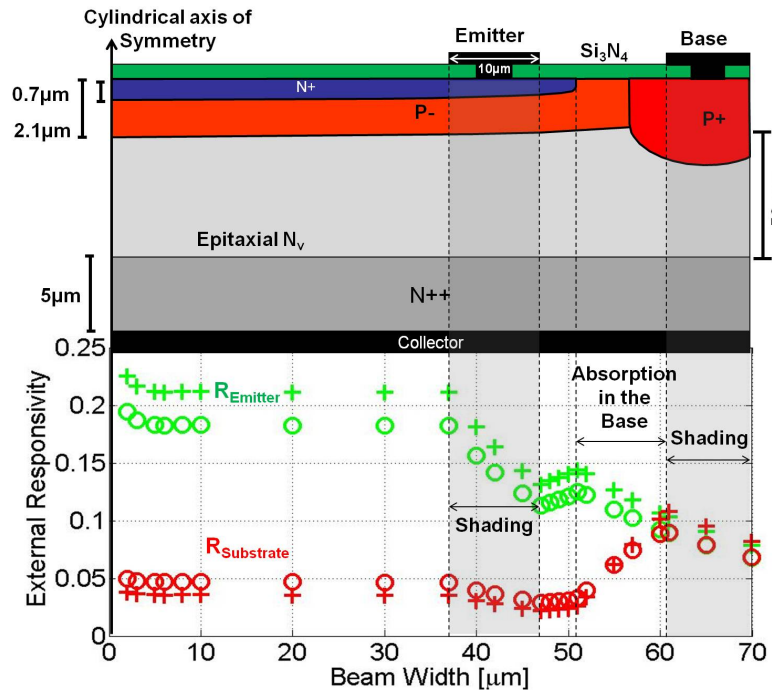


Figure II.56: Under illumination of a 500 nm uniform optical source, the effect of the spatial dependence of photogeneration on the Emitter and Collector responsivities is demonstrated by varying the optical beam width. Both junctions are reversed biased at 1 V. The data presented via the circle marker correspond to a carrier lifetime of 1  $\mu\text{s}$ . The data presented via the cross marker correspond to a carrier lifetime of 1 ns.

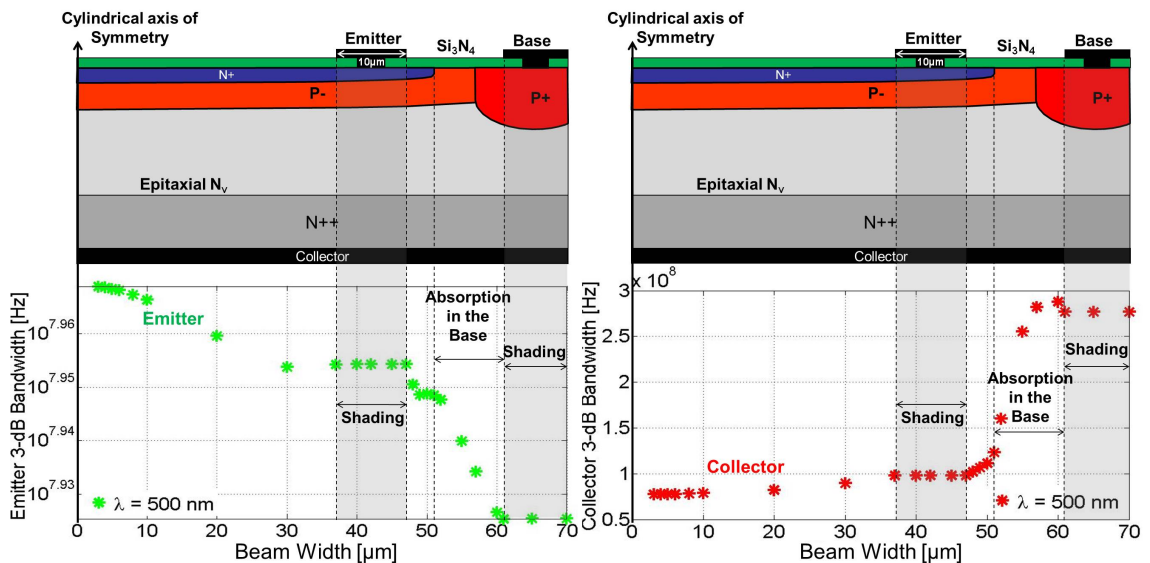


Figure II.57: Under illumination of a 500 nm uniform optical source, the effect of the spatial dependence of photogeneration on the Emitter and Collector Bandwidths is demonstrated by varying the optical beam width. Both junctions are reversed biased at 1 V and the carrier lifetimes are 1 ns. The optical signal has a 10  $\mu\text{W}$  DC component and a 0.1  $\mu\text{W}$  amplitude small signal component.

excess carriers must travel to reach the junction) of each region rather than the length, they are not effected by the changes in the optical beam radius. Thus the effective change in the IPD bandwidth as a function of the optical beam width is dominated by the modulation of the junction area contributing to the junction capacitance.

## II.7 Parasitic Environment Constraints

The cross section of a classic power VD-MOSFET structure is shown in figure II.58. There are some parasitic elements present in this structure, including: the pn-junction diodes, the source/base/drain BJT, and the JFET (only half of the region in depicted) created by the drift region sandwiched between the two base regions. As it was presented in figure II.3, with the exception of the JFET, the monolithic optical detector inherits these parasitic elements.

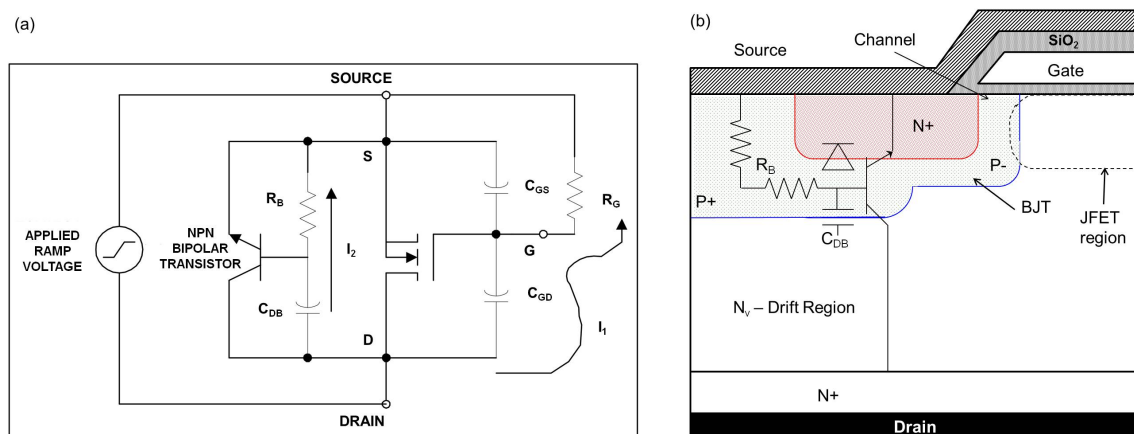


Figure II.58: (a) Equivalent circuit of VD-MOSFET showing two possible mechanisms for  $dv/dt$  induced turn-on [102]. (b) VD-MOSFET cross section showing the physical origin of the parasitic BJT.

### II.7.a Electrical Activation of Parasitic BJT

In a power VD-MOSFET, the turn on of the parasitic BJT formed by the n+ source, p-base and the N<sub>v</sub> drift region is avoided in the DC regime, via electrically shorting the source and base regions together. Moreover, the metal contact overlapping the Source and the p-type Base region also acts as a body contact for the MOS structure of the VD-MOSFET. However, when switching, the parasitic BJT may turn on due to large  $dv/dt$  transients. The cross section view of figure II.58 shows that the Drain of the VD-MOSFET is connected to the Base of the parasitic BJT through the drift/Base junction capacitance which is then connected to the Source contact through the Base resistance. Transients appearing between the Drain and the Source of the power MOSFET induce a current  $I_2$  through the Base resistance. If the voltage drop in the Base becomes higher than the

potential barrier across the drift/Base junction, the parasitic BJT will turn on. Equation II.59 shows the bipolar turn-on transient limit.

$$\left[\frac{dV_D}{dt}\right]_{max} = \frac{V_{bi}}{R_{PB}C_{DB}(V_D)} [7] \quad (\text{II.59})$$

Where  $V_D$  is the drain voltage,  $V_{bi}$  is the built in potential of the emitter-base junction,  $R_{PB}$  is the resistance of the p-base region,  $C_{DB}$  is the drain-base capacitance. A small  $R_{PB}$  value helps in suppressing the turn-on of the internal parasitic BJT present in the VD-MOSFET body. The circuit of figure II.58 (a), shows the two mechanisms for  $dv/dt$  turn-on: (1) turn-on via the parasitic BJT as discussed above, (2) and the Miller drawback which was discussed in Chapter 1.

Unlike the VD-MOSFET, in the optical detector structure the device is no longer functional if the n+ emitter and the base are shorted together, since this is the optical detection junction used for controlling the emitter leakage current. In order to prevent the parasitic BJT, the operating voltage settings must insure that the BJT is in its inverse-off state at all times. By connecting the Base contact to the power transistor Source and always applying positive or null voltages to the Emitter contact, the Emitter leakage current can then be monitored as a function of the optical beam. In this configuration, it is assured that the Emitter/Base and the Base/Collector are always reversed biased; however, there are still the Emitter and the Collector leakage currents and photocurrents flowing through the Base resistance.

Just like the case for the VD-MOSFET, transient limits should be identified in order to insure a safe operating regime for the photodetector when switching the VD-MOSFET Source-Drain voltage. From the equivalent circuit of the photodetector depicted in Figure II.59 (b), the requirements for avoiding the parasitic turn-on of the BJT in transient mode can be identified by equations II.60 and II.61.

$$V_{critic} = R_{PB}(i_C + i_E) = R_{PB}\left[C_{DB}(V_D)\frac{dV_D}{dt} + i_E\right] < [V_E + V_{bi}] \quad (\text{II.60})$$

$$\frac{dV_D}{dt} = \left[\frac{V_E + V_{bi}}{R_{PB}} - i_E\right]/C_{CB} \quad (\text{II.61})$$

Where  $C_{CB}$  is the Collector/Base junction capacitance (note that  $C_{CB}$  and  $C_{DB}$  are the same capacitance),  $i_E$  and  $i_C$  are the Emitter and the Collector leakage currents when transients appear between the Drain (note that the Drain of the VD-MOSFET is the same as the Collector of the IPD) and Source. For maximum  $dV/dt$ , a low  $R_{PB}$  and a large  $V_E$  are desired. Both in the DC and the transient case, a large Emitter current contributes to an earlier parasitic turn-on (a lower  $V_{critic}$  tolerance); thus, there is a limit in maximizing the IPD output Emitter current. Moreover, by comparing Equation II.61 with Equation II.59, it is observed that as long as  $[(V_E/R_{PB} - i_E)/C_{DB}]$  is positive, the maximum  $dV/dt$  is limited by the VD-MOSFET as expressed in Equation II.59. If  $[(V_E/R_{PB} - i_E)/C_{DB}]$  is negative, then the maximum  $dV/dt$  is set by the IPD as expressed in Equation II.61.

Simulation results from Atlas depicted in figure II.60 shows the effect of a 400 V step signal on the substrate in a 25 ns ramp time under dark conditions. As seen the substrate

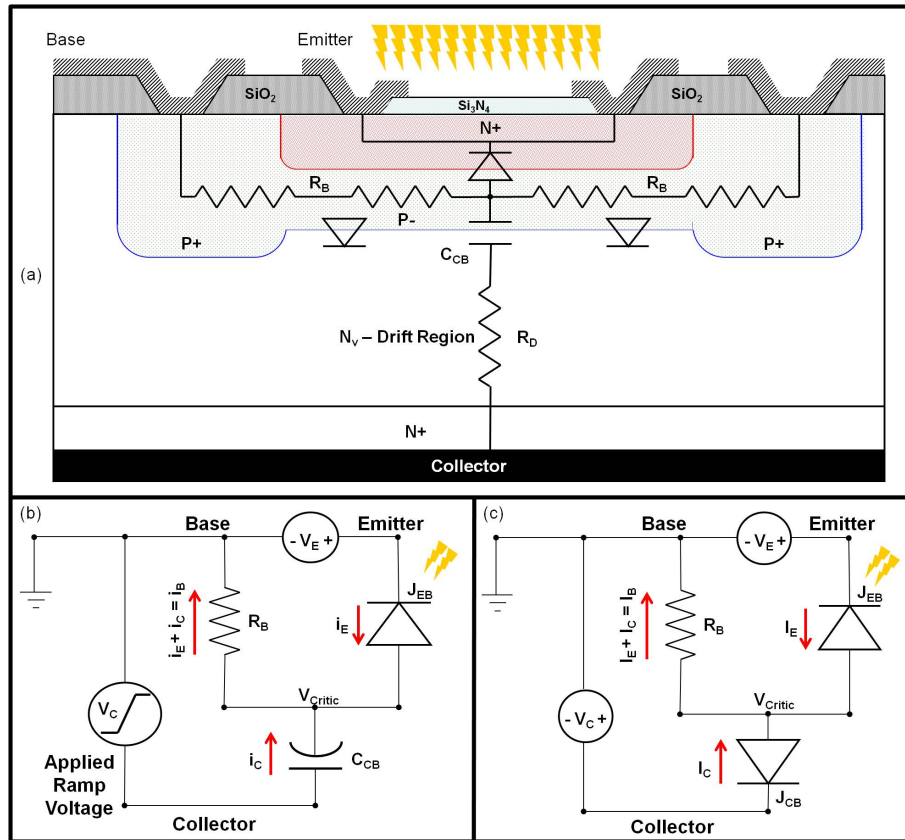


Figure II.59: (a) IPD cross section showing the physical origin of the parasitic BJT. (b) Equivalent circuit of IPD showing two possible mechanisms for parasitic induced turn-on due to due to  $dv/dt$  transients of the collector voltage or (c) voltage drops in the base in DC mode.

transient results in a fast current transient in both the Emitter and the Collector outputs. During this transient a large current flows between the Emitter-Collector and the Emitter-Base junction is temporarily forward biased. The largest current peak corresponds to the  $dv/dt$  at the rising edge of the Substrate voltage signal; this current peak has a  $dt$  of about 1 ns which would correspond to a frequency of 1 GHz. One way to handle these transient effects could be to reject them by using a HF modulation technique and to filter them out before feeding the gate. Another problem to consider is that the IPD (i.e. small contacts) shouldn't be damaged at the peak transient currents; this may set a limit on the smallest detector design. Moreover, the geometry of the detector can be optimized to reduce the peak emitter current for the max  $dv/dt$ .

Figure II.61 shows the Emitter and Collector currents as a function of time for the same voltage transient signal of figure II.60 for two cases: (1) no light and, (2) with light. In either case the transient effect on the currents is the same. Simulations with different optical wavelengths and optical intensities showed a similar behaviour.

Figure II.62 illustrates the effect of the substrate ramp time on the peak current transient levels of the Emitter. Reducing the ramp time from 25 ns to 50 ns shows a reduction

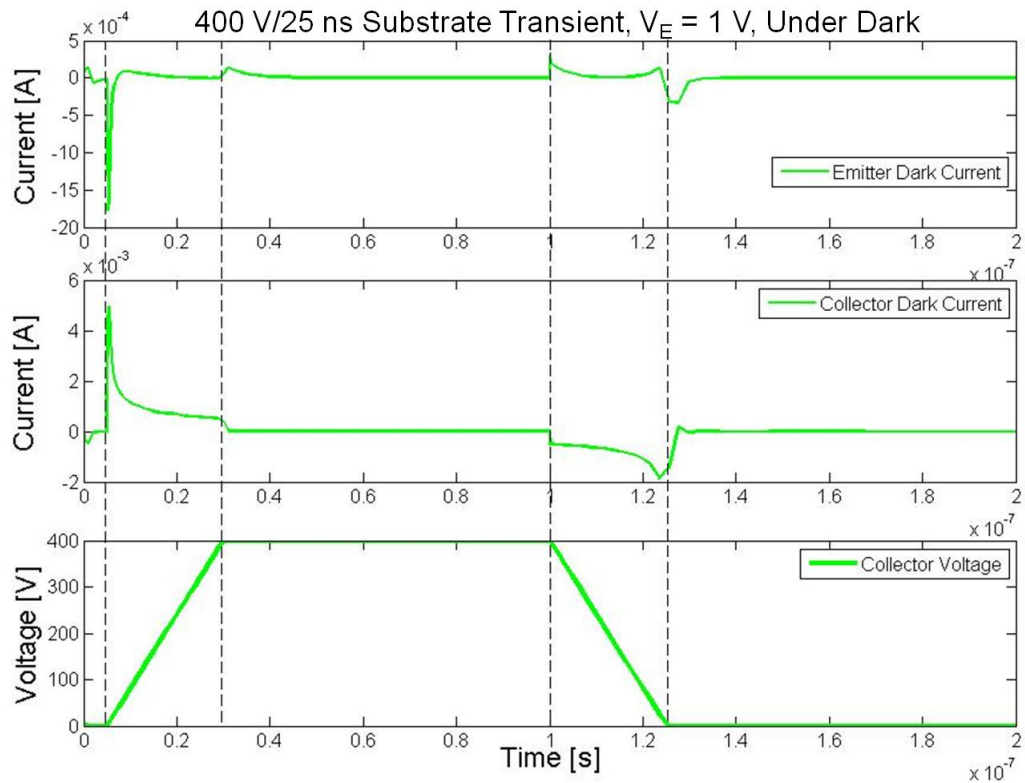


Figure II.60: Substrate transient effect under dark conditions.

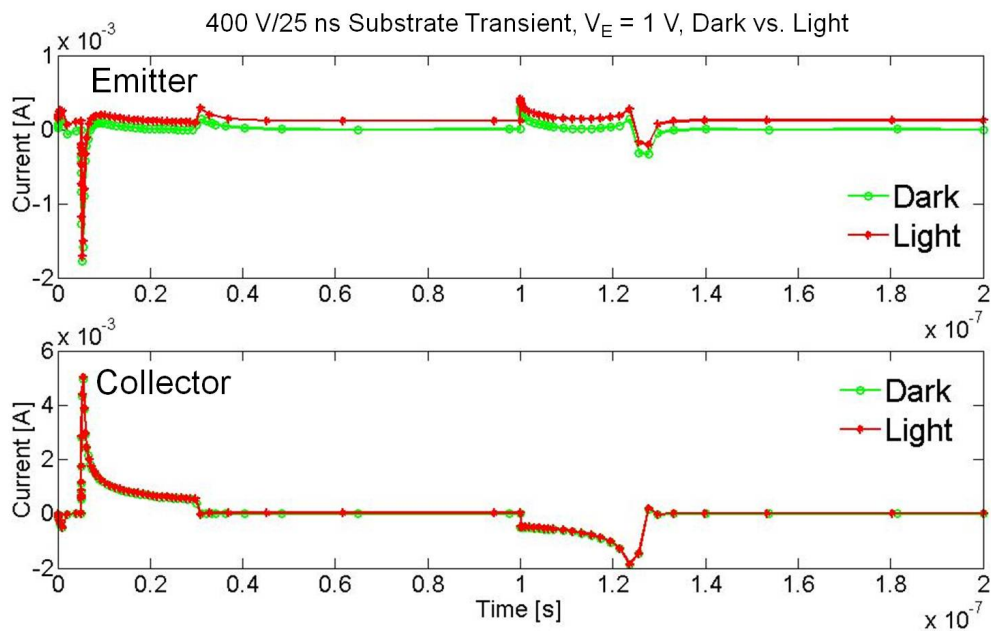


Figure II.61: Substrate transient effect under Illumination from a 500 nm wavelength uniformly distributed optical source with 100  $\mu$ W of power.

in the current peak of the Emitter by roughly 45%.

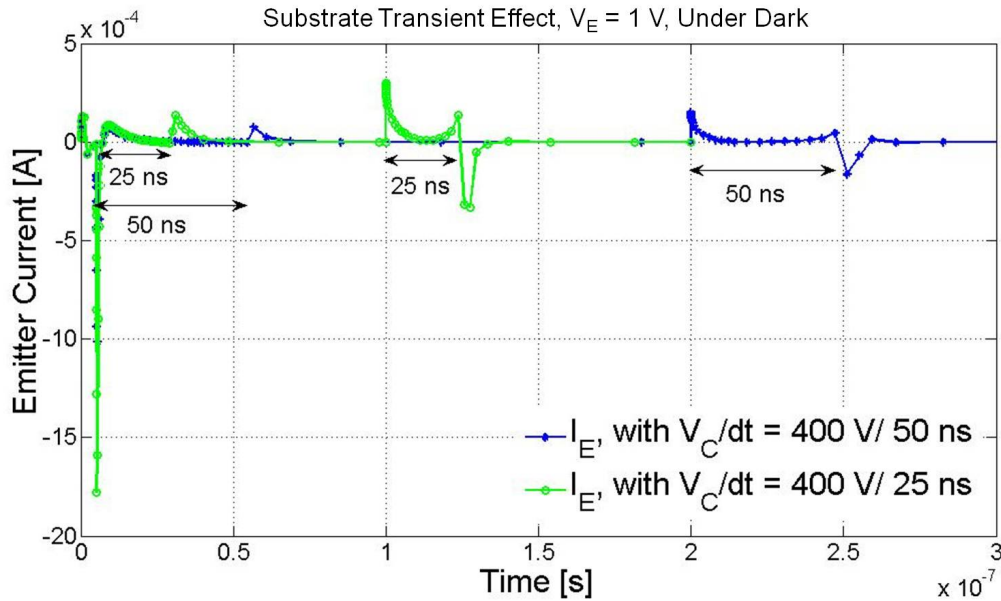


Figure II.62: Substrate transient effect as a function of Collector voltage ramp time.

### II.7.b Optical Activation of Parasitic BJT

Before optimizing the optical detector design, a closer look at the parasitic N-P-N bipolar transistor is necessary in order to define some design and operation constraints. From the equivalent circuit of the photodetector depicted in Figure II.59 (c), the requirements for avoiding the parasitic turn-on of the BJT in DC mode can be identified by equation II.62.

$$V_{critic} = R_{PB}(I_C + I_E) < [V_E + V_{bi}] \quad (\text{II.62})$$

$I_E$  is the Emitter dark current plus the Emitter photocurrent both of which increase with increasing  $V_E$ ; thus, there is a compromise in operating at a large  $V_E$  bias. According to equation II.62,  $R_{PB}$  and  $I_C$  should be minimized in order to avoid the BJT turn-on in the DC mode of operation.  $R_{PB}$  is a design parameter that can be minimized by reducing the carrier path lengths through the design of the contacts and doping wells shape and position. A higher dose of impurities in the Base will also reduce  $R_{PB}$ , however, this is limited by the performance requirement of the VD-MOSFET.  $I_C$  is the Collector dark current plus the Collector photocurrent both of which increase with large reverse voltages on the Collector. Figure II.59 (a) shows the physical origin of the parasitic BJT in the photodetector structure.

Keeping the same IPD area, structure and optical beam radius ( $51\mu m$ ), numerical simulations are repeated at different optical wavelengths while sweeping the optical power from a minimum of  $P_{opt} = 0.1\mu W$  to a maximum of  $P_{opt} = 1$  mW. Figure II.63 (a) and (b) illustrate the photogeneration rate within the structure for an optical wavelength of 500 nm, with an optical power of  $0.1\mu W$  and 1 mW respectively, a collector reverse bias

of 600 V and an Emitter reverse bias of 0.001 V.

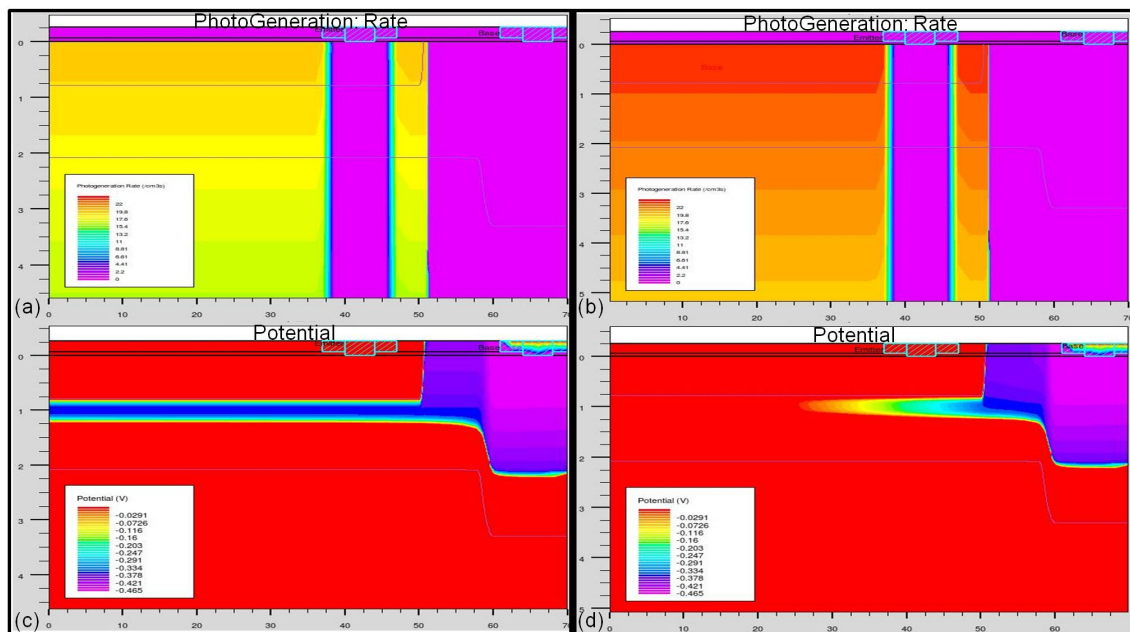


Figure II.63: Photogeneration rate with (a)  $P_{opt-1} = 0.1\mu\text{W}$  (b)  $P_{opt-1} = 1\text{ mW}$ . The corresponding Base potential gradient within the IPD structure with the optical power of (c)  $P_{opt} = 0.1\mu\text{W}$  (d)  $P_{opt} = 1\text{ mW}$ . The Emitter and the Collector are reversed biased at 0.001 V and 600 V respectively and the optical beam radius is 51  $\mu\text{m}$ .

A large photogeneration rate within the device gives rise to a large carrier density which will result in a potential gradient along the path of current flow in the Base. This problem is shown in the potential contours of figure II.63 (c) and II.63 (d); at low current densities, there is a potential well in the Base region but at a high current density the potential barrier seizes to exist at long distances from the contact due to the Base potential drop.

The evolution of the Base potential drop due to the Base current flow as a function of optical intensity is shown in figure II.64, for a short 400 nm, a medium 500 nm and a long 700 nm wavelength.

As discussed earlier, longer wavelengths are absorbed deeper in the device and contribute to the Collector-Base current, meanwhile short wavelengths that are absorbed in shallow depths don't contribute to the Collector current. The Collector region is fully depleted when the Collector is reversed biased at 600 V, thus, the Collector has a very high carrier collection efficiency. As a result, for the same intensity, longer wavelengths contribute to higher current densities and reach the critical maximum current density associated with the forward biasing of the Emitter-Base junction earlier than shorter wavelengths. The Numerical simulation results from Silvaco demonstrate this problem as shown in Emitter and Collector currents and responsivities of figure II.65 for high Collector Voltage of 600 V and a low Emitter voltage of 0.001 V. In the case of a medium optical wavelength around 500 nm, when the Collector is reversed biased at 600 V (i.e.

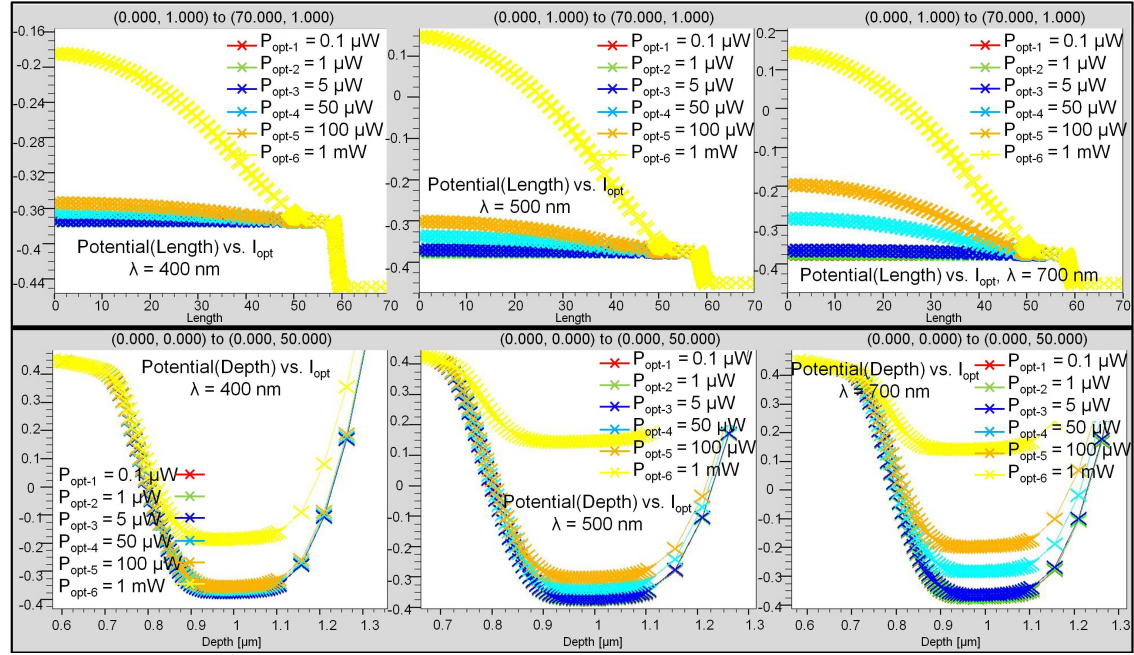


Figure II.64: The top row shows the potential gradient in the Base region along the Base current path length (length = 0  $\mu\text{m}$ , is the center of the device) as a function of the input optical intensity. The bottom row shows the lowering of the Emitter-Base potential barrier as a function of the input optical intensity at the center (the furthest point from the contacts) of the device. The Emitter is reversed biased at 1 V, the Collector is reversed biased at 600 V. The optical beam radius is fixed at 51  $\mu\text{m}$  and the optical power is varied:  $P_{opt-1} = 0.1\mu\text{W}$ ,  $P_{opt-2} = 1\mu\text{W}$ ,  $P_{opt-3} = 5\mu\text{W}$ ,  $P_{opt-4} = 50\mu\text{W}$ ,  $P_{opt-5} = 100\mu\text{W}$ ,  $P_{opt-6} = 1\text{mW}$ .

when the VD-MOSFET is ON), an optical intensity of around 9  $\text{W}/\text{cm}^2$  can activate the parasitic BJT. The Emitter and Collector currents of figure II.67 and the Base current in figure II.66 show how increasing the Emitter voltage increases the critical current density level and in turn the maximum optical intensity limit.

The results above show that for the case when the Collector is high (i.e. 600 V), the IPD has a linear relationship with the input optical intensity until the rise in the Base potential provides a current path through the parasitic BJT structure. Figure II.67 shows the Emitter and Collector currents and responsivities for the case when the Collector is low (i.e. 0.001 V).

The Emitter current is linear with respect to the input optical intensity up to around 20-50  $\text{W}/\text{cm}^2$  depending on the optical wavelength. When the Collector is biased at low voltages, the device can be operated in the linear region at higher optical intensities (roughly 3  $\times$  higher) relative to the case where the Collector is biased at high voltages; this is due to relatively lower  $I_C$  contribution levels to  $I_B$  due to the lower Collector carrier collection efficiency. Moreover, without the large Collector voltage, the Collector depletion region extension onto the Base side is thinner, leaving a wider Base width available for spreading the Base current which then leads to a lower current density. However, optical

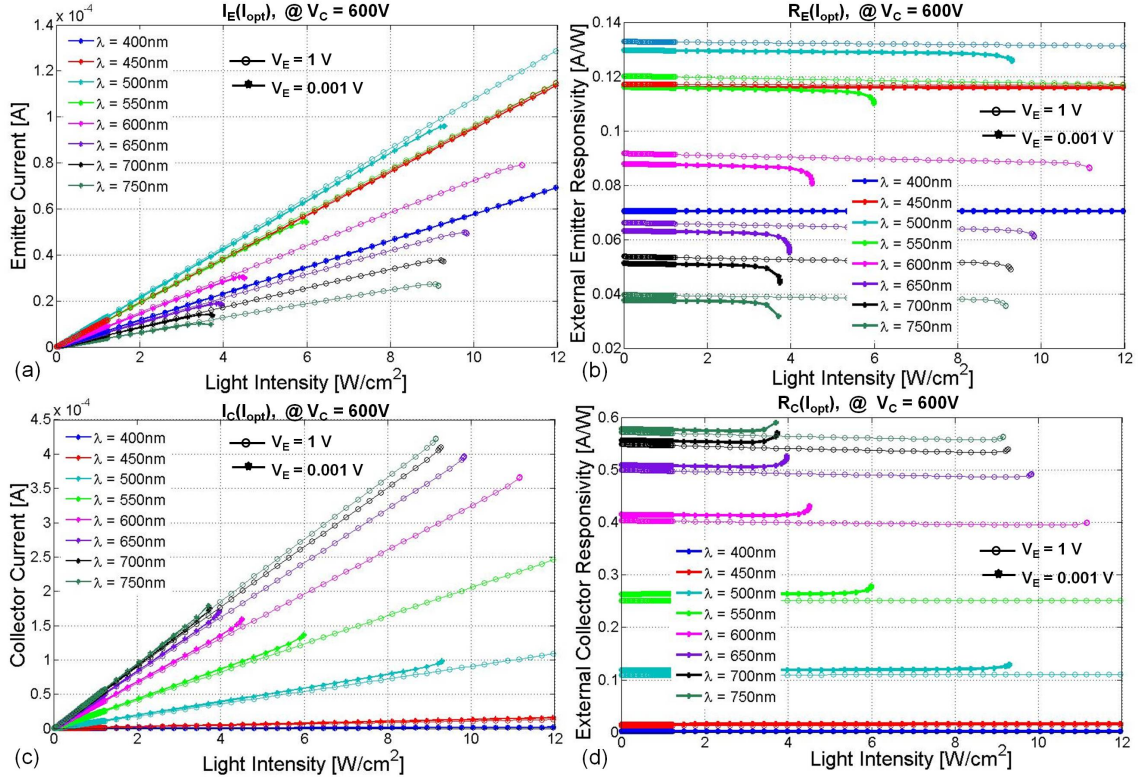


Figure II.65: IPD (a) Emitter and Collector currents and (b) their corresponding responsivities versus input optical intensity. The Emitter is reversed biased at 1 V, the Collector is reversed biased at 600 V, and the optical beam radius is 51  $\mu\text{m}$ .

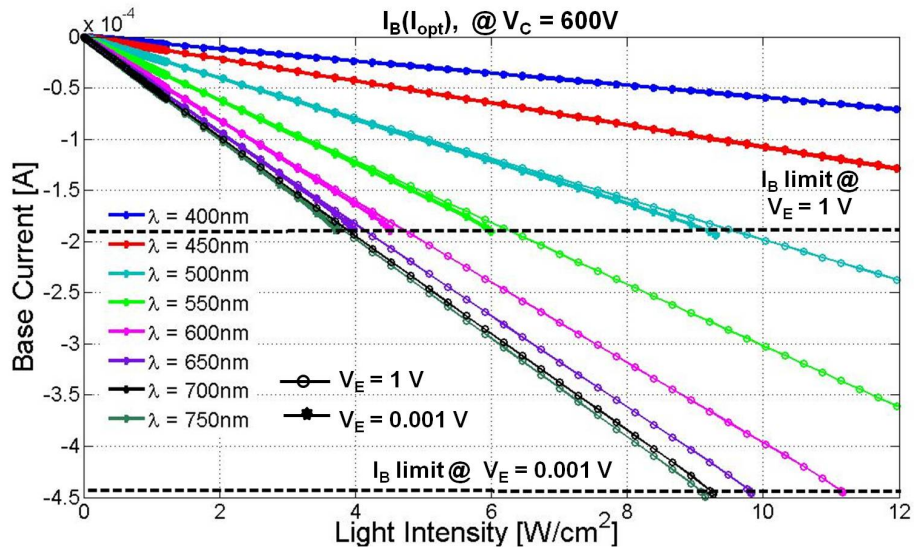


Figure II.66: IPD Base current behaviour versus input optical intensity. The dashed black lines indicate the current limit after which the Emitter-base junction becomes forward biased for the case where the Emitter is reversed biased at 0.001 V (i.e. floating Emitter) and when it is reversed biased at 1 V. The Collector is reversed biased at 600 V and the optical beam radius is fixed at 51  $\mu\text{m}$ .

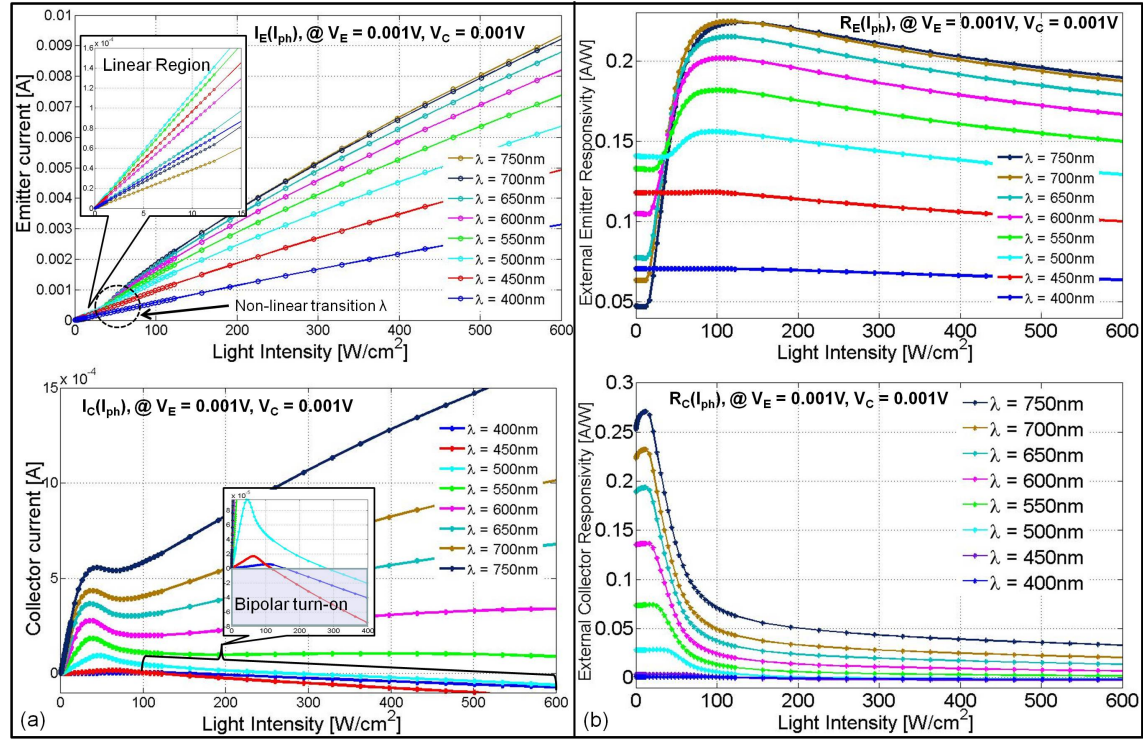


Figure II.67: IPD (a) Emitter current and (b) responsivity and the (c) Collector current and (d) responsivity versus Input optical intensity at a low collector voltage. The Emitter and the Collector are reversed biased at 0.001 V, and the optical beam radius is fixed at  $51 \mu m$ .

intensities above  $20\text{-}40 W/cm^2$  cause a non-linear transition in the IPD behaviour that allows for a temporary gain in the Emitter efficiency followed by a continuous reduction of the Emitter efficiency.

This non-linear transition can be explained by the effective widening of the Base region due to the disappearance of the Collector-Base depletion region at high charge densities associated with high current densities flowing through the Collector-Base region. With no Collector-Base depletion region, the Base current spreads out deeper into the substrate; this is depicted in the current flow lines in the IPD cross sections of figure II.68 as a function of optical intensity. Figure II.69 shows the electron and hole concentration profiles near the Collector-Base junction for a variety of input optical intensities. Figure II.70 shows the potential rise in the Base region both as a function of distance away from the device surface and as a function distance along the Base length for a variety of input optical intensities.

Approximating the optical intensity limit for a given IPD doping profile determines the minimum permitted device area that results in a linear behaviour of the device for a given optical power source. As an example, for an optical source with  $\lambda = 500$  nm and  $P_{opt} = 10 \mu W$ , our IPD linear region is limited by the BJT turn-on at an intensity around  $9 W/cm^2$ ; this implies that the smallest IPD circular design has a radius of around  $6 \mu m$ . Since the IPDs will be powered by optical sources with power levels of a few  $\mu W$ s, the

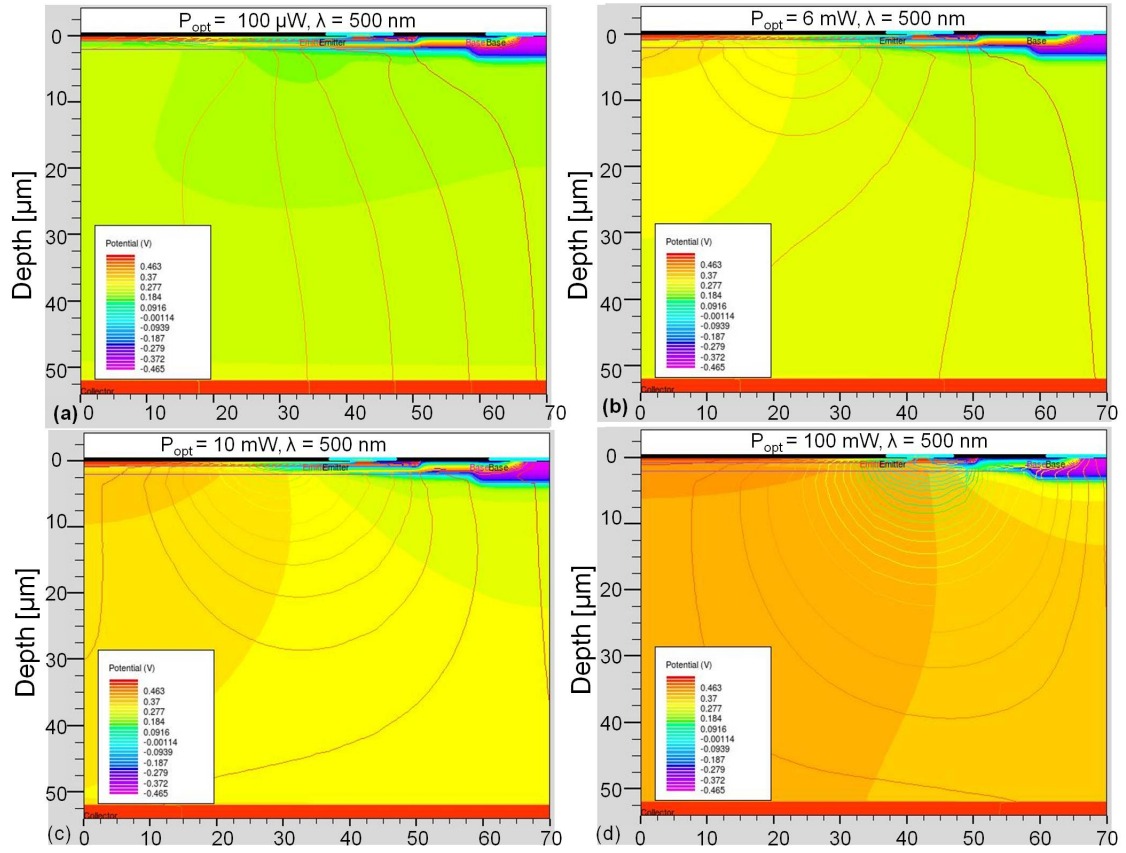


Figure II.68: Potential contours and current flow lines within the IPD structure with (a)  $P_{opt} = 100 \mu\text{W}$ , (b)  $P_{opt} = 6 \text{ mW}$ , (c)  $P_{opt} = 10 \text{ mW}$  and (d)  $P_{opt} = 100 \text{ mW}$ . The Emitter and the Collector are reversed biased at  $0.001 \text{ V}$ , the optical wavelength is  $500 \text{ nm}$  and the optical beam radius is  $51 \mu\text{m}$ .

optical activation of the parasitic BJT is far from limiting the IPD design or operation. Moreover, the IPDs will have radii above  $50 \mu\text{m}$  in order to ease the light beam alignment procedure from the optical source and/or input optical fiber. Smaller IPD designs may be considered when a suitable photonics interface is integrated in the feature; in this case the the parasitic optical activation limits may limit the IPD dimensions.

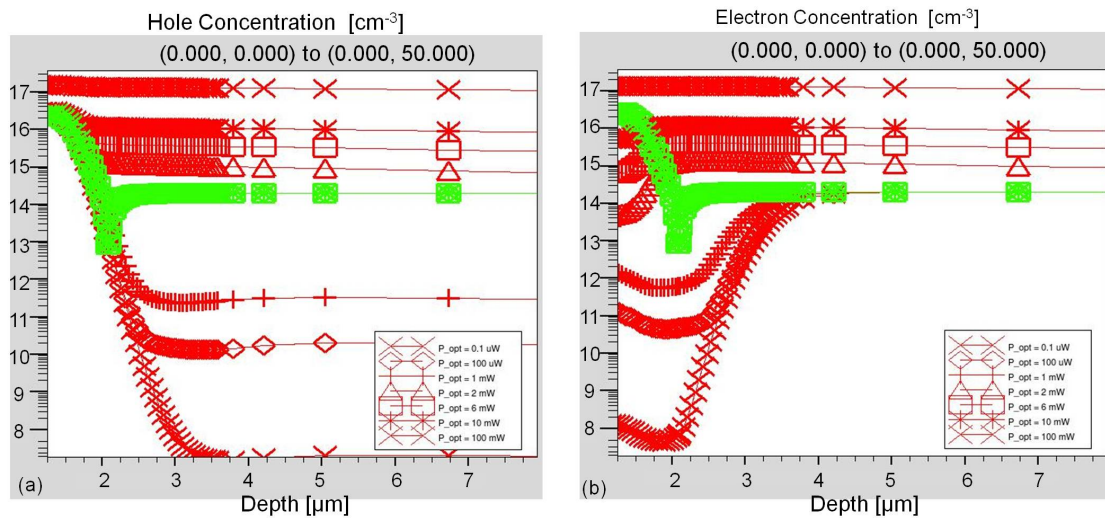


Figure II.69: (a) Electron and (b) hole concentration profiles as a function of distance from the surface of the device for different input optical intensities with  $P_{opt-1} = 0.1 \mu\text{W}$ ,  $P_{opt-2} = 100 \mu\text{W}$ ,  $P_{opt-3} = 1 \text{ mW}$ ,  $P_{opt-4} = 2 \text{ mW}$ ,  $P_{opt-5} = 6 \text{ mW}$ ,  $P_{opt-6} = 10 \text{ mW}$  and  $P_{opt-7} = 100 \text{ mW}$ . The Emitter and the Collector are reversed biased at  $0.001 \text{ V}$ , the optical wavelength is  $500 \text{ nm}$  and the optical beam radius is  $51 \mu\text{m}$ . The Green line shows the net doping density.

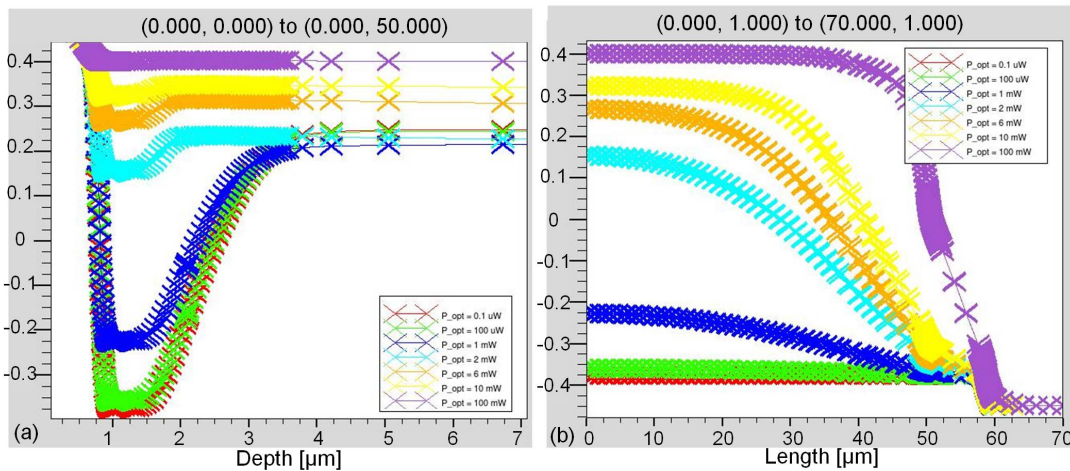


Figure II.70: (a) Potential profile as a function of depth into the device. The cutline is taken at the center of the device. (b) Potential profile as a function of distance along the length of the Base region. The cut-line is taken at a depth of  $1 \mu\text{m}$ . The potential profiles are depicted for different input optical intensities with  $P_{opt-1} = 0.1 \mu\text{W}$ ,  $P_{opt-2} = 100 \mu\text{W}$ ,  $P_{opt-3} = 1 \text{ mW}$ ,  $P_{opt-4} = 2 \text{ mW}$ ,  $P_{opt-5} = 6 \text{ mW}$ ,  $P_{opt-6} = 10 \text{ mW}$  and  $P_{opt-7} = 100 \text{ mW}$ . The Emitter and the Collector are reversed biased at  $0.001 \text{ V}$ , the optical wavelength is  $500 \text{ nm}$  and the optical beam radius is  $51 \mu\text{m}$ .

## II.8 Simulation and Modelling Conclusions and Overview

The vertical structure and doping profile of a 600 V power MOSFET was studied through analytical modelling and finite element simulations in order to demonstrate the possibility of using the Emitter-Base shallow junction as a photodetector capable of generating the electrical gating signal for the power switch. The modelling and simulations are used to illustrate the role of physical mechanisms responsible for the different phenomena within the IPD. Moreover, some of the main links between the different performance parameters, material properties, geometrical and technological parameters are demonstrated. In order to expose the potential of our proposed approach, the simulation and modelling results are analysed to answer two main questions: (1) can the IPD provide the a reliable output gating signal given the power MOSFET structure, parasitic environment, and floating substrate voltage? (2) What are the design parameter value/s and operating conditions that maximize the IPD performance in terms of QE, DC output current level, bandwidth, immunity to noise and the parasitic environment.

To answer the first question, modelling and simulation studies were performed to reveal the sensitivity of the IPD output current signal to, (1) high DC substrate voltages and (2) the input electrical (i.e. fast transient substrate voltages) and (3) optical (i.e.  $I_{opt}$ ) parameters that may activate the IPD's parasitic BJT structure.

1. The IPD output DC current as a function of input DC substrate voltages up to 600V revealed that only Emitter currents generated by wavelengths longer than UV (roughly above 430 nm) are reduced due to increasing substrate voltages as was depicted in figure II.38; this reduction in Emitter current is stronger for longer wavelengths absorbed deeper in the device and it can be as high as 20% in the IR (roughly above 750 nm) range. The high DC substrate voltages are predicted to reduce the maximum achievable QE of the device at around a 500 nm wavelength by roughly 8%. This effect is not considered problematic since for an IPD triggered by an optimal wavelength, the QE (i.e.  $> 0.1$ ) of the device is predicted to generate a current signal above 100s of nAs even after reductions due to the high substrate voltages.
2. Simulations showed that fast (i.e. 25 ns ramp) substrate voltage (i.e.  $\Delta V = 400$  V) transients result in fast current peaks in the Emitter and the Collector that forward bias the Emitter-Base junction for a short time in the range of a few ns as was depicted in figure II.60. This current peak can be reduced by increasing the ramp time, however this is not practical since the ramp times are limited by the power transistor switching requirements and thus can not be made slower. Another way to reduce the transient side effects on the IPD is to increase the Emitter voltage (i.e. avalanche mode IPD), however this needs to be investigated in order to insure that the increased noise levels are acceptable given the low output current levels of the IPD. A third possibility of dealing with the transient currents is to filter them in the signal processing stages following the IPD stage. The filtering solution should be carefully designed so that it does not significantly limit the IPD bandwidth.
3. Simulation results predict that the DC optical activation of the parasitic BJT occurs

earlier when the substrate is reversed biased at a high voltage level (i.e. 600 V); however it is far from limiting the IPD design or operation for optical powers in the range of few  $\mu\text{W}$ s and IPD radii above 10  $\mu\text{m}$ , as was depicted in figures II.65 and II.66.

Thus, according to the performed studies on the power MOSFET vertical structure, parasitic environment, and floating substrate voltage, the parasitic turn on of the BJT due to substrate transients is the only main challenge of the IPD in providing a reliable output gating signal.

To answer the second question, the IPD static and dynamic performance was modelled in Matlab and simulated in Silvaco as a function of optical wavelength, optical intensity, Emitter and Collector voltages, IPD sensitive area, shading, illuminated region, and carrier lifetimes.

The most suitable operating optical wavelength is considered to be one which maximizes the Emitter output current and the ratio of the Emitter to Collector responsivity, meanwhile, minimizes the Emitter current sensitivity to the Collector high voltages. The static study of the IPD predicted a peak responsivity of 0.2 A/W at a 500 nm optical wavelength with a 33% shading factor, when the Emitter and the Collector are reversed biased at 1V and the Silicon wafer has long carrier lifetimes of 1  $\mu\text{s}$  as was depicted in figure II.33. At 500 nm, a high DC substrate reverse voltage up to 600 V is predicted to reduce the maximum achievable responsivity of the IPD by no more than  $\sim 8\%$ . Moreover, the ratio of Emitter to Collector photocurrent is approximately 5.3 as was depicted in figure II.46(a) and a 90 MHz 3dB bandwidth is predicted according to Silvaco simulations of figure II.55. Thus, a 500 nm optical wavelength is predicted to be most suitable for the IPD structure with the same doping profile as a 600 V power MOSFET. In order to improve the efficiency of the IPD at this wavelength, the design process for an optimized ARC was also presented in this chapter which is predicted to improve the IPD efficiency by  $\sim 40\%$ .

Both the modelling and simulation results confirm that the IPD Emitter reponsivity and thus output current level improves when the Emitter junction is reversed biased at higher voltages. If the IPD is polarized in the avalanche gain (due to avalanche multiplication) operating region (i.e.  $> 15\text{V}$ ), the responsivity and the 3 dB bandwidth of the detector are predicted to increase above 0.3 A/W and 400 MHz respectively for a 500 nm optical wavelength as were presented in figures II.36 and II.55. Moreover, as presented in equations II.62 and II.60, the IPD immunity to electrical and optical activation of the parasitic BJT structure can be improved by increasing the Emitter junction reverse voltage. These results suggest that the IPD performance in terms of responsivity, bandwidth and immunity to parasitic turn-ons are improved when the device is polarized in avalanche mode. However, the avalanche multiplication mechanism amplifies the Emitter signal current, the dark current and the background currents indiscriminately. Thus, it is important that the IPD dark current level is kept as low as possible in order not to limit the minimum detectable optical power. Since the avalanche gain comes with a price of noise, noise

analysis and temperature analysis are required for a complete investigation of the most suitable biasing condition for the IPD.

Sensitivity studies of the IPD responsivity to the carrier lifetime parameters revealed that the Emitter responsivity is not sensitive to electron lifetimes and it starts to suffer for hole lifetimes shorter than 10ns as it was depicted in figure II.42. As it was discussed, carrier lifetime values not only present a compromise between the responsivity and the bandwidth of the IPD but they also impact the vertical bipolar diode in the power MOS-FET structure.

The study of the optical beam radius for a fixed detector size and a fixed contact position and a uniform optical beam source, confirmed the theoretical prediction that absorptions in the Base region contribute to the collector current rather than the Emitter current. Moreover, small optical beam radii and small IPD Emitter radii are both predicted to improve the IPD bandwidth as were presented in figures II.57 and II.52. The reduction in efficiency due to contact shadowing was also observed in results of figure II.56.

There are a number of different investigations via modelling and simulation that can be done in the near future in order to add to and improve on the current conclusions and predictions. Temperature and noise analysis are perhaps the two main areas in need of investigation. Moreover, the effect of contact positioning and Gaussian optical beams on the IPD performance should also be investigated.



## Chapter III

---

# IPD Fabrication and Characterization

### SOMMAIRE

---

III.1 INTRODUCTION . . . . .	120
III.2 VD-MOSFET PLANAR FABRICATION PROCESS OVERVIEW . . . . .	121
III.3 POWER BIPOLAR IPD FABRICATION PROCESS . . . . .	123
III.4 IPD MASK LAYOUT DESIGNS . . . . .	126
III.5 FABRICATION RESULTS . . . . .	133
III.6 DC CHARACTERIZATION: SETUP AND MEASUREMENT APPROACH . . . . .	138
III.6.a First Approach: LED Light Sources . . . . .	138
III.6.b Second Approach: Xenon Light Source . . . . .	142
III.6.c MEASUREMENT RESULTS . . . . .	147
III.7 AC CHARACTERIZATION: SETUP AND MEASUREMENT APPROACH . . . . .	151
III.7.a First Approach: Externally modulated LED Optical Source . . . . .	151
III.7.b Second Approach: Externally modulated Laser . . . . .	152
III.7.c Third Approach: Directly modulated Laser . . . . .	154
III.8 SUMMARY . . . . .	156

---

### Abstract

*Having introduced the integration approach and objectives along side the simulation and modelling analysis of the power MOSFET compatible integrated photodetector (IPD) design, in this chapter we will introduce the fabrication, electrical and optical characterization approaches, challenges, procedures and results used for the proposed IPDs.*

### III.1 Introduction

The power bipolar and VDMOSFET fabrication procedures are being continually investigated and have been used in previous projects at G2ELab. Most of the process steps have been developed over time during previous projects at G2ELab and many of the required recipes are available at the CIME Nanotech/Minattec cleanroom facilities. In the case of the IPDs, the fabrication process needs to also accommodate an additional dielectric layer for the anti reflective coating (ARC) which is not part of the power bipolar or VDMOSFET fabrication. Since the IPDs will not be fabricated via standard manufacturers, no standard design rule check (DRC) files are available. Thus, a DRC tailored for the IPD masks is developed in consideration of the equipments available at the CIME cleanroom facilities as well as the IPD designs. Meanwhile, some IPD dimensions are chosen to push beyond the DRC safety margins in order to test the fabrication boundaries and potentially achieve higher performance IPDs. Overall 8 masks are designed in Cadence Virtuoso, associated with custom techfiles. The fabrication process, mask designs and results are presented in detail in the following three sections.

A full investigation of the IPD performance demands the investigation of the static and dynamic responses of the device to electrical and optical input signals as a function of optical wavelength, Emitter and Collector biasing conditions, optical power, temperature, geometry and design. The specific characterization objectives are, to identify:

- the range of achievable IPD QE using the VDMOSFET fabrication process,
- the IPD QE as a function of optical wavelength in order to find the most suitable operating wavelength,
- the IPD QE as a function of Emitter voltages. The IPD performance at low voltages versus in avalanche gain mode need to be compared and studied in order to find the most suitable IPD operating condition; as it was uncovered in Chapter 2, the IPD QE increases for increasing  $V_E$ , meanwhile the IPD dark current levels (which determine the minimum required optical power and noise levels), the optical parasitic turn-on (not significant) and the IPD immunity level to substrate transients are also functions of  $V_E$ . Moreover, QE shifts in the optical wavelength domain depending on  $V_E$  should be quantified.
- the IPD QE dependence on the substrate should be quantified in order to verify the effect of the VDMOSFET floating voltages on the IPD performance.
- the IPD design(s) that maximize the device QE
- the IPD QE as a function of optical intensity in order to locate the IPD's linear operating range,
- the IPD dark current level in order to determine the minimum required optical power
- the range of achievable IPD rise times and bandwidths using the VDMOSFET fabrication process,

- the IPD bandwidth as a function of optical wavelength in order to find the most suitable operating wavelength in terms of frequency response,
- the IPD bandwidth as a function of small signal peak-to-peak optical power in order to verify the linearity of the design
- the IPD bandwidth as a function of  $V_E$  in order to identify the suitable Emitter biasing condition for the device
- the IPD design(s) that maximize the device Bandwidth
- the IPD design(s) with the best QE, rise time, bandwidth and noise immunity compromise
- the temperature effects on the IPD performance and specially on the noise level. The temperature can also shift the QE peak along the optical wavelength spectrum due to ARC refractive index dependencies on the temperature.

Achieving the above characterization objectives requires the development of DC and AC experimental setups that offer accuracy, repeatability and a wide range of tunable inputs such as optical DC power levels, optical wavelengths (including visible range), AC optical signals (square and sine waveforms for step and frequency response analysis), voltages (DC and transient) and temperatures. The different challenges and approaches taken in constructing the DC and AC experimental setups are introduced in this chapter and the IPD characterization results are discussed. IPDs with responsivity of 0.2 A/W and 3-dB bandwidth in 10s of MHz have been measured.

## III.2 VD-MOSFET Planar Fabrication Process Overview

Figure III.1 shows the VD-MOSFET and the U-MOSFET basic cell structures which are the more prevalent structures amongst the vertical power MOSFET devices [7]. The U-MOSFET benefits from lower internal resistance compared to the VD-MOSFET structure due to the elimination of the parasitic junction gate field-effect transistor (JFET) region; however, the UMOS fabrication process requires additional complex fabrication steps (i.e. reactive-ion etching (RIE)) for the gate formation inside the U-trench.

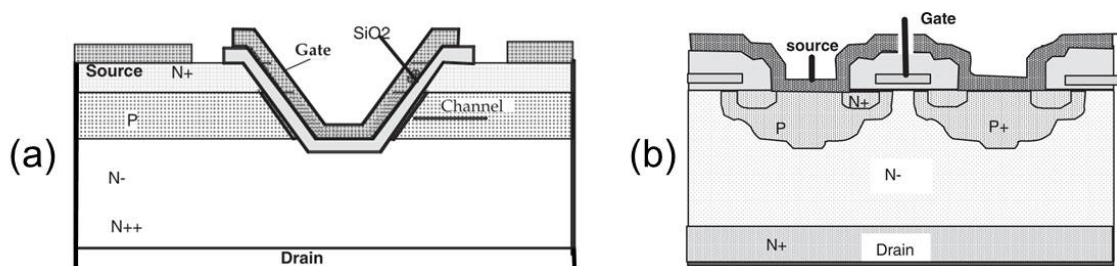


Figure III.1: Cross sectional view of the (a) VUMOS and (b) VDMOS Structures.

The VD-MOSFET fabrication process starts by a N+ doped substrate which forms the drain over which a lightly N<sub>v</sub> (or N- as depicted in figure III.1) doped epitaxial layer is grown to form the drift region as depicted in figure III.2(1). The thickness and doping level of this drift region determine the trade-off between the on-resistance and the breakdown voltage of the device [7].

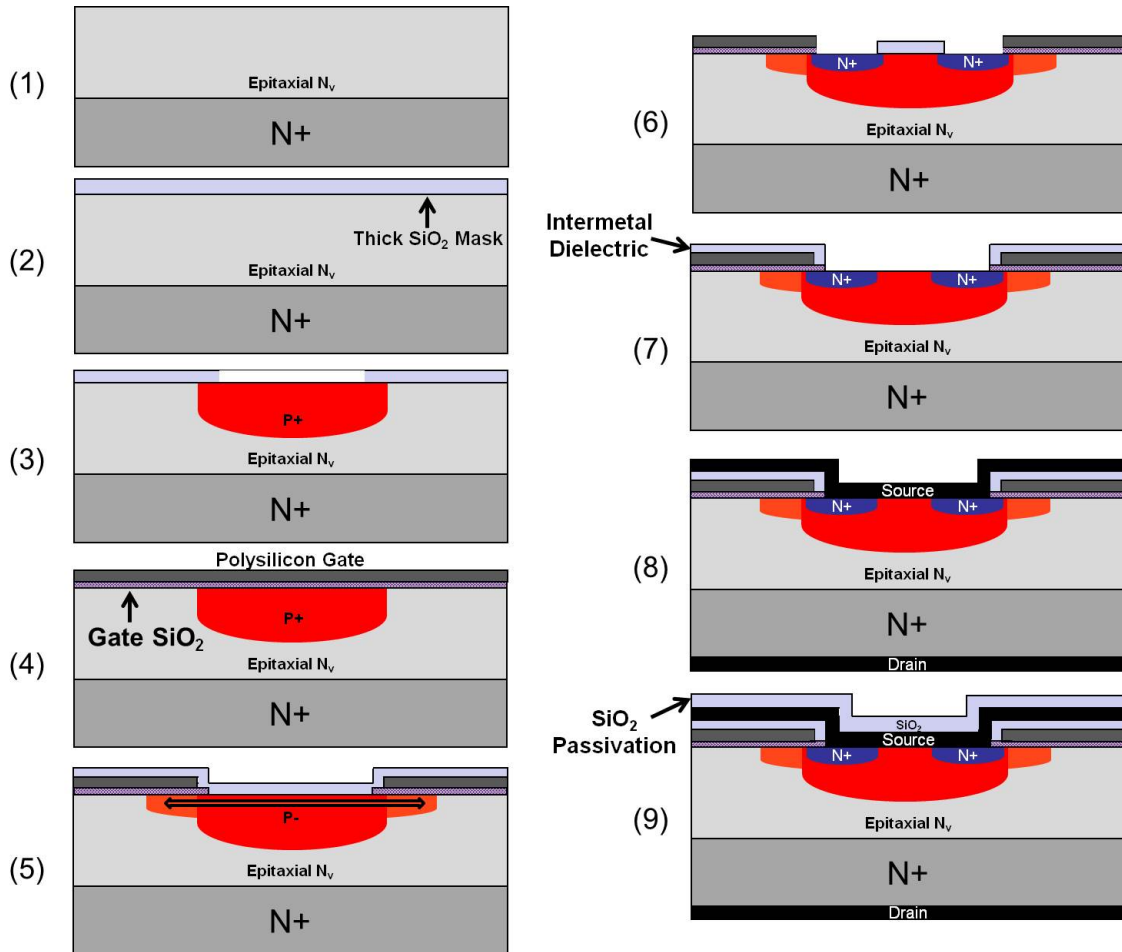


Figure III.2: VD-MOSFET Planar Fabrication Process Flow. Only the major process steps are shown here. Although it is not shown here, the devices are typically fabricated within either guard rings or deep RIE trenches which provide the field termination/junction edge termination required for high voltage operation.

A thick oxide mask is deposited (figure III.2(2)) and etched to create an opening for the first implantation which forms the P+ region (Litho.1: PPLUS) (figure III.2(3)). This P+ region provides an area over which an ohmic contact is formed to short the Channel and Source regions; thus the minimum doping level of the P+ Source region is limited by the ohmic contact criteria.

Before the start of the gate process, all the oxide used for the P+ Mask is etched away except the alignment marks (Litho.2: OZUT). The gate process starts by a thickness controlled growth of a thin SiO<sub>2</sub> layer over which the gate polysilicon is deposited by Low-Pressure Chemical Vapour Deposition (LPCVD) (figure III.2(4)). Then polysilicon and the gate oxide are etched to create an opening for the cells (Litho.3: POLY).

A second implementation/diffusion round forms the P- region (figure III.2(5)); the MOS channel is defined by the diffusion of the P- dopants under the gate during the implant activation stage (self-aligned process). A second thick oxide mask is deposited and opened in preparation for the N+ source implantation (figure III.2(6)). Note that instead of an oxide mask, photoresist masks are also available (Litho.4: NPLUS).

Before the contacts can be formed, an intermetal layer is deposited in order to isolate the gate from the source III.2(7)). This intermetal layer must provide a reliable step coverage over the gate surface and edges. Any defects in the intermetal layer near the polysilicon gate, could result in a short between the gate and the source.

After opening the intermetal layer (Litho.5: OCON), the metal contacts are then deposited III.2(8)) and contact pads are opened (Litho.6: MET1), after which, one final oxide deposition is done to passivate the device III.2(9)).

Overall, there are 5 masks required plus 2 additional masks: one for the edge termination (Litho.7: DRIE) of the devices and a second for defining windows in the passivation oxide layer (Litho.8: MET2) for the wire bonds of the gate and source [7]. It should be added that every doping implantation is followed by a drive stage, moreover, contacts are usually annealed (Rapid thermal annealing, RTA) for improved quality. Process variations can slightly change the number of steps or mask levels.

### III.3 Power Bipolar IPD Fabrication Process

Figure III.3 shows the power bipolar IPD fabrication process flow, and table III.1 lists the bipolar IPD process details and specifications. The numbers used in figure III.3 correspond to the fabrication process labels listed in table III.1. In table III.1, positive and negative photoresists are abbreviated as +PR and -PR respectively. All wet etching of oxide and nitride layers is done in Buffered oxide etch (BOE) baths. The Aluminum wet etching is carried out in a Phosphoric acid ( $H_3PO_4$ ) based bath. The P+ and P- implantations use 800 nm thick oxide hard masks; the N+ implantation uses a -PR mask.

In order to first prove the proposed concept and speed up the fabrication process due to time limitations, the IPDs are fabricated via the power bipolar process without the VDMOSFET polysilicon gate deposition. In total, eight masks are designed for the bipolar IPD process PPLUS, PMNS, OZUT, NPLUS, ARC, OCON, MET1 and DRIE as listed in table III.1. Comparing this with the masks required for the VDMOSFET, PPLUS, OZUT, POLY, NPLUS, OCON, MET1, DRIE, and MET2 (as it was explained in section III.1), reveals two differences:

1. In the VDMOSFET process a PMNS mask is not required since the P- region is self-aligned with the gate as it was explained earlier in section III.1. However, a POLY gate is required for defining the gate region which is not required in the bipolar IPD process. In the bipolar IPD case, the same oxide mask used for the creation of the P+ zone is used for the P- implantation meanwhile a PMNS mask is designed for creating the openings through the oxide. This is depicted in steps 1.7 and 2.4 of figure III.3 and explained in table III.1.

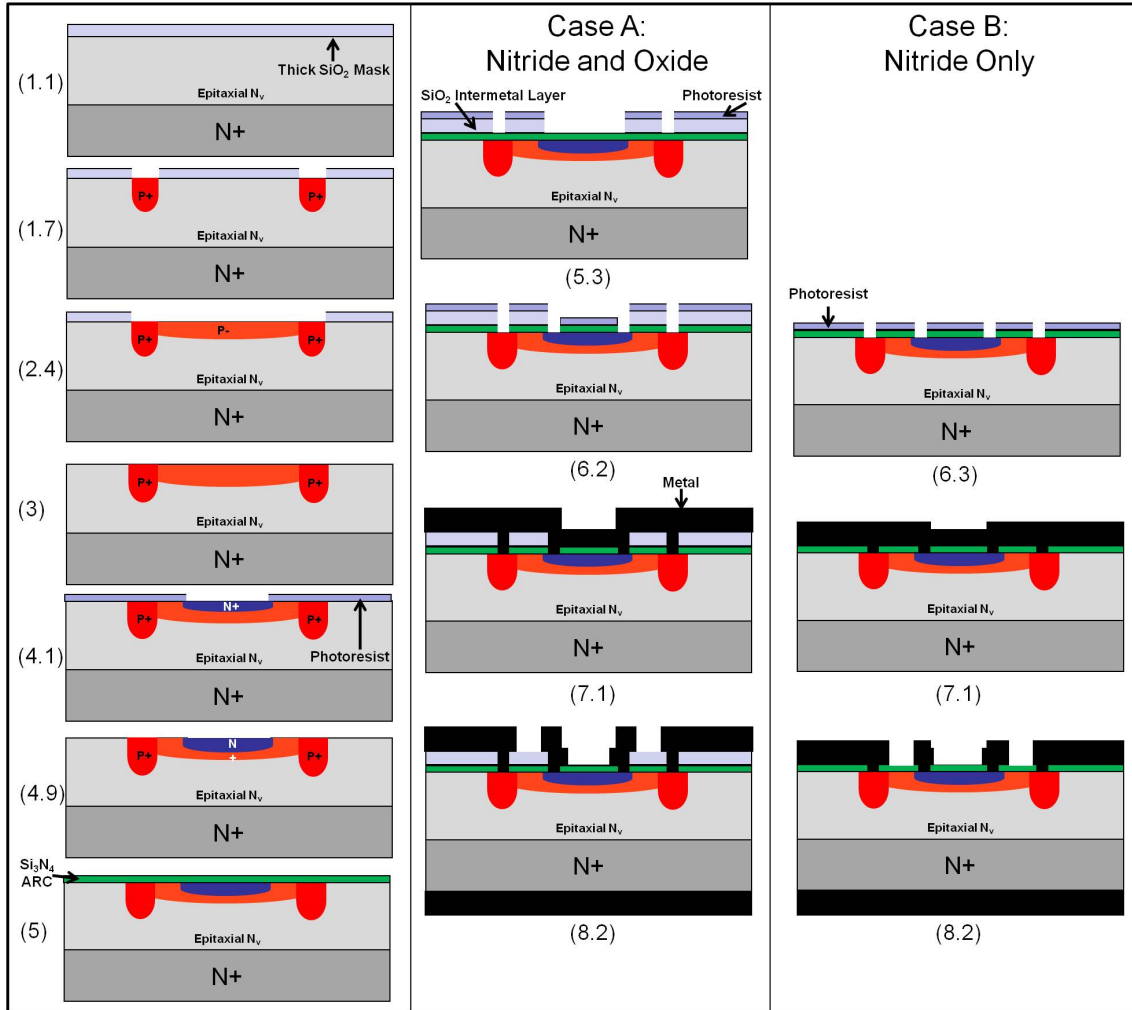


Figure III.3: Bipolar IPD process flow. The left column is followed either by the middle column or the far right column depending on the type of process flow chosen. For a process flow with 2 dielectric layers, Case A follows the left column. For a process flow with 1 dielectric layer dielectric Case B follows the left column.

2. A second etch mask in addition to the OCON mask is required required for defining an optimized ARC for the IPD, namely the ARC mask. This ARC mask needs to be added to the VDMOSFET process.

Using all the bipolar IPD (i.e. eight) Masks allows for depositing two different dielectric materials as depicted in figure III.3 Case A; one material (i.e.  $\text{Si}_3\text{N}_4$ ) could be used to optimize an ARC layer for the optically sensitive surface, meanwhile, a second material (i.e.  $\text{SiO}_2$ ) could be used to provide electrical isolation between the junction edges and the metal contacts and to also reduce the optical transmissions in unwanted regions such as the Base region. This would be an option to separate the constraints of the VDMOS ( $\text{SiO}_2$  CVD) from the ARC (thin SiN).  $\text{Si}_3\text{N}_4$  has a dielectric field strength of roughly  $10^7$  V/cm; for a 60–80 nm thick nitride layer (optimized for the ARC at wavelengths near 500 nm), a  $\approx 2 \times 10^6$  V/cm field is created in the nitride layer when a 15 V potential difference appears

#	Mask	Key Steps	Min. Dimensions
1	PPLUS	Clean and etch backside LTO	10 [ $\mu\text{m}$ ]
1.1		Hard Mask deposition: 800nm-SiO <sup>2</sup>	
1.2		Organic cleaning (Piranha solution)	
1.3		1 <sup>st</sup> Lithography (+ PR)	
1.4		Wet etch in BOE at 33°, PR removal	
1.5		Boron implantation	
1.6		Organic Cleaning (Piranha solution)	
1.7		Annealing	
2	PMNS	2 <sup>nd</sup> Lithography (+ PR)	10 [ $\mu\text{m}$ ]
2.1		Wet etch, PR removal	
2.2		Boron implantation	
2.3		Organic Cleaning (Piranha solution)	
2.4		Annealing	
3	OZUT	3 <sup>rd</sup> Lithography (+ PR)	
3.1		Wet etch all except Alignments, PR removal	
4	NPLUS	4 <sup>th</sup> Lithography (- PR)	10 [ $\mu\text{m}$ ]
4.1		Arsenic implantation	
4.2		PR stripping in RIE	
4.3		Organic Cleaning (Piranha solution)	
4.4		Deposit FrontSide Protection PR	
4.5		Backside pre-etch	
4.6		Backside Arsenic implantation	
4.7		Remove FrontSide PR	
4.8		Organic Cleaning (Piranha solution)	
4.9		Annealing	
5	ARC	Deposit Si <sub>3</sub> N <sub>4</sub> (60-80 nm)	
5.1		Deposit Si <sub>2</sub> O <sub>2</sub>	[SKIPPED]
5.2		5 <sup>th</sup> Lithography (+ PR)	[SKIPPED]
5.3		Etch Oxide	[SKIPPED]
6	OCON	Clean	4 [ $\mu\text{m}$ ]
6.1		6 <sup>th</sup> Lithography (+ PR)	
6.2		Wet etch, PR removal	
7	MET1	Clean	10 [ $\mu\text{m}$ ]
7.1		Aluminium Deposition	
7.2		7 <sup>th</sup> Lithography (- PR)	
7.3		Aluminium Etch	
7.4		PR removal	
7.5		Deposit FrontSide Protection PR	
7.6		Backside Metal (Plasma Ar,10nmTi, 1 $\mu\text{m}$ -Alu, 300nm-TiN)	
7.7		Remove Protection PR and Anneal	
8	DRIE	8 <sup>th</sup> Lithography (+ PR)	
8.1		Process etch Si TP CIME 40 cycles	
8.2		Remove PR	

Table III.1: Bipolar IPD process details and specifications

across it. Since  $2 \times 10^6 \text{ V/cm} < 10^7 \text{ V/cm}$ , it is possible to use only 7 masks (skipping Mask 5), in which case a single  $\text{Si}_3\text{N}_4$  dielectric layer is used as ARC and for junction to metal insulation. Thus, to further simplify the process, the devices are fabricated using seven masks only (by skipping Mask 5) in this fabrication run as depicted in figure III.3 Case B. The IPD structures are not affected in anyway by this process simplification and the substrate high voltage (DC and AC) effects can still be characterized.

### III.4 IPD Mask Layout Designs

As discussed in the previous sections, 8 physical masks are required for the IPD fabrication. These masks are designed in Cadence Virtuoso where each layer is represented by a different color. Designing 8, 5" masks demands a lot of effort and care specially if all the masks are drawn manually and since they can't be tested before fabrication. The amount of effort in completing this task was reduced via adapting the parametrized cell (p-cell) approach available in Cadence. The use of p-cells, permits the change of features by modifying parameters; in this manner, complicated designs are broken into smaller building blocks and different designs are made via modifying instances of other designs. Curved features such as circles, required special attention since they are ultimately approximated by polygons in the final output file and thus may not appear as intended in the design. The resolution of circular shapes are improved by increasing the number of points in the polygons.

Alignment marks are included on the masks to insure that the different layers line up properly. Figure III.4 shows the type of alignment marks included on the mask.

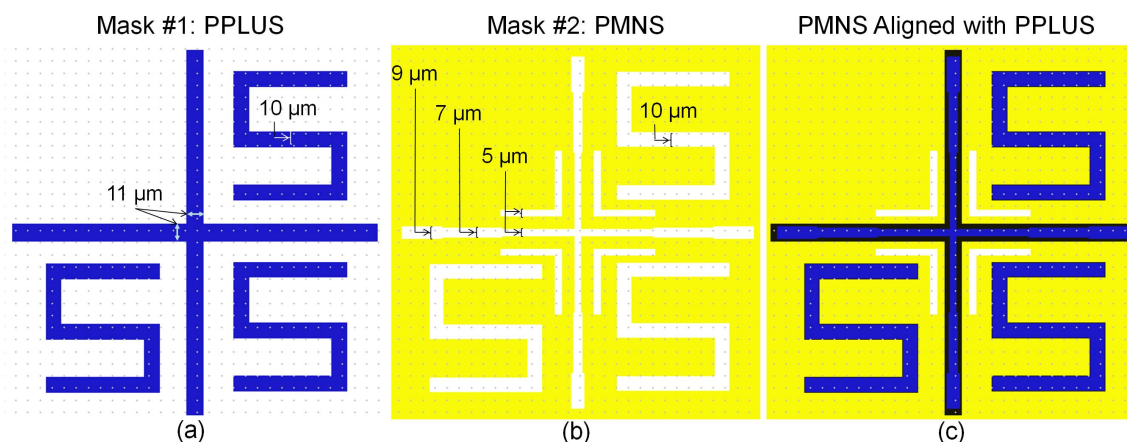


Figure III.4: Alignment process summary allowing optical alignment with a  $1 \mu\text{m}$  accuracy. The change in color from blue to black in the above pictures is due to the overlap of the different layers. The white regions in the above layout pictures represent optical windows on the physical masks. These large optical windows help the user in locating the alignment marks. The long straight lines on top of the alignment region are used for rough alignment.

The number in figure III.4 (a) corresponds to the Mask number (i.e. PPLUS) and this pattern will be transferred onto the wafer when that mask is used. When performing

the next lithography (i.e. PMNS), the cross alignment feature on the mask as depicted in figure III.4 (b), will be aligned to the alignment number that was already printed onto the substrate. To aid the visual observation during alignment, the cross alignment mark in figure III.4 (b) features 3 different regions with widths  $9\ \mu\text{m}$ ,  $7\ \mu\text{m}$  and  $5\ \mu\text{m}$ . Aligning this mark inside the  $11\ \mu\text{m}$  wide cross of figure III.4 (a) provides the user with three different accuracy levels:  $\pm 3\ \mu\text{m}$ ,  $\pm 2\ \mu\text{m}$  and  $\pm 1\ \mu\text{m}$ . The  $\pm 1\ \mu\text{m}$  is achieved when the  $9\ \mu\text{m}$  wide region from the alignment mark in III.4 (b) is perfectly centered within the the  $11\ \mu\text{m}$  wide cross of figure III.4 (a). Similarly, all the different layers are aligned; it should be noted that alignment errors add up with the number of lithography processes. Figure III.5 summarizes the alignment process for processing the 8 layers required for the IPD fabrication. As illustrated by figure III.5, the layers PMNS, NPLUS and ARC are always aligned with the PPLUS layer; this choice of alignment is both relevant for these layers as well as it reduces the additive misalignment error since PPLUS is the first lithography processed. The MET1 layer is aligned with OCON and the DRIE layer is aligned with MET1 layer since these layers have critical misalignment tolerances originating from the IPD designs. As discussed earlier, the masks offer a choice between processing one dielectric or two dielectric layers. In the case of processing two dielectric layers, OCON is aligned with ARC; however for a one dielectric layer OCON is aligned with PPLUS since in this case the ARC layer is not processed as demonstrated in figure III.5. Note that as presented in table III.1, all layers are processed with +PR, except for NPLUS and MET1 which are processed with -PR; the type of PR used does not require the inversion of alignment marks, meanwhile, all other designs on the mask are impacted by the choice of PR.

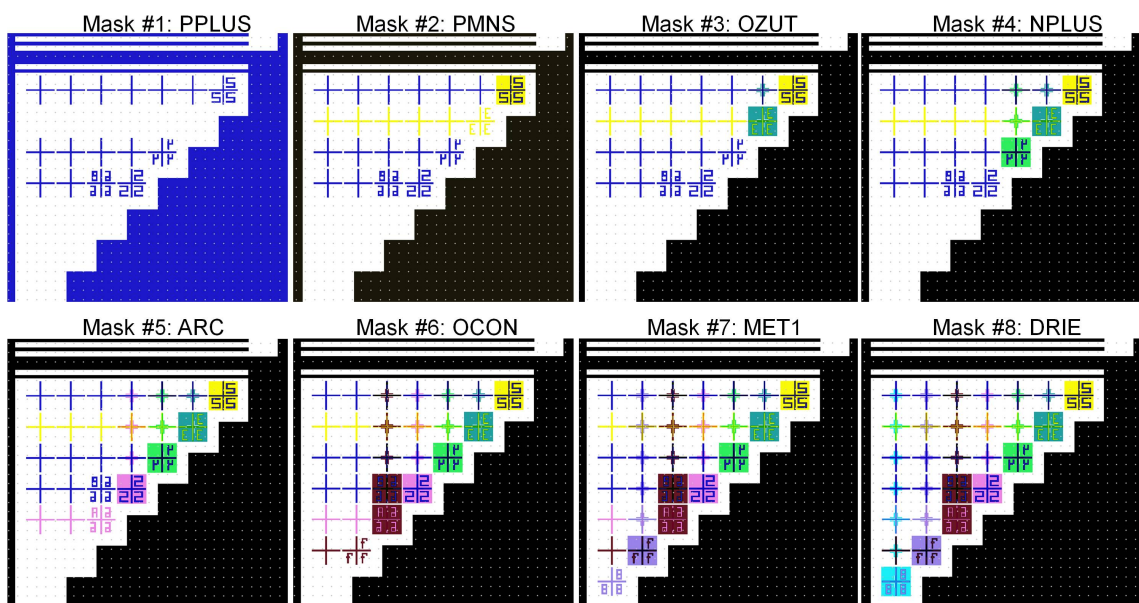


Figure III.5: Mask Alignment Marks. The top left picture corresponds to mask #1 only. Moving from left to right, each picture shows the overlap of all preceding masks, i.e. the top right corner shows the overlap of masks#1, #2, #3 and #4.

Figure III.6 shows the metal layer (Mask 8) layout in Cadence of the entire mask. The

mask includes a total of 289, 5mm  $\times$  5mm dies. The alignment marks are located at c05r09 and c13r09 where, c is the column and r is the row. The different types of designs included on the mask can be divided into 9 general categories: alignment marks, test structures, SRP structures, vertical power diodes, vertical power bipolar junction transistors (BJT), flip-chip integration dies, high voltage IPDs with DRIE termination, high voltage IPDs with guard ring termination and low voltage IPDs. These 9 different categories are color coded on the mask layout view of figure III.6.

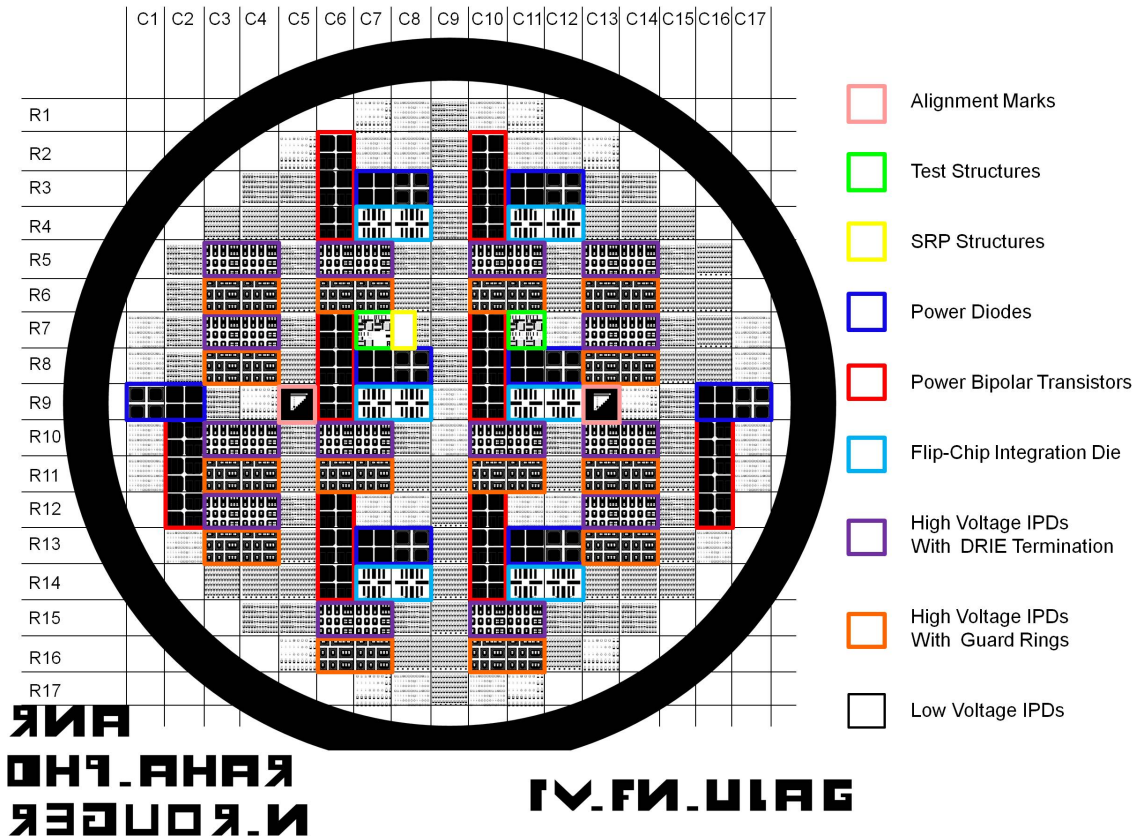


Figure III.6: MET1 mask layout where the dark field represents the MET1 regions.

The wafer includes different test modules such as contact chains, transfer length method (TLMs) structures and SRP pads for process control. Contact chain test modules as demonstrated in figure III.7 contain a large number of contacts where the total resistance between any contacts includes the semiconductor resistance, metal resistance and the contact resistance. The total contact resistance for one chain can be calculated by subtracting the semiconductor resistance from the total resistance; dividing the total contact resistance by twice the number of contacts gives the contact resistance per contact. The total resistance for a chain of  $N$  islands with sheet resistance  $R_{sh}$ , and  $2N$  contacts with contact width  $W$  and separation  $d$  is calculated as follows [103]:

$$R_T = N \frac{R_{sh}d}{W} + 2NR_c \quad (III.1)$$

where the metal resistance is assumed to be insignificant. In a second approach, TLM

structures as depicted in figure III.7, can be used for a full characterization of contact resistance, specific contact resistivity and sheet resistance. In the TLM approach, the total resistance between neighbouring TLM contacts placed at varying distances  $d$  is measured and plotted as a function of  $d$ . The slope of this plot gives the sheet resistance as long as the TLM width  $Z$  is known. The intercept of the plot at  $d = 0$ , gives the total contact resistance  $2R_c$  [103]. Figure III.7 (a) shows the MET1 layout of the N+/P+ test modules designed for characterizing the N+ contact and sheet resistances for N+ doped regions sitting on top of P+ doped regions. Similar to the N+/P+ case, test modules are designed for characterizing contact and sheet resistances of N+ regions on top of P- regions, and for characterising the P+ contact and sheet resistances. These test modules are located on dies c07r07 and c11r07.

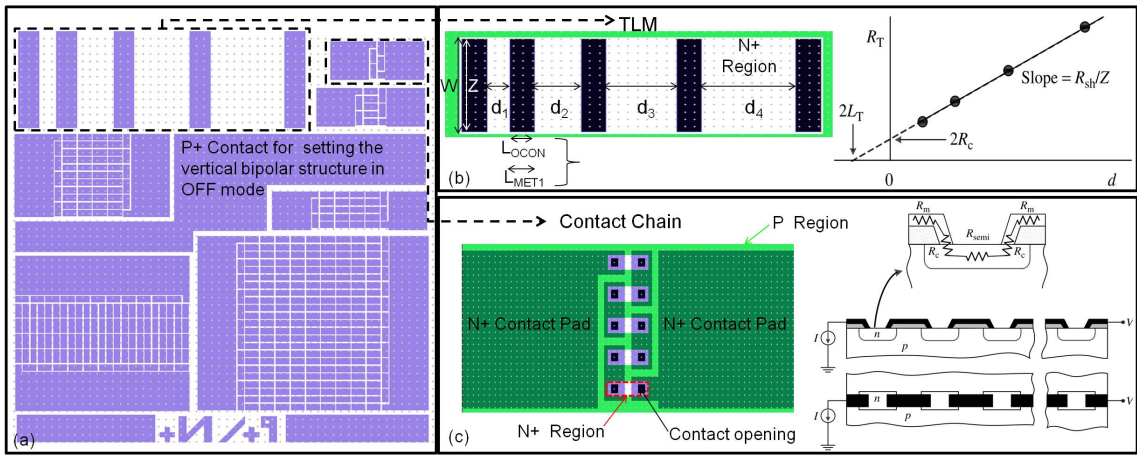


Figure III.7: Test Modules. (a) MET1 layout of the test modules designed for characterizing the N+ contact and sheet resistances for N+ doped regions sitting on top of P+ doped regions. (b) TLM test structures for extracting sheet resistances. In our design  $d_1 = 100\mu\text{m}$ ,  $d_2 = 200\mu\text{m}$ ,  $d_3 = 300\mu\text{m}$ ,  $d_4 = 400\mu\text{m}$ ,  $Z = 500\mu\text{m}$ ,  $W = 530\mu\text{m}$ ,  $L_{OCON} = 100\mu\text{m}$  and  $L_{MET1} = 106\mu\text{m}$ . The overlap of the following mask are shown here: NPLUS, OCON, MET1. (c) Daisy chains test structures for extracting contact resistances. The overlap of the following mask are shown here: NPLUS, OCON, MET1. The black and white diagrams to the right side are from [103].

Previously designed 600V p-n power diodes and n-p-n bipolar power transistors including guard rings and DRIE trench designs were included on the mask in order to verify the fabrication and design process using simpler designs [104] [105] [106]. Figure III.8 shows some example MET1 layouts views of these power bipolar transistors and diodes. Guard rings and DRIE trenches are amongst several existing edge termination methods. It is known that the electric field in power devices peaks at the device edges relative to the electric field within the bulk of the device; this phenomenon reduces the breakdown voltage of the power device if appropriate edge termination is not implemented [5].

A number of different IPDs were designed and included on the mask within guard rings or DRIE trenches for high voltage capabilities. Most of the IPD designs included on the mask are without high voltage termination techniques in order to test the IPD low voltage

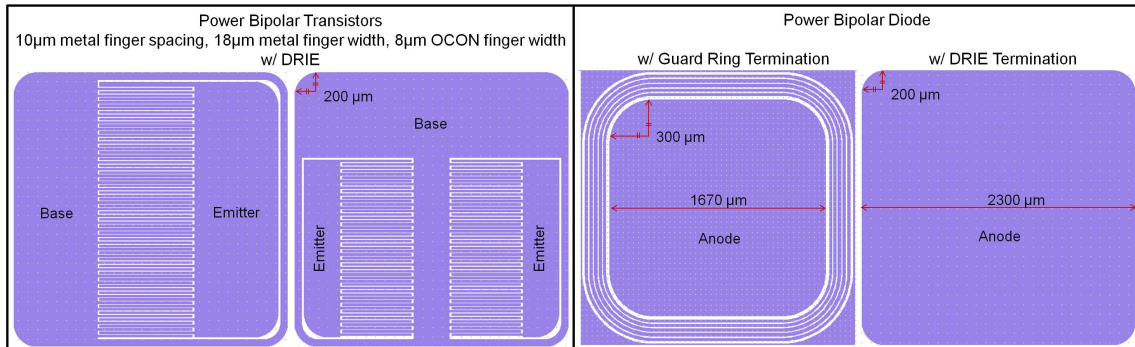


Figure III.8: Power bipolar Transistors and power diodes. Only the MET1 layer is depicted.

performance. Moreover IPDs were arranged in groups of four on a single die with large access pads in anticipation for flip-chip integration techniques (i.e. columns 7, 8, 10, 11 and rows 9, 14). The flip-chip integration die design included 4 additional input/output contacts pads and it is depicted in figure III.9. In such cases, a CMOS transimpedance (TIA) circuit would be assembled as close as possible to the detectors in a flip chip assembly, minimizing electrical parasitics.

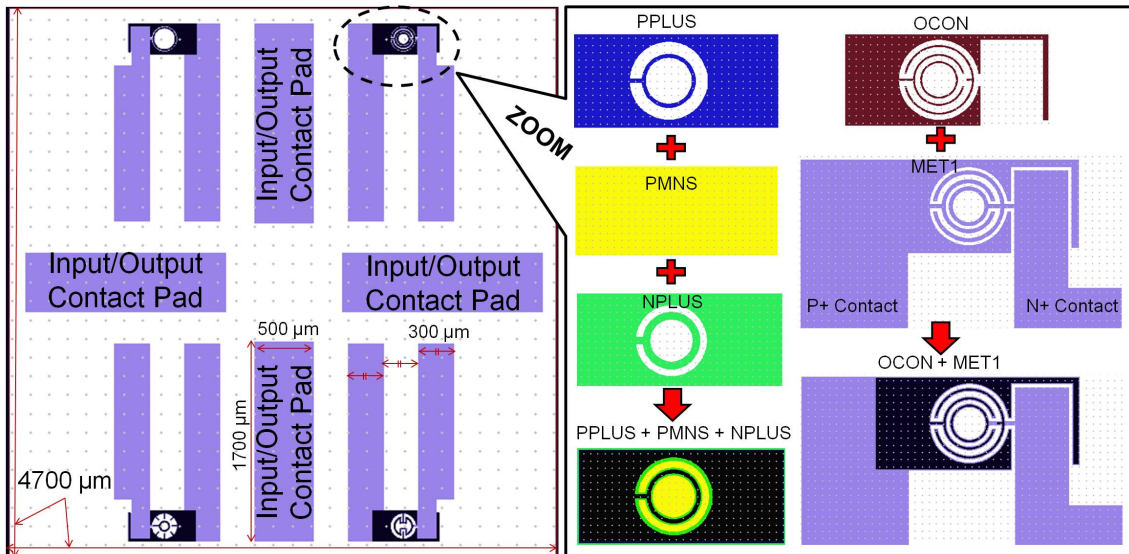


Figure III.9: Flip-Chip Integration Die Layout. 4 IPDs are included in one flip-chip die.

All IPDs include an optimized anti-reflective coating suitable for optical wavelengths near 500 nm. The most basic design is shown in the Cadence layout photo of figure III.10 and is labelled D3a. The cross sectional views in figure III.10, illustrate the cross section of IPD D3a for a P+ and a P- Base region. Devices with P- base region may offer a higher QE and a higher bandwidth due to a wider  $W_D$  and thus a lower  $C_j$  when compared to P+ base devices. In addition, devices are designed with a P+ Base region (i.e. P+/N+ Emitter junction) in order to minimize series resistances specially for larger designs and to improve the IPD tolerance to the parasitic bipolar turn-on constraints. Some of the IPD designs have been repeated for 3 different Emitter radii: 100  $\mu\text{m}$ , 50  $\mu\text{m}$  and 25  $\mu\text{m}$  in

order to study the effect of device size on the bandwidth, responsivity, and the limitations such as the parasitic constraints and optical intensity levels.

When high voltages are applied on the backside contact, a large electric field is spread out through out the lightly doped  $N_v$  region of the device between the Base and the Collector. Since there are multiple devices included on the same die and each device has a finite area, the devices require special edge terminations to reduce the electric field at the device periphery. Figure III.11 shows a cross sectional view of two IPDs (i.e. D3a) with DRIE trenches for edge termination.

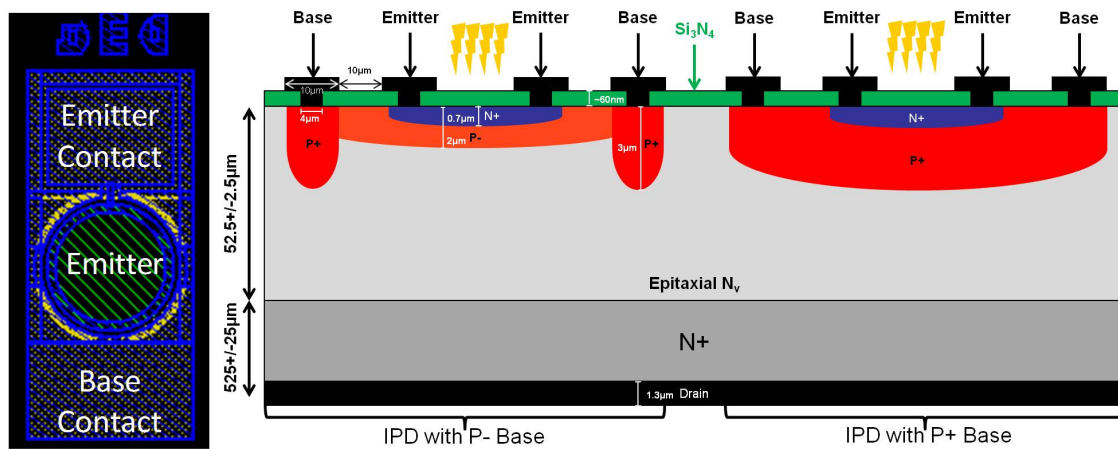


Figure III.10: Left: Top view from Cadence layout. This is the simplest IPD design with a single outer metal ring contact. Right: side view of IPD for devices with P- and P+ Base regions.

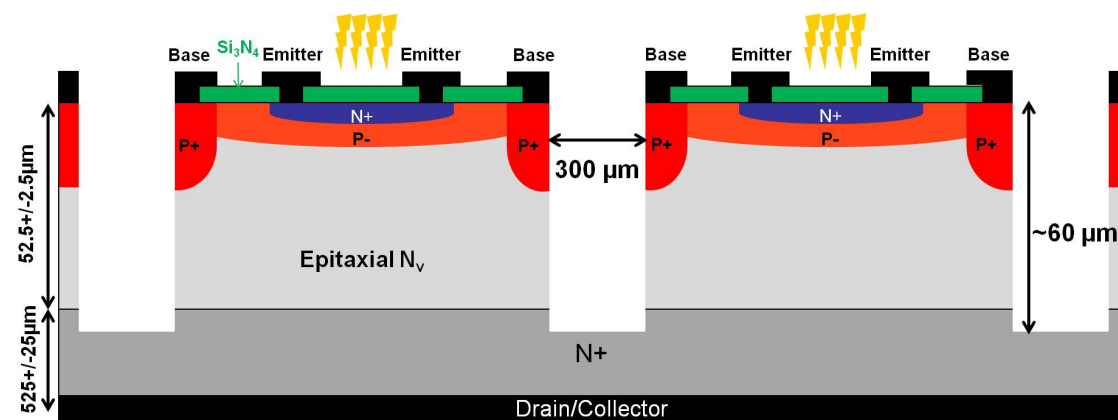


Figure III.11: Side view of high voltage IPD devices with DRIE junction termination.

The IPD designs consider the different compromises between parameters (contact and doping well shape and position) impacting the internal and external QE and bandwidth performance of the device.

- (1) In order to study the impact of the metal contact coverage factor on the QE and

bandwidth:

- Contact size and position are varied in order to account for Shadow losses (impacts external QE) versus series resistances (impacts internal QE and bandwidth),
- During characterization, the incident beam intensity used has a Gaussian profile; thus contacts too close to the center of the device are avoided in most designs.

(2) In order to study the impact of the Emitter and Base doping region shape and position on the QE and bandwidth as well as the parasitic limits:

- The doping regions size, shape and position are varied. Nested, pixelated, and comb structures of the Emitter and Base regions are among the designs as shown in the Cadence layout views of figure III.12. In some of these designs, there is a much higher contact metal coverage factor compared to the simple IPD design (D3a) with a single outer ring contact. This higher shading factor results in higher reflection losses; however, the nested and pixelated designs have a higher ratio of junction to device area and with their junction edges closer to the center of the device where it can be exposed to higher intensity of the incident light (i.e. Gaussian source) these designs may in turn contribute to a higher internal QE. Moreover, a reduced effective RC time constant is anticipated for these designs. It is interesting to analyse the impact of these designs on the QE and bandwidth (an optimization of the device performance based on a compromise between improved bandwidth and internal efficiency at a cost of higher shading losses). Figure III.13 illustrates the layer breakdown and dimension details of one of the nested IPD designs, namely D6j.

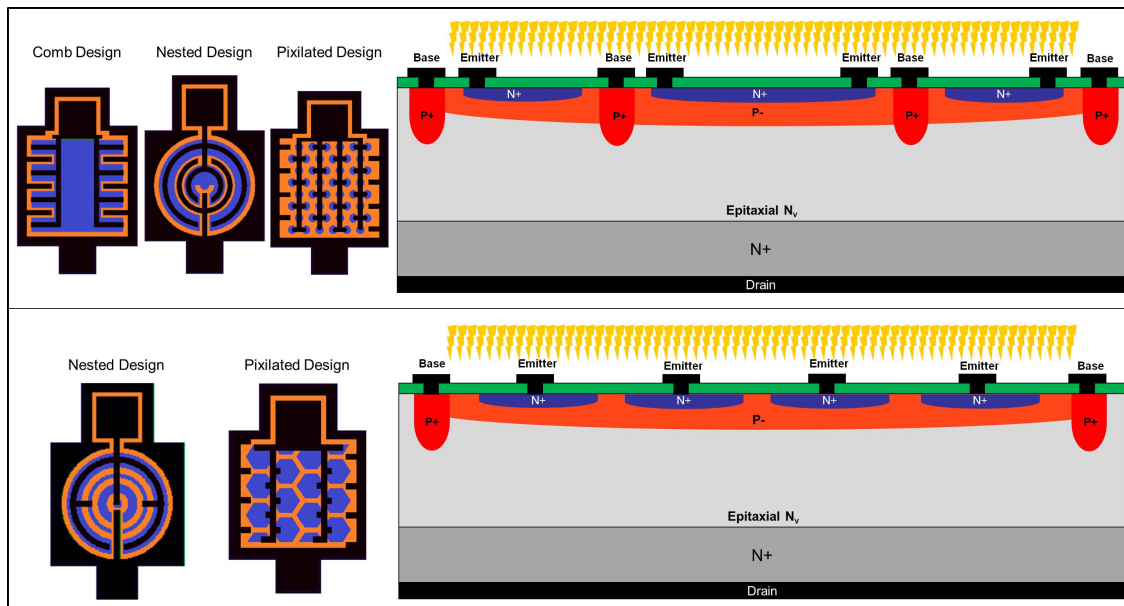


Figure III.12: Left: Top view from Cadence layout. The blue coloured regions are representative of the N+ doped Emitter regions. Right: Side view of IPD Designs, i.e. with Nested Emitter Base regions.

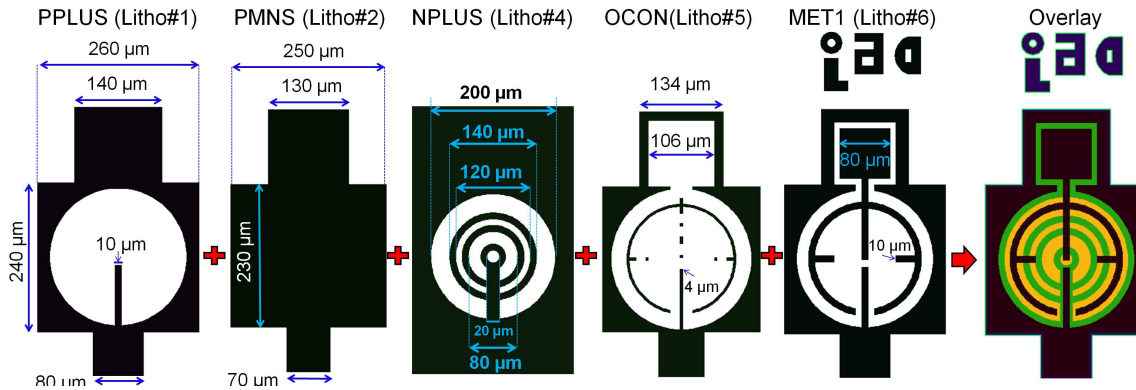


Figure III.13: Example nested IPD design layout detail. From left to right the main mask layouts are depicted. OZUT and DRIE layers are not shown here since they complicate the visual presentation of the device. Note that NPLUS layer (third from left) will use a -PR; thus this mask is inverted and the N+ doped regions are represented by the white color. The far right picture shows the overlap of all the layers presented to its left. The colors represent the following: yellow for N+ Emitter regions, green for P- Base regions, black for metal contact regions.

### III.5 Fabrication Results

Overall, 2 epitaxial (Epi) and 4 Bulk 4" Silicon wafers were fully processed, meanwhile, 4 Bulk wafers were used as dummies for verifying the steps during the fabrication. The specifications for the different wafers are provided in table III.2. The wafers are chosen to have a resistivity of 20 - 40  $\Omega \cdot \text{cm}$  in the  $N_V$  region since this is appropriate for breakdown voltages in the 600 V range. The main difference between the epi wafers compared to the Bulk wafers is that the  $N_V$  region is roughly 52  $\mu\text{m}$  thick and it is grown on top of a thick 525  $\mu\text{m}$  N++ substrate; meanwhile, the Bulk wafers have a 350  $\mu\text{m}$  thick  $N_V$  region. As a result of this difference, the Bulk wafers offer a larger resistance in the vertical direction, nevertheless they wouldn't have a lower breakdown voltage compared to the epi wafers since they have a very thick  $N_V$  region. The life time specifications are not provided for these wafers by the manufacturer.

These devices are fabricated using the power bipolar process (compatible with the VDMOSFET process) at the CIME Nanotech/Minatec cleanroom facilities in Grenoble. The bipolar IPD implantation and annealing process parameters are the same as in the VDMOSFET case; these process details are given in table III.3.

During fabrication, the height of PR and oxide layers were measured via a profilometer and visual observation of the wafers under an optical microscope revealed the quality of lithography (i.e. misalignment error, under or over development) and etch (i.e. under or over etching) processes. Figure III.14 depicts some optical images used for process monitoring at some critical fabrication steps.

Figure III.15 shows macroscopic photos of some of the different IPD designs after fabrication as well as a photo of a low voltage die. As previously presented a variety of contact

Wafer Description	Epi-Wafer	Bulk Wafer	Dummy Bulk Wafer
Substrate type/dopant	N++/Ars	Nv/Phos	Nv/Phos
Orientation	<100>	<100>	<100>
Substrate Resistivity	0,001-0,007 ohm.cm		
Substrate thickness	525 +/- 25 $\mu\text{m}$		
Type/dopant Epi 1	N/Phos	N/Phos	N/Phos
Resitivity Epi 1	20 - 40 ohm.cm	20 - 40 ohm.cm	1-10 ohm.cm
Thickness Epi 1	52,5 -+2,5 $\mu\text{m}$		
Type/dopant Epi 2	N/Phos		
TTV/Bow/Warp ( $\mu\text{m}$ )	10 / 30 / 30		
Flats	primary Flat SEMI Std	primary Flat SEMI Std	primary Flat SEMI Std
front side surface	polished	polished	polished
backside surface	lapped,etched with LTO Seal	lapped,etched	lapped,etched
Total thickness	525 +/- 25 $\mu\text{m}$	350 +/- 25 $\mu\text{m}$	350 +/- 25 $\mu\text{m}$
Quantities of stack	2 wafers	4 wafers	4 wafers
Final Quantities	2	4	0

Table III.2: Bulk and Epi Wafer Specifications

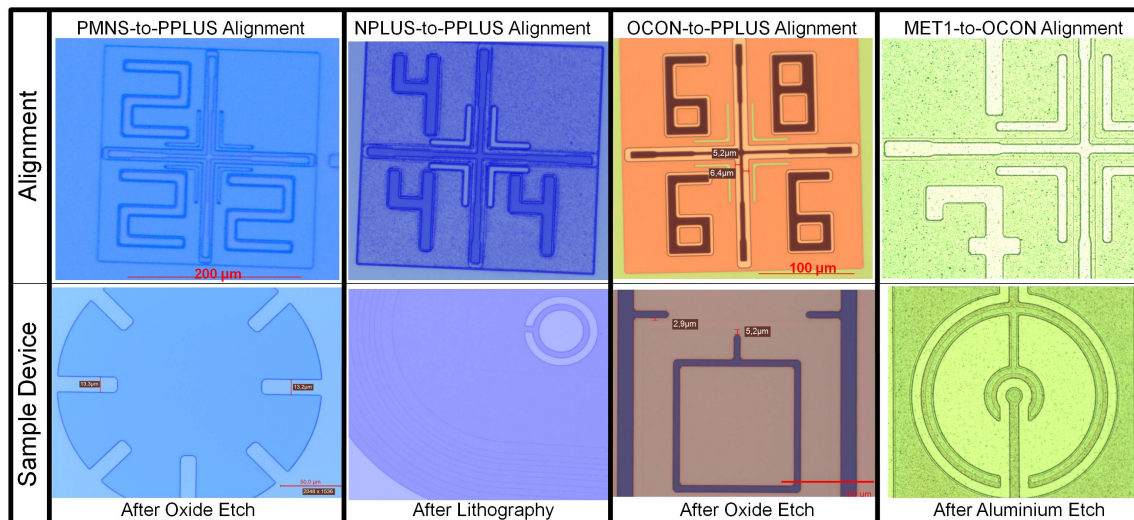


Figure III.14: Microscope images used for monitoring the fabrication quality while in process. The top row shows the alignment accuracy for PMNS, NPLUS, OCON and MET1. The bottom row shows some images from different areas of the wafer corresponding to the process stage indicated by the column labels.

Process	Process Parameter	Equipment
P+ Implantation	Surface: frontside Type/dopant: Boron Dose: $10^{15} \text{cm}^{-2}$ , Energy: 150 keV, Current: $40 \mu\text{A}$ Tilt: $7^\circ$	Implanter
P+ Annealing	Ramp-up: 15min nitro 3000sccm, $750^\circ\text{C}$ to $900^\circ\text{C}$ Stabilisation: nitro 3000sccm, $900^\circ\text{C}$ 2min Oxidation: dryo2 5000sccm, $900^\circ\text{C}$ 15min Ramp-up: nitro 3000sccm 20min, $900^\circ\text{C}$ to $1100^\circ\text{C}$ Stabilisation: nitro 3000sccm, $1100^\circ\text{C}$ 5min Activation: nitro 3000sccm $1100^\circ\text{C}$ 40min Ramp-down: nitro, $1100^\circ\text{C}$ to $750^\circ\text{C}$ 30min Oxidation: dryo2 5000sccm, $900^\circ\text{C}$ 15min	Furnace
P- Implantation	Surface: frontside Type/dopant: Boron Dose: $10^{13} \text{cm}^{-2}$ , Energy: 150 keV, Current: $40 \mu\text{A}$ Tilt: $7^\circ$	Implanter
P- Annealing	Ramp-up: 15min nitro 3000sccm, $750^\circ\text{C}$ to $900^\circ\text{C}$ Stabilisation: nitro 3000sccm, $900^\circ\text{C}$ 2min Oxidation: dryo2 5000sccm, $900^\circ\text{C}$ 15min Ramp-up: nitro 3000sccm 20min, $900^\circ\text{C}$ to $1100^\circ\text{C}$ Stabilisation: nitro 3000sccm, $1100^\circ\text{C}$ 5min Activation: nitro 3000sccm $1100^\circ\text{C}$ 300min Ramp-down: nitro, $1100^\circ\text{C}$ to $750^\circ\text{C}$ 30min Oxidation: dryo2 5000sccm, $900^\circ\text{C}$ 15min	Furnace
N+ Implantation	Surface: frontside Type/dopant: Arsenic Dose: $5 \times 10^{15} \text{cm}^{-2}$ , Energy: 150 keV, Current: $40 \mu\text{A}$ Tilt: $7^\circ$	Implanter
N+ Implantation	Surface: backside Type/dopant: Arsenic Dose: $5 \times 10^{15} \text{cm}^{-2}$ , Energy: 150 keV, Current: $100 \mu\text{A}$ Tilt: $7^\circ$	Implanter
N+ Annealing	Start temperature: $750^\circ\text{C}$ , Gas flow: 3000 sccm- $\text{N}_2$ Ramp-up: $10^\circ\text{C}/\text{min}$ , 3000sccm- $\text{N}_2$ Stabilisation: $900^\circ\text{C}$ , 2min Oxidation: 5000sccm- $\text{O}_2$ , $900^\circ\text{C}$ 10min Ramp-up: $10^\circ\text{C}/\text{min}$ , 3000sccm- $\text{N}_2$ Stabilisation: 5min, $1050^\circ\text{C}$ , $\text{N}_2$ Activation: $1050^\circ\text{C}$ 25min, 3000sccm- $\text{N}_2$ Ramp-down: $-5^\circ\text{C}/\text{min}$ , 3000 sccm- $\text{N}_2$	Furnace

Table III.3: Doping Process Parameters

and doping well shapes have been designed (i.e. pixelated, nested rings, and combs with varying the num. and freq. of the different regions).

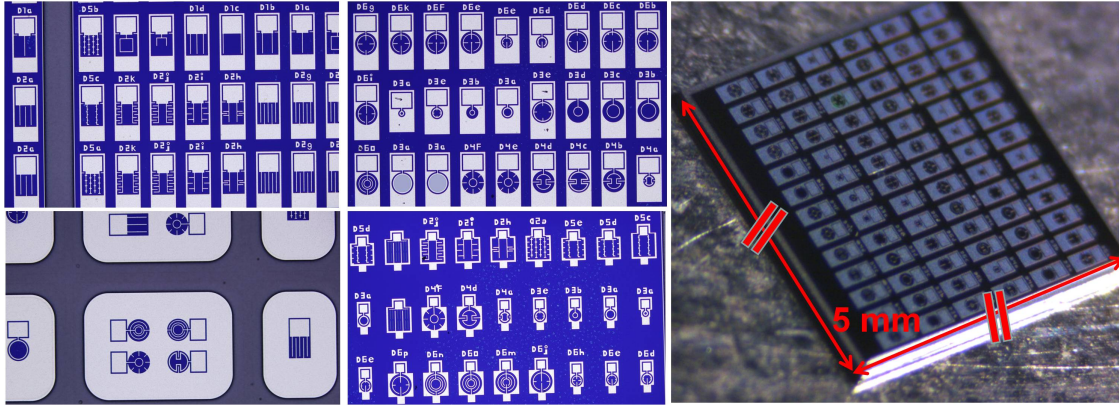


Figure III.15: Fabricated IPD Designs.

TLM test structures show a  $24 \Omega/\square$  sheet resistance for the N+ region which matches the 4-point probe measurements on dummy wafers taken during the fabrication process. 4-point probe measurements on dummy wafers taken during the fabrication process showed a sheet resistance of  $89.51 \Omega/\square$  and  $1178 \Omega/\square$  for the P+ and P- regions respectively, however, TLM measurements of the final chip did not confirm perfectly ohmic P+ contacts (a shallow Schottky behaviour was observed).

Investigation shows that due to a fabrication error there has been a diffusion of p+ dopants throughout all the wafers. This has occurred due to a leakage of the P dopants through the P+ Oxide mask which implies that the thickness of the oxide mask used for the P+ implantation was not sufficient. One way to avoid this problem could be to keep the PR coating on top of the oxide mask during implantation. Never the less, this error needs to be investigated in order to avoid being revisited in any future fabrications. This error was verified by testing if there were any current flow between intentionally isolated p regions. The IV characteristics of isolated P regions with the substrate grounded reveal that there is a current flow between the p regions and that this current flow is dependent on the distance between the contacts as depicted in figure III.16. If the p regions were isolated as were designed, under reverse voltages there should be only a small measurable leakage current that is independent of the contact spacing. As a result of this fabrication error, the guard ring designs will not function as expected, the difference between IPDs with P+ and P- Base regions can't be studied and the devices will have higher dark current levels than expected. Moreover, the IPD dark current shows a higher sensitivity to reverse voltages and an earlier breakdown as shown in figure III.17. As a result, the study of the IPD responsivities as a function of the Emitter reverse voltage is very limited and the avalanche gain can't be studied either. Figure III.17 compares the dark IV characteristics of the same IPD design from a Bulk wafer to an epi wafer. From the wafer information provided in table III.2, the larger  $N_v$  region of the Bulk wafer ( $350 \mu\text{m}$ ) in comparison to the Epi wafer ( $52 \mu\text{m}$ ) would've predicted a lower resistance in the forward IV characteristic of the diodes. This is contrary to the measurement results depicted in figure III.17 (a) where

the forward diode characteristic of the IPD sample from the Bulk wafer shows a lower resistance relative to the sample from the Epi wafer. Moreover, the zoomed in view of the reversed bias region depicted in figure (b) shows that the epi wafer sample has a higher dark current (roughly 2 decades) relative to the sample from the Bulk wafer. As it was reviewed in chapter 2, the forward biased diffusion current increases with longer minority carrier lifetimes meanwhile the generation dark current of a pn junction is inversely proportional to the carrier lifetimes. The IPD dark IV characteristic as predicted by simulations in Atlas demonstrate the effect of carrier lifetimes on the device dark current. This observation leads us to believe that both the Epi wafers and the Bulk wafers have short carrier lifetimes (i.e. a large number of traps in the lattice due to low quality crystal growth) in the range of ns and shorter, meanwhile, the Epi wafers have lower carrier lifetimes relative to the Bulk wafers.

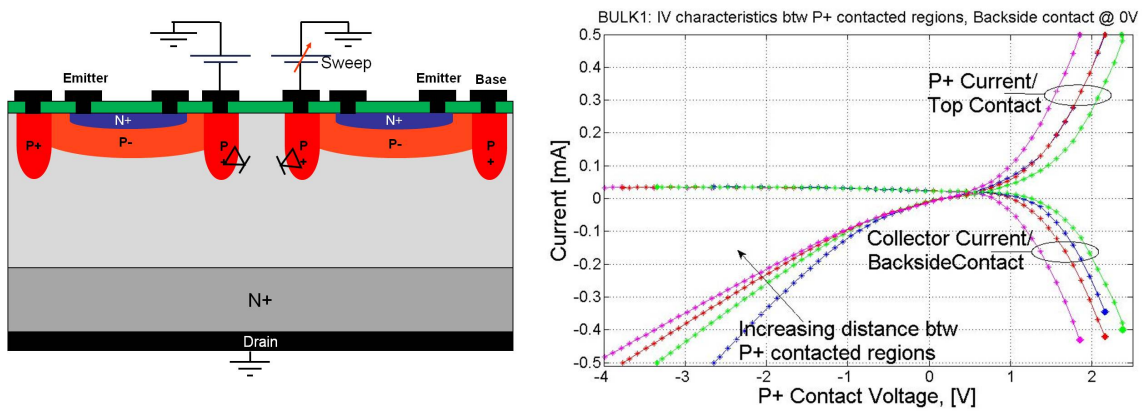


Figure III.16: P+ Mask Leakage Test. The substrate is grounded. The P regions are reversed biased and voltage between them is swept. The cross sectional view depicted here corresponds to that of the design, however, the measurement results indicate that the p regions are connected.

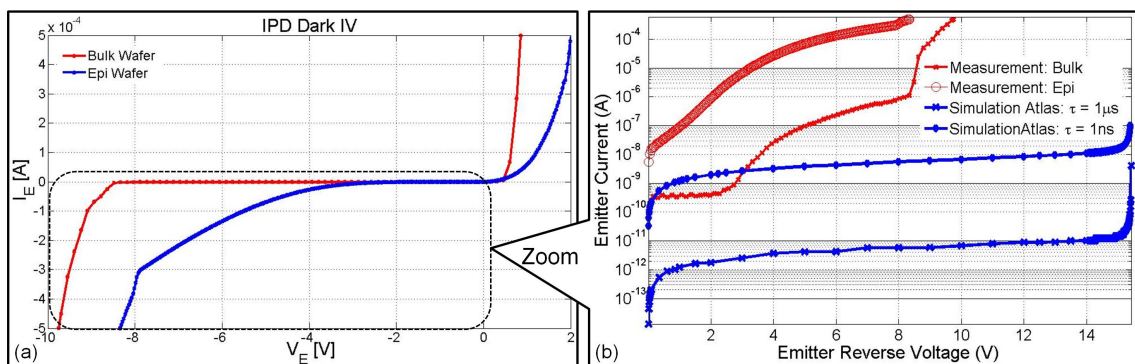


Figure III.17: IPD Emitter reverse IV.

The author would like to thank Victor Gaude, Irene Pheng, Stephane Litaudon and Delphine Constantin for all their input and assistance during the fabrication process. We also would like to acknowledge the support of Loic Vincent and the Microsystem platform (C2m) at Cime nanotech for characterization.

## III.6 DC Characterization: Setup and Measurement Approach

### III.6.a First Approach: LED Light Sources

The first version of the experimental setup was developed in order to characterize the detectors fabricated based on the designs during the thesis of Dr. Nicolas Rouger [88]. The characterization of these old detectors would provide information on the already achieved performance level for these IPD designs. These devices were fabricated using the standard VDMOS process at the CIME Nanotech/Minattec cleanroom facilities in Grenoble. Figure III.18 (a) depicts the doping profiles as measured with SRP as follows:  $2 \times 10^{14} \text{cm}^{-3}$  and  $50 \mu\text{m}$  for the Nv epi layer,  $3.6 \times 10^{16} \text{cm}^{-3}$  and  $2 \mu\text{m}$  for the P- well (P-/Nv junction position),  $4.5 \times 10^{18} \text{cm}^{-3}$  and  $3 \mu\text{m}$  for the P+ well (P+/Nv junction position),  $8 \times 10^{18} \text{cm}^{-3}$  and  $0.77 \mu\text{m}$  for the N+ well (N+/P- junction position). The fabricated photo-detectors have cylindrical shapes with  $100 \mu\text{m}$  diameter circular cross sections as viewed from top and depicted in figure III.18.

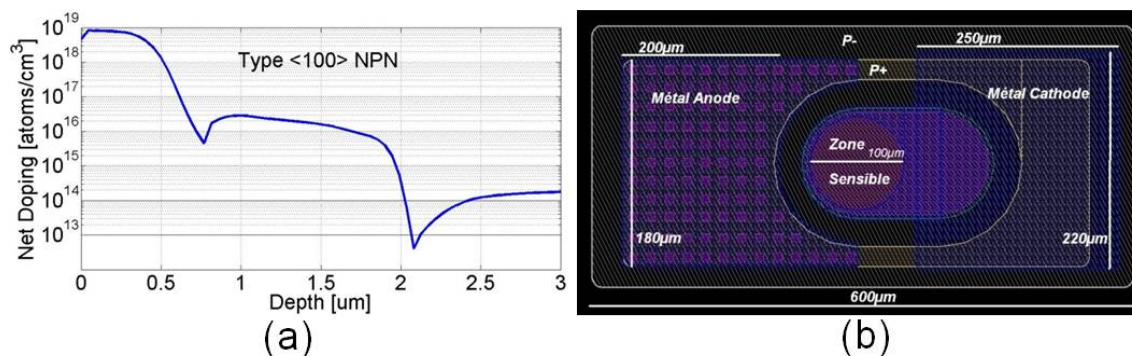


Figure III.18: (a) SRP doping profile. (b) Layout of previous IPD Designs [88].

Obtaining and aligning a  $100 \mu\text{m}$  diameter Gaussian spot size is a challenging task when using non monochromatic light sources such as LEDs which have large apertures and are relatively highly diverging (7.5 degrees). LEDs were mainly chosen for their low costs, their availability in different wavelengths and their direct modulation possibilities. The first version of the DC setup used three LEDs with peak emissions at 460 nm, 525 nm, and 630 nm whose spectral intensities are illustrated in figure III.19. This simple setup uses a spatial filter to achieve a clean Gaussian spot, plus two lenses to focus the light beam into the detector and also offers flexibility when changing LEDs. Figure III.19 shows both a photo of the setup and the achievable optical spot size.

The noise level was minimized by placing the setup under a black box on an optical table. The measured Emitter leakage current was 4 pA at 1 V emitter bias ( $28 \text{nA/cm}^2$ ) and 80 pA at 15 V ( $560 \text{nA/cm}^2$  in avalanche mode) at room temperature. Both the Collector and the Emitter must be biased in order to control the Emitter-Base and Collector-Base space charge region (SCR) extensions. The spectral responsivity of the Emitter and the Collector were measured as a function of the incident optical power and the Emitter

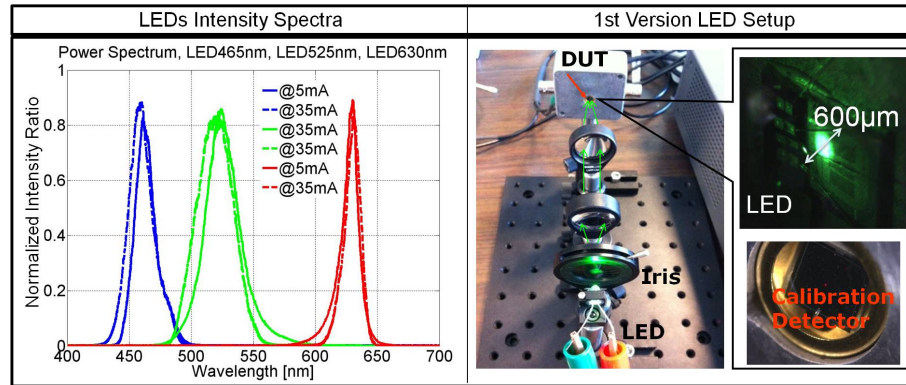


Figure III.19: Left: LED intensity spectrum at three different wavelengths 465 nm, 525 nm and 630 nm and for two different driving currents 5 mA and 35 mA. Right: Photo of the first version of the setup with LED optical sources and the achievable optical spot size.

voltage  $V_E$ . Although the Emitter responsivity is the main interest, the Collector current is characterized to investigate the light absorption in the deeper layers of the structure [89]. The LED sources were powered by a DC power supply and the current was monitored by an ampere meter. A two channel Keithley sourcemeter (2636A) with femto-ampere minimum noise floor was used for biasing the photo-detector and simultaneously measuring its Collector and Emitter currents. For every LED bias condition, the Emitter potential was swept from 0 V - 15 V (the prototypes were designed to reach avalanche at 15 V) at a fixed Collector potential. To obtain the responsivity, the incident power at the surface of the photo-detector was estimated at each wavelength by a calibrated detector with a dark current in the order of 200 nA ( $250 \text{ nA}/\text{cm}^2$  at 0 V - room temperature) and a responsivity between 0.25 A/W at 460 nm and 0.43 A/W at 630 nm. The spectral responsivity and a photo of the calibrated detector are shown in figure III.20. Corresponding to the  $1 \mu\text{A}$  range of the sourcemeter, the current accuracy is in the order of  $\pm 400 \text{ pA}$ . Therefore, the optical power accuracy for the calibration is  $\pm 4 \text{ nW}$  at 460 nm and  $\pm 1 \text{ nW}$  at 630 nm. Using the same current range as during calibration, the minimum measurable responsivity is  $0.4 \text{ mA}/\text{W}$  at 460 nm and  $0.1 \text{ mA}/\text{W}$  at 630 nm. Utilization of smaller current ranges on the sourcemeter can reduce these values.

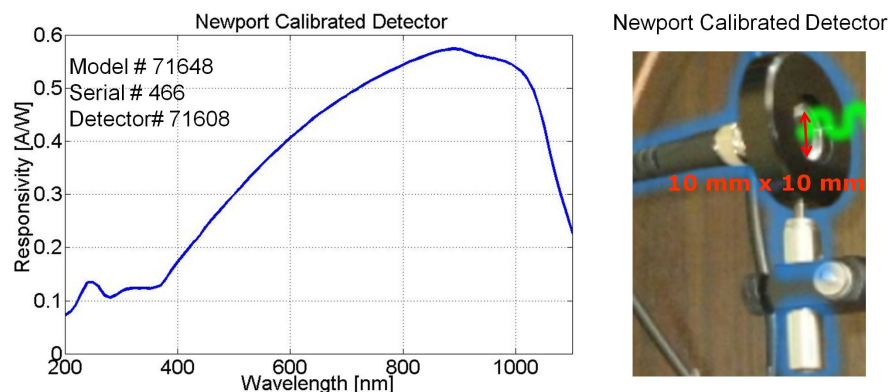


Figure III.20: Newport calibrated detector responsivity and photo.

The  $I_E$  and  $I_C$  currents were measured at the same time as a function of biasing conditions and optical power  $P_{Optical}$  at the three mentioned wavelengths. The responsivity of the detectors were measured to be around 0.007 A/W. This value is expected to be underestimating the true efficiency of the IPD mainly due to calibration errors originating from the large optical spot size relative to the detector size. In order to improve this measurement a second version of the setup using LED sources was constructed as depicted in figure III.21. In comparison to the first version of the setup, the setup of figure III.21 uses two additional aspherical lenses to correct for aspherical aberrations and the use of an optical fiber further cleans out the optical beam resulting in a smaller Gaussian spot of less than 200  $\mu\text{m}$  in diameter. Overall optical power losses were estimated at  $\approx 30\text{dBm}$ . Figure III.22 illustrates the observed IPD reverse bias  $I_E$  as a function of  $V_E$  and  $P_{Optical}$  when measured with the 525 nm LED at a 1V Collector bias.

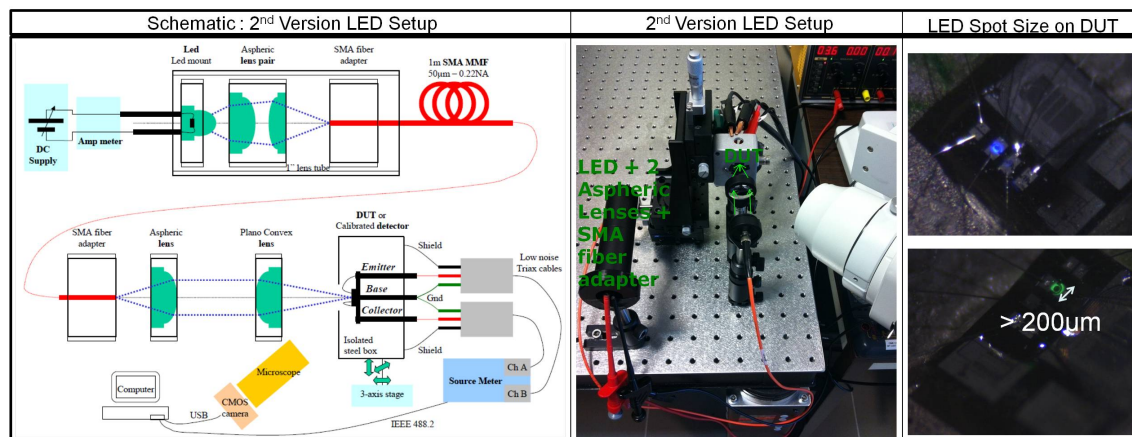


Figure III.21: Left: Schematic of the 2<sup>nd</sup> DC setup approach using LED sources [107]. Middle: Photo of the 2<sup>nd</sup> DC setup approach using LED sources. Right: Reduced LED spot size of less than 200  $\mu\text{m}$ .

Figure III.23 summarizes the spectral responsivity results for the Emitter and Collector. At shorter wavelengths and low bias, the responsivity suffers from two effects: 1) a slightly higher reflectivity at the surface interface reduces the external quantum efficiency 2) a reduced Emitter-Base SCR extension which limits the part of drift photo generated currents to diffusion ones. The total QE for the Emitter is 12.3% at 465 nm, 10.2% at 525 nm and 6.9% at 630 nm at 0V Emitter bias. These values are satisfactory for a non optimized device without any anti reflection coating. The total QE for the Collector is 8% at 465 nm, 18.4% at 525 nm and 31% at 630 nm at 0 V Emitter bias - 1 V Collector bias. It is also noted that the Collector responsivity is reduced by approximately 5 to 10% when the Emitter voltage is increased to 15 V. This reduction is due to the Emitter-Base SCR extension into the P well region which results in the removal of the diffused photo generated carriers from the Collector-Base diffusion current into the Emitter-Base diffusion current.

Figure III.24 shows the Emitter responsivity of the detector as a function of optical power at discrete Emitter biasing conditions when illuminated by a 525 nm wavelength LED source. The DUT has a 100  $\mu\text{m}$  radius which results in an approximate area of 0.03  $\text{mm}^2$ . The results of figure III.24 show the linearity of the photodetector for input

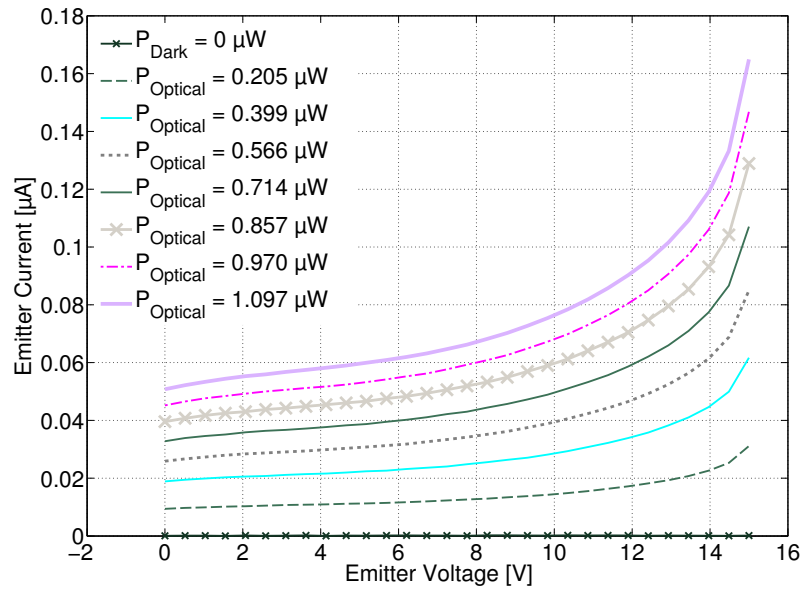


Figure III.22: LIV characterization of the Emitter current with a 525 nm LED [107].

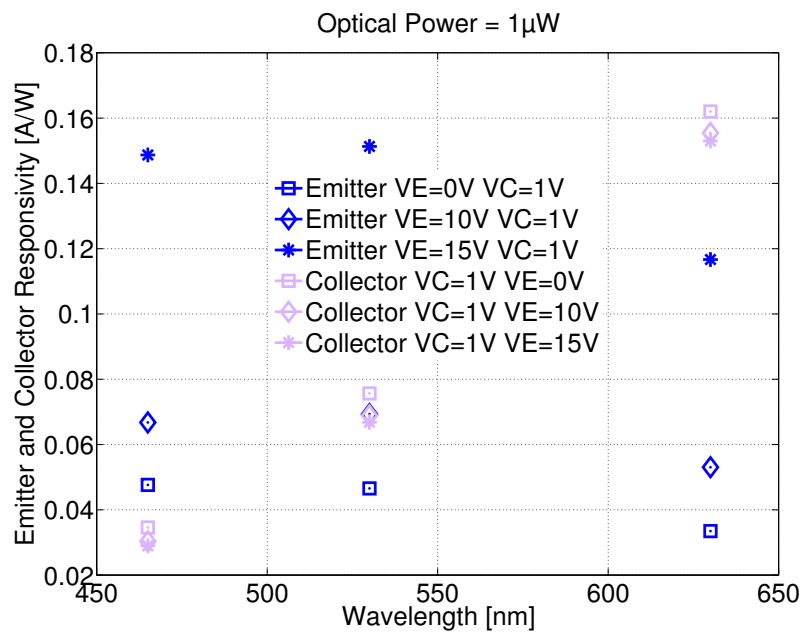


Figure III.23: Emitter and Collector responsivity for three different LED wavelengths [107].

optical powers up to  $1.1 \mu\text{W}$  which corresponds to an optical intensity of approximately  $30\text{pW}/\text{cm}^2$ . In order to verify the linearity of the device at higher optical powers, different optical sources (i.e. Lasers) that can be controlled at higher optical power levels are needed.

These initial measurements with LEDs at only three wavelengths showed a responsivity of  $0.046 \text{ A/W}$  at  $0 \text{ V}$  Emitter bias when triggered with a  $1 \mu\text{W}$ ,  $525 \text{ nm}$  wavelength LED as reported in [107]. The author would like to acknowledge the contributions of Duc Ngoc To during his master internship. He was involved in both the set up development stage as well as the measurement stage.

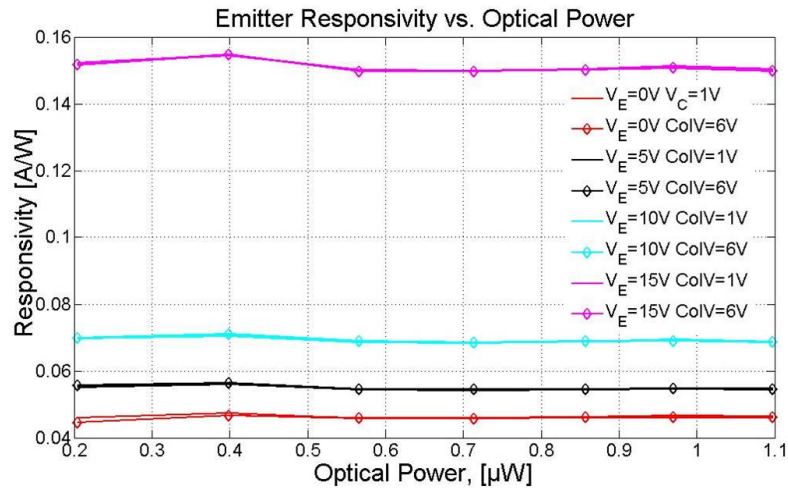


Figure III.24: Emitter responsivity versus optical power. The optical source is a 525nm LED.

### III.6.b Second Approach: Xenon Light Source

Thanks to ANR funding of project SiPowLight, the experimental setup has been radically changed to include the following features as shown in figure III.25:

- A broadband optical source (xenon lamp) for full characterization over a large wavelength range (i.e. 200 nm to 1600 nm) with a high resolution (i.e. 0.1 nm step + 10 nm linewidth).
- Semiconductor laser and LED sources for transient and small signal analysis.
- High reproducibility
- Monitoring of optical source power stability
- High accuracy (i.e. optical noises and electrical noises were quantified and minimized)
- Calibration procedures for calibrating the measurement setup (i.e. optical power)
- Temp. control for temperature characterization and for removing noise due to temperature instabilities
- On wafer and on die probing
- High Voltage (up to 200 V) measurement (i.e. testing DC and transient voltage effects of the backside collector contact)
- Automation for removing human errors and allowing faster measurement times (i.e. GPIB and USB control)

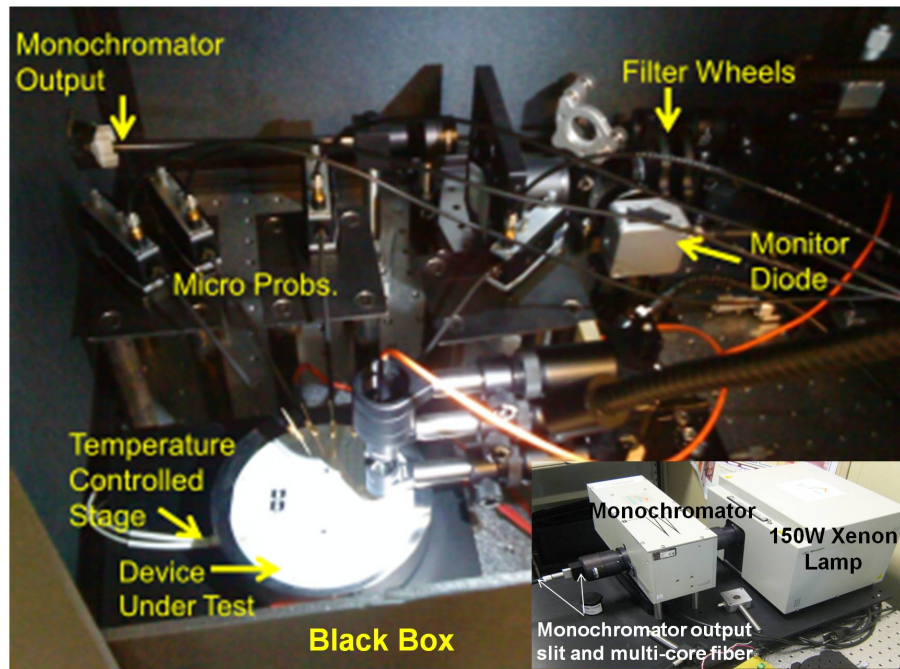


Figure III.25: Picture of the DC experimental setup. The sample (wafer or die) is placed on a temperature controlled stage. The detector under test can be directly biased via micro-probes [108].

Figure III.26 shows a complete schematic diagram of the developed DC measurement setup. This setup offers two possibilities: a direct DC measurement approach or a lock-in amplifier approach. Two Keithley SourceMeter Units are used for all the current measurements: a 2636A unit for the calibrated detector and the device under test (DUT) current measurements, and a 2401 unit for the monitor photodiode current measurements. The Keithley Source measure units can measure dark currents below 1 pA (at 0.15% accuracy  $\pm 120$  fA depending on the measurement range and the chosen connectors) and limit the range of high voltages applied on the backside collector contact to 200 V.

A 150 W white light xenon source followed by a GPIB controlled dual grating monochromator, allows for sweeping the wavelength from 200 nm to 1600 nm with a 0.1 nm step resolution and a full width half maximum (FWHM) of 10 nm (a narrower or wider FWHM is obtainable by changing the monochromator slit resulting in a compromise between bandwidth and signal level). Then, a UV blocking beam splitter sends 30% of the optical power to a monitor diode. The main beam (70% of optical power) is passed through a dual filter wheel with long pass and neutral density filters in order to eliminate second order diffractions from the monochromator (UV emissions are already suppressed by the optical elements, mainly by the beam splitter) and to allow controlled changes in the optical power magnitude in order to investigate noise effects at lower optical powers. Using a combination of optical elements and optical fibers, the diameter of the circular shaped optical spot can be varied from 1 mm down to 100  $\mu\text{m}$ . Figure III.27 shows the measured optical power available at the DUT; this spectrum is strongly related to the Xenon emission spectrum and the optical components and has a maximum optical power level in the order of 35 nW

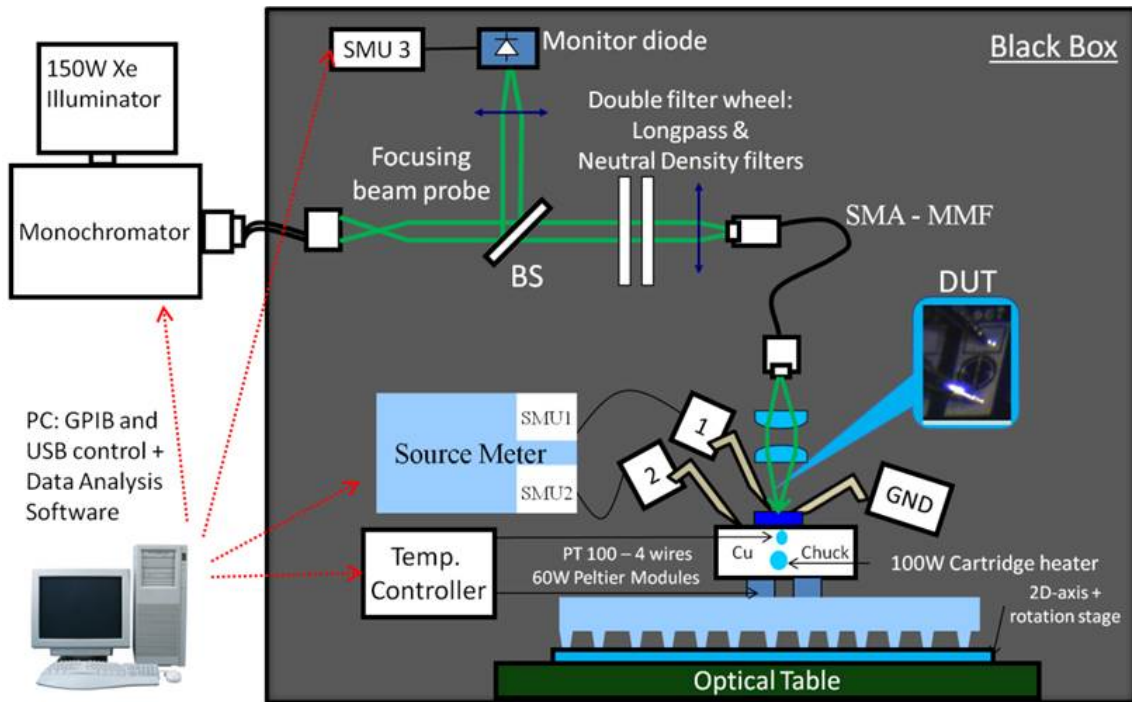


Figure III.26: Schematic diagram of the DC measurement set-up [108].

(due to insertion losses and coupling into different modes. A  $50\mu\text{m}$  MCFiber is used.) [108].

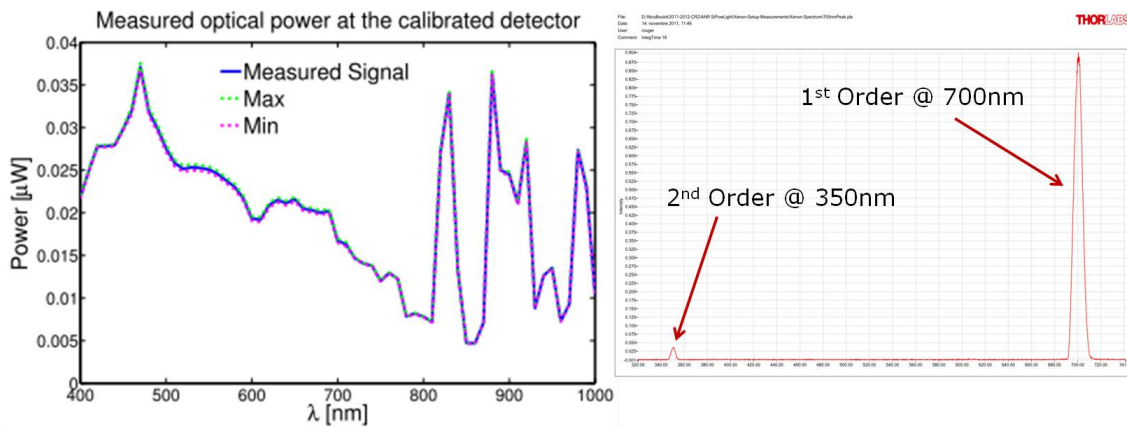


Figure III.27: Left: Measured optical power at the DUT (optical spot size of  $100\mu\text{m}$ ), over a 400 nm -  $1\mu\text{m}$  wavelength range. The monochromator sweep step was 10 nm, and the optical power was measured via current measurement of a calibrated optical detector. This spectral distribution is strongly related to the Xenon emission spectrum [108]. Right: The second order harmonic at 350 nm wavelength is present when the monochromator is wavelength setting is set to 700 nm.

The sample stage includes a bulk copper chuck (to avoid surface oxidation, the chuck is electro-plated with a  $5\mu\text{m}$  thick Nickel layer) equipped with a 100 W heating cartridge,  $3 \times 19$  W Peltier thermo-electrical modules for temperature control and improved cooling, a 4 wire PT100 temperature sensor, and a heat sink for temperature control reference

purposes. A photo of the sample stage is depicted in figure III.28. The temperature control loop is realized through a temperature controller (Thorlabs TED4015), which can sink/source the Peltier modules (up to 225 W) by applying a numerical PID. This temperature system is controlled via USB, and it can reach steady state in three minutes for a 5°C step in temperature, within a  $\pm 0.03^\circ\text{C}$  temperature window in the range of 20°C to 90°C as shown in figure III.29. Faster dynamics can be achieved when the heating cartridges are used (open loop control). Finally, placing the complete setup under a dark box strongly reduces the dark currents and their modification from unwanted external optical sources. Several current measurements under dark conditions were performed using a calibrated detector in order to quantify the noise levels in the electrical measurement systems which in turn set the minimum optical power level that can be reliably measured; a low optical power source equivalent noise level of  $\pm 3$  pW (maximum value, wavelength dependent) was found [108].

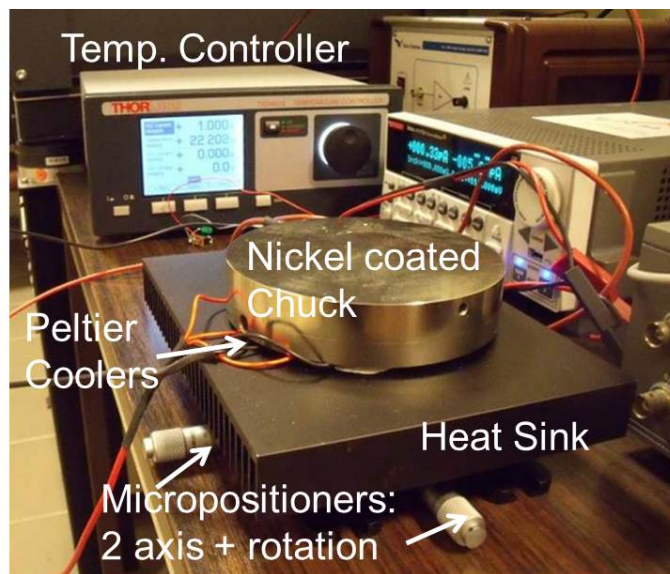


Figure III.28: Photo of the temperature controlled chuck.

Figure III.30 shows a flow chart of the measurement procedure as well as the biasing conditions of the IPD. For each DUT measurement, first, a calibration procedure is carried out. During the calibration process, the wavelength is swept over the chosen wavelength range and the total optical power transferred at each wavelength via the adjusted spot size is calculated from DC current measurements of a commercially available calibrated optical detector with a known responsivity spectrum. This chosen calibrated optical detector has a 10 mm  $\times$  10 mm sensitive surface and a responsivity between 0.25 A/W at 460 nm and 0.43 A/W at 630 nm as it was depicted in figure III.20. Equation III.2 [109] shows the optical power calculation, where  $P_{Opt}$  is the total optical power transmitted at the surface of the detector,  $I_{Cal}$  is the total current from the calibrated detector,  $I_{Cal\_Dark}$  is the dark current from the calibrated detector, and  $R_{esp\_Cal}$  is the responsivity of the calibrated detector as provided by its datasheet.

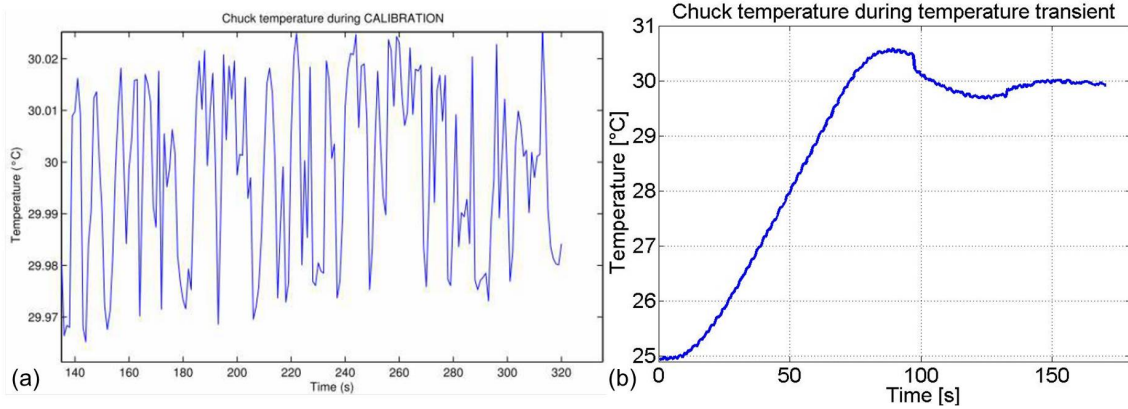


Figure III.29: (a) Temperature control: 20°C - 90°C within +/- 0.03°C. (b) A settling time of 2-4 min for a 5°C temperature step change.

$$P_{Opt}(\lambda) = \frac{I_{Cal}(\lambda) - I_{Cal\_Dark}}{R_{esp\_Cal}(\lambda)} \tag{III.2}$$

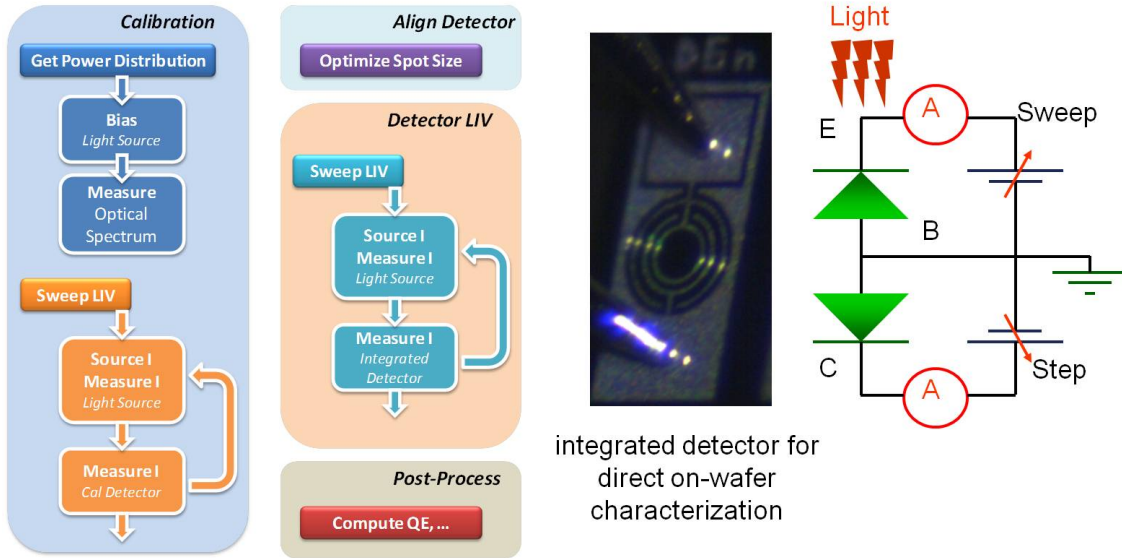


Figure III.30: Measurement Approach. In the flow chart, biasing of the optical source only applies to LEDs and lasers since the Xenon power is not controlled (stabilizes roughly 20 min after being turned-on).

Once the optical power calibration is done, the calibrated detector is replaced by the sample and its currents are measured (photo generated currents and dark currents, both for the emitter and the collector channels). Using the DUT current measurements and the calculated optical power from the calibration stage, the responsivity of the DUT is determined. Any errors in the extracted DUT Responsivity due to ultra low frequency optical power changes can be taken into account by comparing the current in the monitor diode from the calibration sequence to the DUT measurement sequence and applying a correction factor as shown in III.3.

$$R_{esp\_DUT}(\lambda) = \frac{I_{DUT}(\lambda) - I_{DUT\_Dark}}{P_{opt}(\lambda)} \times CorrectionFactor \quad (III.3)$$

$$CorrectionFactor = \frac{I_{Mon\_Cal}(\lambda) - I_{Mon\_Cal\_Dark}}{I_{Mon\_DUT}(\lambda) - I_{Mon\_DUT\_Dark}}$$

Where  $R_{esp\_DUT}$  is the Responsivity of the DUT,  $I_{DUT}$  and  $I_{DUT\_Dark}$  are the total current and the dark current from the DUT respectively,  $I_{Mon\_Cal}$ ,  $I_{Mon\_Cal\_Dark}$ ,  $I_{Mon\_DUT}$ , and  $I_{Mon\_DUT\_Dark}$  are the total current, the dark current of the monitor diode during the calibration stage, and the total current and the dark current of the monitor diode during the DUT measurement stage. The monochromator is equipped with a shutter that is closed when measuring dark currents. During both the calibration and DUT measurement processes, 30% of the incident light is used by a monitor diode. Any variations in the measured currents due to low frequency electrical or optical noises are revealed by comparing the current at the monitor diode during the calibration process to the current measurements during the DUT measurement process. A first measurement error can be estimated by using the calibrated detector as a DUT and thus measuring it twice; this reveals a measurement error of +/- 0.5% in the 360 nm to 560 nm wavelength range as depicted in figure III.31. With the current version of the measurement setup, the DUT measurement sequence can be remotely launched for any different temperature, or biasing conditions.

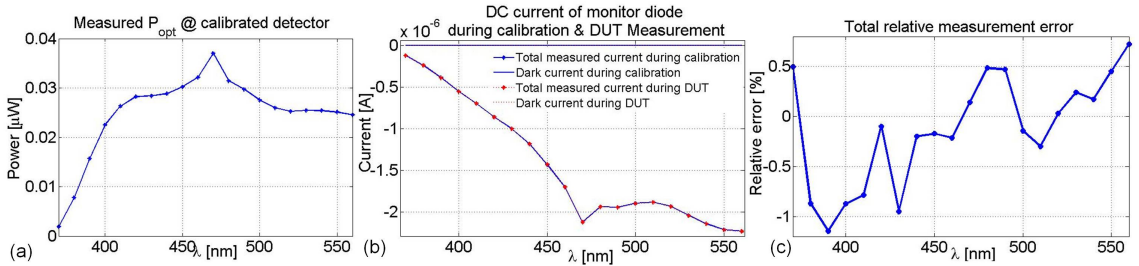


Figure III.31: Measurement error in the 360 nm to 560 nm wavelength range.

The author would like to acknowledge the work of Joseph Magniez and Maxime Dautin on the temperature control of the DC experimental setup during their intern-ship.

### III.6.c MEASUREMENT RESULTS

Figure III.32 (a) shows the measured spectral Emitter and Collector currents of one of the IPDs (D3a), at room temperature using the setup illustrated in figure III.25.

The IPD (D3a) has a maximum responsivity of 0.18 A/W (QE of 45%) at a wavelength of 500 nm and with  $V_E = V_C = 1V$ . This verifies that the use of light sources near 500 nm is the appropriate choice for the IPDs with fabrication processes compatible with 600V VDMOSFET power devices. These measurements also closely match the simulation results shown in Figure III.32 (b). The simulations were based on fitted doping profiles

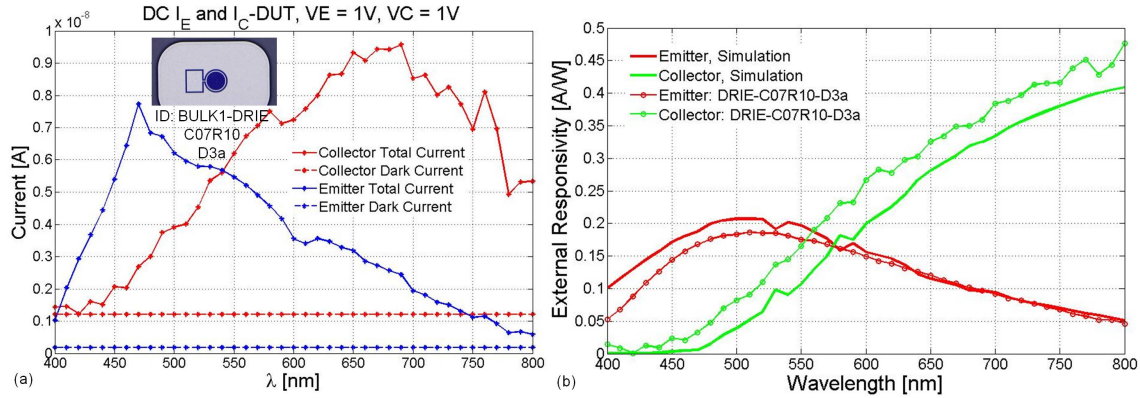


Figure III.32: (a) The IPD Emitter and Collector total and dark current measurement results. Chip ID: DRIE-Bulk, c07r10 where  $c\#r\#\#$  corresponds to the column and row position on the wafer. This IPD (D3a) has an Emitter radius of  $100 \mu\text{m}$ . (b) Experimental and simulation results showing the spectral responsivity with Emitter at 1 V, Collector at 1 V and the Base grounded. These simulation results were obtained from Silvaco with a 2D cylindrical axis of symmetry, a uniform optical source, a  $50 \mu\text{m}$  Emitter radius, SRP fitted doping profiles and initial carrier life times of  $1 \mu\text{s}$ .

and a 2D finite element analysis (Silvaco software, 3D through cylindrical symmetry) as was presented in chapter 2. The measured Emitter responsivity is lower than the predicted simulation results at the shorter wavelengths. This could be explained by higher reflections at the surface, surface recombination, and shorter lifetimes due to imperfections of the Silicon lattice, however further investigations are needed. Moreover, the measured Collector responsivity is higher than the predicted simulation results. This is explained as the fabricated devices have a  $350 \mu\text{m}$  thick substrate region which provides more opportunity for carrier absorption, meanwhile, only a  $50 \mu\text{m}$  substrate was simulated in order to reduce the simulation times. The Substrate (Collector/Base) breakdown voltage is measured on devices with DRIE structures as depicted in the IV characteristic of figure III.33.

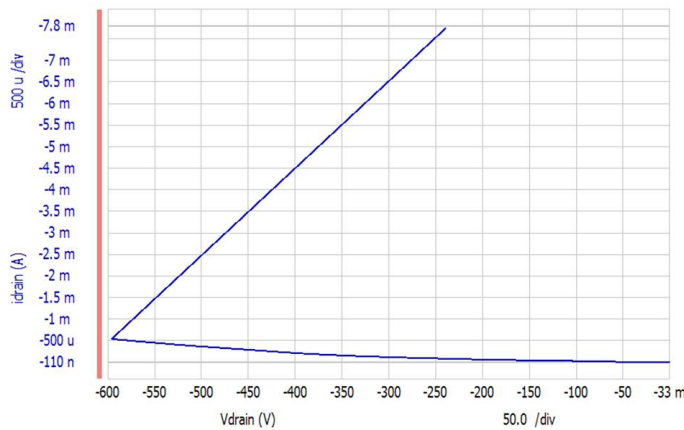


Figure III.33: Measured substrate (Collector/Base) breakdown voltage.

IPD design D3a, whose cross-section(with ARC) was depicted in figure III.10, is fabricated with and without an ARC layer. Figure III.34 shows the effect of the ARC on

the Emitter responsivity of IPD D3a. There is roughly a 50 % increase in the Emitter Responsivity due to the addition of the ARC layer; this is notably higher than the predicted 40 % increase from the analysis in Chapter 2. This unpredicted 10 % increase in the device efficiency could be explained by considering that the  $Si_3N_4$  layer is acting both as an ARC as well as a surface passivation layer. Thus, the device efficiency is improved by reducing surface reflections as well as surface recombinations.

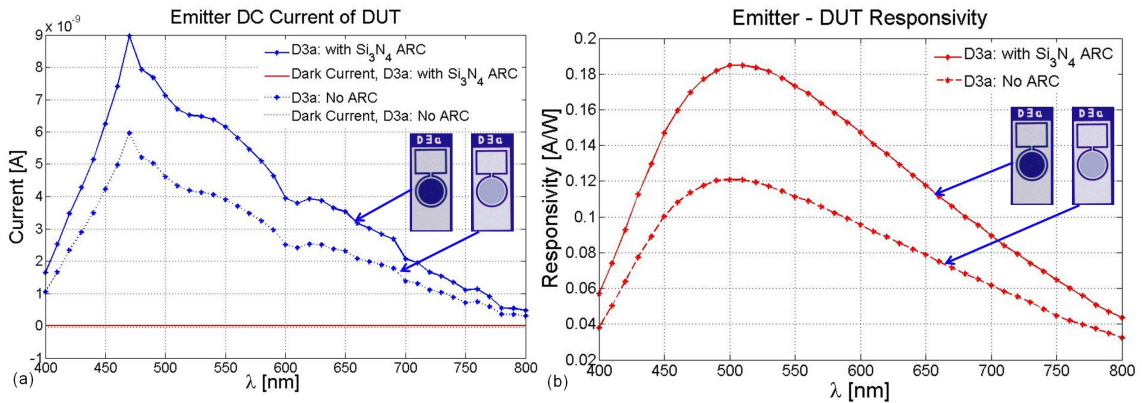


Figure III.34: Current and responsivity measurements of IPD with and without ARC. IPD Emitter radius is  $100 \mu\text{m}$ . Chip ID: Bulk1, c09r08.

Keeping all the same design parameters used in IPD D3a, IPDs with different contact ring diameters have been fabricated in order to see the effect of the contact shadow versus the Emitter series resistance when using a Gaussian optical source. IPD designs, D3a, D3b, D3c, D3d have an outer ring contact radii of  $100 \mu\text{m}$ ,  $80 \mu\text{m}$ ,  $70 \mu\text{m}$  and  $50 \mu\text{m}$  respectively; their corresponding Emitter responsivity measurements are depicted in figure III.35.

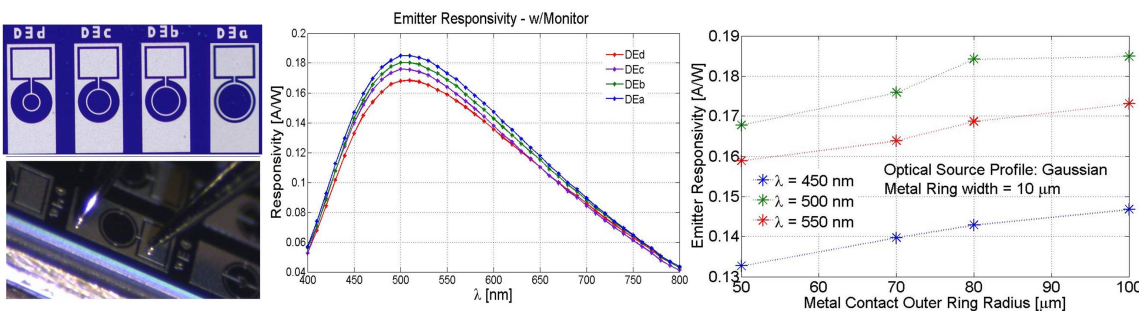


Figure III.35: Effect of contact position relative to the center of a Gaussian optical source on the IPD Responsivity. The IPD Emitter radius is  $100 \mu\text{m}$ . IPD designs, D3a, D3b, D3c, D3d have an outer ring contact radii of  $100 \mu\text{m}$ ,  $80 \mu\text{m}$ ,  $70 \mu\text{m}$  and  $50 \mu\text{m}$  respectively.

Figures III.36 and III.37 show the effect of some of the different designs on the IPD responsivity performance in DC. Due to the very large number of designs (Over 100 different IPDs), a large number of hours is required in order to measure and analyse all the devices accurately. Thus, there are potentially many interesting studies in terms of the effects of the device design parameters on the IPD performance that can be carried out

in the future. As seen from the results of figures III.36 and III.37, nested Emitter and Base regions that offer a large ratio of junction area to device area meanwhile maximizing the ratio of Emitter to Base active region offer an improved responsivity. Moreover these devices are expected to have higher bandwidths since they have shorter Emitter-to-Base contact distances.

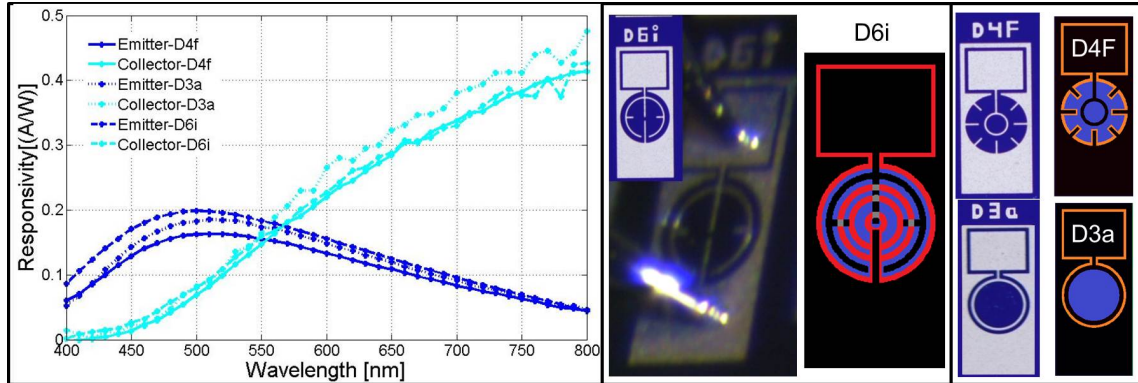


Figure III.36: The effect of some different designs on the IPD DC Responsivity. IPD Emitter radius is 100  $\mu\text{m}$ .

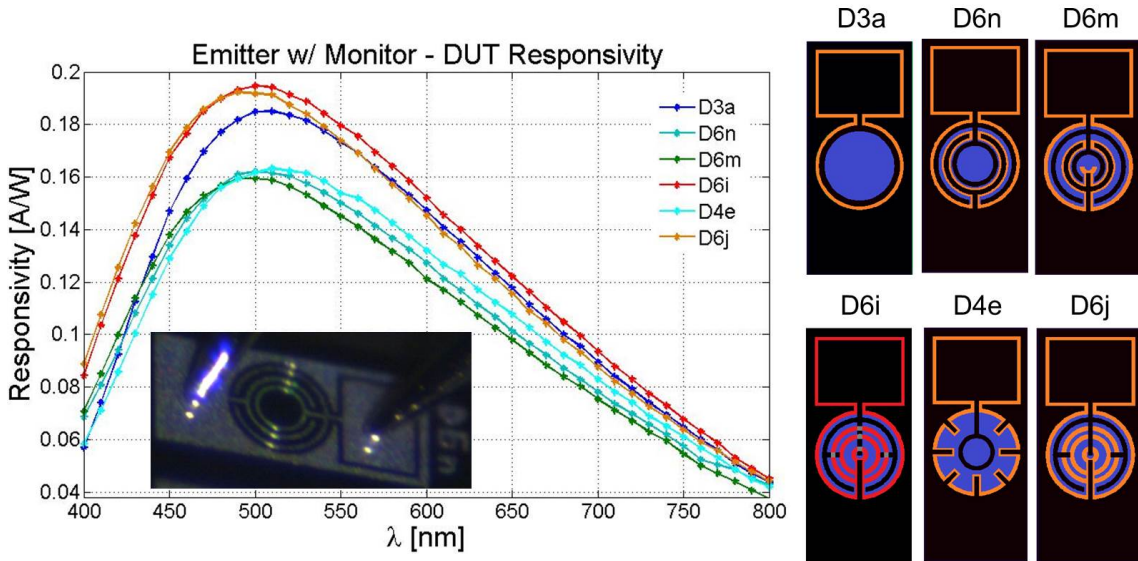


Figure III.37: The effect of some different designs on the IPD DC Responsivity. IPD Emitter radius is 100  $\mu\text{m}$ .

The IPD DC tolerance with respect to increasing Substrate voltages, is tested for Collector voltages as high as 200 V (this is the limit of the 2636 Keithley). As shown in the results of figure III.38, the effect of Collector DC voltages on the Emitter responsivity is insignificant.

In order to complete the DC analysis of this batch of fabricated IPDs some short term work is still required. In order to improve the level of accuracy when comparing results from different devices, it is recommended that the same design be tested on many different

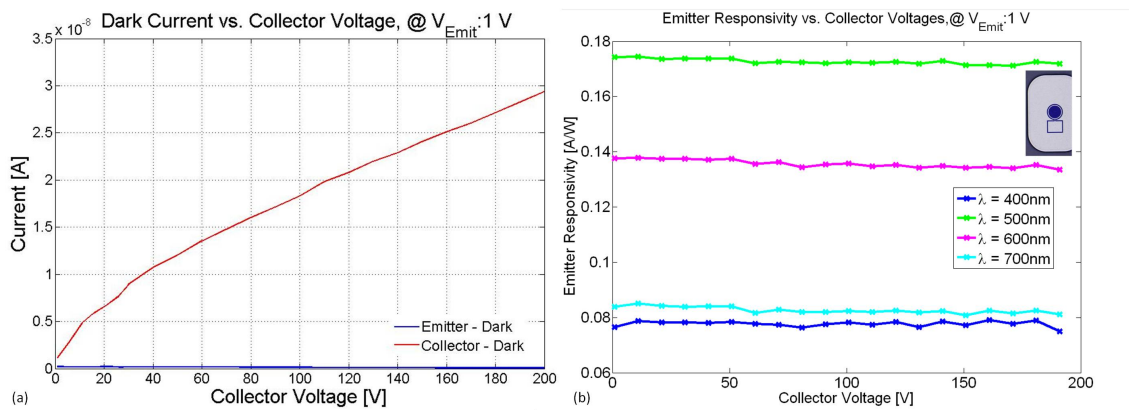


Figure III.38: High Substrate DC Voltage Effect on IPD.  $I_E$  and  $R_E$  versus  $V_C$ . IPD Emitter radius is  $100 \mu\text{m}$ . Chip ID: DRIE-Bulk1, c09r07 where  $c\#\#\#r\#\#\#$  corresponds to the column and row position on the wafer.

chips and error bars be added to the measurement plots. This would reduce any errors originating from inconsistencies across the wafers due to fabrication limitations and thus enable a more clear and conclusive comparison of the different designs. Moreover, the IPD photocurrents, dark currents, QEs, and optical wavelength (corresponding to the peak QE of the device) shifts levels need to be studied as a function of temperature effects. In order to identify the effect of very large substrate voltages on the IPD performance, the IPDs need to be tested with Collector voltages up to 600 V. Since the Keithley SMU can only perform measurements up to 200 V, a higher voltage source is required.

### III.7 AC Characterization: Setup and Measurement Approach

Capacitance-Voltage (CV) measurements of the IPDs show a low Emitter-Base capacitance in the range of 35 pF for detectors of radius  $100 \mu\text{m}$  as depicted in figure III.39. Emitter-Base capacitances as low as 10 pF is measured for IPDs with a  $25 \mu\text{m}$  radius. Collector-Base capacitances for the IPDs are in the range of 120 pF; this maybe exceptionally higher than the value corresponding to the original design due to the fabrication error which has led to the connection of all the P-regions.

#### III.7.a First Approach: Externally modulated LED Optical Source

The dynamic behaviour of the IPD devices fabricated during the thesis of Dr. Nicolas Rouger was introduced in [107] and it showed a bandwidth around 800 kHz. This measurement was completed by Duc Ngoc To during his master internship. Duc designed a current modulator to modulate the LED optical power. The Emitter contact of the detector was connected to a high speed / low noise transimpedance amplifier (TIA), while being DC biased by the sourcemeter (Collector - Base junction biased at 1V). The response to a  $2 \mu\text{W}$  optical power step of the fabricated optical detector connected to a low noise  $10^7 \text{V/A}$  TIA [110] is plotted in figure III.40.

However, due to low optical signal levels, high TIA gains were used, resulting in reduced

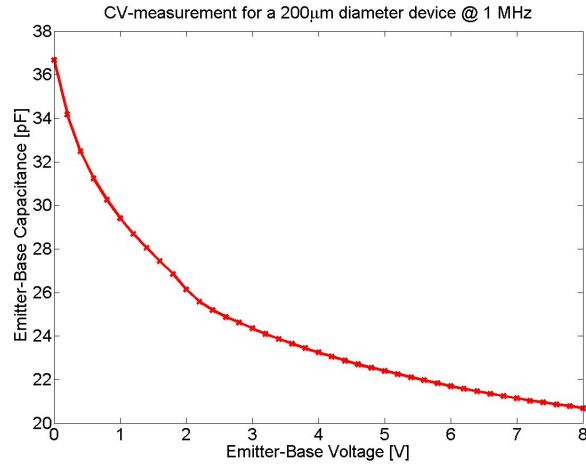


Figure III.39: Emitter/Base capacitance-voltage (CV) measurement of a 200  $\mu\text{m}$  diameter IPD at 1 MHz.

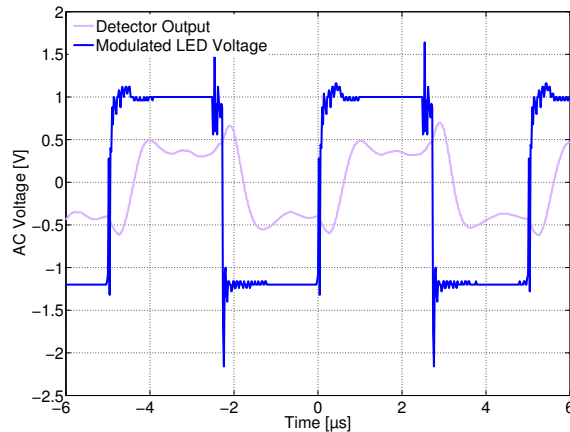


Figure III.40: Emitter transient response to an optical square wave signal at a 200kHz frequency when triggered with the 525nm wavelength LED [107].

measurement bandwidths (limiting the bandwidth to roughly 1MHz). Unfortunately, the measured 3dB bandwidths are in the order of the setup measurement bandwidths [107].

### III.7.b Second Approach: Externally modulated Laser

In order to increase the modulated optical power levels at high frequencies over a wide wavelength range, an extension of the setup for AC measurement has been realized. Figures III.41 and III.42 show the schematic and the photo of the AC setup using a green laser with an external electro optical modulator.

The possible solutions available for investigating the effects of the wavelength on the modulation bandwidth measurements are limited since the wavelength region of interest is in the visible range and near infra-red (460 nm - 800 nm) where high speed directly modulated semiconductor laser sources are limited. The approach here is to apply both external and direct laser modulation techniques. In the case of external modulation, various low cost DC mW lasers can be modulated via a broadband electro optical modulator

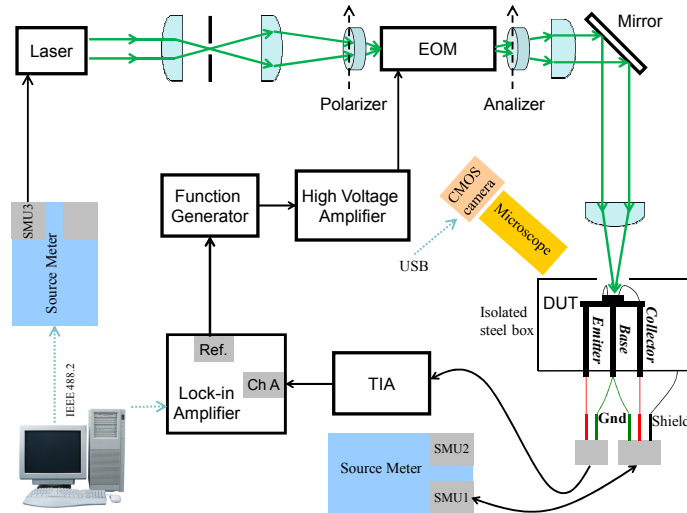


Figure III.41: AC schematic and measurement setup.

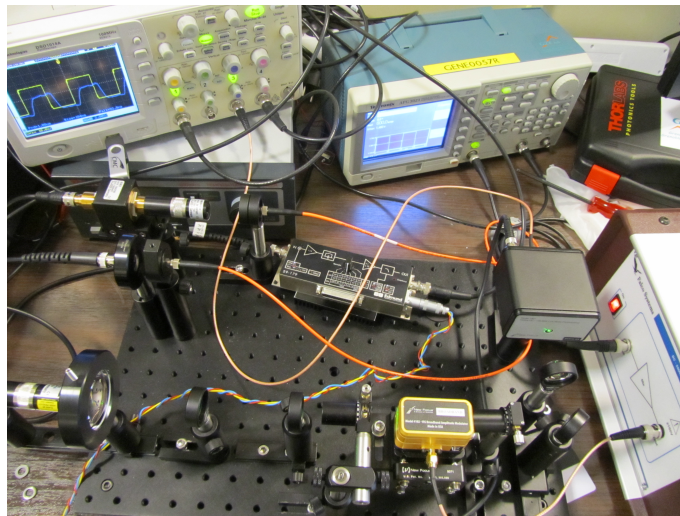


Figure III.42: External amplitude modulation with Green laser.

(EOM, New Focus 4102, 200MHz). The EOM was set up such that a 2:1 modulation extinction ratio at a 530 nm wavelength and a  $120 V_{\pi}$  were achieved as shown in the EOM transmission of figure III.43.

A linear high voltage/high frequency modulator (Falco WMA-300, 5MHz 3 dB Bandwidth with a 50 x fixed gain, +/- 150 V output) is required to drive the EOM in the case of step response or harmonic response investigation. Although the modulation bandwidth of the EOM is 200 MHz, the overall system bandwidth is limited to 5 MHz by the high voltage amplifier. The overall system bandwidth is verified by measuring the step response of a high speed detector with a bandwidth of 125 MHz and an integrated TIA as shown in figure III.44. The main drawbacks of this system are the non linearity of the EOM and the required high voltage electrical driving electronics.

In the case of indirect modulation, unfortunately large insertion losses due to coupling light into and out of the EOM and the optical fiber resulted in very low optical power

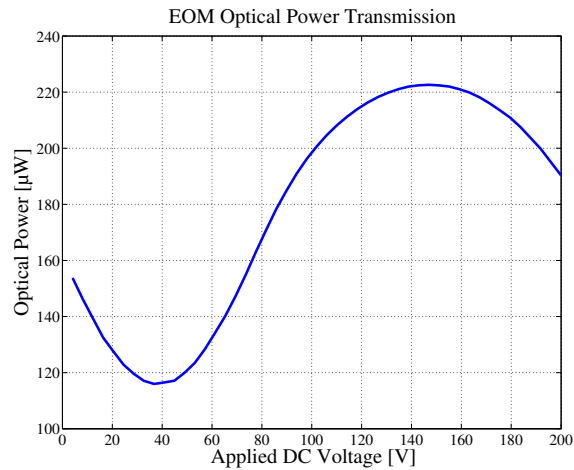


Figure III.43: The optical power transmission of the EOM versus applied DC voltages. DC voltages around 80 V are appropriate for linear region operations.

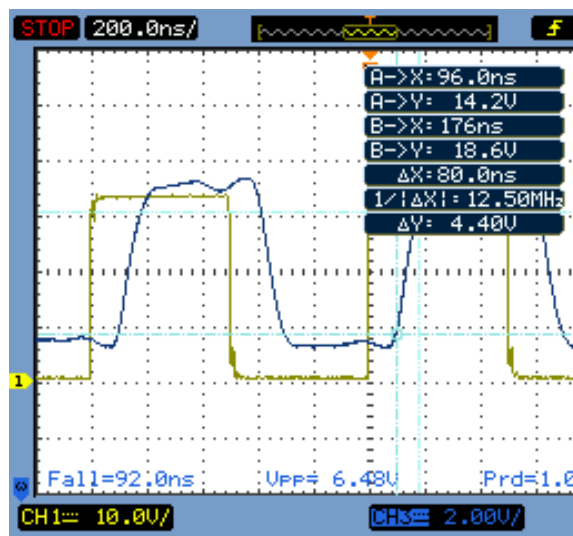


Figure III.44: The step response of the external modulation setup shows a rise time of roughly 80 ns which corresponds to a bandwidth of 4.4MHz. The green line corresponds to the high voltage amplifier input and the blue line corresponds to the voltage output after the IPD and TIA stage.

levels that we were not able to pick up by the IPDs. Reducing these losses in the future can allow the completion of this measurement approach.

### III.7.c Third Approach: Directly modulated Laser

In the case of direct modulation, a 450 nm blue laser [111] is used; this setup is shown in figure III.45.

This blue laser can only provide digital modulation of the signal and thus, only step response analysis are possible. The advantages of this approach are the elimination of

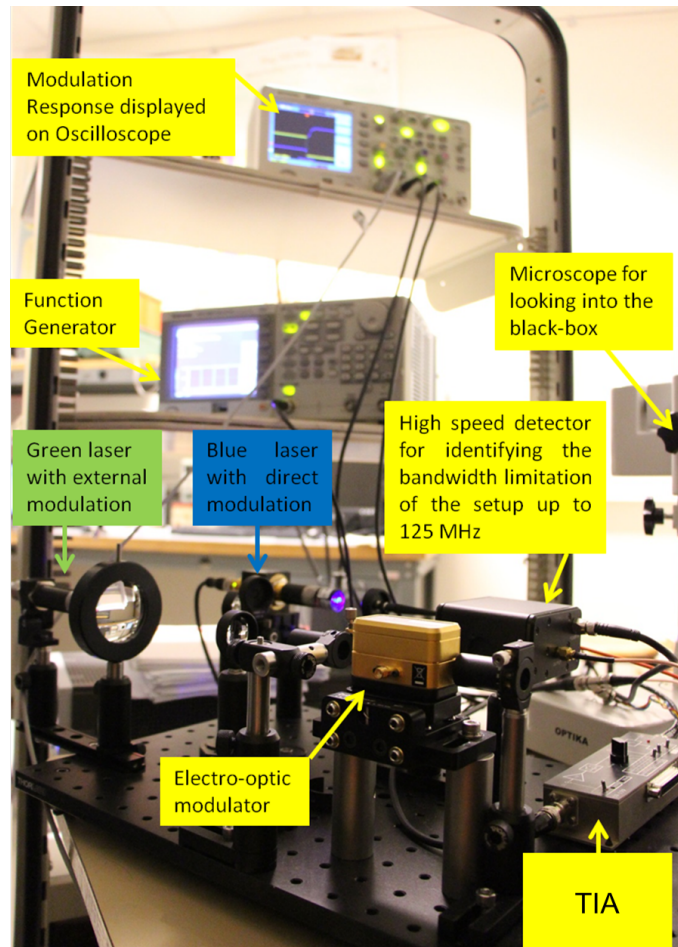


Figure III.45: Direct amplitude modulation with Blue laser.

the non linear EOM and its high voltage amplifier, moreover, the available optical power is higher (there are losses in coupling the light beam into the EOM). The level of optical power available directly effects the level of current available at the output of the IPD. Increasing the output current, allows for lower amplification requirements on the TIA unit and hence less restrictions on the TIA bandwidth. Thus, reducing the optical power insertion losses in order to increase the available optical power at the DUT is highly desirable for the AC characterization. In this setup, the blue laser is powered by a DC voltage source and TTL modulation signal is supplied by a signal generator. The laser output light is directly coupled into an optical fiber and taken into the same black box setup used for the DC analysis and then the fiber is aligned with the DUT. The output of the DUT is put into the TIA (with a low noise  $10^3 V/A$  gain corresponding to an 80 MHz cut-off frequency) and the output of the TIA is monitored on an oscilloscope. A 10 MHz filter on the Oscilloscope was used to remove external noises; however this resulted in a longer  $t_r$ . The devices have bandwidths above tens of MHz. Through visual inspection, it was observed that when lower bandwidth filters were being added to smooth out the output signal, the signal  $t_r$  started to become larger for 20 MHz filters and lower. Thus, the initial AC measurements with the blue laser indicate a high bandwidth above 20 MHz (the IPD tested was IPD D3a). For a higher  $t_r$  measurement accuracy, a PCB should be designed

in order to reduce the interconnection adaptors and wires and to bring the TIA as close as possible to the IPD. The design of an integrated TIA is under progress by Thanh Long Le [90] who is a PHD student at G2ELab currently working with Dr.Rouger and Dr.Crebier.

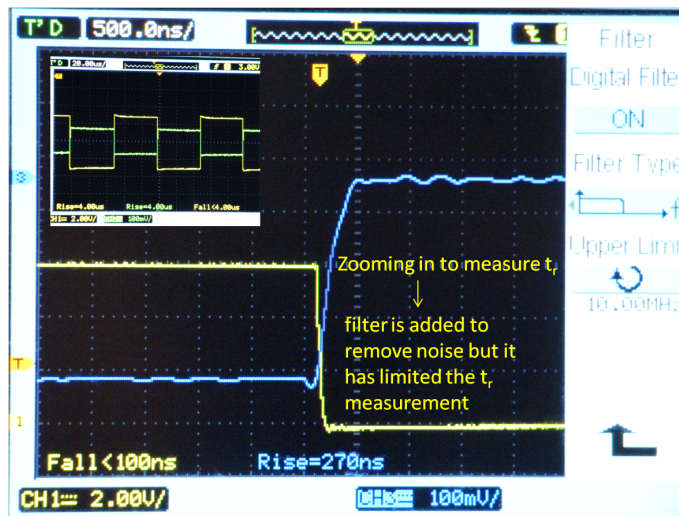


Figure III.46: IPD response to a 450 nm blue laser square signal at 10 kHz. A 10 MHz filter was used to remove external noises.

### III.8 Summary

In the duration of this thesis work, one round of fabrication was carried out, where IPDs were fabricated via the power bipolar process. An unwanted leakage of P-type dopants throughout the wafers affected the IPD characteristics resulting in a number of different complications such as a higher dark current levels and an earlier Emitter-Base junction breakdown voltage. As a result, the IPD Emitter responsivity could only be characterized for Emitter reverse voltages below 2V, the IPD avalanche mode performance couldn't be tested and the difference between IPDs with P+ and P- Base regions couldn't be studied. Nevertheless, the DC characterization of the IPDs at 1V Emitter reverse bias and as a function of Collector reverse voltages as high as 200V, show very promising results that also match closely the spectral responsivities predicted via simulations. It was demonstrated that these IPDs can have responsivities as high as 0.2 A/W when the Emitter junction is reversed biased at only 1V and a 500 nm optical source is used. It was demonstrated that the addition of an optimized (for a 500 nm wavelength)  $\text{Si}_3\text{N}_4$  ARC can increase the IPD responsivity by approximately 50% at a wavelength of 500 nm. No measurable change in the Emitter responsivity was observed for substrate DC voltages up to 200V. The AC characterization of the IPDs also show potentially high bandwidths above 10s of MHz. Based on the current results a set of long term and short term work can be planned in the future. The possible short term works on DC and AC characterization of the IPDs are as follows:

- reproducibility study: There are a number of possible error sources that may affect the measurement reproducibility and accuracy such as: the experimental setup and

fabrication non-uniformities throughout the wafer. The detailed explanation of the DC experimental setup discussed how special care have been taken in reducing measurement errors due to the setup (i.e. source meter current range settings that offer current accuracy in the order of a few hundreds of pAs, temperature control of  $\pm 0.03^\circ\text{C}$  for temperatures between  $20^\circ\text{C}$  to  $90^\circ\text{C}$ , and optical power calibration with 0.5% accuracy). The impact of fabrication non-uniformities on the measurement results can be taken into account by measuring the same IPD design on many different dies from the same wafer and plotting the average spectral responsivity with corresponding error bars. The error bars are a result of measurement variation between different dies on the wafer. These variations due to fabrication (i.e. non-uniform PR thickness) are manifested as dispersions around the designed dimensions such as the metal widths and contact opening widths. If large variations are observed, optical inspections of the devices via microscope may also help reveal the source of these variations only if they are visible in the finished devices (i.e. metal widths or misalignments).

- Contact position effects: First, the IPDs designed for studying the effect of contact positions need to be measured several times as explained above, in order to insure the differences measured are not within the range of the non-uniformity error bars. Second, changes in the IPD responsivities should be plotted as a function of shading factor where the shading factor takes into account the Gaussian nature of the optical source:  $\text{Shading factor} = (\text{The amount of optical power shadowed by contacts}) / (\text{Total amount of optical power})$ . In order to demonstrate this result, the optical power distribution of the source over the IPD illuminated area needs to be measured.
- Temperature effects: Since the IPDs have higher dark currents and breakdown voltages due to the unwanted p-type dopant leakage connecting all the p-regions throughout the wafer, the effect of temperature on the IPD dark currents may not necessarily corresponds to the intended IPD design. However, the temperature effects on the ARC optimal wavelength and photocurrent can be characterized in the current IPD devices.
- Substrate high DC voltage effects: Since the IPDs are to be integrated with 600 V VDMOSFETS, the effect of DC Substrate voltages up to 600V on the IPD performance need to be demonstrated. The IPD substrate contact is on its backside and it can be controlled by controlling the voltage of the chuck the die is place upon. In the current DC setup a 2636 Keithley source is used to control the voltage of a conductive chuck via a banana connection; however this Keithley is limited to 200Vs. Thus, a voltage source that can be operated upto at least 600V is required.
- Substrate transient effects: The setup needs to accommodate the application of fast voltage transients (i.e. [400V to 600V]/[25ns to 100 ns]) on the chuck in order to characterize the effect of substrate transients on the IPD performance.

- **Improve AC setup:** The current AC measurement setups suffer from two major challenges: (1) the reduced available optical power levels due to high insertion losses (i.e. coupling into/out of fibers, coupling into the EOM in the case of external laser modulation) require a high amplification stage after the IPD which in turn introduces bandwidth and noise limitations in the setup. (2) High noise levels from probe stations, cables, adapters, and the TIA further limit the possible measurable bandwidth with the current AC setup. A PCB can be designed to remove the probe stations and reduce the number of required cables and adapters in efforts to improve the bandwidth measurement capabilities of the setup.
- **Demonstrate switching control:** Although VDMOSFETs were not fabricated alongside the IPDs during the first fabrication round, a discrete assembly can be used to demonstrate the transfer of gating signals via the IPD to a VDMOSFET. A PCB can be designed to assemble together the IPD, its appropriate TIA stage, signal treatment stage, driver and the VDMOSFET. This approach requires that the IPDs be wire-bonded and the TIA, driver and power switches will be commercial available chips that can be soldered to the PCB tracks.
- **Reduce optical spot size:** The current achievable optical spot size is in the range of 200  $\mu\text{m}$  diameter. There are many designed devices with diameters of 100  $\mu\text{m}$  and 50  $\mu\text{m}$  that require the same size or smaller optical spot size diameters. Controlling the optical spot diameter down to 10s of  $\mu\text{ms}$  would allow studying the effect of IPD sizes and optical spot sizes on the IPD DC and AC performance.

In the long term to do list, a second round of fabrication is required with the following objectives:

- To remove the fabrication P-type dopant leakage error and in turn remove its consequent complications that limited the IPD characterizations during the first round of fabrication (i.e. IPD avalanche performance, effect of P- and P+ Base region on the different IPD designs).
- To include the IPD within the VDMOSFET. Since the first fabrication round demonstrated a number of positive outcomes that seem to suggest a fair potential for success in our proposed IPD galvanic isolation approach, the IPDs will be fabricated in the second round via the full VDMOSFET process. The finished wafer will feature power dies that include VDMOSFETs and their associated IPDs (VDMOSFET source contact connected with the IPD Base contact).
- To demonstrate the switching of a 600V VDMOSFET via the IPD on the same power die.
- To demonstrate the switching of a 600V VDMOSFET via a CMOS integrated detector using flip-chip technology.

- 
- To characterize the temperature effects on the IPD performance. Assuming there are no complications in the second fabrication round, the IPD dark currents and breakdown voltages should be closer to the simulation predictions. Thus, an accurate study of temperature effects can be performed for temperatures between 20°C-90°C using the current DC setup. The setup would need to be upgraded to allow temperature studies in the range of 100°C to 200°C as well since power chips could reach temperatures in the range of 150°C.



In summary, we have studied the potential of using the shallow pn-junction inherently available within the vertical power transistor structure as an optical receiver for transmitting the necessary gating signals from the control unit to the power switch. We have demonstrated that photodetectors can be processed via the vertical power transistor process without any cost or complexity penalties; moreover, they can be operated within the parasitic environment of the power die. Thus, we have proposed a low cost, high speed, low power optical galvanic isolation integrable within the power die. Several different IPDs were simulated, designed, fabricated and characterized. The contributions during this research include:

- Fabrication via the power bipolar process of (1) test structures such as contact chains, transfer length method (TLMs) structures and SRP pads for process control, (2) 600V vertical power diodes, (3) 600V vertical power bipolar junction transistors, (3) flip-chip integration dies, (4) high voltage IPD designs with DRIE termination, (5) high voltage IPD designs with guard ring termination, and (6) low voltage IPDs. Several different IPDs were designed with varying Emitter and Base doping region and contact geometrical shapes and dimensions including: simple rings, nested, pixelated, and comb structures. The IPDs were coated with a  $\text{Si}_3\text{N}_4$  anti reflective coating optimized for maximum optical transmission at a wavelength of 500 nm. 8 physical 5" masks were designed for this process.
- Demonstration of low power, high efficiency IPDs using the 600V power VDMOSFET compatible fabrication process, with responsivities as high as 0.2 A/W when the Emitter junction is reversed biased at only 1V and a 28nW, 500 nm optical source is used. The addition of an optimized (for a 500 nm wavelength)  $\text{Si}_3\text{N}_4$  ARC resulted in an increase in the IPD responsivity by approximately 50% at a wavelength of 500nm.
- Demonstration of IPDs fabricated via the 600V power VDMOSFET compatible fabrication process, whose output is not affected via high substrate DC voltages up to 200V; thus, making them suitable for tolerating the high DC floating voltages of the power VDMOSFET.
- Demonstration of IPDs with high bandwidths above 10s of MHz.
- Development of an electro-optical characterization system including a broad band optical source with an optical wavelength range of 200nm to 1600nm with a 0.1nm selectivity resolution, an optical power calibration stage, temperature control and computer control.

In order to complete the full characterization of the proposed IPD the following near future work are suggested:

- Substrate Tests: The effect of high voltage transients (i.e. [400V to 600V]/[25ns to 100ns]) and DC voltages up to 600V on the IPD performance,
- Full Bandwidth Analysis: The IPD bandwidths as a function of optical wavelength, applied voltages, optical beam radii and IPD size and geometry,
- Noise and Temperature: The effect of Temperature on the IPD DC and AC performance (signal-to-noise ratio as a function of temperature).
- Planar Hybrid Integration: The driving approach can be validated by switching a commercial VDMOSFET by the IPD. The IPD can be connected to its appropriate CMOS processing chip (including the TIA + K voltage gain, a gate driver and an efficient self driver supply) and a VDMOSFET via a planar integration approach on a PCB as depicted in figure IV.1.

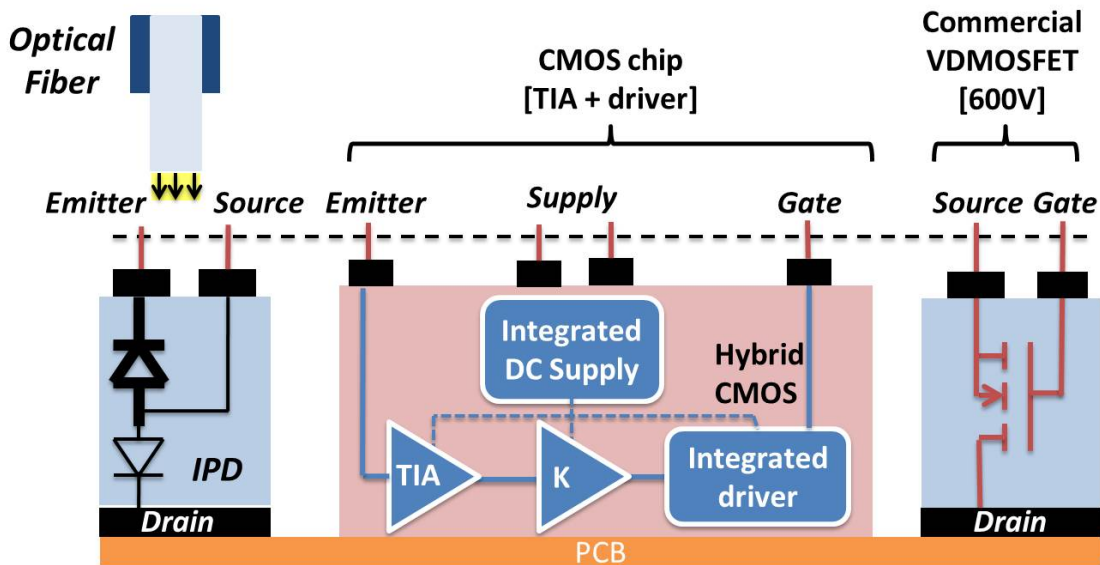


Figure IV.1: Approach verification via a planar hybrid integration on PCB.

The long term goal is to develop a fully integrated, power-efficient power function including a suitable optical galvanic isolation, its associated signal processing and power switch driver circuitries, and the power switch. The suggested long term future work includes:

- Mixed (Monolithic + Hybrid) Planar Integration: The power die (this is the monolithic component including the IPD and VDMOSFET) can be connected to its appropriate CMOS processing chip (including the TIA + K voltage gain, a gate driver and an efficient self driver supply) via a planar integration approach on a PCB in order to demonstrate the switching action of the VDMOSFET as controlled by the

---

IPD. A direct bonded copper (DBC) would be used for better insulation between chips and effective heat dissipation. Light can be supplied to the detector by means of an optical fiber or an edge emitting laser depending on the IPD design. This planar hybrid integration can also be tested with the IPD integrated within the CMOS chip rather than the power die,

- **Flip-Chip Hybrid Integration:** a CMOS chip with readout circuit (TIA + K voltage gain), a gate driver and an efficient self driver supply, is flip-chipped on the power die (including the IPD and VDMOSFET). In order to demonstrate the controlled switching action of the VDMOSFET, the IPD can be triggered by (a) light that is edge or vertically coupled by means of an optical fiber, (b) a flip-chip optical interconnect chip that provides light coupling by means of grating couplers and waveguides, (c) an optical source such as an LED or an edge emitting laser aligned to edge trigger the IPD in free space, or (d) optical signals by waveguides and grating couplers.
- **Smart Power Chip Integration:** The necessary TIA, processing and driver circuitry are integrated within the power die along side the IPD and VDMOSFET in order to investigate the potential of a fully integrated power function. This solution is depicted in figure IV.2.
- **Integrated optical routing interface:** An compatible integrated optical routing and interface needs to be designed for the optical triggering of the IPD as depicted in figure IV.3. Specially in the case of integrating passive optical elements such as waveguides and grating couplers, temperature effects need to be investigated to insure reliability.
- **Optical Detection and Supply Integration:** In addition to the IPD that has been developed in this thesis to transfer the gate signal, a second IPD biased under the conditions of a solar cell could be integrated to provide the necessary power supply. The generated voltage at terminals of this second IPD can be converted by a DC-DC converter to charge a storage capacitor for power supply purposes. This approach can simplify the CMOS circuitry since the floating power supply is eliminated. In this case, a more powerful optical source with a DC and AC component would be required in order to deliver both the energy and the gating signal. One option to investigate is the integration of the two optical detectors in the CMOS processing chip which is connected to the power die on a DBC via wire bonding. A second option would be to integrate the two optical detectors in the smart power die as depicted in figure IV.4. Since the second IPD is used as a solar cell to output a voltage, it needs to be forward biased; in this case the parasitic bipolar is an issue and needs to be suppressed from turning on.

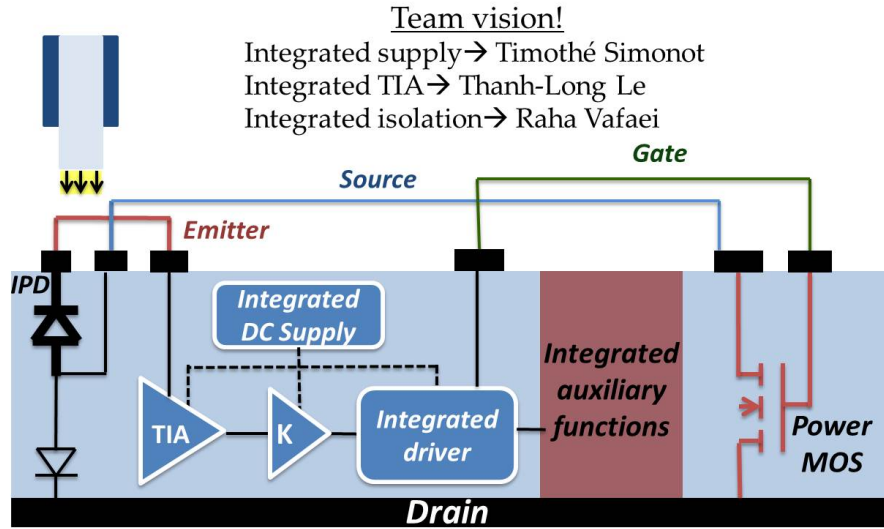


Figure IV.2: Smart power chip integration approach.

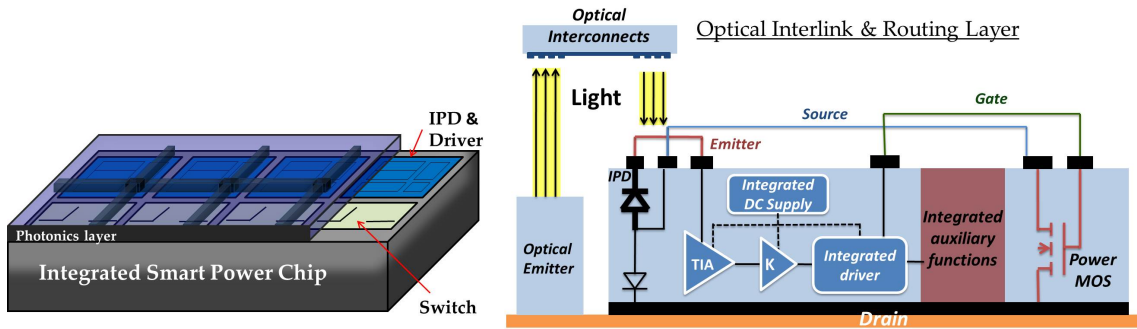


Figure IV.3: Smart power chip with an integrated photonic chip that provides at minimum the optical routing interconnects as well as the necessary grating couplers.

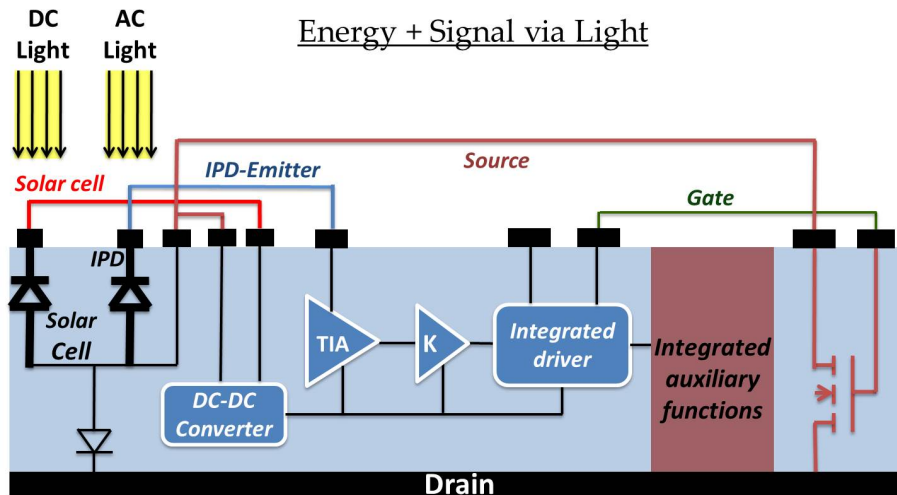


Figure IV.4: In addition to the IPD, a second IPD biased under the conditions of a solar cell could be integrated to provide the necessary power supply.

### SOMMAIRE

---

V.1 INTRODUCTION ET MOTIVATION: INTÉGRATION MONOLITHIQUE D'UNE ISOLATION OPTIQUE . . . . .	166
V.1.a L'Etat de l'Art et les Objectifs du Projet . . . . .	167
V.1.b Approches d'intégration et la Structure de IPD . . . . .	171
V.2 SIMULATIONS ET CARACTÉRISATION . . . . .	173
V.3 CONCLUSIONS . . . . .	175

---

### Abstract

*Dans les convertisseurs de puissance, les interrupteurs de puissance peuvent fonctionner à de niveaux de tension élevés. Dans ce cas, leurs commandes externes qui fonctionnent à de tensions plus basses doivent être électriquement isolées. Des transformateurs ou d'optocoupleurs ont été traditionnellement mis en oeuvre afin d'isoler les commandes rapprochées. Cette thèse présente une nouvelle solution optique dans laquelle un détecteur optique est intégré de façon monolithique au sein d'un transistor de puissance de 600 V à l'aide de sa structure verticale. Ce détecteur optique intégré (IPD) fournit un faible courant à une commande rapprochée qui va ensuite l'amplifier afin de commander le transistor de puissance. La commande rapprochée peut être représentée par une composant type flip-chip ou elle peut également être monolithiquement intégrée. L'IPD a une très faible consommation, une bande passante élevée (BW) et de l'isolation galvanique optique entre le dispositif d'alimentation et sa commande. Les contraintes imposées par la structure du dispositif d'alimentation et sa fabrication limitant les performances de l'IPD sont étudiées ainsi que son mode de fonctionnement. Des analyses ont été conduites suite à de travaux de modélisation analytique, des simulations avec la méthode des éléments finis et de validation expérimentale. La responsivité spectrale ( $R$ ) des détecteurs de 400 nm à de longueurs d'ondes proches au spectre infrarouge a été mesurée et une valeur maximale de la responsivité de 0,2 A/W à 500 nm a été atteinte. Les résultats des mesures montrent une faible capacité de l'émetteur de l'ordre de 35 pF à 10 pF pour de détecteurs de diamètre dentre 50  $\mu\text{m}$  à 200  $\mu\text{m}$ . Les premières mesures AC indiquent une BW au dessus de 20 MHz.*

## V.1 Introduction et Motivation: Intégration monolithique d'une isolation optique

L'application principale de cette étude, est liée plus généralement aux technologies de l'électronique de puissance. L'objectif pour l'électronique de puissance est la gestion et la modulation de transfert d'énergie électrique avec un rendement élevé. Avec l'utilisation généralisée de l'électronique dans l'industrie, le transport, le médecine et les secteurs de la consommation, les systèmes électroniques de puissance jouent un rôle plus important dans le paysage énergétique, à la fois en termes d'efficacité et de coût. La figure V.1 montre du large spectre d'applications balayé par les convertisseurs de puissance. Un baisse performance des convertisseur de puissance peut causer des impact significatif sur l'environnement et l'économie. En conséquence, il y a un intérêt croissant envers les conceptions innovantes qui peuvent améliorer la qualité de la conversion de puissance à haut niveau d'efficacité. Dans cette optique, les solutions intégrables et génériques à des coûts maîtrisés sont particulièrement attendues.

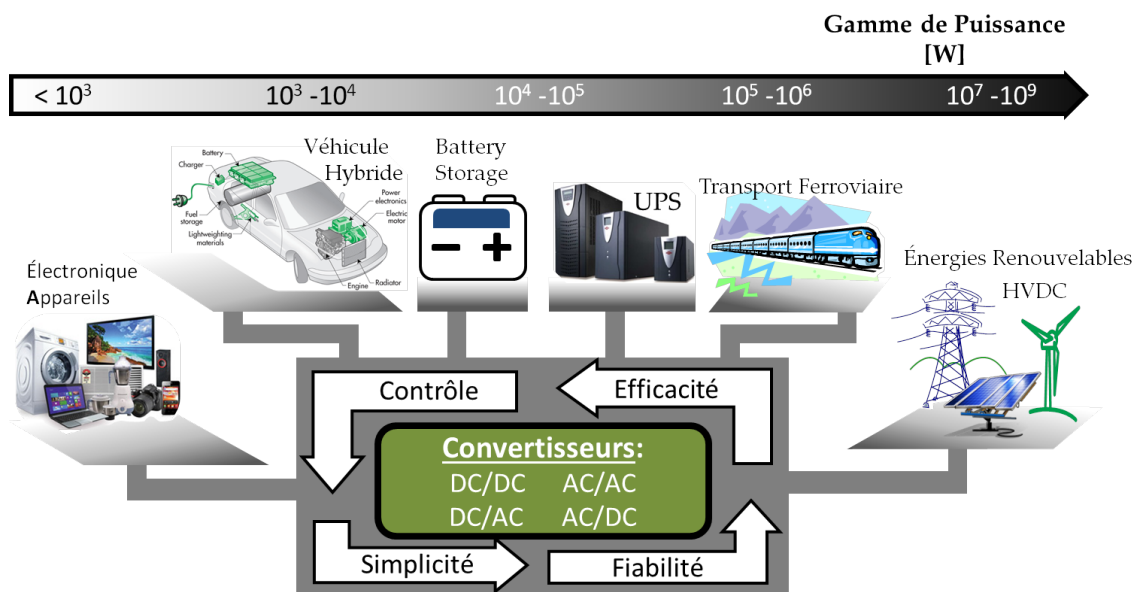


Figure V.1: Solutions en électronique de puissance étant utilisés pour une large gamme d'applications.

La convertisseur de puissance peut se subdiviser lui-même en plusieurs sous-systèmes, tels que les composants actifs, les composants passifs, les organes de contrôle et de commande, et la gestion du refroidissement. La figure V.2 montre les plusieurs sous-systèmes fonctionnels et structurels qui constituent une convertisseur d'énergie ainsi que les échanges permanents de chaleur et électromagnétiques entre les composants.

Le circuit externe de commande génère des ordres de commutation et il fonctionne avec des signaux de basse tension alors que la commande rapprochée contrôlant de façon optimale la charge et décharge de la capacité d'entrée du composant de puissance peut-être qu'il faut fonctionner sous haute tension (les transistors High Side dont le potentiel de

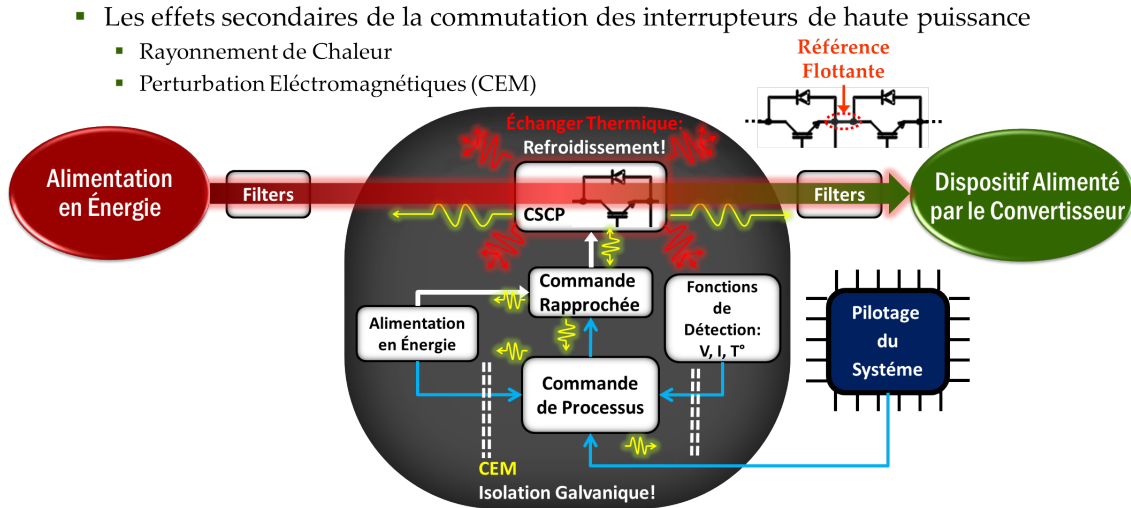


Figure V.2: Fonctionnement d'un interrupteur et l'environnement associé au sein du système. Les rayonnements électromagnétiques et thermiques entre les fonctions au sein du système de l'interrupteur d'alimentation sont illustrés.

référence sont flottant par exemple). Il est nécessaire donc d'utiliser un étage d'isolation galvanique entre le circuit externe et la commande rapprochée.

Dans le but d'effectuer une isolation galvanique de haut niveau parmi des solutions optique au sein des convertisseurs de puissance, particulièrement entre les composants de puissance et la partie commande, l'intégration monolithique d'un détecteur optique sur un composant MOSFET vertical 600V est proposé dans cette thèse. Cette intégration est réalisée sans modification du procédé de fabrication VMOS. Maintenant, nous allons examiner brièvement quelques-uns des différentes méthodes de isolation galvanique entre le circuit externe de commande et la commande rapprochée.

### V.1.a L'Etat de l'Art et les Objectifs du Projet

Les solutions existantes pour réaliser l'isolation galvanique entre la commande externe et la commande rapprochée sont nombreuses et comprennent: les transformateurs électromagnétiques ou piézoélectriques (numériques ou pulsé), les optocoupleurs, les fibres optique, les coupleurs capacitifs ou par les émetteurs et les récepteurs de radiofréquence. En général, il existe deux approches principales: (1) une unité d'isolement galvanique qui fournira seulement le signal d'information généré par le circuit externe. Dans ce cas, le signal isolé doit ensuite être amplifié par les circuiteries supplémentaires afin de fournir l'énergie nécessaire pour la commutation du transistor de puissance. (2) Une unité d'isolement galvanic qui isolera et transmettra un signal déjà amplifié avec l'énergie suffisante.

La plupart des solutions de transfert isolé d'ordres de commutation aujourd'hui sont majoritairement des solutions discrètes. Ces solutions discrètes limitent les tailles des structures de conversion ainsi les possibilités d'intégration dans les cas d'un nombre élevé de semiconducteurs à piloter. Les possibilités d'intégration de ces modes d'isolation reposent

sur la compatibilité fonctionnelle et des procédés technologiques spécifiques qu'il faudra associer à ceux des composants de puissance. la figure V.3 (a) montre un exemple de micro-transformateur qui est intégré monolithiquement avec un transistor the puissance, son circuit de pilotage complète et son circuit de alimentation. Cette solution se traduit par une faible consommation et un design très compact dont la fabrication est compatible avec CMOS. La propriété du matériau et de l'épaisseur de la couche diélectrique limite les performances d'isolation de cette conception, à peu près, jusqu'à 5 kV. Dans le cas des transformateurs d'impulsions (figure V.3 (b)) il est possible de fournir à la fois la signal isolé et ainsi que l'énergie nécessaire mais c'est toujours une solution discrète. La figure V.3 (c) représente une solution de transformateur numérique intégré par Analog Devices. Il s'agit d'un produit commercial qui utilise une approche similaire à celle de la figure V.3 (a) sauf qu'il s'agit d'une intégration au niveau du PCB, et non pas sur une seule puce.

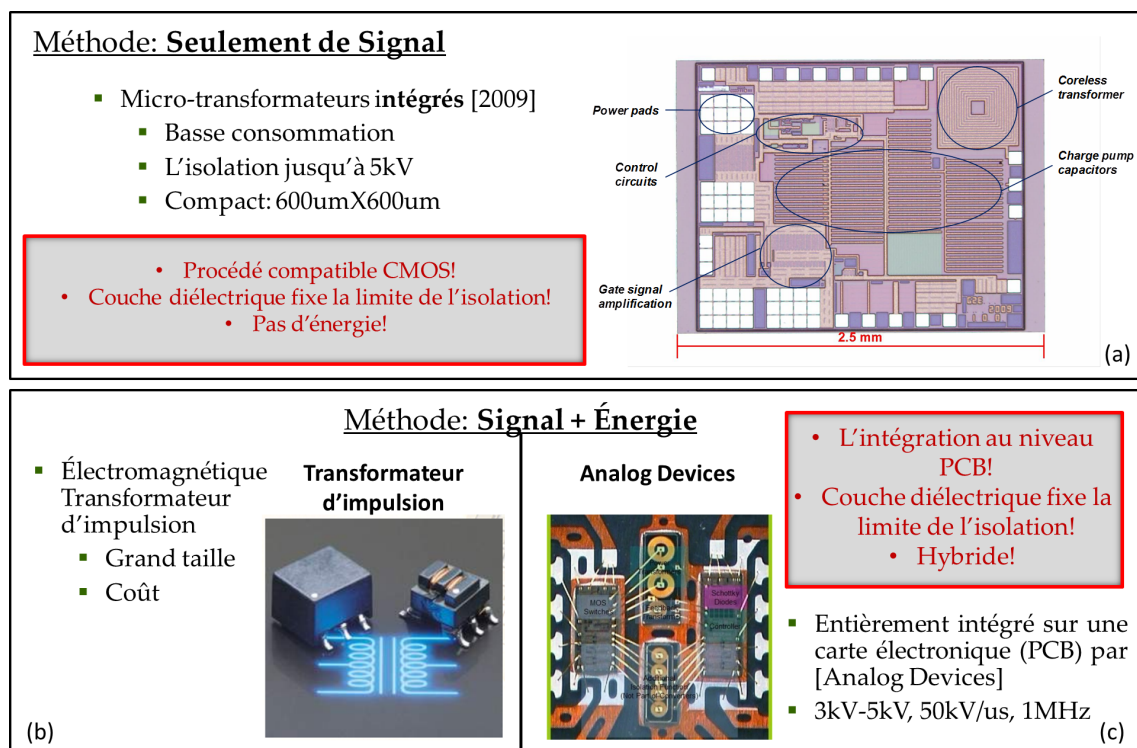


Figure V.3: (a) Micro-transformateurs intégrés [104] [112] (b) Transformateur d'impulsion, (c) Micro-transformateurs intégrés par Analog Devices [29].

Puisque la lumière permet d'avoir le plus haut niveau d'isolation galvanique, des méthodes qui permettent son intégration monolithique avec les dispositifs de puissance présentent un intérêt que la communauté électronique de puissance aspire à une fonction de puissance totalement intégrée. Un dispositif d'isolation optique déjà très bien connue est l'optocoupleur (figure V.4). La performance de l'optocoupleur est cependant limitée par son packaging et par la distance entre la LED et le détecteur ainsi que le matériau diélectrique à l'intérieur de packaging. L'opto-coupleur isole uniquement le signal et donc une étape d'amplification supplémentaire est nécessaire pour fournir l'énergie requise. En plus, les optocoupleurs sont des solutions discrètes.

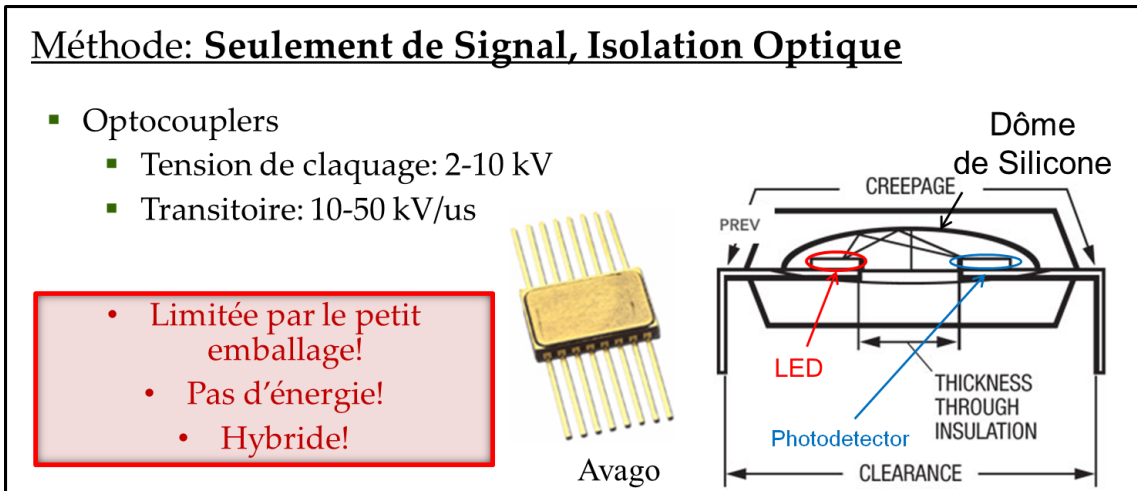


Figure V.4: Optocoupleurs [49] [51].

Pour les applications où les niveaux d'isolation très élevées sont nécessaires, le signal est isolé par des fibres optiques (figure V.5 (a)). Les postes de redressement HVDC et les compensateurs statiques d'énergie réactive SVC sont les seules applications qui ont besoin d'être déclenché directement par la lumière. Dans cet approche, l'énergie de déclenchement est transportée par fibre optique et elle est transmise au composant de puissance (des thyristors) via une connectique adaptée.

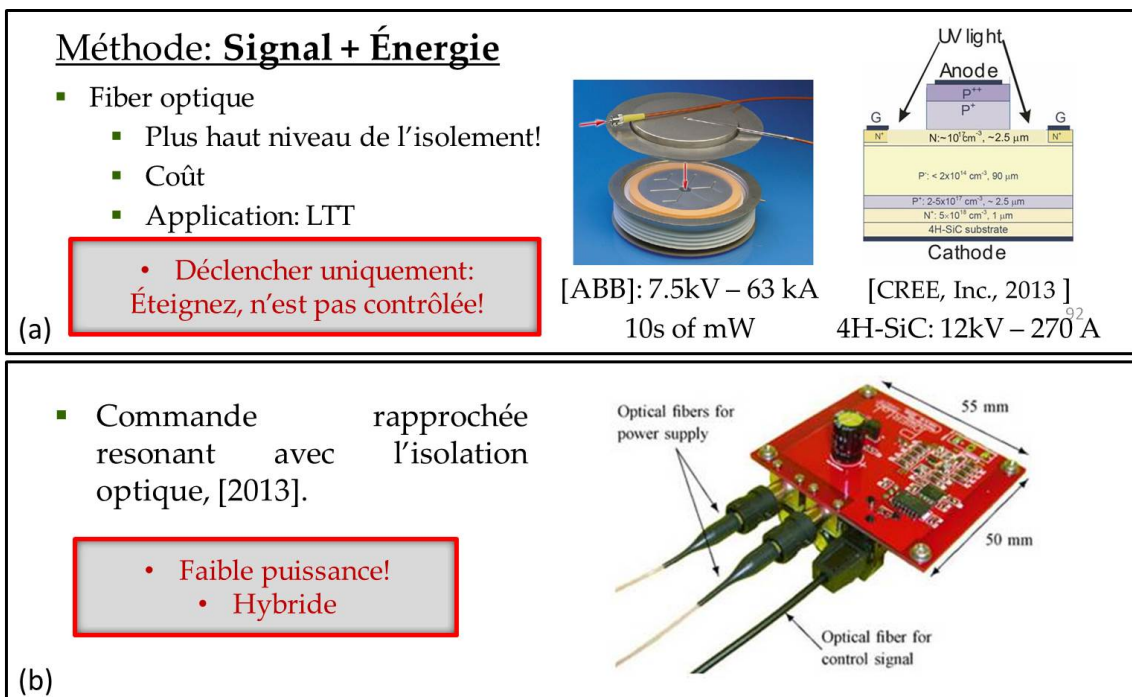


Figure V.5: (a) Thyristor à déclenchement optique [70][73], (b) Commande rapprochée résonante avec un signal de commande opto-isolé et avec son alimentation [76].

En 2013, Dr. Fujita présenté dans IEEE transactions électroniques de puissance, une isolement optique énergie + signal (figure V.5 (b)), où l'alimentation DC est composée de deux diodes laser (SDL-2320-L2: JDSU) onde entretenue à 400 mW connectés via deux fibres optiques de 1,5 m, à deux convertisseurs photovoltaïques de puissance (PPC-12E: JDSU) de 12V appropriés dans la gamme de 810 nm de longueur d'onde. L'isolement du signal de commande de déclenchement a été fournie par une connexion de fibre optique entre un émetteur optique (GP1FAV55TK0F: SHARP) et son récepteur (GP1FAV55RK0F: SHARP). Le clé pour accomplir les exigences du niveau de puissance optique est celui de baisser la consommation de puissance du conducteur.

Dans sa thèse en 2008, le Dr. Nicolas Rouger a proposé un détecteur optique qui pourrait être réalisé en utilisant la même procédé de fabrication utilisé pour la construction du dispositif de puissance VDMOSFET; ce détecteur optique peut alors être utilisé comme un dispositif d'isolement galvanique monolithique. Quatre structures ont été considérés comme représenté sur la figure V.6. Il a été trouvé que seulement le jonction émetteur/base au dessus pourrait être utilisée car la jonction base/collecteur sera fortement affecté par les tensions flottantes du contact de substrat de la face arrière du dispositif de puissance.

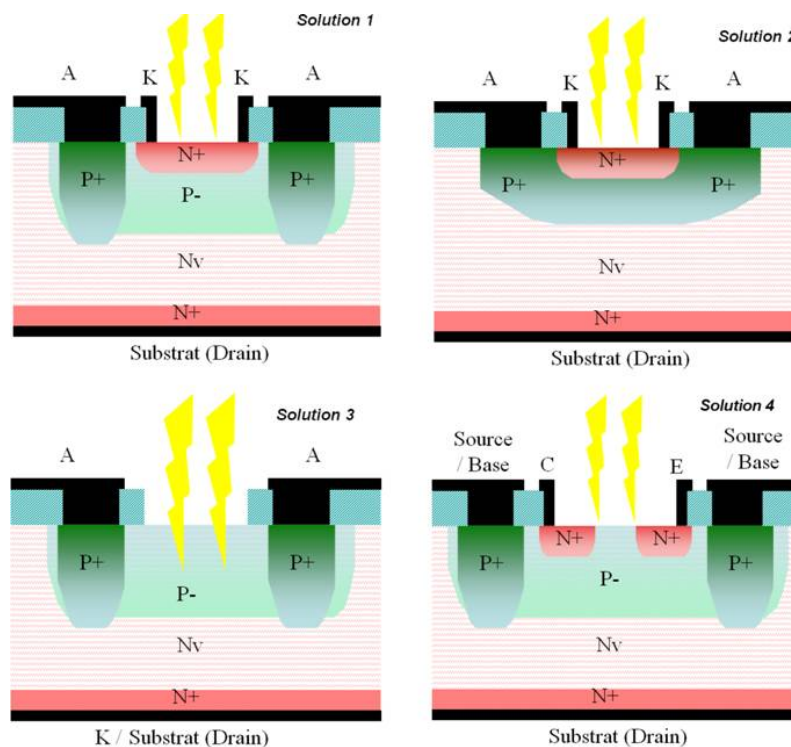


Figure V.6: Solutions possibles pour un photorécepteur utilisant le procédé de fabrication VDMOS. [88].

Figure V.7 montre le design d'un Photodiode Intégrée (IPD) avec une diamètre de 100  $\mu\text{m}$  qui a été fabriqué en 2008 et sa caractéristique courant-tension (IV) en fonction d'une lumière incidente arbitraire (à gauche: sans lumière, à droite: avec la lumière). En utilisant la mesure de courant-tension-lumière (LIV), sa sensibilité a été estimée à 0,03 A/W avec

un laser non-étalonné de 600 nm en longueur d'onde.

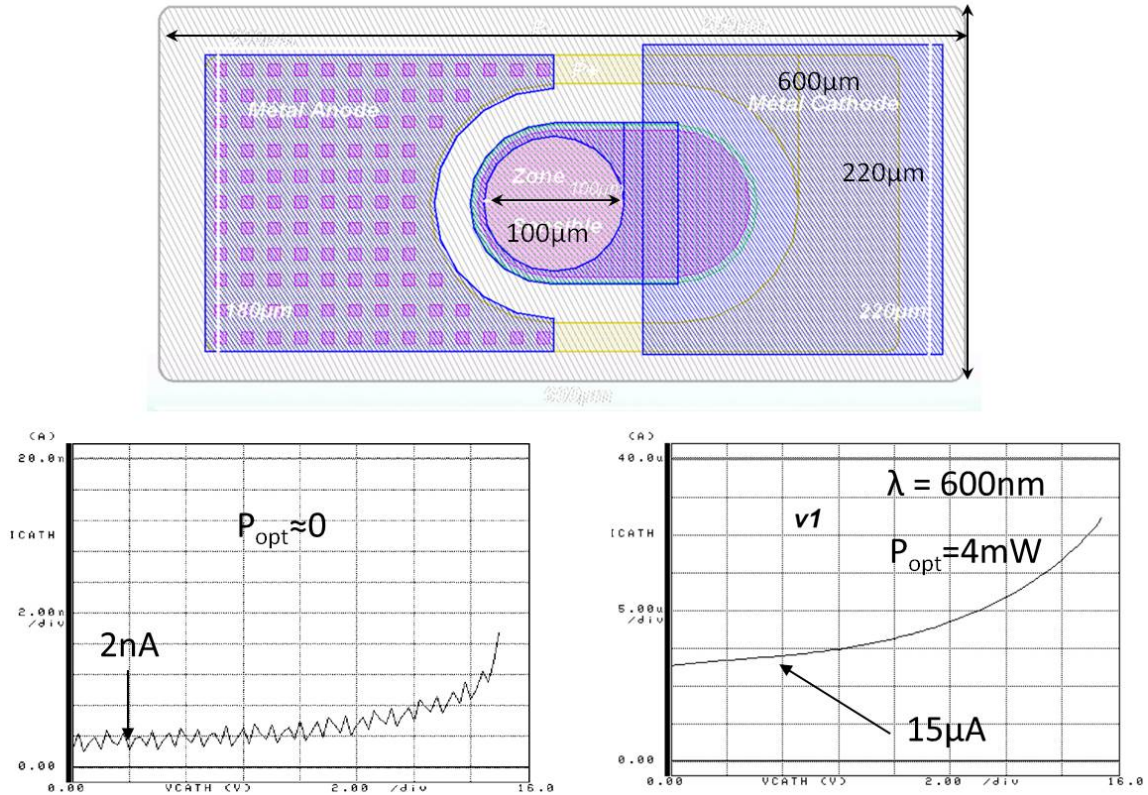


Figure V.7: Dessus: Conception sous Cadence du récepteur optique avec un diamètre de 100  $\mu\text{m}$  et de substrat de charge périphériques P+ [37] [88]. Bas: Caractéristique statique inverse des variantes du récepteur optique. à gauche, sans lumière, à droite: avec la lumière [37] [88].

Bien que les premiers résultats sont prometteurs, des analyses plus approfondie de expérimentale et modélisation aux côtés des systèmes de mesure DC et AC plus précis et avancés sont nécessaires pour une caractérisation complète de l'IPD; seulement dans ce cas, il peut être déterminé si le projet IPD est vraiment un candidat approprié et compatible pour l'intégration monolithique avec les interrupteurs de puissance verticaux 600 V.

### V.1.b Approches d'intégration et la Structure de IPD

Le façon d'implémenter le IPD dans la chaîne de commande de l'interrupteur de puissance est présentée dans le figure V.8. Une interface optique est intégrée au sein même du composant de puissance (des fonctions intégrées pouvant éventuellement être intégrées au sein même du composant de puissance) et elle peut être déclenché par un faisceau optique avec quelques  $\mu\text{W}$ s de puissance, ainsi il permet une gamme de faible puissance, à faible coût, et de petites sources optiques tels que des lasers à semi-conducteurs et les LEDs. La sortie du détecteur optique sera un signal de courant dans la gamme de quelques 100s de nA. Ce signal de courant de sortie ne contient que l'information de commande; afin de fournir

l'énergie suffisante requise pour commuter le VDMOSFET, le signal de sortie du détecteur optique est amplifié à un étage de TIA avant d'alimenter la grille du VDMOSFET.

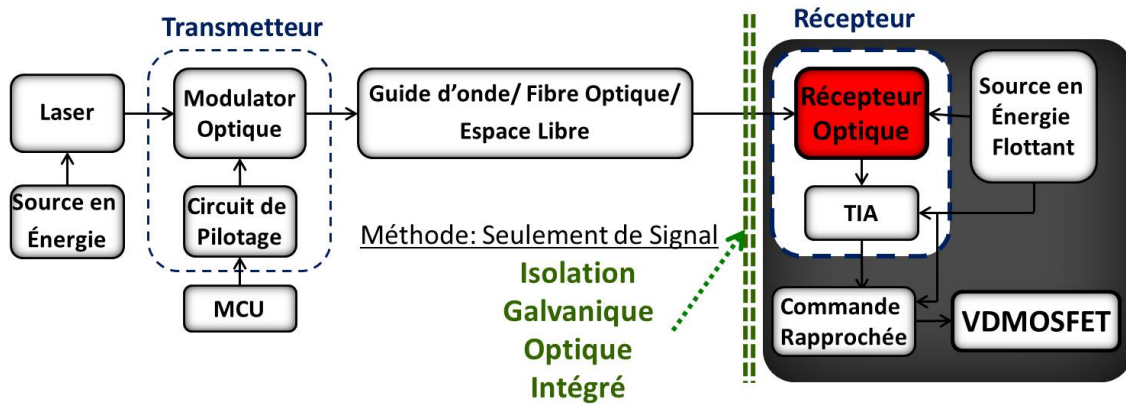


Figure V.8: Liaison optique appliquée à la commande des transistors de puissance.

Le IPD se basent uniquement sur la structure du transistor bipolaire vertical N<sup>+</sup>/P<sup>-</sup>/N<sub>v</sub>/N<sup>+</sup>, élément structurel des composants de puissance VDMOS. La figure V.9 démontre la compatibilité technologique entre la VDMOSFET et l'IPD en comparant une vue en coupe de leurs structures. Nous avons proposé d'utiliser la jonction Emetteur (N<sup>+</sup>)/Base (P<sup>-</sup>) comme interface optique, en maintenant toujours le potentiel de Base au potentiel le plus bas (en l'occurrence la Source du VDMOSFET) du composant monolithique. Dans ces conditions, l'auto-isolation de la jonction Emetteur/Base est ainsi toujours assuré. La représentation du circuit de l'approche d'intégration choisi et l'étude est présenté sur la figure V.10.

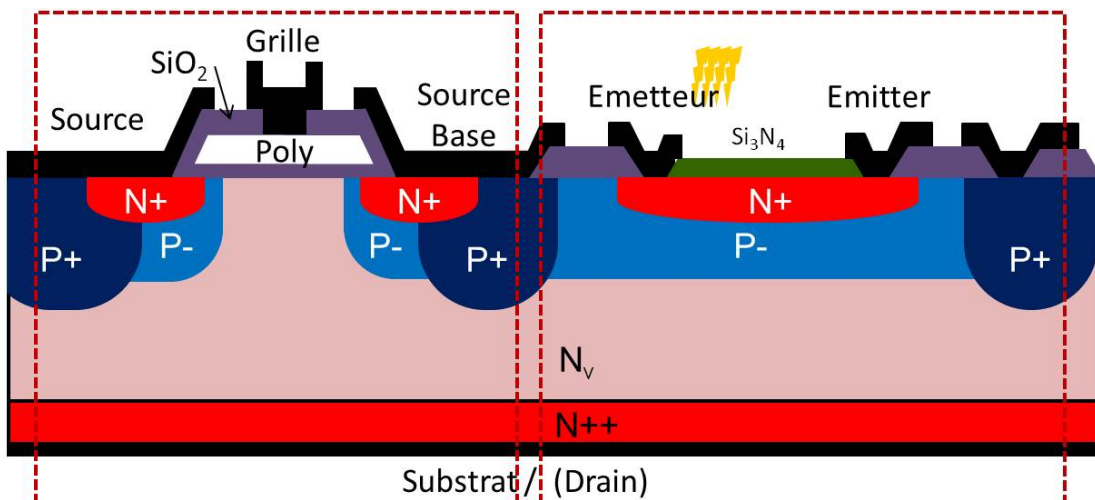


Figure V.9: Le transistor NPN vertical utilisé pour les éléments qui composent le détecteur à intégrer

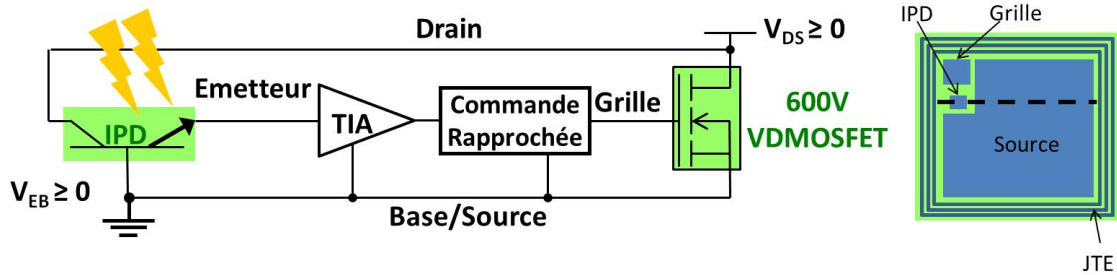


Figure V.10: La représentation du circuit de l'approche d'intégration choisi et l'étude

## V.2 Simulations et Caractérisation

Dans cette section, nous allons présenter seulement une petite partie du travail de cette thèse, notamment: les résultats de simulation par éléments finis des courants DC de l'émetteur, base et collecteur en fonction de la longueur d'onde optique, et les caractéristiques statiques et dynamiques de l'IPD.

S'il vous plaît se référer au chapitre 2 de la thèse (en anglais) où des résultats de modélisation et de simulation par éléments finis pour les structures IPD possible révèlent les mécanismes de fonctionnement de l'IPD et ses performances statiques et dynamiques en fonction de la longueur d'onde optique d'entrée, la puissance optique, la position du rayon optique, petite fréquence du signal et de polarisation de l'IPD. En outre, les restrictions imposées par la structure du dispositif d'alimentation vertical et le dispositif d'alimentation flottant potentiel de substrat, sur la performance IPD et le mode de fonctionnement sont analysés par la modélisation et la simulation. Reportez-vous également au chapitre 3 pour plus de détails sur les conceptions de masque, procédé de fabrication, la conception des banc de caractérisation, et l'analyse de mesure différente.

Figure V.11 (a) représente la réponse spectrale optique des différents courants circulant à travers la structure qui ont été obtenus de simulations par éléments finis dans l'Atlas. Le photocourant émetteur est maximisée pour des longueurs d'onde optiques autour de 500 nm, en attendant le photocourant Collecteur est maximisée pour des longueurs d'onde optiques autour de 850 nm. Figure V.11 (b), montre les QEs de l'IPD correspondant aux courants de la figure V.11 (a). Dans ces simulations, une largeur de faisceau optique égale à la surface photo-sensible exposée de la région d'émetteur est utilisé dans le but de montrer l'efficacité maximale obtenue sans perte de contact d'ombre.

Figure V.11 (c) montre les responsivités pour le cas de 100% QE en rouge et après pertes de réflexion en vert ainsi que les responsivités internes et externes de l'IPD (émetteur) en bleu et noir respectivement. Comme on peut le voir, la responsivité IPD s'écarte sensiblement du cas idéal. Les responsivités extérieures des différentes régions de la structure sont présentés sur la figure V.11 (d).

Les IPDs ont été fabriqués avec un processus qui est 100% compatible avec le processus de fabrication de l'interrupteur d puissance vertical et donc il n'y a pas de

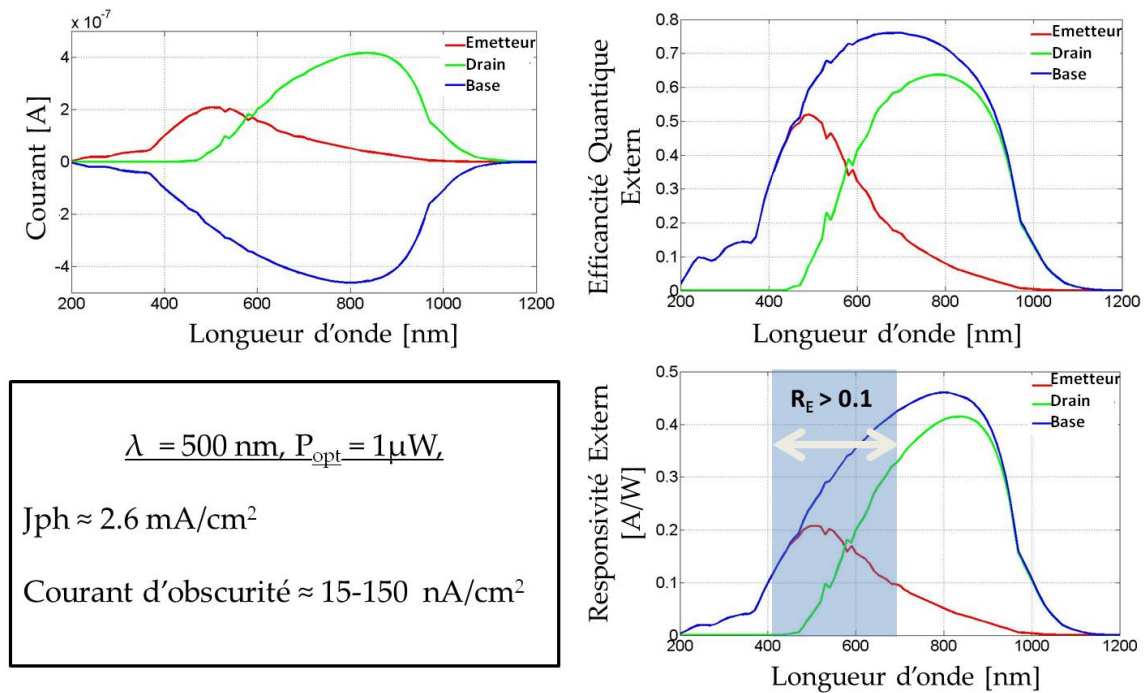


Figure V.11: Résultats de la responsivité spectrale de  $V_E = V_C = 1 \text{ V}$ ,  $\tau_n = \tau_p = 1 \mu\text{s}$ ,  $P_{\text{opt}} = 1 \mu\text{W}$  pour un IPD avec un diamètre de Emetteur à  $50 \mu\text{m}$ . (A) courants spectrales et leurs (b) QEs correspondant de les régions de l'émetteur, collecteur et la base de l'IPD. (c) dans le cas de 100% QE des pertes en rouges et après réflexion en vert. Les responsivités internes et externes de l'IPD (émetteur) sont en bleu et noir respectivement. (d) Les composantes de la réponse spectrale avec un faisceau optique uniformément répartie correspondant à les régions d'émetteur, collecteur et la base de l'IPD. Le rayon du faisceau est de  $37 \mu\text{m}$ , qui est égale à la surface exposée de la région d'émetteur. Ainsi, il n'y a pas de pertes d'ombrage.

frais supplémentaires ou des pénalités de complexité de traitement. Quelques échantillons fabriqués sont représentés sur la figure V.12.



Figure V.12: Images au microscope de quelque détecteurs fabriqués.

Afin de permettre la caractérisation des performances et de la dépendance de la sensi-

bilité en fonction de la tension du substrat jusqu'à 600 V, Certains composants ont aussi été intégrés au sein d'une périphérie en tension. Les caractéristiques statiques et dynamiques de IPD sont présentées sur les figure V.13 (a) et (b). La sensibilité spectrale des détecteurs intégrés est de l'ordre de 0.2 A/W (figure V.13 (b)) pour une longueur d'onde optique de 500 nm et par conséquent, la minimisation de la puissance optique garantit la détection d'information. Une bande passante de 10 MHz a été mesurée (figure V.13 (b)), limitée actuellement par notre banc de caractérisation.

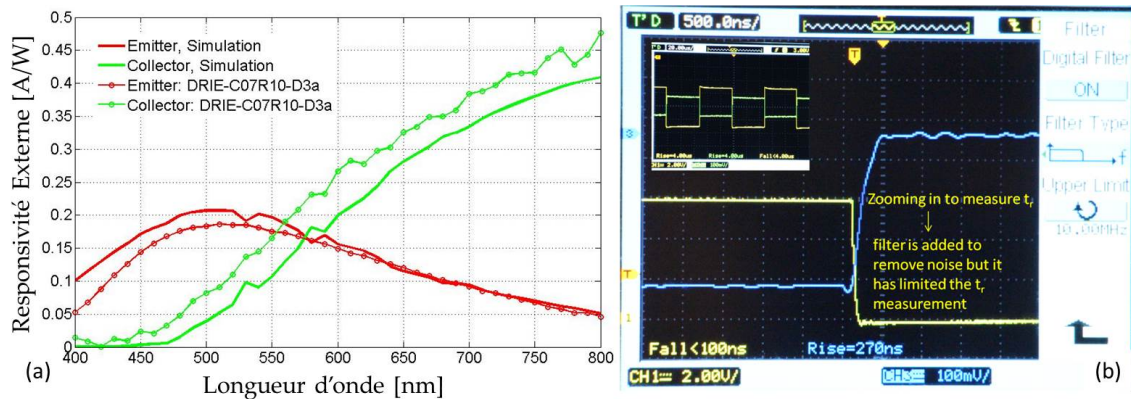


Figure V.13: (a) Simulation (traits pleins) et caractérisation de la sensibilité spectrale statique. (b) Mesure de la réponse indicielle d'un détecteur optique.

### V.3 Conclusions

Une solution de transfert isolé d'ordres de commutation pour composants de puissance a été conçue, fabriquée et caractérisée, afin de réaliser une isolation galvanique performante et intégrée. Une solution optique et haute fréquence a été présentée et mise dans son contexte qui démontre une sensibilité au-delà de 0.2 A/W et d'une bande passante au-delà de 10 MHz. Ces valeurs sont à ce jour les plus élevées mesurées dans des applications d'intégration fonctionnelle monolithique puissance commande et tout à fait compatibles avec l'utilisation dans le contexte des convertisseurs d'électronique de puissance. Afin de valider notre solution optique proposée, cette approche doit maintenant être transférée pour le pilotage de plusieurs semiconducteurs de puissance à potentiels de référence flottants.

---

## MONOLITHIC INTEGRATION OF A PHOTODETECTOR FOR CONTROL PURPOSES WITHIN VERTICAL POWER TRANSISTORS

**Abstract** The work presented in this PhD manuscript deals with the monolithic integration of an optical galvanic isolation unit within the vertical FET structure of a 600V power transistor. The optical galvanic isolation unit is a photodetector that is responsible for transferring the gating information signal from an external control unit to the power switch. The necessary energy to switch the power device is provided by means of a TIA followed by a gate driver. This document has four chapters: introduction and motivation: Integrated galvanic isolation for power devices, Compatible integrated photodiodes (IPDs) for power switches: Modeling and design, IPD fabrication and characterization, and conclusions and future work. The results of this research work are interesting for a wide range of applications specially as the power electronic community strives for a fully integrated power function with lower implementation costs and reliable, high level galvanic isolation solutions that are compact and cost effective.

**Keywords** *photodetector modelling and design, low cost monolithic integration, optical insulation, galvanic isolation, optical signal transmission, vertical FET technology.*

## L'INTÉGRATION MONOLITHIQUE D'UN PHOTODÉTECTEUR À L'INTÉRIEUR DES TRANSISTORS DE PUISSANCE VERTICAUX POUR DES FINS DE COMMANDE

**Résumé** Les travaux présentés dans ce manuscrit traite de l'intégration monolithique d'une unité d'isolement galvanique optique à l'intérieur de la structure d'un transistor de puissance vertical à effet de champ 600V. L'unité d'isolement galvanique optique est un photodétecteur qui est responsable du transfert du signal de commande de parti une unité de commande externe à le transistor de puissance. L'énergie nécessaire pour commuter le dispositif de puissance est fournie au moyen d'un TIA, suivie d'une commande de grille. Le mémoire de thèse se structure en quatre chapitres équivalents: Introduction et motivation: l'isolement galvanique intégrée pour les dispositifs de puissance, photodiodes intégrés compatibles (JVP) pour les interrupteurs de puissance: Modélisation et conception, IPD fabrication et la caractérisation, et les conclusions et les travaux futurs. Les résultats de ces travaux de recherche sont intéressants pour un large spectre d'applications, spécialement pour les fonctions d'alimentation entièrement intégrés avec et coût de fabrication réduit et des solutions fiables, de haut niveau galvaniques isolement qui sont compacts et rentable.

**Mots clés** *Modélisation et conception de photodétecteur, intégration monolithique fonctionnelle bas coût, isolation et transmission par voie optique, la technologie de FET vertical*

---

## Bibliography

- [1] K. Sozanski, *Digital Signal Processing in Power Electronics Control Circuits*. Springer Verlag Longdon, 2013, ch. 1.
- [2] R. Herzer, "Integrated gate driver circuit solutions," in *Integrated Power Electronics Systems (CIPS), 2010 6th International Conference, IEEE*, 2010.
- [3] T. L. Skvarenina, Ed., *The Power Electronic Handbook*. CRC Press LLC, 2002.
- [4] Alcatel-lucent. Bell labs top 10 innovations. [Online]. Available: [http://www3.alcatel-lucent.com/wps/portal/!ut/p/kcxml/04\\_Sj9SPykssy0xPLMnMz0vM0Y\\_QjzKLd4w3MXMBSYGYRq6m-pEoYgbxjgiRIH1vfV-P\\_NxU\\_QD9gtzQiHJHR0UAPA8KJg!/delta/base64xml/L3dJdyEvd0ZNQUFzQUMvNEIVRS82X0FfNDZL](http://www3.alcatel-lucent.com/wps/portal/!ut/p/kcxml/04_Sj9SPykssy0xPLMnMz0vM0Y_QjzKLd4w3MXMBSYGYRq6m-pEoYgbxjgiRIH1vfV-P_NxU_QD9gtzQiHJHR0UAPA8KJg!/delta/base64xml/L3dJdyEvd0ZNQUFzQUMvNEIVRS82X0FfNDZL)
- [5] B. Baliga, *Fundamentals of Power Semiconductor Devices*. Springer Science + Business Media, LLC, 2008.
- [6] J. Biela, M. Schweizer, S. Waffler, and J. Kolar, "SiC versus Si?evaluation of potentials for performance improvement of inverter and DC-DC converter systems by sic power semiconductors," *IEEE Industrial Electronics Society*, vol. 58, no. 7, pp. 2872 – 2882, 2011.
- [7] R. Perret, Ed., *Power Electronics Semiconductor Devices*. ISTE Ltd and John Wiley & Sons, Inc, 2009.
- [8] (ECPE). Homepage of the european center for power electronics. [Online]. Available: <http://www.ecpe.org>
- [9] (CPES). Homepage of the US center for power electronics systems. [Online]. Available: <http://www.cpes.vt.edu>
- [10] (AIST-PERC). Homepage of the national institute of advanced industrial science and technology - power electronics research center, japan. [Online]. Available: <http://www.aist.go.jp/aiste/annual/2005/environment/perc/percmain.html>
- [11] F. Blaabjerg, A. Consoli, J. Ferreira, and J. Van Wyk, "The future of electronic power processing and conversion," *IEEE Industry Applications Society*, 2005.

- [12] J.-L. Sanchez, P. Austin, M. Breil, J.-P. Laur, J.-C. Crebier, L. Aubard, and C. Schaeffer, "State of the art and trends in power integration," in *Integrated Power Systems (CIPS), 4th International Conference*, 2006, pp. 1 – 6.
- [13] J.-L. Sanchez, "State of the art and trends in power integration," in *International Conference on Modeling and Simulation of Microsystems*, 1999, pp. 20 – 29.
- [14] J. Kolar, J. Biela, S. Waffler, and T. Friedli, "Performance trends and limitations of power electronic systems," in *Integrated Power Electronics Systems (CIPS), 6th International Conference*, Mar. 2010, pp. 1 – 20.
- [15] I. Rectifier, "Data sheet IR 2135, IR 2235," International Rectifier, Tech. Rep.
- [16] S. Microelectronics, "Data sheet, L6384," ST Microelectronics, Tech. Rep., 2003.
- [17] M. S.Pawel, Rossberg and R. Herzer, "600V SOI gate drive HVIC for medium power applications operating up to 200 °c," in *Proc. ISPSD*, 2005, pp. 55 – 58.
- [18] S. K. S. Gupta, J.C. Beckman, "Improved latch up immunity in junction-isolated smart power ICs with unbiased guard ring," *IEEE Electron Device Letters*, vol. 22, no. 12, 2001.
- [19] T. Takahashi, "Power conversion processor architecture and HVIC technology for AC motor drive," in *Proc. CIPS*, 2000, pp. 73–81.
- [20] D. Tam, "New 1200V integrated circuit changes the way 3-phase motor drive inverters are designed," International Rectifier, Tech. Rep., 2008.
- [21] H. Akiyama, N. Yasuda, J. Moritani, and K. Takanashi, "A high breakdown voltage IC with lateral power device based on SODI structure," in *Proc. ISPSD*, 2004, pp. 375 – 378.
- [22] T. Yamane, S. Ikeda, and A. Nakagawa, "Three-phase sinusoidal current PWM brushless motor driver ICs," in *Proc. ISPSD*, 2004, pp. 147 – 150.
- [23] M. Huque, L. Tolbert, B. Blalock, and S. Islam, "Silicon-on-insulator-based high-voltage, high-temperature integrated circuit gate driver for silicon carbide-based power field effect transistors," *Power Electronics, IET*, vol. 3, no. 6, pp. 1001 – 1009, Nov. 2010.
- [24] C. Caramel, P. Austin, J.-L. Sanchez, E. Imbernon, and R. B., "Interaction analysis and insulation techniques for short-circuit integrated protection structure," in *Proc. ISPSD*, 2006, pp. 1 – 4.
- [25] J.-L. Sanchez and all, "Realization of P+ walls through-wafer for bidirectional current and voltage power integrated devices," in *Proc. ISPSD*, 2003, pp. 195 – 198.
- [26] I. Bertrand and all, "New lateral dmos and igbt structures realized on a partial soi substrate based on lego process," in *Bipolar/BiCMOS Circuits and Technology Meeting*, 2005, pp. 74 – 77.

- [27] S. LEFEBVRE and B. MULTON, “Commande des semi-conducteurs de puissance: contextes.” *Techniques de l'ingénieur*, no. D3230, August 2002.
- [28] Avago, “Safety considerations when using optocouplers and alternative isolators for providing protection against electrical hazards,” Avago Technologies, Tech. Rep., 2010.
- [29] B. Chen, “Fully integrated isolated DC-to-DC converter and half bridge gate driver with integral power supply,” 1st International Workshop on Power Supply on Chip, Analog Devices, Tech. Rep., 2008.
- [30] J.-C. Crebier and N. Rouger, “Loss free gate driver unipolar power supply for high side power transistors,” *IEEE Transactions on Power Electronics*, vol. 23, no. 3, pp. 1565 –1573, May 2008.
- [31] D. Vasic, F. Costa, and E. Sarraute, “Piezoelectric transformer for integrated MOS-FET and IGBT gate driver,” *Power Electronics, IEEE Transactions on*, 2005.
- [32] R. Kliger, “Integrated transformer-coupled isolation,” *Instrumentation & Measurement Magazine, IEEE*, 2003.
- [33] D. Oliveira, M. Batista, L. Barreto, and P. Praca, “A bidirectional single stage DC-DC converter with high frequency isolation,” in *Applied Power Electronics Conference and Exposition (APEC), 2013 Twenty-Eighth Annual IEEE*, 2013.
- [34] H. Fan and H. Li, “High-frequency transformer isolated bidirectional DC-DC converter modules with high efficiency over wide load range for 20 kVA solid-state transformer,” *Power Electronics, IEEE Transactions on*, vol. 26, no. 12, pp. 3599 – 3608, Dec. 2011.
- [35] L. Peng, R. Wu, X. Fang, Y. Toyoda, M. Akahane, M. Yamaji, H. Sumida<sup>3</sup>, and J. K. Sin, “A novel 3D TSV transformer technology for digital isolator gate driver applications,” in *Proceedings of The 25th International Symposium on Power Semiconductor Devices & ICs (ISPSD)*, 2013.
- [36] S. Mazumder and T. Sarkar, “Optically-activated gate control of power semiconductor device switching dynamics,” in *IEEE International Symposium on Power Semiconductor Devices IC's*, 2009, pp. 152 –155.
- [37] N. Rouger and J.-C. Crebier, “Integrated photoreceiver for an isolated control signal transfert in favour of power transistors,” in *IEEE International Symposium on Power Semiconductor Devices and IC's*, May 2008, pp. 213 –216.
- [38] A. Alessandria, L. La Magna, M. Renna, and L. Fracapane, “Integrated si-based opto-couplers: a novel approach to galvanic isolation,” in *Solid-State Device Research Conference, 2002. Proceeding of the 32nd European*, 2002, pp. 647 – 650.
- [39] M. Lazarus, K. Loungis, and V. Allen, “Optically controlled high-speed switching of a power transistor,” *Circuits and Systems I: Fundamental Theory and Applications, IEEE Transactions on*, vol. 47, no. 4, pp. 528 – 535, 2000.

- [40] F. Zeltner, S. IISB and Erlangen, “Insulating IGBT driver with PCB integrated capacitive coupling elements,” in *Integrated Power Electronics Systems (CIPS), 6th International Conference on*, 2010.
- [41] S. Brehaut and F. Costa, “Gate driving of high power igbt by wireless transmission,” in *IEEE Power Electronics and Motion Control Conference*, 2006, pp. 1–5.
- [42] B. Wang, M. Riva, J. Bakos, and A. Monti, “Integrated circuit implementation for a gan hfet driver circuit,” *Industry Applications, IEEE Transactions on*, vol. 46, no. 5, pp. 2056–2067, Sept.-Oct. 2010.
- [43] A. Devices. Digital isolators. [Online]. Available: [http://www.analog.com/en/interface-isolation/digital-isolators/products/index.html#Isolated\\_Gate\\_Drivers](http://www.analog.com/en/interface-isolation/digital-isolators/products/index.html#Isolated_Gate_Drivers)
- [44] C. Batard *et al.*, “Wireless transmission of igbt driver control,” in *IEEE Applied Power Electronics Conference and Exposition*, 2009, pp. 1257–1262.
- [45] K. Gingerich and C. Sterzik, “The ISO72x family of high-speed digital isolators,” Texas Instruments, Tech. Rep., 2006.
- [46] Avago. Digital isolators. [Online]. Available: [http://www.analog.com/en/interface-isolation/digital-isolators/products/index.html#Isolated\\_Gate\\_Drivers](http://www.analog.com/en/interface-isolation/digital-isolators/products/index.html#Isolated_Gate_Drivers)
- [47] Opto-isolator. [Online]. Available: [http://en.wikipedia.org/wiki/Optical\\_coupler](http://en.wikipedia.org/wiki/Optical_coupler)
- [48] J. Seah Eng Lee, A. Jaus, P. Sullivan, and C. Teck Bee, “Building a safe and robust industrial system with avago technologies optocouplers,” Avago Technologies, Tech. Rep., 2008.
- [49] V. Ching and F. Chwan JYE, “Ensuring rigorous isolation in field bus designs,” Avago Technologies, Tech. Rep., 2012.
- [50] (Avago). Optoisolation and optical sensor products selection guide. [Online]. Available: [http://www.google.fr/url?sa=t&rct=j&q=&esrc=s&source=web&cd=4&ved=0CEMQFjAD&url=http%3A%2F%2Fwww.avagotech.com%2Fdocs%2FAV00-0263EN&ei=WvtaUuPJHePX0QXDvoCoAg&usg=AFQjCNHrrJ4IYuZZcS6MJGfriqJA3WM9bw&sig2=4-vm1Vd\\_kBbXB6nmYnXaog&bvm=bv.53899372,d.d2k&cad=rja](http://www.google.fr/url?sa=t&rct=j&q=&esrc=s&source=web&cd=4&ved=0CEMQFjAD&url=http%3A%2F%2Fwww.avagotech.com%2Fdocs%2FAV00-0263EN&ei=WvtaUuPJHePX0QXDvoCoAg&usg=AFQjCNHrrJ4IYuZZcS6MJGfriqJA3WM9bw&sig2=4-vm1Vd_kBbXB6nmYnXaog&bvm=bv.53899372,d.d2k&cad=rja)
- [51] Avago. Hcpl-665k. [Online]. Available: [http://www.avagotech.com/pages/en/optocouplers\\_hermetic/10\\_mbd\\_high\\_cmr\\_four\\_channel/hcpl-665k/](http://www.avagotech.com/pages/en/optocouplers_hermetic/10_mbd_high_cmr_four_channel/hcpl-665k/)
- [52] P. Horowitz Winfield Hill, *The Art Of Electronics*. Cambridge University Press, 1989.
- [53] B. Kennedy, “Implementing an isolated half-bridge gate driver,” Analog Devices, Tech. Rep., 2012.
- [54] Electromagnetic induction. [Online]. Available: [http://en.wikipedia.org/wiki/Faraday%27s\\_law\\_of\\_induction#Faraday.27s\\_law](http://en.wikipedia.org/wiki/Faraday%27s_law_of_induction#Faraday.27s_law)

- [55] V. Nguyen, J.-C. Crebier, and P. Jeannin, "Compact, isolated and simple to implement gate driver using high frequency transformer," in *APEC*, 2011.
- [56] L. Ourak, A. Ghannam, D. Bourrier, and C. Viallon, "Solenoidal transformers for magnetic materials integration," in *APMC*, 2012.
- [57] Transformer types. [Online]. Available: [http://en.wikipedia.org/wiki/Transformer\\_types#Pulse\\_transformer](http://en.wikipedia.org/wiki/Transformer_types#Pulse_transformer)
- [58] SCHURTER, "Efficient EMC solutions," SCHURTER, Tech. Rep., 2009.
- [59] B. Chen, "Application note AN-937: Gate drive characteristics and requirements for HEXFET power MOSFETs," International Rectifier, Tech. Rep., 1995-2013.
- [60] B. Kennedy, "Reducing the size and complexity of an isolated," Analog Devices, Tech. Rep., 2011.
- [61] B. Bell, "Gate drive transformers vs. fully integrated isolators in isolated DC-DC power converters," National Semiconductor Corporation, Tech. Rep., 2010.
- [62] Y. Koike and M. Asai, "The future of plastic optical fiber," *Nature, NPG Asia Materials*, vol. 1, pp. 22-28, 2009.
- [63] O. Ziemann, J. Krauser, P. Zamzow, and W. Daum, *POF Handbook: Optical Short range Transmission Systems*. Springer, 2008.
- [64] (Berkeley). Electromagnetic spectrum. [Online]. Available: <http://www.lbl.gov/MicroWorlds/ALSTool/EMSpec/EMSpec2.html>
- [65] *Tutorial: Fiber Optic Basics*, 1996-2013.
- [66] M. Wappmannsberger, "Galvanic isolation for IGBT-driver," Avago Technologies, Tech. Rep., 2013.
- [67] J. e. a. Nishizawa, "Fabrication and optical-switching results on the integrated light-triggered and quenched static induction thyristor," *Electron Devices, IEEE Transactions*, vol. 33, no. 12, pp. 2031 - 2040, Dec. 1986.
- [68] B. Danielsson and A. P. Syst., "Hvdc valve with light-triggered thyristors," in *IEEE AC and DC Power Transmission*, Sep. 1991.
- [69] S. L. Rumyantsev, M. E. Levinshtein, M. Shur, T. Saxena, Q. Zhang, A. K. Agarwal, L. Cheng, and J. W. Palmour, "Optical triggering of 12 kV 1 cm<sup>2</sup> 4H-SiC thyristors," *Materials Science Forum*, vol. 740 - 742, pp. 990-993, 2013.
- [70] (Siemens). New static var compensator (SVC) for australia. [Online]. Available: <http://www.ptd.siemens.de/artikel0507.html>
- [71] T. Sarkar and S. K. Mazumder, "Epitaxial design of a direct optically controlled gaas/algaas-based heterostructure lateral superjunction power device for fast repetitive switching," *IEEE Transactions on Electron Devices*, vol. 54, no. 3, pp. 589 -600, 2007.

- [72] F. Zhao, M. Islam, P. Muzykov, and A. Bolotnikov, "Optically activated 4H-SiC p-i-n diodes for high-power applications," *IEEE Electron Device Letters*, vol. 30, pp. 1182 – 1184, 2009.
- [73] F. Zhao and M. Islam, "Optically activated SiC power transistors for pulsed-power application," *IEEE Electron Device Letters*, vol. 31, pp. 1146 – 1148, 2010.
- [74] W. Naoki, K. Tsunenobu, and S. Jun, "4H-SiC pn photodiodes with temperature-independent photoresponse up to 300 °C," *Applied Physics Express*, vol. 5, 2012.
- [75] C. James, C. Hettler, and J. Dickens, "Design and evaluation of a compact silicon carbide photoconductive semiconductor switch," *IEEE Transactions on Electron Devices*, vol. 58, pp. 508 – 511, 2011.
- [76] H. Fujita, "A resonant gate-drive circuit with optically isolated control signal and power supply for fast-switching and high-voltage power semiconductor devices," *Power Electronics, IEEE Transactions*, vol. 28, no. 11, pp. 5423 – 5430, 2013.
- [77] M. E. Thomas, *Optical Propagation in Linear Media: Atmospheric Gases and Particles, Solid-State Components, and Water*. Oxford University Press, 2006.
- [78] S. M. Sze and K. N. Kwok, *Physics of Semiconductor Devices, Third Edition*. JOHN WILEY & SONS, JNC., 2007.
- [79] C. o. E. Committee on Materials for High-Temperature Semiconductor Devices National Advisory Board and T. Systems, Eds., *Materials for high-temperature semiconductor devices*. National Academy Press, Washington, DC, NMAB-474, 1995, 1995.
- [80] M. Welker, D. Zipperer, S. Malzer, R. Windisch, P. Heremans, and G. Dohler, "High-speed low-energy photoconductive receiver with high gain," in *SPIE*, 2001.
- [81] X. Li, J. E. Carey, J. W. Sickler, M. U. Pralle, C. Palsule, and C. J. Vineis, "Silicon photodiodes with high photoconductive gain at room temperature," *Optics Express*, vol. 20, no. 5, pp. 5518–5523, 2012.
- [82] M. Yang, J. Thomas, K. Rim, D. Rogers, and J. e. a. Schaub, "A high-speed, high-sensitivity silicon lateral trench photodetector," *Electron Device Letters, IEEE*, vol. 23, no. 7, pp. 395 – 397, 2002.
- [83] S. Assefa, F. Xia, S. W. Bedell, Y. Zhang, T. Topuria, P. M. Rice, and V. Y.A., "CMOS-integrated high-speed MSM germanium waveguide photodetector," *Optics Express*, vol. 18, no. 5, pp. 4986–4999, 2010.
- [84] A. Pospischil, M. Humer, M. M. Furchi, D. Bachmann, R. Guider, T. Fromherz, and T. Mueller, "Cmos-compatible graphene photodetector covering all optical communication bands," *Nature Photonics*, 2013.
- [85] J. Mathews, R. Roucka, C. Weng, J. Tolle, J. Menéndez, and J. Kouvetakis, "Germanium p-i-n photodiode on silicon for integrated photonic applications," in *Proc. SPIE 7606, Silicon Photonics*, 2012.

- [86] L. Vivien, A. Polzer, D. M. Morini, J. Osmond, J. M. Hartmann, P. Crozat, E. Casan, C. Kopp, H. Zimmermann, and J. M. Fedeli, “Zero-bias 40Gbit/s germanium waveguide photodetector on silicon,” *Optics Express*, vol. 20, no. 2, pp. 1096–1101, 2012.
- [87] S. Klinger, M. Berroth, M. Kaschel, and M. e. a. Oehme, “Ge-on-Si p-i-n photodiodes with a 3-dB bandwidth of 49 GHz,” *Photonics Technology Letters, IEEE*, vol. 21, no. 13, pp. 920 – 922, 2009.
- [88] N. Rouger, “Intégration monolithique des fonctions d’interface au sein de composants de puissance à structure verticale,” Ph.D. dissertation, Institut Polytechnique de Grenoble, laboratoire de Génie Électrique de Grenoble, 2008.
- [89] N. Rouger, J.-C. Crebier, and O. Lesaint, “Integrated low power and high bandwidth optical isolator for monolithic power mosfets driver,” in *IEEE International Symposium on Power Semiconductor Devices and ICs*, may 2011.
- [90] T. L. Le, “Isolation galvanique intégrée pour nouveaux transistors de puissance,” Ph.D. dissertation, Institut Polytechnique de Grenoble, laboratoire de Génie Électrique de Grenoble, 2015.
- [91] Abundance of the chemical elements. [Online]. Available: [http://en.wikipedia.org/wiki/Abundance\\_of\\_the\\_chemical\\_elements#Abundance\\_of\\_elements\\_in\\_the\\_Earth](http://en.wikipedia.org/wiki/Abundance_of_the_chemical_elements#Abundance_of_elements_in_the_Earth)
- [92] O. Trapp, R. Blanchard, L. Lopp, and T. Kamins, Eds., *Semiconductor Technology Handbook*. Technology Associates, 1985.
- [93] W. Shockley, “The Theory of p-n Junctions in Semiconductors and p-n Junction Transistors,” *Bell System Technical Journal*, vol. 28, pp. 435 – 489, 1949.
- [94] R.-Y. Sah, R. N. Noyce, and W. Shockley, “Carrier Generation and Recombination in P-N Junctions and P-N Junction Characteristics,” in *Proceedings of the IRE*, vol. 45, no. 9, Sep. 1957, pp. 1228 – 1243.
- [95] J. Moll and N. Murray Hill, “The Evolution of the Theory for the Voltage-Current Characteristic of P-N Junctions,” in *Proceedings of the IRE*, vol. 46, no. 6, Jun. 1958, pp. 1076 – 1082.
- [96] D. L. PULFREY, *Understanding Modern Transistors and Diodes*. Cambridge University Press, 2010.
- [97] Silvaco, “Atlas User’s Manual Device Simulation Software,” Silvaco, Tech. Rep., 2008.
- [98] M. Fox, *Optical Properties of Solids*. New York, Oxford University Press, 2003.
- [99] A. Yariv and Y. Pochi, *Photonics, Optical Electronics in Modern Communications*. New York, Oxford University Press, 2007.
- [100] J. Zhao, A. Wang, and M. Green, “24.5Substrates and 24.7Progress in Photovoltaics: Research and Applications, vol. 7, pp. 471 ? 474,, Nov. 1999.

- [101] W. Shockley and W. Read, "Statistics of the Recombinations of Holes and Electrons," *Journal of Physical Review*, vol. 87, p. 835, 1952.
- [102] V. Barkhordarian, "Power MOSFET basics," International Rectifier, Tech. Rep.
- [103] D. K. SCHRODER, *SEMICONDUCTOR MATERIAL AND DEVICE CHARACTERIZATION*. A JOHN WILEY & SONS, INC., PUBLICATION, 2006.
- [104] T. Simonot, "Conception et hybridation de l'environnement électronique des composants de puissance à structure verticale," Ph.D. dissertation, Institut Polytechnique de Grenoble, laboratoire de Génie Électrique de Grenoble, 2011.
- [105] H. N. XUAN, "Méthodes et modèles pour une approche de dimensionnement géométrique et technologique d'un semi-conducteur de puissance intégré. application à la conception d'un mosfet autonome," Ph.D. dissertation, Institut Polytechnique de Grenoble, laboratoire de Génie Électrique de Grenoble, 2011.
- [106] K. Vladimirova, "Nouveaux concepts pour l'intégration 3d et le refroidissement des semi-conducteurs de puissance à structure verticale," Ph.D. dissertation, Institut Polytechnique de Grenoble, laboratoire de Génie Électrique de Grenoble, 2012.
- [107] R. Vafaei, N. Rouger, D. To, and J.-C. Crebier, "Experimental investigation of an integrated optical interface for power mosfets drivers," *IEEE Electron Device Letters*, vol. 33, 2012.
- [108] R. Vafaei, N. Rouger, and J.-C. Crebier, "Performance Measurements of an Optical Detector Designed for Monolithic Integration with a Power VDMOS," in *IEEE I2MTC*, May 2013.
- [109] M. Cvijetic, *Optical Transmission Systems Engineering*. ARTECH HOUSE, INC., 2004.
- [110] (Edmunds). Variable gain high speed current amplifier dhpca-100. [Online]. Available: [http://www.femto.de/images/pdf-dokumente/de-dhpca-100\\_r9.pdf](http://www.femto.de/images/pdf-dokumente/de-dhpca-100_r9.pdf)
- [111] (Z-Laser). Z40m18h-f-450-lp45. [Online]. Available: [http://www.datasheetlib.com/datasheet/1167261/z40m18h-f-450-lp45\\_z-laser.html](http://www.datasheetlib.com/datasheet/1167261/z40m18h-f-450-lp45_z-laser.html)
- [112] T. Simonot, N. Rouger, and J. Crebier, "Design and characterization of an integrated cmos gate driver for vertical power mosfets," in *IEEE Energy Conversion Congress and Exposition*, 2010, pp. 2206 –2213.

